Geometric Nonlinear Finite Element and Genetic Algorithm Based Vibration Energy Harvesting from Functionally Graded Nonprismatic Piezolaminated Beams

Alok Ranjan Biswal

Department of Mechanical Engineering
National Institute of Technology Rourkela

Geometric Nonlinear Finite Element and Genetic Algorithm Based Vibration Energy Harvesting from Functionally Graded Nonprismatic Piezolaminated Beams

Dissertation submitted in partial fulfillment

of the requirements of the degree of

Doctor of Philosophy

in

Mechanical Engineering

by

Alok Ranjan Biswal

(Roll Number: 512ME106)

based on research carried out

under the supervision of

Prof. Rabindra Kumar Behera

and

Prof. Tarapada Roy

Department of Mechanical Engineering
National Institute of Technology Rourkela
November, 2017

November 11, 2017

Certificate of Examination

Roll Number: *512ME106*

Name: *Alok Ranjan Biswal*

Title of Dissertation: *Geometric Nonlinear Finite Element and Genetic Algorithm Based Vibration Energy Harvesting from Functionally Graded Nonprismatic Piezolaminated Beams.*

We the below signed, after checking the dissertation mentioned above and the official record book (s) of the student, hereby state our approval of the dissertation submitted in partial fulfilment of the requirements for the degree of *Doctor of Philosophy* in Mechanical *Engineering* at *National Institute of Technology Rourkela*. We are satisfied with the volume, quality, correctness, and originality of the work.

Tarapada Roy Co-Supervisor	Rabindra Kumar Behera Principal Supervisor
Hara Prasad Roy Member, DSC	Pradip Sarkar Member, DSC
Robin Davis P Member, DSC	Kalipada Maity Chairperson, DSC
HOD Mechanical Engineering	External Examiner

Department of Mechanical Engineering
National Institute of Technology Rourkela

Prof. Rabindra Kumar Behera

Associate Professor

Prof. Tarapada Roy

Assistant Professor

November 11, 2017

Supervisors' Certificate

This is to certify that the work presented in the dissertation entitled *Geometric Nonlinear Finite Element and Genetic Algorithm Based Vibration Energy Harvesting from Functionally Graded Nonprismatic Piezolaminated Beams* submitted by *Alok Ranjan Biswal*, Roll Number 512ME106, is a record of original research carried out by him under our supervision and guidance in partial fulfilment of the requirements for the degree of *Doctor of Philosophy* in *Mechanical Engineering*. Neither this dissertation nor any part of it has been submitted earlier for any degree or diploma to any institute or university in India or abroad.

Tarapada Roy

Assistant Professor

Rabindra Kumar Behera

Associate Professor

Dedication

In memory of my Father

To My mother
With love and eternal appreciation

Alok Ranjan Biswal

Declaration of Originality

I, *Alok Ranjan Biswal*, Roll Number *512ME106* hereby declare that this dissertation entitled *Geometric Nonlinear Finite Element and Genetic Algorithm Based Vibration Energy Harvesting from Functionally Graded Nonprismatic Piezolaminated Beams* presents my original work carried out as a doctoral student of NIT Rourkela and, to the best of my knowledge, contains no material previously published or written by another person, nor any material presented by me for the award of any degree or diploma of NIT Rourkela or any other institution. Any contribution made to this research by others, with whom I have worked at NIT Rourkela or elsewhere, is explicitly acknowledged in the dissertation. Works of other authors cited in this dissertation have been duly acknowledged under the sections "Reference" or "Bibliography". I have also submitted my original research records to the scrutiny committee for evaluation of my dissertation.

I am fully aware that in case of any non-compliance detected in future, the Senate of NIT Rourkela may withdraw the degree awarded to me on the basis of the present dissertation.

November 11, 2017
NIT Rourkela   *Alok Ranjan Biswal*

Acknowledgment

Before I dwell on the amount of hard work, long hours and sometimes infuriating moments which have littered the last few years. I am very fortunate to come across with a great number of people whose inspiration, guidance, help, and support helped in my field of research, and they deserve special thanks. Without them, I would never have been able to finish this dissertation.

First and foremost, my deepest sense of gratitude and indebtedness to my supervisors **Prof. Rabindra Kumar Behera** and **Prof. Tarapada Roy** for their countless advises and patient encouragement. They shared with me their brilliant insight and great vision on my research. They showed me as an example how to be a good researcher but at the same time a great leader and personnel. I have been really fortunate to have these advisors who could provide me such a wonderful guidance to this long journey. They not only gave me the freedom to explore on my own but also guided me when my steps flattered. Their patience and insightful advice helped me to conquer a number of hurdles over time. These abilities, as well as their passion for science and learning, will continue to affect my future endeavours. I remain grateful to them forever.

Besides my supervisors, I am highly obliged to **Prof. Animesh Biswas**, our Honourable Director, and **Prof. Kamalakanta Mahapatra**, Dean (Academic Affairs) of National Institute of Technology Rourkela for giving an opportunity to be a part of this institute of national importance and provided me the academic support.

I would like to express my deepest gratitude to **Prof. Dayal Ramakrushna. Parhi**, Head of the department, Department of Mechanical Engineering, for his moral support. He shared his vast knowledge and experience in the research field and provided me tremendous help to counter the tough and trying moments. I am incredibly grateful to the members of my doctoral scrutiny committee (DSC):**Prof. K. P. Maity** (Chairman, DSC), Department of Mechanical Engineering, **Prof. H. Roy**, Department of Mechanical Engineering, **Prof. P. Sarkar**, Department of civil Engineering and **Prof. R. Davis P**, Department of civil Engineering for their indebted help and valuable suggestions during the research work. I would also like to express my sincere gratitude to Ex DSC member **Prof. (Mrs) A.V.Asha**, Department of civil Engineering for her timely valuable suggestion during research work. I extend my heartfelt thanks to all the faculty and staff members of the Mechanical Engineering for their continuous encouragement and suggestions.

I would like to thank **Sudhansu Meher, M L Pavankishore**, **Ashirbad Swain, Benedict Thomas, Vigneshwaran K, Bala Murugan S** and **Bashir Asdaque** who apart

from becoming lab mates over the last few years, (almost) always opened their door to me when I needed someone to bounce ideas off, subdue frustrations or just have a coffee with. Meanwhile, without these researchers, many problems would have taken a longer to solve. I thank my fellow mates **Swayam Bikash Mishra, Priyadarshi Tapas Ranjan Swain, Swastik Pradhan, Manisha Priyadarshini, Ashutosh Pattanaik, Mantra Prasad Satpathy, Bikash Ranjan Moharana, and Subrat Bhuyan** for the stimulating discussions, for the sleepless nights we were working together before deadlines, and for all the fun we have had in the last four years. The time spent with them will remain in my memory for years to come.

Finally, I would like to thank my family to whom I owe a great deal. To my late father **Mr. Umesh Kumar Biswal** thank you for showing me that the key to life is enjoyment. To my brother **Mr. Deepak Ranjan Biswal** and sister-in-law **Mrs. Ipsita Nayak** thank you for their sacrifices and constant support. Also thanks to my elder sister **Mrs. Mousumi Manjari Biswal**, brother-in-law **Mr. Prasanna Das** and my nephew **Prince** for standing nearby me in all those days. And finally, the one person who has made this all possible has been my mother **Mrs. Snehalata Biswal**. She has been a constant source of support and encouragement and has made an untold number of sacrifices for the entire family, and specifically for me to continue my education. She has been a great inspiration to me. Hence, great appreciation and enormous thanks are due to her, for without her understanding, I am sure this thesis would never have been completed. I thank you all.

November 11, 2017   *Alok Ranjan Biswal*
NIT Rourkela   Roll Number: 512ME106

Abstract

Energy harvesting technology has the ability to create autonomous, self-powered systems which do not rely on the conventional battery for their operation. The term energy harvesting is the process of converting the ambient energy surrounding a system into some useful electrical energy using certain materials. Among several energy conversion techniques, the conversion of ambient vibration energy to electrical energy using piezoelectric materials has great deal of importance which encompasses electromechanical coupling between mechanical and electrical domains. The energy harvesting systems are designed by incorporating the piezoelectric materials in the host structure located in vibration rich environment. The work presented in this dissertation focuses on upgrading the concept of energy harvesting in order to engender more power than conventional energy harvesting designs.

The present work deals with first the finite element (FE) formulation for coupled thermo-electro-mechanical analysis of vibration energy harvesting from an axially functionally graded (FG) non-prismatic piezolaminated cantilever beam. A two noded beam element with two degrees of freedom (DOF) at each node has been used in the FE formulation. The FG material (i.e. non-homogeneity) in the axial direction has been considered which varies (continuously decreasing from root to tip of such cantilever beam) using a proposed power law formula. The various cross section profiles (such as linear, parabolic and cubic) have been modelled using the Euler-Bernoulli beam theory and Hamilton's principle is used to solve the governing equation of motion. The simultaneous variation of tapers (both width and height in length directions) is incorporated in the mathematical formulation. The FE formulation developed in the present work has been compared with the analytical solutions subjected to mechanical, electrical, thermal and thermo-electro-mechanical loading. Results obtained from the present work shows that the axially FG nonprismatic beam generates more output power than the conventional energy harvesting systems. Further, the work has been focussed towards the nonlinear vibration energy harvesting from an axially FG non-prismatic piezolaminated cantilever beam. Geometric nonlinear based FE formulation using Newmark method in conjunction with Newton-Raphson method has been formulated to solve the obtained governing equation. Moreover, a real code GA based constrained optimization technique has also been proposed to determine the best possible design variables for optimal power harvesting within the allowable limits of ultimate stress of the beam and voltage of the PZT sensor. It is observed that more output power can be obtained based on the present optimization

formulation within the allowable limits of stress and voltage than that of selection of design variables by trial and error in FE modelling.

Contents

List of Figures

xxii

List of tables

Nomenclature

$Y(x,T)$	Material Properties
x	Arbitrary distance from the fixed end of the beam
T	Average temperature between top and bottom surfaces of the beam.
L_b	Length of the beam
np	Power gradient index
$A_b(x)$	Cross-sectional area of the beam at any arbitrary distance from the fixed end
c_b	Width taper
c_h	Height taper
q_u, q_w	Nodal degrees of freedom
θ	Surface temperature vectors
N_w	Hermite cubic interpolation or shape function
N_θ	Interpolation or shape function for constant temperature function
ε_1	Bending strain
B_w, B_{nw}	Linear and nonlinear strain displacement matrix
B_v	Electric potential gradient matrix
c_v	Specific heat at constant volume
P	Output Power
σ	Stress over the piezoelectric patch
R	External load resistance
ζ_i	Damping ratio of the structure
Q_r	Electrode surface charge
$H(u)$	Fitness function
ω	Natural frequency
M_b^e, M_p^e	Element mass matrix of beam and piezoelectric patch

$K_b{}^e$, $K_p{}^e$ Element stiffness matrix of beam and piezoelectric patch

$K_{pb}{}^e$ Piezoelectric coupling matrix

$K_{pp}{}^e$ Capacitance matrix

$K_{b\theta}{}^e$ Thermo-elastic stiffness matrix

$K_{p\theta}{}^e$ Pyroelectric stiffness matrix

Chapter 1

Introduction

1.1 Background

In the present world, the human civilization is unmistakably moving towards the technological way of life. The portable products have touched their highest demands. These devices not only provide unbelievable power but also add versatility in communication and way of solving problems. However, the miniaturization of wireless devices are hindered by conventional batteries, which acts as the traditional power sources of many portable electronics and wireless sensors in current technology. Besides, the disadvantages of batteries also include the finite amount of energy or limited time span, large maintenance requirements, very high mass to electrical power ratio, and possibly hazardous chemicals and their environmental effects. The limited time span of a battery makes the device not so reliable because it may stop working at any time without warning. The dead battery has to be replaced which is a tedious and expensive task, especially when the device is located in a remote location. The very high mass to electrical power ratio of a battery impedes the development of light-weight wireless devices. Most batteries often involve hazardous chemicals, so inappropriate disposal or recycling may induce dangerous elements into the environment. More dangerously, a battery explosion is also caused by the misuse or malfunction of a battery. This may lead to vital property loss. Consequently, batteries have to be replaced for miniature wireless devices. In this context, if the ambient energy in the surrounding medium could be obtained, then it may be used to replace or charge the battery.

1.2 A potential solution—energy harvesting

Based on this, the concept of energy harvesting comes into an act which emphasizes on capturing the ambient waste energy and converting it into useable electricity. Since small autonomous wireless devices such as wireless sensors developed in MEMS technology demand a little power, small scale energy harvesting devices show the potential to replace the conventional batteries by converting ambient waste energy into

electricity and powering these low power consumption and small sized devices. Since last few decades, several research works have been conducted to achieve small volume and completely self-powered electronics devices. Some of the systems are microelectromechanical systems (MEMS) and remote sensing devices.

1.2.1 Mechanical vibration

For the last few decades, a variety of ambient sources such as solar, thermal, acoustic noise, acoustic energy, nuclear power, human, and mechanical vibration have been studied as an additional energy supplier. Among them, vibration driven power generators, thermoelectric generators, and solar cells are more widely studied because of their pervasiveness, high efficiency, and potentials for miniaturization. However, thermal energy is hard to control, cannot be used for a medical implant, and its conversion efficiency is found to be lower. The outdoor solar energy has the much higher power density than that of indoor solar energy. On the contrary, mechanical vibration has been demonstrated to offer great potential, limited lifespan and relatively high power density where there is an insufficient light source. Vibration sources can be readily found in accessible locations such as air ducts and building structures.

1.2.2 Mechanical structures

Among the several mechanical structures the cantilever beam is the simplest one and the most widely used configuration for energy harvesting. It allows for tuning the resonant frequency to match the frequency of the ambient vibrations. Therefore, causing larger structural deformations and large strain will produce electrical energy for a given input.

1.2.2.1 Structural modifications

For a piezoelectric energy harvester, the reasonable goal is to maximize the amount of energy produced for a given ambient vibration condition. Therefore, one of the objectives of the proposed research is to study the effect of energy harvester geometry on the corresponding voltage and output power. A modified model based on the earlier studies is proposed which may give better results than the previous models; however, it also has limitations when compared with finite element analysis (FEA). In the design of more complex piezoelectric energy harvesters (PEH) structures, FEA is preferred, as traditional

analytical modelling for such structures may be impractical. As a result, more design options can be considered to study the behavior of PEH electrical energy generation.

1.2.2.2 Geometric nonlinearity

The analysis of linear systems is much easier due to its limited application, but in reality, majority of natural systems are nonlinear. Unlike linear systems, the principle of superposition does not hold good for nonlinear systems. In fact, in any mechanical system, several types of nonlinearity may exist; the most common are material, geometrical, and inertial. Further, the presence of dynamic loadings in most of the beam structures lead to large oscillation amplitudes and therefore, involved in the geometrically nonlinear regime. Geometric nonlinearity is associated with large displacements that results in nonlinear strain-displacement relationship. If the large-amplitude vibrations are accompanied by large changes in the curvature, it is required to employ a nonlinear relationship between the curvature and the displacement. As the low mass and highly flexible structures are credentially essential for piezoelectric energy harvesting systems, the geometric nonlinear effects due to large deformations cannot be overlooked. Hence, for accurate estimation of voltage sensed by piezoelectric material along with output power of an energy harvester, the geometric nonlinear effect is essentially needed.

1.2.3   Functionally graded material

In present world, the requirement for optimum performance from every product while keeping the designs simple has given rise to special materials for customized applications. For this case the composite materials have been receiving a lot of attention. One of the benefits of the composite materials is that their properties could be functionally oriented to suit a specific application. Such composites are termed as Functionally Graded Materials (FGM).

FGM are one of the most emerging materials nowadays which are used in various engineering applications. By varying the gradient composition of constituents, properties such as modulus of elasticity and mass density could vary continuously in the desired direction to maintain continuity in stress and strain fields. Functionally graded materials are combinations of two or more materials whose volume fractions change gradually along desired special directions, resulting in a smooth and continuous change in their

effective properties. The flexibility of the resulting materials encompasses the structural design spaces by implementing the desired multi-functional response with a minimal weight increase. The FGMs are mainly manufactured by combining metals and ceramics. Since ceramics withstand the high temperatures and provide a thermal defending to the given system, and metals can give the structural support to the given system, such materials are useful for high-temperature applications with specified physical properties. The material properties of the FGMs change with volume fractions of its constituent phases along the spatial directions. It is therefore possible to modify properties like strength, toughness, and thermal capability of the material. Due to the variation in properties they are increasingly used in many engineering sectors like space vehicles, aerospace, automotive, biomedical, optics, electronics, and military applications, etc. According to the variation FGM are subdivided into two categories- axially and transverse based FGM. In the axially based FGM, all the material properties vary in different proportions along the longitudinal axis. But in the latter case all the material properties varies in transverse direction. Though the material can be graded in spatial direction, axially based FGM is treated as a good alternative to overcome the principal disadvantages of others such as residual stresses, locally plastic deformation, debonding between adjacent surfaces of different materials and so on.

1.3 Modes of transducers

To design and build vibration-based energy harvesting devices, three types of electromechanical transducers such as electrostatic, electromagnetic, and piezoelectric are utilized as shown in Figure 1.1 [1]. The approximate power density of the above three conversion mechanisms are compared and the piezoelectric energy harvesting devices were observed to possesses many advantages over other two mechanisms such as simple configuration, high converting efficiency, and precise control. Apart from this, the piezoelectric power generators present higher power output, simpler configuration, and potential of miniaturization. It is therefore chosen as objective of the study of this dissertation.
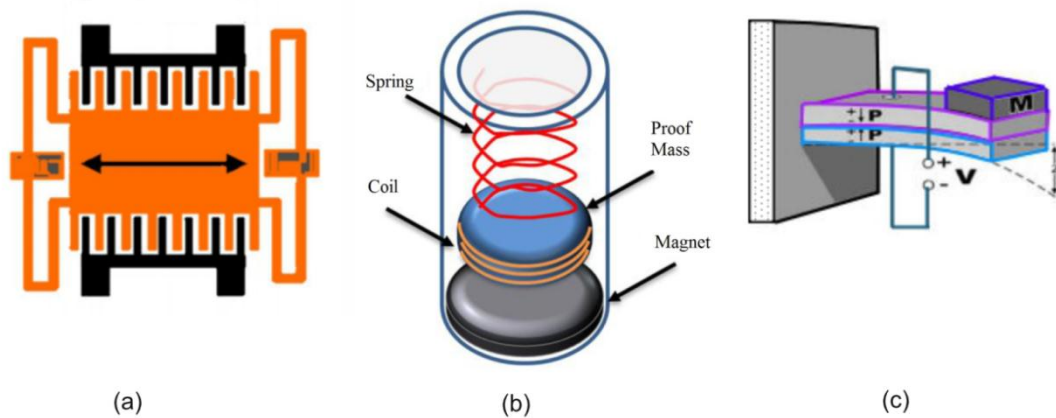
Figure 1.1 Schematic diagrams of (a) electrostatic transducers (b) electromagnetic transducers (c) piezoelectric transducers

1.3.1 Piezoelectricity

Piezoelectricity is the phenomenon of coupling between the mechanical and electrical states of the material. The materials showing the piezoelectric effects are called as piezoelectric materials. The piezoelectric effect is categorized into two parts such as the direct and inverse piezoelectric effects. In the simplest terms, direct piezoelectric effect exhibit when an electric charge collects on the surface of the electrodes of the strained piezoelectric material. On the contrary, in inverse piezoelectric effect, the materials undergo deformation when a potential difference exhibit in the electrode. The inverse piezoelectric effect was mathematically derived from the fundamental principle of thermodynamics. These two effects usually coexist in a piezoelectric material.

1.3.2 Piezoelectric materials

With the fast growing field of smart materials systems in micro electro mechanical systems (MEMS) the analysis of piezoelectric materials has received a significant attention in the last decade. The piezoelectric materials belong to the class of materials called ferroelectrics in which the molecular structure is oriented in such a fashion that it exhibits a local charge separation called as an electric dipole. These electric dipoles are oriented randomly throughout the material composition. When the material is heated above the Curie temperature under a very strong electric field, the electric dipoles reorient themselves about the electric field. This process is termed as poling. After the material is cooled these dipoles continue to maintain their orientation and exhibit the

piezoelectric effect. The poled material undergoes expansion and contraction when an electric field is applied. However, the electric field can be applied to any surface of the material, each resulting a different stress and strain generation.

The property of piezoelectric effect can be easily observed in several natural crystals such as Berlinite, sucrose, Topaz, Rochelle salt, quartz etc. However, in the field of engineering applications, the electromechanical coupling between mechanical and electrical states of the material has to be adequately strong. To satisfy these applications, manmade piezoelectric ceramics have been developed. The most prevalent engineering ceramic, PZT (Lead Zirconate Titanate) was developed in the 1950s at the Tokyo Institute of Technology, and several versions of it, such as PZT-5A and PZT-5H are most frequently used piezoceramic today in many engineering applications. As found from the literature, PZT-5A and PZT-5H are the most widely executed piezoceramic, as far as energy harvesting is concerned. The foremost important advantages of piezoelectric materials are large power densities and ease of its application in energy harvesting. The usable voltage output can be obtained directly from the piezoelectric material when vibration input is applied. For instance, an input voltage is required in electrostatic energy harvesting which can be altered between the capacitor elements due to vibration. The requirement of an external input voltage is eliminated in piezoelectric energy harvesting in which the voltage output arises from the constitutive law of the material. Further, unlike electromagnetic devices, piezoelectric devices can be fabricated both in micro and macro-scale owing to the well-known thin and thick film fabrication techniques. Later, macro fibre composites (MFC) were developed with the advantage of higher strain and sensing capabilities. However, it was observed that the MFC was less effective for power harvesting than the PZT due to its very low current generation.

The piezoelectric properties must encompass a sign convention to facilitate this ability to apply electric potential in mutually three perpendicular directions. For simplicity, the piezoelectric material can be generalized for two modes as shown in Figure 1.2. The first is the 31 mode for bending configuration and the second is 33 mode for stack configuration. The two modes of operation can be understood by assuming that the poling direction is always in the '3' direction. In the 31 mode, the electric field is applied in the '3' direction, and the material is strained in perpendicular to the poling direction or in

6

the '1' direction. In the 33 mode, the electric field is applied in the '3' direction, and the material is strained in the poling or '3' direction.
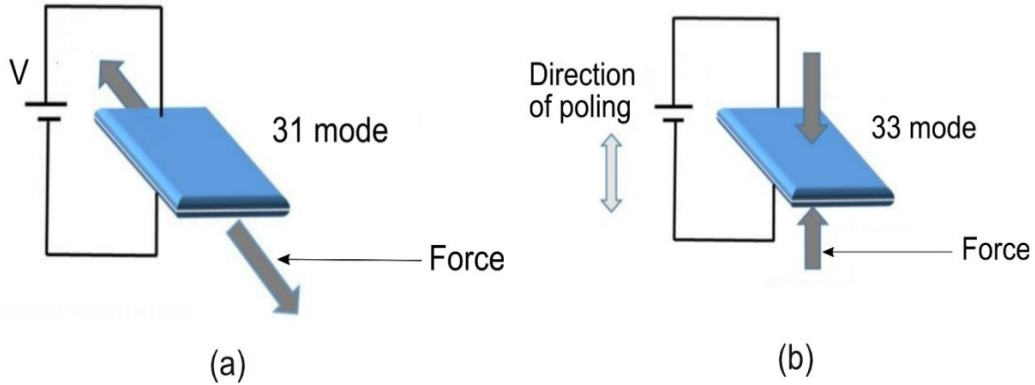
Figure 1.2 Schematic diagrams of (a) 31 mode piezoelectric coupling (b) 33 mode piezoelectric coupling

Vibration-based energy harvesting using piezoelectric materials has received an emergent attention over the last decade. The research motivation in this field is due to the condensed power requirement of small electronic components, such as the wireless sensor networks used in structural health monitoring applications. The vital aim in this research field is to power such small electronic devices using the vibration based energy available in the environment. If this can be achieved, the requirement of an external power source, as well as the periodic maintenance and replacement for battery can be minimized.

As far as sensing is concerned, the piezo material is connected to a very high resistance which prevents the current, considering that the voltage is a direct measure of the strain of the material. By dropping this resistance, a current will flow, providing power to a load; which is the basis of power harvesting. In the mechanical domain, the material is attached to a surface which is strained in any fashion, be it harmonic, or random. The material undergoes strain as well, thereby generating the electrical current irrespective of the voltage. From basic electrical theory, power is the multiplication of voltage and current indicating that electrical power is being transferred out of the piezoelectric material. This power can then be used for a number of applications. The scope of this thesis is to maximize the output of the system dealing with the mechanical parts which of direct concern.

1.4 Electrical circuit in energy harvesting

While using piezoelectric materials as a means of gathering energy from the surroundings, in most cases it is necessity that a means of storing the energy generated be used. Without accumulating a significant amount of energy, the power harvesting system will not be a feasible power source for most electronics. Hence an electric interface is necessary for the energy harvesting system to ensure the voltage compatibility with the electric load or energy storage element. In this context to get the output power a classic interface energy harvesting circuit has been considered in the present research.

1.5 Analysis of energy harvester

The electromechanical response of a piezoelectric energy harvester and the amount of power it generates are completely dependent on the nature of the ambient energy. The power density of an energy harvester is defined as the output power divided by the device volume for a given input. In vibration-based energy harvesting, the input (excitation) is often characterized by the acceleration and frequency level. Therefore, unless the input energy is provided, the power density is an insufficient parameter to compare different energy harvesters. The piezoelectric energy harvester can be modelled and analysed under various forms of dynamic loading such as periodic excitation, random excitation in different forms such as white noise, moving load excitation of long bridges, excitation due to strain fluctuations on huge structures, and transient base excitation. Apart from this, energy harvesting from aeroelastic vibrations of structures with piezoceramic layers under airflow excitation is an important subject. However, this research is limited to only transient impulse input to the structure for output voltage and power responses.

Further, the effectiveness of the piezoelectric energy harvester has to be ensured in extremely hot or cold conditions. These conditions may rigorously affect the energy harvester in different ways. Hence, during design of such structures, the thermal effect which is an essential feature must be taken care of. Although mechanical and electrical coupling interaction affects the performance of the devices, the presence of variation of temperature can also influence the voltage/charge generation in the piezoelectric

sensor/actuators. The existence of such temperature gradient can introduce both pyroelectric and thermal strain effects to the distributed sensor and deflection in dynamic oscillations.

1.5.1 Finite element modelling

For problems involving complicated geometries, loadings and material properties, it is generally not possible to obtain the solutions of ordinary or partial differential equations by classical methods. Hence, the researchers rely upon numerical methods such as finite element (FE) method for acceptable solutions. The FE formulations of the problem result in a system of simultaneous algebraic equations for solutions, rather than solutions of partial differential equations. These numerical methods yield an approximate value of the unknowns of the problem at discrete numbers of points in the continuum. Hence, the process of modelling involves discretising equivalent smaller bodies interconnected to two or more elements called as nodal points or nodes. In FE process instead of solving the problem for the whole body, formulations are made for each finite element and are combined to obtain the solutions for the whole body.

1.6 Optimization algorithms

Optimisation is a process which finds the best or optimal solution for a given problem. The optimization problems involve the determination of variables so that an objective function reaches an optimum value (maximum or minimum) subjected to some constraints. Algorithms to solve these type problems are often classified into two groups: Classical methods and Heuristic methods. The classical methods are based on the gradient values computation (derivatives) which provides the search direction of the algorithm. In Heuristic methods, the optimisation parameter changes based on random decisions. Though classical methods are widely used, it is often impossible to ensure that the final solution found by these strategies is the global optimum. This depends on the level of complexity of optimization problem. In such cases, heuristic algorithms like simulated annealing, genetic algorithms, particle swarm are better options for the problem.

All optimisation problems are covered by three factors such as, an objective function, a set of unknowns or variables and a set of constraints. The objective function is the mathematical expressions for a given problem that needs to be minimized or maximized. In manufacturing processes, the profit or the cost is considered to be the objective function which has to be maximised or minimised. The objective function is greatly affected by the set of unknowns or variables, e.g., in manufacturing; the variables are the resources used or the total time period. The set of constraints allow the variables to take on certain values and exclude the others, e.g. in manufacturing one constraint is time, which should always be non-negative. The different types of search algorithm techniques are presented in Figure 1.3.

Genetic Algorithm (GA) is an adaptive heuristic search algorithm based on evolutionary philosophies of natural choices and genetics. It represents an intelligent exploitation of a random search preferably to solve optimization problems.GA is completely based on Darwin's theory of evaluation 'Survival of the fittest'. Out of a number of optimisation techniques, GA is chosen due to the following reasons:

- It does not require derivatives information or auxiliary knowledge. It requires only objective function and fitness value.
- It searches population of points in parallel rather single point.
- It uses probabilistic rules not deterministic.

GAs are based on the evolution of biological systems. An objective function is identified to calculate the fitness of contender solutions and the contender solutions are encoded by binary strings or by finite real numbers with decimal representations. For a traditional GA, a population of N contender solutions is chosen from the space encoded solutions and fitness of each string is evaluated. A mating pool is selected from the population of contender solutions. The genetic operators like crossover and mutation act on the mating pool to give the next set of contender solutions for the next iteration. The algorithms (selection, crossover, and mutation) used in the simulation for both binary and real coding are described herewith.

```
                              Search Optimization
                                      │
         ┌────────────────────────────┼────────────────────────────┐
         ▼                            ▼                            ▼
  Calculus based              Guided random               Enumerative
    technique                search technique               technique
         │                            │                ┌───────────┴────────────┐
  ┌──────┴──────┐                     │                ▼                        ▼
  ▼             ▼                     │           Uninformed               Informed
Indirect      Direct                  │             search                  search
 method       method                  │
                │                      │
         ┌──────┴──────┐              │
         ▼             ▼              │
      Newton       Finonacci         │
                                      │
      ┌──────────┬──────────┬────────┴────────┐
      ▼          ▼          ▼                  ▼
    Tabu        Hill     Simulated        Evolutionary
   search     climbing   Annealing         Algorithm
                                      ┌──────────┴──────────┐
                                      ▼                     ▼
                                   Genetic              Genetic
                                 Programming           Algorithm
```
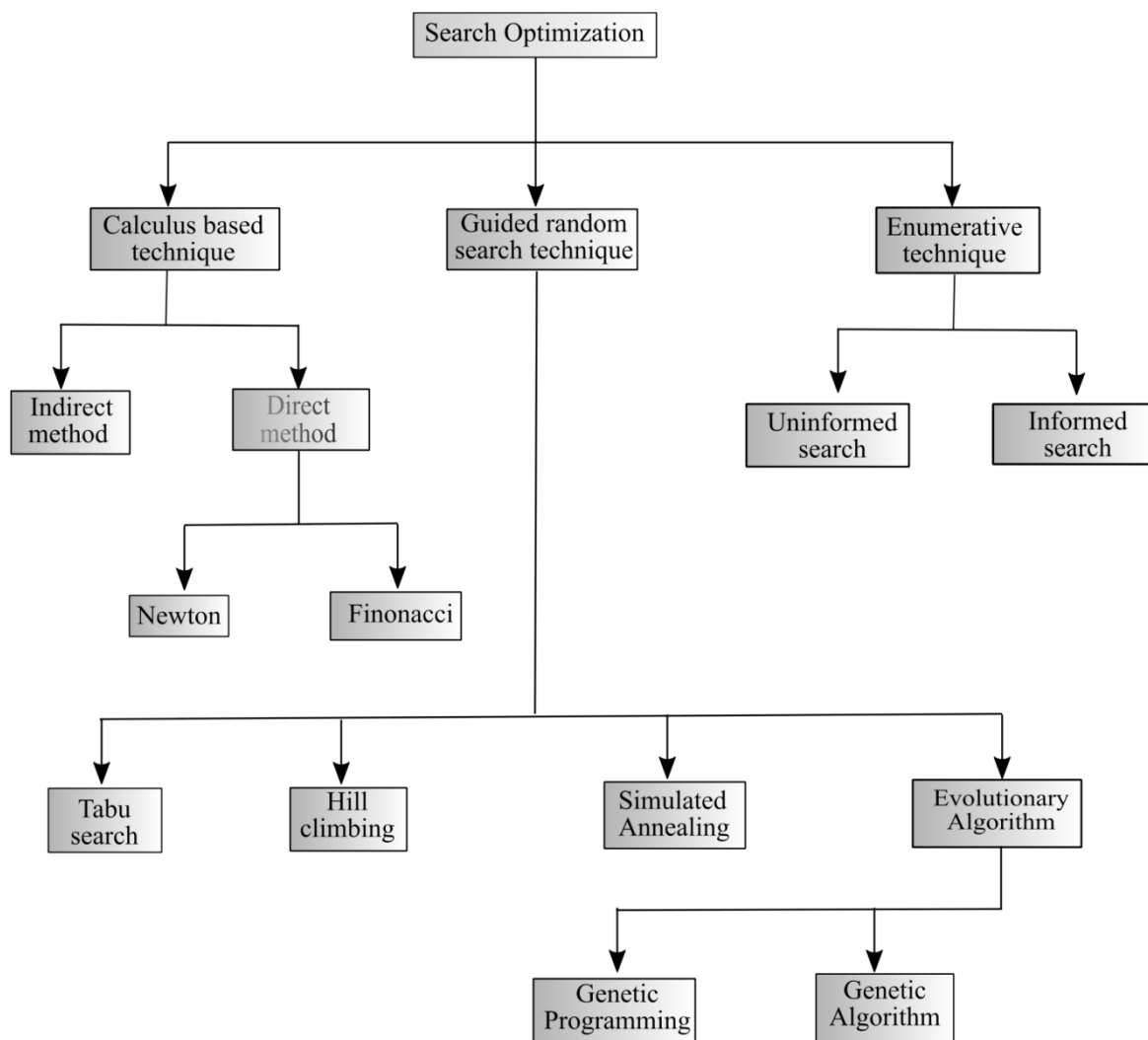
Figure 1.3 Nomenclature of the optimization technique

a. *Selection*

This algorithm generates a new population of chromosomes from the current chromosomes by probabilistically selecting higher ranked contenders according to the fitness. The most commonly used methods of selecting chromosomes for parents to crossover are Roulette wheel, Rank, Steady state n, Boltzmann and tournament selections.

b. *Crossover*

Crossover is a genetic operator that combines two chromosomes to produce a new chromosome. The concept behind the crossover is that the new chromosome may

be better than both the parents if it takes the best characteristics from each of the parents. It selects genes from parent chromosomes and creates new offspring. The crossover operator is of many types such as one point, two-point, heuristic, uniform and Arithmetic crossovers.

c. *Mutation*

The mutation operator takes place after the crossover is performed. It is used to maintain the genetic diversity from one generation of chromosomes to the next. It alters one or more gene values in a chromosome from its initial state. This results an entirely new gene value added to the mating pool. With this new gene value, the GA may be able to reach a better solution than the previously possible. Various types of mutation operators are used, such as Flip bit, uniform, non-uniform and Gaussian.

d. *Elitist selection*

The algorithm is sometimes functional to ensure that the new solutions generated by crossover and mutation are accepted for next iteration.

The real coded GAs are getting more attention presently in solving continuous search problems after the success of binary coded GAs. The real coded GAs differs from the binary coded GAs in concern with coding variables. The real coded GAs work directly with the variables instead of coding of problem variables. The basic difference between real coded GA and binary coded GA is in their recombination operator. Though some real coded crossover operators were recommended, most of them are based on intuition and without proper analysis. Therefore, a real coded crossover operator has been developed and more emphasis is given to the development of such search characteristics. In this case, the simulated binary crossover (SBX) operator has been found to work satisfactorily in many practical problems when compared to existing real-coded crossover implementations. It is observed that the real-coded GAs with SBX operator performs better than binary coded GAs in solving some problems. One important advantage of the SBX operator is that it can prevent children solutions to any random closeness to the parent solutions; thereby implementing a separate mating scheme for which better enactment is not required. Eventually, real-coded GAs with SBX operator has been effectively used to find multiple Pareto optimal solutions in solving many design problems.

These simulation results are worth promising and suggest the application of real coded GAs with SBX operator to real-world optimization problems.

1.7 Applications and scope of present work

Any energy harvesting solution must be adapted separately to the respective application. Consequently, energy converters, energy stores and electronics are adjusted as per the energy requirements of the user and excitation conditions. Some of the important applications are condition monitoring and structural health monitoring (SHM), data monitoring and data transmission, product monitoring during transport, etc. Apart from this, very interesting energy harvesting technologies are still in the laboratory that could change the face of the energy harvesting industry over the next few years such as medical and fitness devices, MEMS pyroelectric generator, Nantennas, etc.

Energy harvesting is aimed towards producing energy from the waste vibration and makes it possible to use further in different applications. So to generate maximum possible energy it is important to focus on improvement in the direction of geometric profile, material properties, effective electromechanical coupling, etc. Moreover, it is very much indispensable that the harvester should work efficiently in different environmental conditions. An efficient finite element procedure for thermo-electro-mechanical analysis is essential for designing of such structures in energy harvesting. In view of this the present work aims at

- To develop a mathematical model for nonprismatic beams (such as linear, parabolic and cubic crosssection profiles) with tapers in both width and height directions.
- To formulate a mathematical model for axially FG beam based on power law, with temperature varying mechanical properties towards the free end of the beam.
- To formulate a two-noded finite beam element for detailed modelling and analysis of nonprismatic piezolaminated axially FG beams under combined mechanical and thermal loading.
- To formulate a two-noded finite beam element for detailed modelling and analysis of nonlinear nonprismatic piezolaminated axially FG beams
- To develop a real coded GA based constrained optimization technique (ultimate stress of beam, PZT and breakdown voltage of PZT) to get optimum design variables for maximizing the output power.

13

- To perform a comparative study between prismatic and nonprismatic homogeneous beams on the basis of tip displacement, frequency, output voltage and output power responses.

- To study the effects of simultaneous variation of width and height tapers on homogeneous and axially FG nonprismatic beams on output responses.

- To study the output (static and dynamic) responses of axially FG nonprismatic piezolaminated beam under combined mechanical and thermal loading.

- To study the output responses of axially FG nonprismatic piezolaminated beam with temperature dependent material properties towards the free end of the beam.

- To study output responses such as tip displacement, voltage and power of nonlinear nonprismatic axially FG beams.

- To obtain optimal output power using a real coded GA based constrained optimisation technique along with design variables of axially FG nonprismatic beams under impulse and combined impulse-thermal loading.

- To obtain optimal output power using a real coded GA based constrained optimisation technique along with design variables of nonlinear axially FG nonprismatic beams.

1.8 Outline of the thesis

This thesis has been organized as follows

Chapter 1 briefly introduces energy harvesting and significance of structural design, improvement in material properties, importance of geometric nonlinear effects and optimal output power from such structures.

Chapter 2 overviews a comprehensive study to understand the state of art of energy harvesting. The theoretical and research background, including the theory of piezoelectricity, geometric and material variations, and modelling in thermal environment are studied.

Chapter 3 presents the FE based piezo-thermo-elastic analysis of nonprismatic piezolaminated axially FG beams for energy harvesting.

Chapter 4 describes the FE based mathematical modelling of nonprismatic axially FG beam with geometric nonlinear effects on output voltage and power.

Chapter 5 depicts the formulation of proposed real coded GA based constrained optimal output power from such structures.

Chapter 6 provides the validation of developed FE code for structural, electromechanical, piezothermoelastic and experimental of present formulation. A detailed comparison among the modelled nonprismatic beams with temperature dependent material properties on frequency, output voltage and power have been carried out.

Chapter 7 presents the nonlinear structural validation of the present FE code and comparison of results for the static and dynamic responses of the modelled structures.

Chapter 8 depicts the results of real coded GA based constrained optimal output power without and with the effect of temperature varying material properties and the superiority of the present method over conventional trial and error method.

Chapter 9 outlines the important conclusions drawn from the present work and the scope for further work.

Chapter 2

Literature Review

Due to the recent advancements in wireless sensor networks technology, the demand for portable electronics and wireless sensors are growing rapidly. These devices not only face the present challenges but also have wide applications in various remote areas as monitoring bridge vibration, gas monitors in a coal mine, and even wild animals as a global positioning system (GPS). In all these cases, the replacement of the battery is too costly, unfeasible and sometimes impossible. By scavenging energy from the surrounding environment, the time between battery replacements may be extended or even eliminated, depending on the power requirements of the applications.

As far as energy harvesting is concerned, it is already used in the form of a windmill, watermill, geothermal and solar energy. These energy sources that are called as renewable energy sources emerge as future power sources. These energy sources can generate few KW to MW level of power also, known as macro energy harvesting technology. On the contrary micro energy harvesting technology is specifically considered as an alternate source for conventional battery. Micro energy harvesting technology is based on mechanical vibration, mechanical stress and strain, thermal energy from the furnace, sunlight or room light, the human body and chemical or biological sources, which can generate mW or µW level of power.

2.1   Piezoelectric energy harvesting

There are several methods existing which replace the use of batteries for power supply. Use of piezoelectric materials is one of the versatile methods, which can supply energy at the expense of energy lost due to vibration. This energy could be used to lengthen the life of the power supply or in the ideal case provides almost endless energy for the sensor's lifespan. In past few decades, substantial researches have been commenced related to power harvesting. Piezoelectric materials have a significant role in present era for scavenging energy from the ambient environment. As vibration is a major

concern in most of the structural machinery, it is possible to scavenge energy from these structures by incorporating the piezoelectric materials as sensors which transform the mechanical energy into electrical energy. In the following paragraphs, some progressive works are illustrated in this direction.

The purpose of the piezoelectric material is to convert mechanical energy into electrical energy using a very simple structure. For most of the wireless sensor network system, piezoelectric energy harvesting is emphasized as self-power sources [2]. When pressure is applied certain crystalline materials such as quartz, Rochelle salt, tourmaline, and barium titanate develop electricity which is known as the direct effect of piezoelectricity [3]. On the contrary, these crystals undergo deformation when an electric field is applied, which is termed as the converse effect. Direct effect can be used as a sensor or energy transducer, and converse effect can be used as an actuator. Sensors are the most vital electronic devices which can be used almost everywhere due to the recent advancement in wireless and Micro Electro Mechanical System (MEMS) technology. These sensors are wireless and need their power supply. Conventional batteries are used to supply power to these sensors. However, problems may arise due to the limited lifespan and high mass to output ratio of conventional batteries.

Several efforts have been laid in the field of energy conversion and discovered that piezoelectric materials are best suitable for conversion of mechanical to electrical energy and vice versa [4]. A comprehensive analysis of the piezoelectric energy harvesting using low-profile transducers and the results for various energy harvesting prototype devices were discussed [5]. A brief discussion on the selection of piezoelectric materials for on and off resonance applications was also carried out. From the discussion it was observed that the energy density of piezoelectric energy harvesting devices was 3to 5 times higher than electrostatic and electromagnetic energy harvesting devices. It was introduced that by using piezoelectric ceramics, the energy can be collected by walking [6]. The power harvesting from piezoelectric shoes using unimorph strip made from piezoceramic composite material from a multilayer laminate of PVDF was discussed [7]. It was further explored by harnessing the parasitic energy from piezoelectric shoes by using simple mechanical structures and flexible piezoelectric materials which results in a comfortable piezoelectric shoe design.

To improve the output power generation emphasis had been given to piezoelectric materials. Some of the works related to this are presented. A single crystal piezoelectric ceramic lead magnesium niobate–lead zirconate titanate (PMN-PZT) was analysed for shunt damping performance and power generation.The obtained results were validated with existing experiments and analytical results [8]. The comparison of performances between two piezoelectric compositions PZT with 1 % Mn and PMN–25PT were conducted. It was observed that the coupling coefficient of PMN–25PT had a higher value than PZT based model [9]. It was also shown that by using the composition more than twice energy could be scavenged as compared to PZT based model. Three types of piezoelectrics such as single crystal PMN-PZT, polycrystalline PZT-5A, and PZT-5H-type monolithic ceramics were examined in a unimorph cantilever beam for best design energy harvester for low-power applications. It was concluded that single crystal energy harvester produced more energy as compared to other two models [10]. The piezoelectric energy harvesting performances were presented using Zr-doped $PbMg_{1/3}Nb_{2/3}O_3$-$PbTiO_3$ (PMN-PZT) single crystal beam. The obtained results were compared with the experimental results [11]. A resonance-based multilayer vibration energy harvester was presented using $0.71Pb (Mg_{1/3} Nb_{2/3}) O_3$–$0.29PbTiO_3$ (PMN-PT) single crystal. The output power (approximately 5 mW) with peak voltage (approximately 4 V) was measured which specify the proficiency of the material for energy harvesting [12].

The piezoelectric ceramic was investigated subjected to external mechanical stresses. This ceramic was prepared experimentally by tape casting of slurries comprising $SrTiO_3$ (STO).From this investigation, it was observed that the specimen with STO produced more power than specimen without STO when subjected to high stresses [13]. A micro piezoelectric power generator was proposed comprising a composite fixed-free beam with nickel metal mass. About 0.89V AC and 2.16 mW power were generated from the proposed generator which replaced the germanium based rectifier as far as energy storage is concerned [14]. The piezo composite was analysed for energy harvesting which consists of layers of glass/epoxy, PZT ceramic and carbon/epoxy. The numerical and experimental validation were carried out and observed that the piezo composite had greater potential for harvesting energy subjected to vibration [15]. Similarly, another piezoelectric material named aluminium nitride (AlN) was analysed for energy harvester because of resulting high voltage output. It was observed that maximum of 60 µW output power can be scavenged at a resonant frequency of 575 Hz [16]. The analysis was also

carried out on fabrication and evaluation of energy harvesting device employing epitaxial PZT thin film. The experimental and analytical results were compared and observed that epitaxial PZT thin film had potential for improvement in energy harvesting device performance [17]. Apart from this, the piezoelectric flexural transducers were investigated experimentally. During this investigation the boundary conditions such as frequency and electrical load were employed for the development of the generator [18]. The comparison between analytical and experimental studies was conducted for a piezoelectric bimorph cantilever beam with one and two input base transverse and longitudinal excitations. The results obtained from polar base excitation for off-axis input motions were validated with experimental results which is relevant for practical implementation [19].

Several beam structures were analysed using piezo films especially suitable for shoe inserts and walking type excitation. The resulting strain obtained, were functions of material and geometric properties of the structure. The optimum configuration was determined by comparing the energy harvested from these structures[20].Various factors affecting the power harvesting were analysed such as excitation magnitude, energy, and voltage required, and the capacitor magnitude, type of piezoelectric used and appropriate storage capacitor [21]. An innovative energy harvesting backpack was developed using polyvinylidene fluoride (PVDF) in which electrical energy was generated from the differential forces between the wearer and backpack [22]. To examine the effectiveness of electro-mechanical conversion properties between PVDF and ionic conductive polymer energy, harvesting comparison was proposed. The obtained simulation results were compared with the existing analytical models using spring-mass-damper subjected to axial loading [23].

The energy harvesting from a cantilever beam and a plate were evaluated using Euler–Bernoulli beam theory. Two different forcing functions such as harmonic oscillations and random noise were used to drive the system responses. The proposed models were validated by comparing it with the experimental data. A parametric study was also performed to optimize the cantilever beam's power generation capability [24]. The modelling and analysis of bimorph piezoelectric cantilever beam were developed using analytical approach for voltage and power generation. Euler–Bernoulli beam and Timoshenko beam theory were used in the approach. The results were compared with the existing results in the literature such as energy method and electrical equivalent

19

circuit method. The existing models and the proposed model then implemented in MATLAB environment and simulated with the power conversion circuit. The results obtained are well suited with the experimental values [25]. The electromechanical finite element modelling of a vibration power harvester and its validation with experimental studies were conducted with five major solution techniques [26].

The compact size energy harvesters were built by considering space available for AA size batteries. Each harvester comprised of a rectifier circuit with four diodes and a capacitor. A series of piezoelectric energy harvesters with circular and square cross-sections were made and tested at different frequency and amplitude. It was observed that the voltage reached about 16 V and 25 V for circular and square cross-sections, respectively at 50 Hz frequency. The maximum power scavenged was near about 625 μW. Again it was concluded that square section provides better efficiency as compared to circular cross-section at higher amplitudes [27]. A theoretical model was proposed using beam element and experiments were performed to harvest power from PZT material. It was concluded that a simple beam bending can provide the self-power source of the strain energy sensor [28]. The conversion of mechanical impact energy into electrical energy from a lumped model consisting of mass, spring and damper were studied [29]. It was observed that the piezoelectric material can be used both as a sensor and a generator of power. The piezoelectric sensor performance along with viability of the self-powered sensor was discussed [30, 31]. For low-frequency vibration energy harvesting application, a piezoelectric cantilever was proposed with a silicon proof mass [32]. The average power and power density were found to be 0.32 W and 416 W/cm^3 respectively. To improve the frequency flexibility and power output, an array of power generator was developed based on thick film cantilever [33]. An improvement was observed in terms of electric power of 4 mW and around 4 V output voltages for a given resistive load.

Theoretical modelling of the piezoelectric energy harvesting system puts emphasis on the structures and on the electrical behaviour of the piezoelectric patch. An improved mathematical model was proposed and discussed related to the issues generated by mathematical modelling such as piezoelectric coupling, base motion modelling, and physical modelling. The correction factor of single degree of freedom for base excitation model was also proposed which is further used by many researchers for energy harvesting. Apart from this, a closed form solution of piezoelectric bimorph with series

and parallel connections of piezoelectric ceramics were discussed [34-36]. The vibration-based piezoelectric energy harvester was optimised by incorporating an inductor along with a resistive load. It was observed that the energy harvested can be enhanced by considering the inductor in the electrical circuit [37]. A comparison between the electromagnetic system and piezoelectric system with PZT ceramic embedded at one end and fixed at other end was made. From the results, a strong similarity in signal level between them was observed [38]. A FE based electromechanically coupled plate model was presented. The model was based on Kirchhoff plate assumptions for predicting the output power with the inclusion of the effect of electrodes used. The results obtained from the simulations were validated with experimentation and analytical solutions for an unimorph beam [39].

The energy conversion efficiency was calculated under the steady-state condition for a coupled piezoelectric power harvester. It was observed that the optimised variables, strongly dependent on the electromechanical coupling parameters [40]. The modelling of a piezoelectric energy harvester was proposed incorporating the electro-mechanical system. The interaction between the host structure and the electrical circuit was characterized by a rectifier with nonlinear effect. It was also shown that maximum power density can be obtained by varying the nondimensional inductance of the circuit [41]. A Timoshenko piezoelectric beam model was anticipated to compare the results obtained in Euler–Bernoulli beam models. The exact behaviours of tip deflection, voltage, current and power of the piezolaminated structure were reported. Apart from that, the shape of the beam was optimised using the heuristic code and the obtained results were validated with the experimental results [42, 43]. The mechanical nonlinear strain stiffening effect was proposed in a passive adaptive system and experimentally observed that, the frequency adaptability of more than 40% for a fixed-fixed beam at $2g$ acceleration obtained. The proposed solution was perfectly applicable for industrial machinery where abundant availability of high amplitude vibrations are available [44].

A unimorph piezoelectric cantilever was analysed theoretically for energy harvesting with unequal piezoelectric and nonpiezoelectric lengths. It was observed that for a given frequency, maximum open circuit voltage can be obtained when the ratio of nonprismatic-to-prismatic length is greater than unity. Similarly, the maximum output power can be

obtained when the ratio of nonprismatic-to-prismatic length is equal to unity [45]. The dynamic modelling of piezoelectric harvesting oscillator was prepared considering the nonlinear differential equation [46]. The concept of noise and nonlinearity was emphasized in that work. A guideline was presented for harvesting optimal energy using unimorph cantilever beams. It was perceived that the poling behaviours were prime factors to explore the losses in nonuniform poling. A parametric study was carried out to find the effects of electrode patterns, dimensions and layer dimensions on poling factor. The design guidelines were provided to confirm that optimum energy could be scavenged by developing piezoelectric MEMS devices [47]. A piezoelectric cantilever bending model was developed considering the assumptions of Euler–Bernoulli beam theory. Hamilton's principle was used for establishing the governing equation and solved by modal decomposition method. The mathematical model was prepared considering the direct piezoelectric effect to enhance the conversion efficiency from mechanical energy to electrical energy. It was shown that more voltage and bandwidth were generated in the second mode as compared to the first mode of resonant frequency [48]. A mathematical formula was developed to envisage the output power conversion efficiency of piezo generators and emphasis was given to improve such efficiency [49].

The energy harvesting from clamped-clamped axially loaded beam subjected to transverse excitation was examined [50]. A nonlinear Euler –Bernoulli theory was incorporated to model the electromechanical beam. The obtained theoretical results were validated through experimental data. The use of a unimorph cantilever beam as a new piezoelectric energy harvester undergoing bending–torsion vibrations was proposed [51]. The suggested design comprises a single piezoelectric layer and a pair of asymmetric tip masses. A parametric study of the dynamics of the system was conducted to determine the geometric properties that enhance the harvested electrical power. An increase in 30% of harvested power with this design was observed compared to the case of beams subjected to bending only. The energy harvesting from a bluff body subjected to transverse galloping oscillations with different cross-section geometries (such as square, D, and triangular) were investigated [52]. It was observed that electrical load resistance and the cross-section geometry affect the onset speed of galloping. The optimum harvested powers were attended with minimum transverse displacement amplitudes for all selected cross-section geometries. Again an energy harvester was studied for a multi-layered cantilever beam having a tip mass with geometric, inertia and piezoelectric

nonlinearities [53]. A parametric study was performed to investigate the effects of the nonlinear piezoelectric coefficients and the excitation amplitude of the system response. The nonlinear distributed parametric model was used for validation of the experimental setup and for the design of energy harvesting devices. The dynamic response of a piezoelectric material attached to a bistable laminate plate is inspected based on the experimentally generated voltage time series [54].

The piezo aeroelastic energy harvester under the combined effect of vibratory base excitations and aerodynamic loadings were investigated [55]. A series of experiments were conducted at various wind speeds and amplitudes of base excitation. It is revealed that the output power was significantly influenced by the base excitation. Further, an aero-electromechanical model in which nonlinear responses of a piezoelectric cantilever-type energy harvester under combined effect of galloping and base excitations were determined [56]. The model was validated by performing a series of experiments at different wind speeds and base excitation amplitudes. The short circuit and open circuit resonant frequency were used to investigate the performance of the bimorph device. The piezoelectric energy harvester subjected to both base excitations and vortex-induced vibrations were examined [57]. The effects of wind speed, electrical load resistance and base acceleration on the coupled frequency, electromechanical damping and performance of the harvester were investigated by considering the linear and nonlinear analyses. The regular and chaotic responses of a vibrational energy harvester consisting of a vertical piezolaminated beam and a tip mass were examined by a harmonic force [58].

2.2   Justification for focusing on power enhancement

The idea of carrying electronic devices and never bothering about the lifespan of batteries could be far closer than one would think. This thought has instigated the desire for self-powered electronics to grow rapidly, leaving only one constraint before these devices can become a reality. The one matter that still needs to be resolved is a way to produce sufficient energy to power the necessary electronics. The major drawback in the field of power harvesting depicts on the fact that the generated power is far too small to power most electronics by piezoelectric materials. Therefore, more attention needed to be put on methods of increasing the amount of energy generated by the power harvesting

device that will allow becoming a source of power for portable electronics and wireless sensors. In order to improve the output power emphasis has been given not only to the piezoelectric materials but also the geometric configuration of the energy harvester, the material used and the environment conditions in which the harvester works. Some of the works in these directions are presented in the subsequent paragraphs.

2.2.1 Nonprismatic energy harvesters

Non-prismatic beams are of great importance in different fields of engineering, whose cross-section profile changes gradually along their length. These beams not only meet the architectural and aesthetical needs but also optimize the weight and strength of the structure. Due to these advantages of non-prismatic members, it plays a significant role in the field of construction and aerospace structures. Some of the studies on energy harvesting from nonprismatic beams are discussed. A cantilever beam with a proof mass at its free end was modelled and the effects of geometrical and physical parameters on the performance of power generation was described [59]. It was specified that for the same volume of PZT, the trapezoidal beam could produce more than twice energy than prismatic beam [60]. However, uniform strain distribution along the beam could not be produced from the existing cantilever beams, and consequently, maximum energy from vibration could not be achieved. The effects of shape variations of a cantilever beam on the performance of energy harvester were examined [61]. In that work two types of shape variations (such as linear and quadratic) were considered to design the energy harvester for generating maximum energy at low frequencies. It was concluded that quadratic shape energy harvester can generate two times more energy as compared to rectangular shape harvester for a particular resistance value. An electromechanically coupled beam with varying cross-sectional area was modeled for energy harvesting, and the obtained results were experimentally verified [62]. Two types of beam conditions (trapezoidal taper and reversed trapezoidal taper) were considered to find out the effects of electromechanical behaviour on energy harvesters. The large deflections of nonlinearly elastic cantilever nonprismatic beams made from materials obeying the generalized Ludwick constitutive law were discussed [63].

Tapering of the beams has gained more popularity in recent years in the field of energy harvesting. The tapering increases the average strain in the beam and consequently the

charge generated by the piezoelectric material. From the literature survey, it was observed up to 30% of improvement in the generated output power. With the help of the numerical simulations, it was found that the tapering has an impact only for certain design configurations, namely for cantilevers with long slender beams. But for cantilevers with short wide beams, the tapering has no significant effect on the output power of the harvester [64]. The piezoelectric energy harvester with different beam shapes was analysed. The mathematical formulation of the compound piezoelectric structure was established using Rayleigh–Ritz method. The obtained results were validated with experiments considering triangular and rectangular-shaped beams. The results showed that triangular-shaped beams are more effective than rectangular-shaped ones regarding maximum output power [65]. The experiments on the response of a variable width beam were performed and concluded that reversed trapezoidal beam with large end free produces more energy than a trapezoidal shape with large end clamped and both are better than the rectangular shape [66].

2.2.2 Functionally graded beam

The material properties of the functionally graded (FG) beams change with volume fraction of its constituent phase along the spatial directions. So it is possible to modify properties like strength, toughness, and thermal capability. So FG beams are increasingly used in many engineering sectors like space vehicles, aerospace, automotive, biomedical, optics, electronics and military applications. Some of the works in the field of FG beams are enlightened in the following sections.

2.2.2.1. *Transverse functionally graded beam*

The free vibration analysis of a simply supported FG beam with piezoelectric layers subjected to axial compressive loads was studied. The various effects of volume fractions, the effects of applied voltage and axial compressive loads on the vibration frequency were presented. It was concluded from the analysis that the piezoelectric actuators induce tensile piezoelectric force produced by applying negative voltages that significantly affect the free vibration of the FG beam. The vibration frequency increases when the applied voltage is negative [67]. The differential transformation method (DTM) was applied for investigating the free vibration analysis of FG beams with arbitrary boundary conditions, including various types of elastically end constraints. By using DTM,

the natural frequencies and mode shapes were presented. For free vibration of the beam, Al_2O_3/Al was considered for the study. It was seen that there was considerable variation of frequencies and mode shapes when the stiffness of spring becomes large [68].

The free vibration analysis of a functionally graded ordinary (FGO) twisted Timoshenko beam of cantilever type was investigated. The shape functions were derived from differential equations of static equilibrium. The mass and stiffness matrices were obtained from the energy equation. The various material properties along the thickness direction are assumed to vary according to a power law. It was observed from the analysis that increasing the pretwist angle, the first natural frequency increased whereas the second natural frequency decreased. The simultaneous effects of power law index and pretwist angle on first natural frequency were conducted and observed that it was marginal [69].

The bending analysis of a simply supported FG beam subjected to uniformly distributed load (UDL) was investigated. The material properties of the FG beam varied continuously in the thickness direction based on power law. The position of the natural surface of the FG beam was obtained, and its influence on the deflection of the beam under UDL was studied [70]. The numerical calculations for natural frequencies of FG simply supported beams were presented. The first order Timoshenko beam theory and third-order shear deformation theory were applied for the analysis of FG beam [71]. The nonlinear forced vibration analysis of a beam made of FG material was presented. The modelling of the beam was carried out using Euler-Bernoulli beam theory and von Karman geometric nonlinearity. The effects of material properties on the nonlinear dynamic behaviour of FG beam were discussed. The frequency response equation of the system was presented, and the effects of different parameters on the response of the system were investigated [72].

The static analysis of a simply supported FG beam subjected to UDL was investigated. The Ritz method along with Timoshenko beam and higher order shear deformation theories were implemented for modelling of the FG beam. The variation of material properties of the beam in the thickness direction according to the power-law formula was considered. The effect of various material distributions on the displacements and the stresses of the beam were examined. It was indicated from the analysis that stress

distributions in FG beams are very different from those in isotropic beams [73]. The effects of boundary conditions, volume fraction and shear deformation on natural frequencies and mode shapes of a FG beam were investigated. It was assumed that the beam properties vary along the thickness direction following a power law. It was found that the beam theory developed for laminated composite beam could be used for free vibration analysis of shear deformable FG beams [74]. The geometric nonlinear formulation of FG beam was analysed considering total Lagrangian method. Two examples were considered, in which the behavior of graded cross-section beams were compared with homogeneous material beams. The material gradation was incorporated in the formulation, and its corresponding effect on axial, shear and fractural deformation was considered. From the analysis, the beam with graded material showed a substantial difference as compared to a homogeneous beam having same cross sectional rigidity [75].

With the adaptive displacement interpolation functions, the structure was analysed using beam element. The static, dynamic and vibration problems have been solved using this approach. The important feature of this analysis was using adaptive displacement interpolation function which helped in solving problems with variable cross section, FG beams, and various coupled problems. It was realised from the analysis that the approach was well satisfied both with accuracy and convergence perspective with the existing available results [76]. The FG ordinary beam and FG sandwich beam using finite element method were analysed on Winkler's elastic foundation. It was observed that the fundamental frequencyand buckling load, increases with the modulus of the foundation. The obtained results were compared with both type of property distribution and also for both steel-rich bottom and Al-rich bottom beam. It was noticed that beam with steel-rich bottom becomes stronger when the properties followed the power law. It is also found that, the fundamental frequency of FG sandwich beam increases with the modulus of the foundation [77]. The static and dynamic analyses of FG Plates of rectangular cross section based on higher order shear deformation theory were presented. The various mechanical properties of the plate were assumed to vary continuously in the thickness direction by power law distribution regarding volume fraction of the constituents. The stresses and displacements of the plate were computed considering Metal–Ceramic mixture. It was observed that the response was in transitional position compared to both

metal and ceramic. It was concluded that the present model showed well approximations with generalized shear deformation theory [78].

The dynamic behaviour of FG beam excited with random moving load was studied. The Euler-Bernoulli beam theory has been used for modelling the beam. The dynamic equation of motion has been solved in state space. The effects of structural damping on the result have been illustrated through various graphs and diagrams. The deflection of the beam at any arbitrary point has been calculated and expressed as an integral equation[79]. An attempt was made to design the material specimen whose behaviour shows similar result under mechanical loading of FG materials for the dynamic analysis. The numerical results were simulated to validate the existing results. The frequency analysis has shown the convergence of the proposed method with the increase in simulation steps [80].

The dynamic characteristics of FG beam with gradation in axially or transversally in thickness direction based on power law were presented. The Principle of virtual work has been used for deriving the equation of motion under Euler-Bernoulli theory assumptions. The analysis has been carried out for vibration characteristics and dynamic behaviour of the FG beam using FEM. It was concluded that the gradation in axial direction affects the frequencies and mode shapes of the beam whereas, no substantial variation is detected for gradation in thickness direction [81]. The dynamic stability of microbeams made up of FG material based on Timoshenko beam theory and modified coupled stress theory were investigated. The variation of material properties of the beam was assumed in the thickness direction and estimated through Mori-Tanaka homogenization technique. A simple power law based variation was taken for the analysis of the beam [82].

The analytical relationships between critical buckling load of a FG material beam based on Timoshenko beam theory and Euler-Bernoulli beam theory were derived, subjected to an axial compressive load. Various boundary conditions of the beam were taken into consideration such as simply supported, clamped –free and clamped-clamped. The material properties such as density, Poisson's ratio, and Young's modulus were assumed to vary in the thickness direction. The critical buckling load was derived using Eigenvalue problem and observed the same value for both Timoshenko beam and homogeneous

Euler-Bernoulli beam for the same boundary conditions. The obtained results were in well agreement with the numerically derived result using shooting method [83]. The FG beam was analysed using two separate FE formulations such as Euler-Bernoulli beam theory and Timoshenko beam theory. It was observed that the fundamental frequency and mode shapes were significantly affected by transverse shear for low length to thickness ratio. The significance of transverse shear on both frequency and mode shapes were demonstrated thoroughly for different boundary conditions. It was concluded that for structural members having low length to thickness ratio, the transverse shear effect should be taken into consideration for both homogeneous and FG beams [84]. The dynamic stability of FG beam with piezoelectric layer subjected to an axial compressive load for simply supported beam on an elastic foundation was studied. The material properties of the beam were graded in the thickness direction. It was concluded from the analysis that graded beams with smaller foundation coefficient showed more stability [85].

2.2.2.2. *Axially functionally graded beam*

The dynamic analysis of an axially FG beam with simply supported edges was analysed using Euler-Bernoulli beam theory. The material properties such as Young's modulus and mass density vary continuously in the axial direction according to the power law formula. The Lagrange method was used for deriving the governing equation of motion of the FG beam. The effect of the velocity of moving load, excitation frequency and material distribution on dynamic behaviour were analysed [86]. The free vibration analysis of nonuniform beams which possess nonhomogeneity in mass density and Young's modulus under different boundary conditions were studied. The natural frequencies were derived in closed form expressions. Extensive numerical analyses were carried out using Monte-Carlo, Boobnov-Galerkin and finite element methods. From the analysis, it was observed that the static deflection of nonhomogeneous beam coincides with the uniform beam under uniformly distributed load [87].

The vibration and buckling analysis of simply supported axially graded beams in which the inertial coefficients and stiffness vary in axial direction were discussed. The natural frequencies of the axially graded beam were derived in closed form expression. From the analysis, it was observed that the variation of material properties are preselected as polynomial functions that produce the exact mode shapes of inhomogeneous beam [88].

To find the solutions for the dynamic equation of inhomogeneous FG simply supported beam a semi-inverse method was used. The material properties such as material density and Young's modulus vary in polynomial functions, and the closed form expressions were used for finding the natural frequencies. It was observed that the proposed method well suited for axially FG beam [89]. The FG beam subjected to transverse load was also studied. The Young's modulus of the beam was varying exponentially in the thickness direction, keeping the Poisson's ratio constant. The Euler–Bernoulli beam theory used in the analysis by the assumption that plane sections remain plane and normal to the beam axis. It was observed from the analysis that the stresses and displacements depend on a nondimensional parameter for a given variation of Young's modulus. Again as the stress concentration occurred in thick beams, showed less effective when loading took place on the softer side of the FG beam as compared to homogeneous one [90]. The free vibration analysis of an axially FG beam with non-uniform cross-section was studied. An innovative and modest approach was presented for the natural frequencies of the beam with variable mass density and flexural rigidity. Various support conditions such as simply supported, free ends and clamped for transforming the governing equation to Fredholm integral equations were considered.

By considering the non-trivial solution of Fredholm integral equation, the natural frequencies of the system were determined. The effectiveness of the method was validated by comparing with the numerical results available for tapered beams of variable depth or width and graded beam with polynomial nonhomogeneity. Furthermore, the natural frequencies of the graded beam consist of aluminium and zirconia under typical end support conditions was determined. The effect of gradient and geometrical parameters were evaluated and proposed that the analysis would be highly beneficial for optimum design of non-homogeneous nonprismatic beam structures [91].

The structural analysis of an axially FG tapered beam using finite element method was studied. The modelling of the beam was carried out using Euler-Bernoulli beam theory. The shape functions for the proposed beam element derived the same procedure as that of the homogeneous uniform beam element. The simultaneous effects of material properties and varying cross-sectional areas were included in the assessment of the system matrices. The stability analysis, transverse vibration and longitudinal vibration of

the tapered beam with various boundary conditions were evaluated, considering the polynomial variation of material density and flexural rigidity. Moreover, the convergence results for all cases were also studied [92]. Further, the free vibration and stability analysis of an axially FG tapered Timoshenko beam was studied using finite element approach. The exactness of the proposed element enhanced by considering the precise variations of profile cross-section and material properties in the evaluation of the structural matrices. The convergence studies were carried out considering several numerical examples. The various effects such as taper attached proof mass and material nonhomogeneity on natural frequencies and buckling load were investigated [93]. The free vibration and stability analysis were studied for an axially FG tapered Euler–Bernoulli beam through the differential equation of motion. A new differential transform element method (DTEM) was proposed which improves the rate of convergence results. Apart from this, differential quadrature element method of lowest-order (DQEL) was used to solve the governing differential equation of motion. The free transverse, longitudinal frequencies, and critical buckling load were obtained using both the DTEM and DQEL methods considering several numerical examples of tapered Euler–Bernoulli beams made of axially FG materials [94].

The vibration and buckling analysis of an axially FG simply supported beam using semi-inverse method was studied. The classical beam theory was used to model the beam. By considering the predefined frequency and buckling load, the young's modulus variation was obtained in the axial direction concerning axial coordinates. From the analysis it was observed, an exponential variation of young's modulus in the axial direction for vibration and buckling problems [95].The theoretical analysis of a fourth order differential equation of the FG beam with material properties variation was studied. The variation of material density and young's modulus could be responsible for variation in volume fraction in one layer of the beam or different layers of a multi-layered sandwich beam. The classical beam theory has been used to establish the governing equation of the FG beam. Apart from this the shear deformation, mass inertia and mass distribution effect have been taken into account. The Eigen frequencies and corresponding Eigen modes were calculated by considering several numerical experiments for one layer beam and multi-layered sandwich beam. The obtained results were compared with the commercially available FE codes for two-dimensional solid elements [96].

2.2.3 Thermal loading

It is obvious to incorporate the thermal effects in the coupled electromechanical models. The temperature is treated as an additional state variable to account for thermal effects in addition to the piezoelectric effects. Thermal effects become a prime aspect when the piezoelectric structure has to work in extremely hot or cold situations. These conditions may rigorously affect the response of piezoelectric structures in different ways. Some of the substantial works in this direction are presented here:

The fully coupled thermopiezomechanical field equations in weak form were discussed. The field equation includes the linearized constitutive equation, electrodynamics and the entropy production inequality. The objective was to provide an appraisal to these equations to found a concept for a numerical solution based on the finite element method. The temperature is coupled with the mechanical displacement and electric potential only through the one time derivatives. The equation can be solved separately in static case and a separate solution method proposed for dynamic case. The influence of temperature on the behaviour of the smart structure was discussed [97]. The generalized plane strain deformations of laminated plates subjected to thermal, electrical, and mechanical boundary conditions at the edges were studied. To determine the coefficients in the series the continuity equation at the interfaces, boundary conditions at the top and bottom surfaces and edges were used. The results were obtained for laminated plates with different geometric boundary conditions such as clamped, simply supported or clamped-free. The results obtained should ascertain the accuracy of various plate theories and finite element formulations [98].

The thermopiezoelastic characteristics of the piezoelectric beam and its applications in sensing and optimal control were studied. The linear thermopiezoelastic theory with Timoshenko beam assumptions was used to derive the generic thermopiezoelastic theory for the piezolaminated composite beam. The Hamilton's principle was used to determine the governing equations using linear constitutive equations. The proposed structure was first modelled analytically and then numerical simulations were presented to visualize the dynamics and state-of-control. The effects of thermoelastic and pyroelectric couplings on the dynamics of the structure and the control procedure were considered and deliberated. From the observation, it was concluded that the control procedure cannot be disturbed by

applying a thermal gradient [99]. The general solution for dynamics of piezothermoelastic problems of an isotropic piezoelectric material was derived. When the inertia terms were ignored the general solution reduced to the quasistatic problems. The general solution was used to find the response of a rectangular plate subjected to axisymmetric heating. The numerical results were also presented. It was observed that the stresses at some point reached the maximum value at the beginning of heating rather than at the steady state [100].

The Hamilton's principle and finite element method were used for the response of piezothermoelastic plate. The linear shape functions and first order shear deformation theory were used in the formulation. The dynamic equations of motion were solved using Newmark method. The numerical results were presented for a given prescribed thermal and a sudden mechanical loading on the thermoelastic composite plate. The piezoelectric layers were attached to the surface of the plate which suppressed the amplitude of vibration through electric potential difference. The controlled and uncontrolled responses were presented graphically. From the analysis, it was found that the displacement due to the thermal effects plays a major role in the precision of piezo-control system [101]. The coupled electro-thermo-elastic equations were used for analysis of smart structures with piezoelectric patches. The coupled equations have been derived from the conservation principle of mass, energy and charge conversion. The related constitutive equation has been derived using the second law of thermodynamics. By incorporating the linear equations and using finite element method the induced electric potentialand deformation subjected to external mechanical, electrical and thermal loadings in the piezo and non piezo material, have been obtained. The theoretical formulation and the solution procedure have been validated by comparing the results with the existing results [102].

The finite element model for the active control of thermally induced vibration of laminated composite shells with piezoelectric sensors and actuators were studied. Nine-noded shell element was implemented to model the structure. The mass, stiffness and thermal expansion of the piezoelectric patch were considered in the mathematical formulation. An active control of the dynamic response of the structure in a closed loop was studied by considering the coupling between sensor and actuator with the host structure. The cylindrical shell was taken into consideration and observed from the

analysis that thermally induced vibration can be suppressed using actuator and sensor. The effects of control gain and piezoelectric layer area coverage have been studied. It was observed that damping can be enhanced by increasing the control gain and piezoelectric layer area coverage [103].

An enhanced lower-order shear deformation theory (ELSDT) for the analysis of smart structure under combined loads (including thermal, electrical and mechanical loads) was proposed. The proposed theory was to minimise the error between the first-order shear deformation theory and the higher-order shear deformation theory. The C^0 shape functions were used for coupling between mechanical, electrical, and thermal problems. The accuracy and robustness of the theory were verified through a number of numerical examples [104].

The piezothermoelastic behaviour of a smart fiber reinforced polymer (FRP) composite shell structure with bonded piezoelectric sensor and actuator was developed. Eight noded finite shell element was used for the FE analysis. To make the strain equations complete Koiter's shell theory, as well as twist curvature component, has been incorporated. The transverse shear effect has also been incorporated according to Mindlin's hypothesis. The pyroelectric effect has been amalgamated in the mathematical formulation along with the mechanical and electrical loading. It was observed from the analysis that pyroelectric effect has a significant role in the response of the structure. Various smart shell panels such as ellipsoidal, doubly curved cylindrical and spherical have been considered, and the responses of coupled thermo-electro-mechanical have been presented [105]. The FE modelling of piezothermoelastic composite beam with distributed piezoelectric sensor and actuator layers were discussed. The mathematical modelling of the composite beam is based on the higher order displacement, electric and linear temperature fields. Two noded Hermitian beam element with virtual work principle was considered for the analysis. For active vibration control of the composite beam subjected to impulse and thermal loading, a constant-gain velocity feedback control approach has been used. The pyroelectric effect on the vibration control is thoroughly investigated. From the analysis, it was observed that the proposed model show good result compared to the existing models. Apart from this, the thermal deformation of the composite beam was predicted using piezoelectric structures [106].

2.3   Geometric nonlinearity

The effect of large deformation or geometric nonlinear effects in slender beams for energy harvesting can't be overlooked. As nonlinearity is a natural phenomenon that exists in almost every structure, its effect on various output responses is needed to be studied. Some of the works in this direction are presented here.

The detailed investigation of the 3-D stress field of multi-layered plates based on the von Karman strain displacement relations was presented. A third-order zigzag plate theory was developed for multi-layered, anisotropic plates with a surface-bonded piezoelectric actuator layer. The numerical results were presented for simply supported plates with surface bonded top and bottom actuators under transverse loading. Various comparisons were made between available solutions and approximate analyses. For all cases, it was found that the effectiveness of active control of displacement increased with decreasing length to thickness ratio [107]. The effects of large deformations on the surface bonded piezoelectric material as well as in the structure were demonstrated. Electromechanical, piezoelectric constitutive equations were adopted for the analysis based on energy method. The first order shear deformation theory was adopted for the displacement fields. The nonlinear equilibrium equation was solved by an incremental, iterative technique based on Newton–Raphson method and examined considering the electromechanical coupling effects. The effects of nonlinearity on the structural responses due to axial and transverse loading for both cantilever and simply supported beams have been investigated [108]. The nonlinear dynamic responses of piezolaminated structures were studied. The Lagrangian formulation and the principle of virtual work were used for the finite element formulations. Twenty noded solid elements was taken into account for analysis of the piezolaminated structure. To verify the accuracy of the present formulation, numerical examples were studied. The convergence of the formulation and the practicality for the solutions of the large deformation dynamic responses of the piezolaminated structure, were investigated. [109]. It was observed from the analysis that the amplitude of deflection, frequency and output voltage are significantly influenced by the large deformation of structures The transient large amplitude vibration response of thin composite structures and its control by piezoelectric layers were discussed. The first order shear deformation (Reissner-Mindlin) theory was employed considering a nonlinear finite shell element with coupled piezoelectric layers. The proposed model could be used

in smart structures integrated with piezoelectric sensors and actuators at the top and bottom surfaces. From the analysis it was observed that for prediction of sensor output voltage, numerical analyses were very much sensitive towards geometric nonlinearities [110].

The nonlinear vibration control of space structures was presented. The members of the structures were modeled as a beam-column element. The structural member was subjected to an axial force, transverse shear forces and moments. The shear stresses transmitted to the structural members by the piezoelectric actuators bonded to the surface were derived. The feasibility of active control of nonlinear dynamic response of space structures with the piezoelectric patch was studied considering the weak form of the governing equation and assumed stress field. The viability of the approach was demonstrated by considering several numerical examples [111]. The vibration control of beam-type plates using piezoelectric sensors and actuators with geometrically nonlinear deflection and wavelet based deformation identification was presented. The identification was performed by transferring the nonlinear equation into a set of nonlinear algebraic equations composed of electric charges and currents on piezoelectric sensors. The signals of deflection and velocity were identified by employing a control law with negative feedback. The control voltage applied to the actuator was determined by the weighted residual method. Several numerical simulations were carried out to demonstrate the proposed approach [112]. For nonlinear harvester, the experimental measurements of harvested power under different motion speeds and resistances were found which were in good agreement with the numerical analysis. The obtained results established the effectiveness of the proposed resistance optimization method for nonlinear energy harvesting from human motions [113].

The electromechanical coupling, control and dynamics of the piezoelectric laminated circular plate with large initial deformation were investigated. The piezoelectric layers were uniformly distributed over the top and bottom surface of the circular plate. The von Karman type of geometric nonlinearity was used. The control effect was introduced through a control moment on the circumference of the circular plate. The solutions were derived from the dynamic equations. The nonlinear deflections and natural frequencies of the plate subjected to high voltage were studied [114]. Similarly, the electromechanical coupling, control and dynamics of thermal buckling of a nonlinear piezoelectric laminated circular plate with large initial deformation were investigated. The active control of

nonlinear deflections, thermal buckling and natural frequencies of the plate were studied, and nonlinear effects are calculated [115].

The nonlinear active control of a piezoelectric laminated spherical shallow shell was investigated. The piezoelectric layers were uniformly distributed over the top and bottom surface of the shell. The governing equations were formulated and a semi-analytical method was adopted for solving it. From the numerical result, it was observed that the nonlinear deformation and natural frequency could be controlled by a control high voltage across the piezoelectric layers. In addition, the large amplitude effect on natural frequency was discussed by Galerkin method and KBM perturbation method [116]. The effect of large deformations on the piezoelectric materials and the structures under time varying loads were investigated. The piezoelectric constitutive relations derived by Tiersten were adopted. The first order shear deformation theory was adopted for the displacement field. The von Karman plate equation was used for large deformation analysis of the beam. An iterative technique was implemented for analysis of nonlinear equilibrium equations. The active control of PVDF bimorph beam with nonlinear effect was investigated [117].

The nonlinear vibrations of piezoelectric layered beams using FE reduced order model were presented. The geometric nonlinearity was taken into account in the model based on Von Karman nonlinear strain-displacement relationships. A parametric excitation term was introduced in the governing equation due to geometric nonlinearity. The analysis of reduced order model was done using harmonic-based continuation method. The proposed model was validated with the existing model in the literature. The model was suggested to be used in nanoelectromechanical systems [118]. The dynamic analysis of beams for large deformation was analysed in the frequency domain. A quantitative comparison was made between models formed by p-FEM and isogeometric analysis method. The principle of virtual work was used for the derivation of governing equation, considering Timoshenko beam theory. Harmonic balance method was used for the periodic responses of the structure. In the frequency domain, the nonlinear equations of motion were solved by arc-length continuation method. From the study, it was observed that isogeometric analysis method showed a better result than p-FEM when same numbers of degrees of freedom were used [119]. The forced vibration of cross-beam

incorporating the effect of geometric non-linearity under harmonic excitation was studied. The vibration analysis was carried out by reducing the dynamic system into an equivalent static system. The response of the structure was found under harmonic excitation by solving the individual beams using multi-dimensional secant method, otherwise known as Broyden's method. The proposed method was validated through the results generated in ANSYS 11.0. In addition to this, the response was studied for various loading and contact location of the beams [120].

2.4 GA based optimisation

Over the last few decades, GA has been extensively used as search and optimization tools in various practical problem fields, including sciences, commerce, engineering, artificial intelligence and robotics. The principal reasons for their attainment are ease of use, broad applicability and global perspective. As real coded GA takes a little advantage over binary coded GA, some of the works related to real coded GA are presented.

The binary coded GA in which the string length depends on the precision was presented. The computational complexity is more for higher precision due to greater requirements in string length and population size. Again, for coding the decision variables, a fixed coding system is used. The boundary of decision variables must be used such that the optimum value can be achieved. But in many practical problems, such information is unknown previously. Hence, a real-coded genetic algorithm is implemented in which real parameters are directly used as decision variables. The real coded GA is much easier than binary coded GAs. However, the main problem arises for creating new offspring by using a pair of real parameters [121]. In binary coded GA, good properties could not be attained from the use of the binary alphabets. However to overcome this issue, real coded GAs are implemented which seem particularly natural, tackling with various optimisation problems. An upright summary for crossover and mutation operators of real parameters and the behaviour of such real coded GA were provided [122].

An improved GA-based optimal vibration control of composite shell structures was presented. A linear quadratic regulator control scheme was used for maximising the damping ratio based on real-coded GA. The actuator voltage was kept within the limit to

maximize the damping ratio. From the result, it was observed that combined GA-based optimal actuators placement and GA-based linear quadric regulator (LQR) control scheme showed superior result than conventional active vibration control using LQR schemes. In addition to this, the improved GA-based optimal placement and LQR control scheme not only leads to increased closed-loop damping ratio but also shows a drastic reduction in input/actuation voltage compared to the already published results [123]. The finite element and GA based vibration energy harvesting from a tapered piezolaminated cantilever beam was discussed. Euler–Bernoulli beam theory was used for modelling various cross sections of the beam. The governing equation of motion was derived by using Hamilton's principle. The effect of structural damping has also been incorporated in the FE model. The effects of taper (both in the width and height directions) on output power for three cases of shape variation (such as linear, parabolic and cubic) along with frequency and voltage were analysed. A real-coded genetic algorithm-based constrained (using ultimate stress and breakdown voltage) optimization technique has been formulated to determine the best possible design variables for optimal harvesting power. A comparative study is also carried out for output power by varying the cross section of the beam, and GA based optimization scheme shows better results than the available conventional trial and error methods [124].

    A parallel-structured real-coded GA (RCGA), named the RGA-RDD, for numerical optimization was developed. The proposed RGA-RDD assimilates three specially designed evolutionary operators namely ranking selection (RS), direction based crossover (DBX) and the dynamic random mutation (DRM) to specify the evolutionary process. Unlike the conventional RCGAs, the RGA-RDD incorporates a coordinator in the inner parallel loop to establish the operations like DBX and DRM so that a global optimum is obtained. Besides, this parameter selection guideline was provided for the settings of the proposed RGA-RDD. The efficiency and applicability of the proposed RGA-RDD are validated through a variety of benchmarked problems, followed by comprehensive comparisons with some existing evolutionary algorithms. Extensive simulation results revealed that the performance of the proposed RGA-RDD is far better than the comparative methods in finding the global optimum for real-parameter optimization problems [125]. Further, a real-coded GA (RCGA) for constrained optimization problem was presented. The effectiveness and applicability of proposed GA were demonstrated with various benchmarked constrained optimization problems. The extensive comparison

with the existing algorithms shows that, the proposed GA gives faster convergence and better solution accuracy for constrained problems. As a specific application, the proposed RCGA was applied to optimize the film growth of a vapour deposition reactor. The simulation results showed a better coefficient of performance using the proposed GA [126].

The global optimal solution of complex problems using extended version of real coded GA (RCGA) was presented. As GA consists of several genetic operators such as selection, crossover and mutation operators, which offers the choice to be modified to improve the performance of particular operation. The new crossover techniques incorporating Boltzmann's distribution (BD) and Metropolis algorithm (MPA) were discussed, which will improve the quality of solution as well as the rate of convergence to the optimum solution [127]. An improved real-coded GA (IRGA) was used for unit commitment (UC) of a typical optimization problem in electric power system. The model was proposed to optimise the emission control and energy savings. The swap window and hill-climbing operators were used in real number coding method and compared with the other algorithmic approaches. From the solution analysis, it was concluded that the proposed algorithm provide better improvement in computational time and effectiveness [128].

The implementation of a new selection method and crossover operation in a real-coded GA was presented. The new selection method comprised an elitist subpopulation, an off-spring subpopulation and a mutated subpopulation. The crossover operation was carried out considering a probabilistic approach in which the distance between the individuals was measured. The level of variance in crossover operation was deliberated considering the concept of allowance. The proposed approach was validated and verified by several engineering optimization problems [129]. A new crossover operator called the double distribution crossover (DDX) was proposed in real coded GA. The performance of DDX was compared with available real-coded crossover operator namely Laplace crossover (LX). The DDX was followed by a mutation operator named power mutation (PM) to get a new real coded GA called DDX-PM. The performance of both algorithms such as DDX-PM and LX-PM were compared by function evaluation. [130].

2.5 Summary

Even though several research works have been carried out for energy harvesting from piezolaminated beams but still there is a gap in the modelling and analysis of arbitrarily varying cross sections such as linear, parabolic and cubic (considering tapers in both directions) with material non-homogeneity along the longitudinal axis of the beam. Apart from this the piezothermoelastic behaviour along with energy harvesting from the structure under combined thermo-mechanical loading with temperature dependent material properties yet not analysed. Furthermore, FE based geometric nonlinear formulation of piezolaminated FG beam for vibration energy harvesting has not been yet exposed. Therefore, the main objective of the present research work is to model and analyse an axially piezolaminated FG beam with geometric nonlinear effects in thermal environment for optimal vibration energy harvesting within the allowable limits of stress of the beam and PZT as well as the breakdown voltage of PZT patch. A real coded GA based constrained optimization technique has also been developed to avoid the underestimation or overestimation of power and premature failure of the beam, and also to determine the best possible set of design variables which mostly influence the vibration energy harvesting.

Chapter 3

Mathematical Modelling and Analysis of Nonprismatic Axially FG Beams under Combined Mechanical and Thermal Loading

3.1 Introduction

As per the justification provide in Section 2.2 of Chapter 2 for focussing on enhancement of power density of piezoelectric energy harvester, this chapter deals with the FE based mathematical modelling of the nonprismatic axially FG piezolaminated beam under combined mechanical and thermal loading. Attention has been given towards different cross sectional profiles for generating a uniform strain profile along the beam length resulting in significant increase in output power density. Further, FG beam is used in the formulation by varying the properties (such as mass density, modulus of elasticity, Poisson's ratio and shear modulus) axially to maintain the continuity in stress and strain fields. Moreover the mathematical formulation consists of the simultaneous effects of mechanical and thermal loading. Although mechanical and electrical coupling interaction affects the performance of the piezoelectric devices, the presence of variation of temperature can also influence the voltage generation in the piezoelectric sensor. The temperature term can introduce both pyroelectric and thermal strain effects to the distributed sensor and deflection in dynamic oscillations.

3.2 Mathematical formulation for vibration Energy harvesting

The mathematical formulations involve the modelling of the axially FG (i.e.

material non-homogeneity) beam, the cross sectional profiles, and the static and dynamic equations of a piezolaminated beam in both thermal and mechanical environment for output power. The Hamilton's principle has been used for solving the governing equation of motion with FEA. The details of the above formulations are presented in the following subsections.

3.2.1 Assumptions made for the present formulation

The following assumptions have been made for the detailed mathematical formulations of the beam.

3.2.1.1   Assumptions in structural analysis

- The cross sections which are plane and normal to the longitudinal axis remain plane and normal to it after deformation.
- The shear deformations are neglected.

3.2.1.2   Assumptions in electromechanical analysis

In addition to the assumptions in the structural analysis, the following assumptions have been made for electric field and electric potential.
- The variation of electric potential is linear in thickness direction and the electric potential is constant over the piezoelectric layer.
- Linear constitutive equations of the piezoelectric material have been considered.
- No shear strain is induced by the electric field in poling direction.

3.2.1.3   Assumptions in piezothermoelastic analysis

The following assumptions have been made in conjunction with structural and electromechanical analysis:
- The variation of thermal load is linear in the thickness direction.
- The temperature is taken as constant on top and bottom surface of each element of the beam structure.

3.2.2 Modelling of axially FG beam

The beam is modelled as FG, i.e., non-homogeneity of material properties (such as density, Young's modulus, and Poisson's ratio) in the axial direction. The following mathematical expression has been proposed to determine such FG properties of the beam in the axial direction (which is continuously decreasing towards the tip of the cantilever beam).

$$Y(x,\theta) = Y_b(\theta)\left[1 - \frac{x}{(k+1)L_b}\right]^{np}$$

where,

$$Y_b(\theta) = Y_0\left[Y_{-1}\theta^{-1} + 1 + Y_1\theta_1 + Y_2\theta^2 + Y_3\theta^3\right]$$

(3.1)

Here, $Y(x, \theta)$ denotes the material property such as density, Young's modulus, Poisson's ratio, shear modulus and coefficient of linear expansion respectively, which is both position and temperature dependent. The terms Y_0, Y_{-1}, Y_1, Y_2, and Y_3 are constants in the cubic fit of the material property. θ is the average temperature between top and bottom surface of the modelled beam. The terms *k and np* are positive integer parameter (to avoid the material properties to be zero at the tip of cantilever beam) and the power gradient index. L_b is the length of the beam.

3.2.3   Mathematical modelling of cross section profiles of the beam

Three different cross-sectional profiles are considered to study the responses of the piezo laminated beam. They are:

Case (A): $$A_b(x) = A_0\left(1 - c_b\frac{x}{L_b}\right)\left(1 - c_h\frac{x}{L_b}\right)$$ (3.2)

Case (B): $$A_b(x) = A_0\left(1 - c_b\frac{x}{L_b}\right)^2\left(1 - c_h\frac{x}{L_b}\right)^2 \quad \text{and}$$ (3.3)

Case (C): $$A_b(x) = A_0\left(1 - c_b\frac{x}{L_b}\right)^3\left(1 - c_h\frac{x}{L_b}\right)^3$$ (3.4)

The geometric profiles of the modelled beams are shown in Figure 3.1 (a)-(c). The width and height tapers of the beam are denoted as c_b and c_h respectively, which could vary in the range of $0 \leq c_b \leq 1$ and $0 \leq c_h \leq 1$. When $c_b = c_h = 0$, the beam will become a uniform one and when $c_b = c_h = 1$ the beam will be taper to a point at $x = L_b$. The transverse cross-

sectional area of the beam near the clamped end is A_0, which gradually decreases towards the free end.
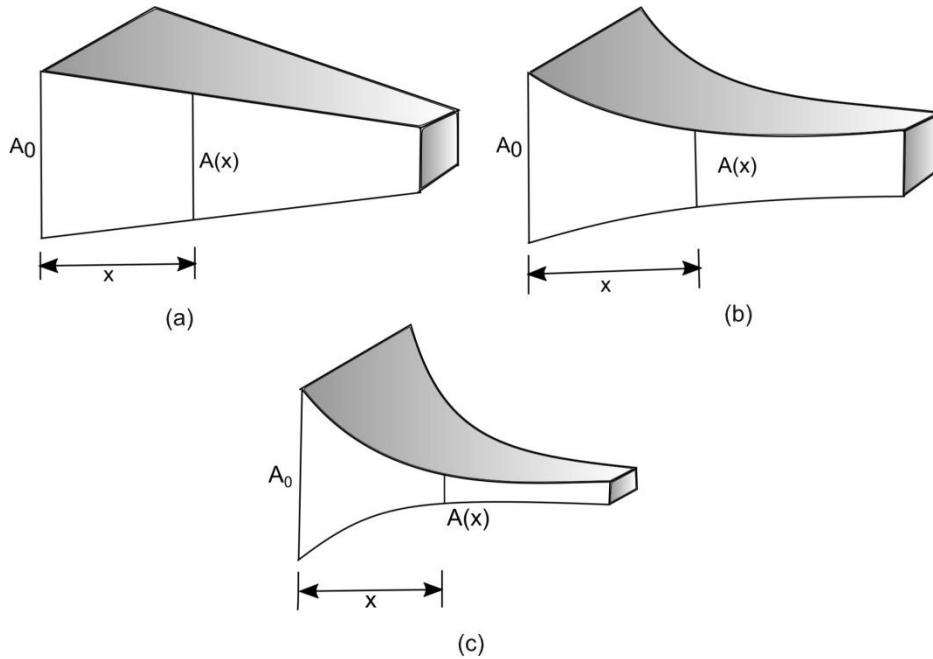
Figure 3.1 Geometric profiles of (a) Linear (Case-A) (b) Parabolic (Case-B) and (c) Cubic (Case-C) beam.

3.2.4 FE modelling and analysis of non-prismatic piezolaminated beam
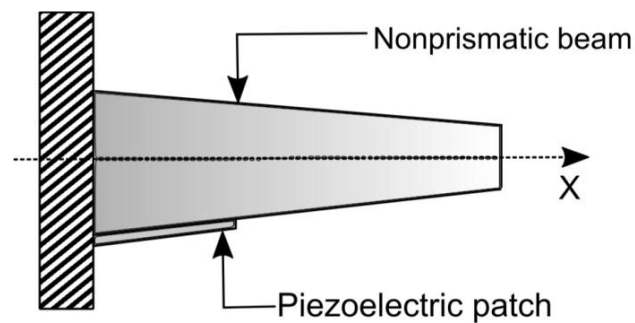
Figure 3.2 Cantilever non-prismatic beam with piezoelectric patch

A cantilever non-prismatic beam with the piezoelectric patch is shown in Figure 3.2. The piezoelectric patch is mounted as a sensor on the surface of the beam. The bonding agent's stiffness and mass are neglected. The piezolaminated cantilever beam is

modelled as a piezoelectric patch, which includes the sensor dynamics and the remaining beam elements based on classical beam theory.

3.2.5   Displacement field

The displacement field of the beam in x, y and z-direction can be written as

$$u(x,y,z) = -z\psi(x) = -z\left(\frac{\partial w_0}{\partial x}\right),$$

$$v(x,y,z) = 0, \text{ and}$$

$$w(x,y,z) = w_0(x),$$

(3.5)

where, *u, v and w* denote the time-dependent axial, lateral and transverse displacements along *x, y and z*-axes, respectively. The terms $w_0(x, t)$ is the transverse displacement of any point in the midplane ($z = 0$). The term ψ is the rotation of the midplane about z-axis. The axial displacement at any point in the midplane ($z = 0$) is neglected as its effect is negligible as compared to transverse displacement. Moreover, as output power is greatly influenced by bending strain, the membrane strain is neglected for the above expressions.

3.2.6   Shape function

The nonprismatic beam element with two degrees of freedom at each node is shown in Figure 3.3 In FE modelling, each nodal point is assumed to experience two degrees of freedom, i.e., transverse displacement (*v*) and rotation (*ψ*), which are supposed to act due to the shear force and bending moment.
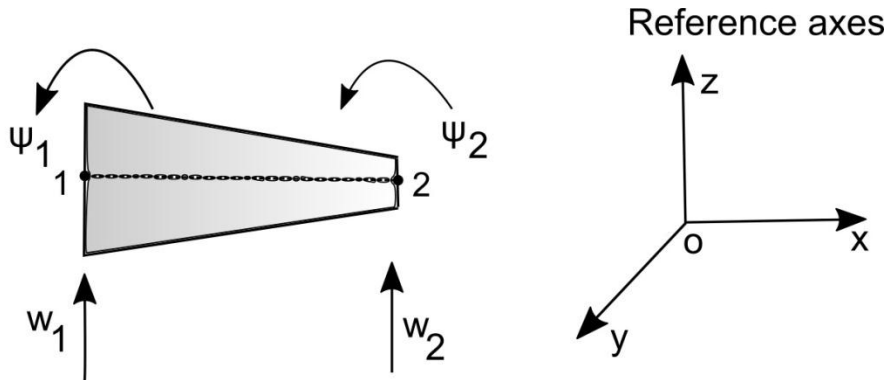
Figure 3.3 Nodal degrees of freedom of a nonprismatic beam element

Assuming the transverse displacement variation through the element length to be cubic polynomial,

$$w_0(x) = a_1 x^3 + a_2 x^2 + a_3 x + a_4 \tag{3.6}$$

where, the terms a_1, a_2, a_3 and a_4 are unknown constants which can be obtained using the boundary conditions. The displacement field could be interpolated in terms of degrees of freedom of nodes and shape functions based on the concept of FEM as

$$\{w_0(x)\} = [N_w]\{q_w\} \tag{3.7}$$

Here, q_w and N_w signifies the nodal degrees of freedom and the bending shape functions, respectively. The shape function is interpolated in matrix form as

$$N_w = [N_1 \quad N_2 \quad N_3 \quad N_4]$$
where,

$$N_1 = 1 - \frac{3x^2}{L_e} + \frac{2x^3}{L_e^3} \qquad N_2 = x - \frac{2x^2}{L_e} + \frac{x^3}{L_e^2} \tag{3.8}$$

$$N_3 = \frac{3x^2}{L_e^2} - \frac{2x^3}{L_e^3} \qquad N_4 = -\frac{x^2}{L_e} + \frac{x^3}{L_e^2}$$

where, L_e is the length of the beam element.

3.2.7 Strain displacement relationship

Using equations (3.5) and (3.7)the axial strain-displacement relationship for the beam element can be written as

$$
\begin{aligned}
\varepsilon_1 &= -z\frac{\partial^2 w_0}{\partial x^2} \\
&= -z\frac{\partial^2([N_w]\{q_w\})}{\partial x^2} \\
&= -z[B_w]\{q_w\}
\end{aligned}
\tag{3.9}
$$

where, B_w is the strain-displacement matrix of the beam element.

3.2.8 Piezothermoelastic constitutive equation

It is assumed that the proposed piezolaminated structure is exposed to three different fields such as elastic, electric and thermal fields. The three dimensional constitutive equations of piezothermoelasticity expressing the coupling between elastic, electric and thermal fields can be expressed as

47

$$
\begin{bmatrix} \sigma_1 \\ \sigma_2 \\ \sigma_3 \\ \sigma_4 \\ \sigma_5 \\ \sigma_6 \end{bmatrix} = \begin{bmatrix} C_{11}^E & C_{12}^E & C_{13}^E & C_{14}^E & C_{15}^E & C_{16}^E \\ C_{21}^E & C_{22}^E & C_{23}^E & C_{24}^E & C_{25}^E & C_{26}^E \\ C_{31}^E & C_{32}^E & C_{33}^E & C_{34}^E & C_{35}^E & C_{36}^E \\ C_{41}^E & C_{42}^E & C_{43}^E & C_{44}^E & C_{45}^E & C_{46}^E \\ C_{51}^E & C_{52}^E & C_{53}^E & C_{54}^E & C_{55}^E & C_{56}^E \\ C_{61}^E & C_{62}^E & C_{63}^E & C_{64}^E & C_{65}^E & C_{66}^E \end{bmatrix} \begin{Bmatrix} \varepsilon_1 \\ \varepsilon_2 \\ \varepsilon_3 \\ \varepsilon_4 \\ \varepsilon_5 \\ \varepsilon_6 \end{Bmatrix} - \begin{bmatrix} e_{11} & e_{21} & e_{31} \\ e_{12} & e_{22} & e_{32} \\ e_{13} & e_{23} & e_{33} \\ e_{14} & e_{24} & e_{34} \\ e_{15} & e_{25} & e_{35} \\ e_{16} & e_{26} & e_{36} \end{bmatrix} \begin{Bmatrix} E_1 \\ E_2 \\ E_3 \end{Bmatrix} - \begin{bmatrix} \lambda_1 \\ \lambda_2 \\ \lambda_3 \\ \lambda_4 \\ \lambda_5 \\ \lambda_6 \end{bmatrix} \Delta\theta \quad (3.10)
$$

$$
\begin{bmatrix} D_1 \\ D_2 \\ D_3 \end{bmatrix} = \begin{bmatrix} e_{11} & e_{12} & e_{13} & e_{14} & e_{15} & e_{16} \\ e_{21} & e_{22} & e_{23} & e_{24} & e_{25} & e_{26} \\ e_{31} & e_{32} & e_{33} & e_{34} & e_{35} & e_{36} \end{bmatrix} \begin{Bmatrix} \varepsilon_1 \\ \varepsilon_2 \\ \varepsilon_3 \\ \varepsilon_4 \\ \varepsilon_5 \\ \varepsilon_6 \end{Bmatrix} + \begin{bmatrix} \xi_{11}^\sigma & \xi_{12}^\sigma & \xi_{13}^\sigma \\ \xi_{21}^\sigma & \xi_{22}^\sigma & \xi_{23}^\sigma \\ \xi_{31}^\sigma & \xi_{32}^\sigma & \xi_{33}^\sigma \end{bmatrix} \begin{Bmatrix} E_1 \\ E_2 \\ E_3 \end{Bmatrix} + \begin{bmatrix} p_1 \\ p_2 \\ p_3 \end{bmatrix} \Delta\theta \quad (3.11)
$$

$$
and \quad s = \begin{bmatrix} \lambda_1 & \lambda_2 & \lambda_3 & \lambda_4 & \lambda_5 & \lambda_6 \end{bmatrix} \begin{Bmatrix} \varepsilon_1 \\ \varepsilon_2 \\ \varepsilon_3 \\ \varepsilon_4 \\ \varepsilon_5 \\ \varepsilon_6 \end{Bmatrix} + \begin{bmatrix} p_1 & p_2 & p_3 \end{bmatrix} \begin{Bmatrix} E_1 \\ E_2 \\ E_3 \end{Bmatrix} + \alpha_T \Delta\theta \quad (3.12)
$$

where, stress and strain tensors are represented as σ and ε respectively. C represents the elastic matrix coefficients and a vector of applied electric field is represented by E. The term λ represents the thermal stress coefficient, $\Delta\theta$ represents the temperature rise from stress free temperature T_0, and D represents a vector of electric displacement. The term e represents the piezoelectric coupling coefficient, ξ represents the permittivity and p represents the pyroelectric tensor. The exponent E and σ indicates the parameters at constant electric field and stress respectively. The term s denotes the entropy and α_T represents expansion coefficient which can be given as $\alpha_T = \dfrac{\rho C_v}{T_0}$ where, C_v is the specific heat at constant volume and ρ is the mass density.

Assuming that the piezoceramic material is poled along the axis 3 and viewing it as transversely isotropic, many parameters in the above expression becomes either zero or can be expressed in terms of other parameters. Subsequently, the equations, (3.10) (3.11) and (3.12) are simplified to

$$
\begin{bmatrix} \sigma_1 \\ \sigma_2 \\ \sigma_3 \\ \sigma_4 \\ \sigma_5 \\ \sigma_6 \end{bmatrix} = \begin{bmatrix} C_{11}^E & C_{12}^E & C_{13}^E & 0 & 0 & 0 \\ C_{21}^E & C_{22}^E & C_{23}^E & 0 & 0 & 0 \\ C_{31}^E & C_{32}^E & C_{33}^E & 0 & 0 & 0 \\ 0 & 0 & 0 & C_{44}^E & 0 & 0 \\ 0 & 0 & 0 & 0 & C_{55}^E & 0 \\ 0 & 0 & 0 & 0 & 0 & C_{66}^E \end{bmatrix} \begin{bmatrix} \varepsilon_1 \\ \varepsilon_2 \\ \varepsilon_3 \\ \varepsilon_4 \\ \varepsilon_5 \\ \varepsilon_6 \end{bmatrix} - \begin{bmatrix} 0 & 0 & e_{31} \\ 0 & 0 & e_{31} \\ 0 & 0 & e_{33} \\ 0 & e_{24} & 0 \\ e_{15} & 0 & 0 \\ 0 & 0 & 0 \end{bmatrix} \begin{Bmatrix} E_1 \\ E_2 \\ E_3 \end{Bmatrix} - \begin{bmatrix} \lambda_1 \\ \lambda_2 \\ \lambda_3 \\ 0 \\ 0 \\ 0 \end{bmatrix} \Delta\theta \quad (3.13)
$$

$$
\begin{bmatrix} D_1 \\ D_2 \\ D_3 \end{bmatrix} = \begin{bmatrix} 0 & 0 & 0 & 0 & e_{15} & 0 \\ 0 & 0 & 0 & e_{24} & 0 & 0 \\ e_{31} & e_{31} & e_{33} & 0 & 0 & 0 \end{bmatrix} \begin{Bmatrix} \varepsilon_1 \\ \varepsilon_2 \\ \varepsilon_3 \\ \varepsilon_4 \\ \varepsilon_5 \\ \varepsilon_6 \end{Bmatrix} + \begin{bmatrix} \xi_{11}^\sigma & 0 & 0 \\ 0 & \xi_{22}^\sigma & 0 \\ 0 & 0 & \xi_{33}^\sigma \end{bmatrix} \begin{Bmatrix} E_1 \\ E_2 \\ E_3 \end{Bmatrix} + \begin{bmatrix} 0 \\ 0 \\ p_3 \end{bmatrix} \Delta\theta \quad (3.14)
$$

$$
s = \begin{bmatrix} \lambda_1 & \lambda_2 & \lambda_3 & 0 & 0 & 0 \end{bmatrix} \begin{Bmatrix} \varepsilon_1 \\ \varepsilon_2 \\ \varepsilon_3 \\ \varepsilon_4 \\ \varepsilon_5 \\ \varepsilon_6 \end{Bmatrix} + \begin{bmatrix} 0 & 0 & p_3 \end{bmatrix} \begin{Bmatrix} E_1 \\ E_2 \\ E_3 \end{Bmatrix} + \alpha_T \Delta\theta \quad (3.15)
$$

Further, as the structure is modelled based on the Euler–Bernoulli beam assumptions, the stress components other than the one-dimensional bending stress (σ_1) becomes negligible for which,

$$
\sigma_2 = \sigma_3 = \sigma_4 = \sigma_5 = \sigma_6 = 0 \quad (3.16)
$$

Hence, the equations (3.13), (3.14) and (3.15) become

$$
\sigma_1 = C_{11}^E \varepsilon_1 - e_{31} E_3 - \lambda_1 \Delta\theta \quad (3.17)
$$

$$
D_3 = e_{31} \varepsilon_1 + \xi_{33}^S E_3 + p_3 \Delta\theta \quad (3.18)
$$

$$
s = \lambda_{1_1}^T \varepsilon_1 + p_3^T E_3 + \alpha_T \Delta\theta \quad (3.19)
$$

From equations (3.17) and (3.18) the direct and inverse piezoelectric equations can be obtained by neglecting the thermal field terms as

$$
\sigma_1 = C_{11}^E \varepsilon_1 - e_{31} E_3 \quad (3.20)
$$

$$
\text{and} \quad D_3 = e_{31} \varepsilon_1 + \xi_{33}^S E_3 \quad (3.21)
$$

The strain (ε_1) in the piezoelectric material induces a polarization ($e_{31}\varepsilon_1$) by the direct piezoelectric effect which marks the beginning of formulation for piezoelectric sensor.

3.2.9   Electrical potential in the piezoelectric patch

The component of electric field in the thickness direction (E_3) is dominant for a thin piezoelectric patch. Hence, a non-zero component of electric field can be accurately approximated in the thickness direction. Therefore, it is assumed that the electric potential varies only in thickness direction and remains constant for the other two directions (i.e. *1* and *2* directions). Since the electric potential is assumed constant, the negative gradient of the electric potential other than thickness direction is zero. In the present work, it is assumed that the electric potential varies linearly in thickness direction and only one electrical degree of freedom is considered for the piezoelectric patch. With this approximation, the electric field strength in terms of the electric potential for the piezoelectric patch can be expressed as

$$-E = \begin{bmatrix} E_1 \\ E_2 \\ E_3 \end{bmatrix} = \begin{bmatrix} 0 \\ 0 \\ \dfrac{1}{t_p} \end{bmatrix} \{v\} \tag{3.22}$$

where, t_p is the thickness of the piezoelectric layer and v is the electric potential of the piezoelectric patch. Since the electric field is non-zero only in the thickness direction, the field strength in other two directions is removed. Therefore, the electric field vector for an element can be expressed as

$$-E_3 = [B_v]\{v\} \tag{3.23}$$

Where, B_v is the electric field gradient matrix of the piezoelectric patch. Due to the presence of piezoelectric patch, an additional degree of freedom is introduced at the elemental level.

3.2.10 Temperature field

The temperature field is considered as a linear function in the thickness direction. Each element has two temperature degrees of freedom (for bottom surface and top surface) are considered. The expression of temperature field for the element can be written as

$$\theta(x,z) = \left(\frac{1}{2} - \frac{z}{t_p}\right)\theta_b + \left(\frac{1}{2} + \frac{z}{t_p}\right)\theta_t$$

$$= \left[\frac{1}{2} - \frac{z}{t_p} \quad \frac{1}{2} + \frac{z}{t_p}\right]\begin{Bmatrix}\theta_b \\ \theta_t\end{Bmatrix} \tag{3.24}$$

$$= [N_\theta]\{\theta\}$$

where, θ_t, θ_b are the top and bottom surface temperatures. N_θ is the linear interpolation vector for the temperature variation through the depth. The term θ is the vector of surface temperatures.

3.2.11 Governing equation using Finite element procedure

The governing equation has been derived using the conventional FE procedure. It involves the derivation of FE equations for both static and dynamic analysis of a modelled piezothermoelastic beam.
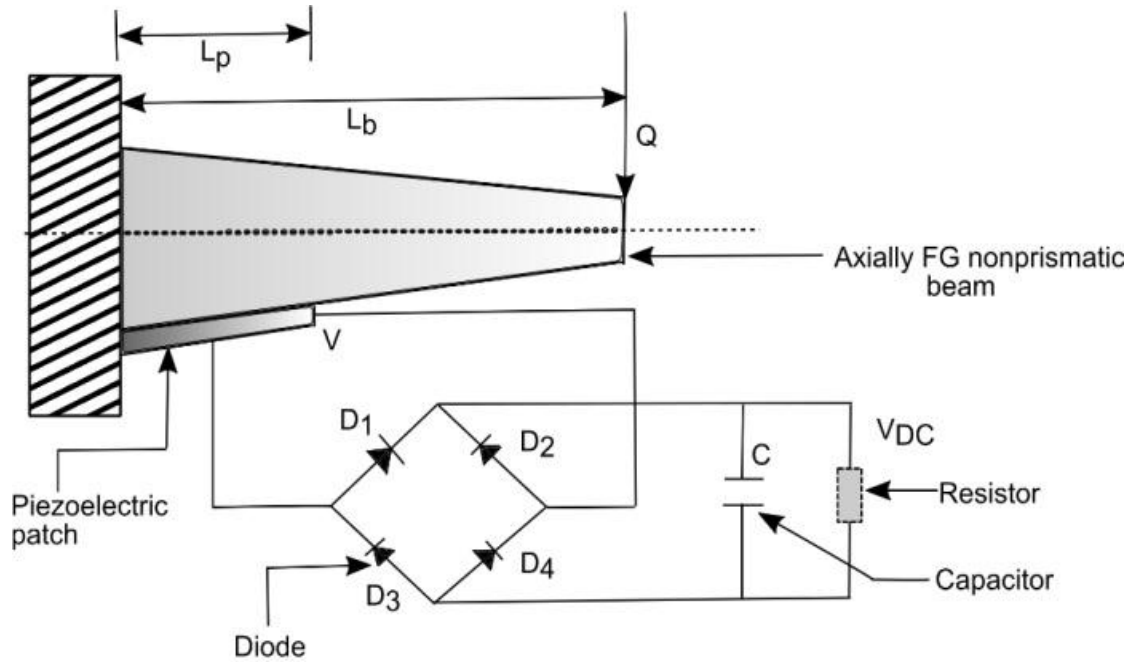
Figure 3.4 Axially FG non-prismatic piezolaminated cantilever beam with the classic electric interface

For the analysis, an axially FG non-prismatic cantilever beam with a piezoelectric patch of length L_p near the clamped end is considered (shown in Figure 3.4). An electric interface is connected to both surfaces of the piezoelectric patch for obtaining the

voltage. Due to the external load resistance a current will flow through the circuit which consequently generate power. The detailed static and dynamic formulations for the model are presented in the following sections.

3.2.11.1 *Static finite element equation*

The variation of total potential energy of the element is given by using Hamilton's principle as

$$\delta \Pi = \int_{t_1}^{t_2} [\delta (T_p - W)\ dt = 0 \tag{3.25}$$

where, T_p is the internal potential energy consisting of elastic strain energy of the structure (T_{es}), electric potential energy of the piezoelectric patch (T_{ep}) and the internal energy due to thermal fields (T_{et}) as

$$T_p = T_{es} + T_{ep} + T_{et} \tag{3.26}$$

The external work done W consists of work done due to applied mechanical forces and the applied electrical charges. The terms used in equation (3.26) can be deduced as follows:

    a. Elastic strain energy of the structure

$$T_{es} = \frac{1}{2} \int_V \{\varepsilon_1\}^T \sigma_1 dV$$

$$= \frac{1}{2} \int_V \{\varepsilon_1\}^T (C_{11}^E \varepsilon_1 - e_{31} E_3 - \lambda_1 \Delta\theta)\ dV$$

$$= \frac{1}{2} \int_V \{\varepsilon_1\}^T C_{11}^E\ \varepsilon_1\ dV - \frac{1}{2} \int_{V_p} \{\varepsilon_1\}^T e_{31} E_3\ dV - \frac{1}{2} \int_V \{\varepsilon_1\}^T \lambda_1 \Delta\theta)\ dV$$

$$= \frac{1}{2} \{q_w\}^T \left[\int_V z^2 [B_w]^T C_{11}^E\ [B_w]\ dV \right] \{q_w\} + \frac{1}{2} \{q_w\}^T \left[\int_{V_p} (-z)[B_w]^T e_{31}\ [B_v]\ dV_p \right] \{v\} \tag{3.27}$$

$$- \frac{1}{2} \{q_w\}^T \left[\int_V (-z)[B_w]^T \lambda_1\ [N_\theta]\ dV \right] \{\theta\}$$

$$= \frac{1}{2} \{q_w\}^T [K^e] \{q_w\} + \frac{1}{2} \{q_w\}^T [K_{pb}^e]\{v\} - \frac{1}{2} \{q_w\}^T [K_{b\theta}^e]\{\theta\}$$

    b. Electric potential energy of the piezoelectric patch

$$T_{ep} = -\frac{1}{2}\int_V E_3^T D_3 dV$$

$$= -\frac{1}{2}\int_V E_3^T \left(e_{31}\varepsilon_1 + \xi_{33}^S E_3 + p_3 \Delta\theta\right) dV$$

$$= -\frac{1}{2}\int_{V_p} E_3^T e_{31}\varepsilon_1\, dV_p - \frac{1}{2}\int_{V_p} E_3^T \xi_{33}^S E_3\, dV_p - \frac{1}{2}\int_{V_p} E_3^T p_3 \Delta\theta\, dV_p$$

$$= \frac{1}{2}\{v\}^T\left[\int_{V_p}(-z)[B_v]^T e_{31}[B_w]\, dV_p\right]\{q_w\} - \frac{1}{2}\{v\}^T\left[\int_{V_p}[B_v]^T \xi_{33}^S [B_v]\, dV_p\right]\{v\} \tag{3.28}$$

$$+ \frac{1}{2}\{v\}^T\left[\int_{V_p}[B_v]^T p_3[N_\theta]\, dV_p\right]\{\theta\}$$

$$= \frac{1}{2}\{v\}^T[K_{bp}^e]\{q_w\} - \frac{1}{2}\{v\}^T[K_{pp}^e]\{v\} + \frac{1}{2}\{v\}^T[K_{p\theta}^e]\{\theta\}$$

c. Internal energy due to thermal field

$$T_{et} = -\frac{1}{2}\int_V \Delta\theta s\, dV$$

$$= -\frac{1}{2}\int_V \Delta\theta \left(\lambda_1^T \varepsilon_1 + p_3^T E_3 + \alpha_T \Delta\theta\right) dV$$

$$= -\frac{1}{2}\int_V \Delta\theta \lambda_1^T \varepsilon_1\, dV - \frac{1}{2}\int_{V_p} \Delta\theta p_3^T E_3\, dV_p - \frac{1}{2}\int_V \Delta\theta^T \alpha_T \Delta\theta\, dV$$

$$= -\frac{1}{2}\{q_w\}^T\left[\int_V(-z)[B_w]^T \lambda_1^T [N_\theta]\, dV\right]\{\theta\} + \frac{1}{2}\{v\}^T\left[\int_{V_p}[B_v]^T p_3^T [N_\theta]\, dV_p\right]\{\theta\} \tag{3.29}$$

$$- \frac{1}{2}\{\theta\}^T\left[\int_V[N_\theta]^T \alpha_T [N_\theta]\, dV\right]\{\theta\}$$

$$= -\frac{1}{2}\{q_w\}[K_{b\theta}^e]\{\theta\} + \frac{1}{2}\{v\}^T[K_{p\theta}^e]\{\theta\}$$

$$- \frac{1}{2}\{\theta\}^T\left[\int_V[N_\theta]^T \alpha_T [N_\theta] dV\right]\{\theta\}$$

where, dV is the volume element given by

$$dV = dV_b + dV_p \tag{3.30}$$

The subscripts *b* and *p* represents the beam and the piezoelectric material, respectively, and dV_b and dV_p are given by

$$dV_b = \int_{-t_0/2}^{t_0/2}\int_0^L\int_0^b dx dy dz \tag{3.31}$$

$$dV_p = \int_{t_0/2}^{\left(\frac{t_0}{2}+t_{p0}\right)} \int_0^L \int_0^b dx\,dy\,dz \tag{3.32}$$

Hence, the internal energy of the structure can be written as,

$$T_p = \frac{1}{2}\{q_w\}^T[K^e]\{q_w\} + \frac{1}{2}\{q_w\}^T[K_{pb}^e]\{v\}$$
$$+ \frac{1}{2}\{v\}^T[K_{bp}^e]\{q_w\} - \frac{1}{2}\{v\}^T[K_{pp}^e]\{v\} + \{v\}^T[K_{p\theta}^e]\{\theta\}$$
$$- \{q_w\}[K_{b\theta}^e]\{\theta\} - \frac{1}{2}\{\theta\}^T\left[\int_V [N_\theta]^T \alpha_T [N_\theta]\,dV\right]\{\theta\} \tag{3.33}$$

Now, the work done by the external forces and electric charges can be obtained as

$$W = \int_A \{q_w\}^T \{q(x,y)\}dA - \int_A \{v\}^T \{g(x,y)\}dA$$
$$= \{q_w\}^T \{Q^e\} + \{v\}^T \{G^e\} \tag{3.34}$$

Now substituting the first variation of equation (3.33) and equation (3.34) in equation (3.25)

$$\int_{t_1}^{t_2} \begin{bmatrix} \{\delta q_w\}^T[K^e]\{q_w\} + \{\delta q_w\}^T[K_{pb}^e]\{v\} + \{\delta v\}^T[K_{bp}^e]\{q_w\} \\ -\{\delta v\}^T[K_{pp}^e]\{v\} + \{\delta v\}^T[K_{p\theta}^e]\{\theta\} \\ -\{\delta q_w\}^T[K_{b\theta}^e]\{\theta\} - \{\delta q_w\}^T\{Q^e\} - \{\delta v\}^T\{G^e\} \end{bmatrix} = 0 \tag{3.35}$$

From the equation (3.35), the system of equations for an element can be obtained as

$$[K^e]\{q_w\} + [K_{pb}^e]\{v\} - [K_{b\theta}^e]\{\theta\} = \{Q^e\} \tag{3.36}$$

$$[K_{bp}^e]\{q_w\} - [K_{pp}^e]\{v\} + [K_{p\theta}^e]\{\theta\} = \{G^e\} \tag{3.37}$$

Where,

$$[K^e] = [K_b^e] + [K_p^e] \tag{3.38}$$

$$[K_b^e] = \int_0^{L_e} [B_w]^T E_b(x) I_b(x)[B_w]\,dx \tag{3.39}$$

$$[K_p^e] = \int_0^{L_e} [B_w]^T E_p I_p(x)[B_w]\,dx \tag{3.40}$$

$$[K_{pb}^e] = -\int_0^{L_e} z[B_w]^T e_{31} A_P(x)[B_V]\,dx \tag{3.41}$$

$$[K^e_{bp}] = [K^e_{pb}]^T \tag{3.42}$$

$$[K^e_{pp}] = \int_0^{L_e} [B_v]^T \xi^S_{33} A_p(x)[B_v]dx \tag{3.43}$$

$$[K^e_{b\theta}] = \int_0^{L_e} -z[B_w]^T \lambda_1 A_b(x)[N_\theta]\, dV_b \tag{3.44}$$

$$[K^e_{p\theta}] = \int_0^{L_e} [B_v]^T p_3 A_p(x)[N_\theta]dV_p \tag{3.45}$$

After assembling the elemental stiffness matrices of piezothermoelastic beam the global set of equations become

$$\begin{pmatrix} [K] & [K_{pb}] & -[K_{b\theta}] \\ [K_{bp}] & -[K_{pp}] & [K_{p\theta}] \end{pmatrix} \begin{Bmatrix} \{q_w\}_{global} \\ \{v\}_{global} \\ \{\theta\}_{global} \end{Bmatrix} = \begin{Bmatrix} \{Q\} \\ \{G\} \end{Bmatrix} \tag{3.46}$$

By taking the thermal strain effect and pyroelectric effect as force vectors on the right hand side, the equation (3.46) can further be written as

$$\begin{pmatrix} [K] & [K_{pb}] \\ [K_{bp}] & -[K_{pp}] \end{pmatrix} \begin{Bmatrix} \{q_w\}_{global} \\ \{v\}_{global} \end{Bmatrix} = \begin{Bmatrix} \{Q\} + [K_{b\theta}]\{\theta\}_{global} \\ \{G\} - [K_{p\theta}]\{\theta\}_{global} \end{Bmatrix} \tag{3.47}$$

The modelled beam in electrical domain is assumed to be open-circuited for the analysis. For open circuit, the differences in the electrical potentials between the electrodes are unknown considering charge equal to zero (*G* =0) which is deduced to the following equation as

$$\begin{pmatrix} [K] & [K_{pb}] \\ [K_{bp}] & -[K_{pp}] \end{pmatrix} \begin{Bmatrix} \{q_w\}_{global} \\ \{v\}_{global} \end{Bmatrix} = \begin{Bmatrix} \{Q\} + [K_{b\theta}]\{\theta\}_{global} \\ -[K_{p\theta}]\{\theta\}_{global} \end{Bmatrix} \tag{3.48}$$

3.2.11.2 *Dynamic finite element equation*

The dynamic equations of motion of the modelled system can be represented using Hamilton's principle as

$$\delta\Pi = \int_{t_1}^{t_2} [\delta\,(T_k - T_p + W)]\, dt = 0 \tag{3.49}$$

where, T_k is the kinetic energy, T_p is the total electromechanical enthalpy and *W* is the work done, respectively. The terms t_1 and t_2 represents the time constants at which all first variations vanishes. The equation (3.49) can further be represented as

$$\delta \Pi = \int_{t_1}^{t_2} [\delta T_k - \delta(T_{es} + T_{ep} + T_{et}) + \delta W)]\, dt = 0$$

$$\Rightarrow \int_{t_1}^{t_2} \delta T_k\, dt - \int_{t_1}^{t_2} \delta(T_{es} + T_{ep} + T_{et})\, dt + \int_{t_1}^{t_2} \delta W\, dt = 0$$

(3.50)

The terms used in equation (3.50) can be obtained as follows.

Part 1. The kinetic energy of the system is

$$T_k = \int_V \frac{1}{2} \{\dot{w}_0\}^T \rho \{\dot{w}_0\}\, dV$$

$$\int_{t_1}^{t_2} \delta T_k\, dt = \int_{t_1}^{t_2} \delta \left[\int_V \frac{1}{2} \{\dot{w}_0\}^T \rho(x)\{\dot{w}_0\}\, dV \right] dt$$

$$= -\int_{t_1}^{t_2} \left[\int_V \{\delta w_0\}^T \rho(x)\{\ddot{w}_0\}\, dV \right] dt$$

(3.51)

$$= -\int_{t_1}^{t_2} \{\delta q_w\}^T \left[\int_V [N_w]^T \rho(x)\, [N_w]\, dV \right] \{\ddot{q}_w\}\, dt$$

$$= -\int_{t_1}^{t_2} \{\delta q_w\}^T [M^e]\{\ddot{q}_w\}\, dt$$

Part 2. The total electromechanical enthalpy of the system is

$$\int_{t_1}^{t_2} \delta T_p\, dt = \int_{t_1}^{t_2} \delta(T_{es} + T_{ep} + T_{et})\, dt$$

$$= \int_{t_1}^{t_2} \begin{bmatrix} \{\delta q_w\}^T [K^e]\{q_w\} + \{\delta q_w\}^T [K_{pb}^e]\{v\} + \{\delta v\}^T [K_{bp}^e]\{q_w\} \\ - \{\delta v\}^T [K_{pp}^e]\{v\} + \{\delta v\}^T [K_{p\theta}^e]\{\theta\} - \{\delta q_w\}^T [K_{b\theta}^e]\{\theta\} \end{bmatrix} dt$$

(3.52)

Part 3. The work done by the external force is

$$\int_{t_1}^{t_2} \delta W\, dt = \int_{t_1}^{t_2} \delta \left[\int_A \{q_w\}^T \{q(x,y)\}dA - \int_A \{v\}^T \{g(x,y)\}dA \right] dt$$

$$= \int_{t_1}^{t_2} \left[\int_A \{\delta q_w\}^T \{q(x,y)\}dA - \int_A \{\delta v\}^T \{g(x,y)\}dA \right] dt$$

(3.53)

$$= \{\delta q_w\}^T \{Q^e\} + \{\delta v\}^T \{G^e\}$$

Now, substituting equations (3.51)-(3.53) into equation (3.50)

$$\int_{t_1}^{t_2} \{\delta q_w\}^T \left(-[M^e]\{\ddot{q}_w\} - [K^e]\{q_w\} - [K_{pb}^e]\{v\} + [K_{b\theta}^e]\{\theta\} + \{Q^e\}\right) dt$$

$$+ \int_{t_1}^{t_2} \{\delta v\}^T \left(-[K_{bp}^e]\{q_w\} + [K_{pp}^e]\{v\} - [K_{p\theta}^e]\{\theta\} + \{G^e\}\right) dt = 0 \tag{3.54}$$

From equation (3.54), it is observed that the partial differentiation of q_w and v can be any arbitrary value and cannot be equal to zero. Therefore the equation (3.50) is valid only if

$$[M^e]\{\ddot{q}_w\} + [K^e]\{q_w\} + [K_{pb}^e]\{v\} - [K_{b\theta}^e]\{\theta\} = \{Q^e\} \tag{3.55}$$

$$[K_{bp}^e]\{q_w\} - [K_{pp}^e]\{v\} + [K_{p\theta}^e]\{\theta\} = \{G^e\} \tag{3.56}$$

where,

$$[M^e] = [M_b^e] + [M_p^e]$$
$$\text{and } [K^e] = [K_b^e] + [K_p^e] \tag{3.57}$$

The equations (3.55) and (3.56) represent the dynamic equation of one element. These equations can be represented in matrix form as

$$\begin{pmatrix} [M^e] & [0] & [0] \\ [0] & [0] & [0] \end{pmatrix} \begin{Bmatrix} \{\ddot{q}_w\} \\ \{\ddot{v}\} \\ \{\ddot{\theta}\} \end{Bmatrix} + \begin{pmatrix} [K^e] & [K_{pb}^e] & -[K_{b\theta}^e] \\ [K_{bp}^e] & -[K_{pp}^e] & [K_{p\theta}^e] \end{pmatrix} \begin{Bmatrix} \{q_w\} \\ \{v\} \\ \{\theta\} \end{Bmatrix} = \begin{Bmatrix} \{Q^e\} \\ \{G^e\} \end{Bmatrix} \tag{3.58}$$

After assembling the elemental matrices the global set of equations can be obtained and written as

$$\begin{pmatrix} [M] & [0] & [0] \\ [0] & [0] & [0] \end{pmatrix} \begin{Bmatrix} \{\ddot{q}_w\}_{global} \\ \{\ddot{v}\}_{global} \\ \{\ddot{\theta}\}_{global} \end{Bmatrix} + \begin{pmatrix} [K] & [K_{pb}] & -[K_{b\theta}] \\ [K_{bp}] & -[K_{pp}] & [K_{p\theta}] \end{pmatrix} \begin{Bmatrix} \{q_w\}_{global} \\ \{v\}_{global} \\ \{\theta\}_{global} \end{Bmatrix} = \begin{Bmatrix} \{Q\} \\ \{G\} \end{Bmatrix} \tag{3.59}$$

For open circuit condition, the differences in electrical potential between the electrodes are unknown considering charge equal to zero (*G=0*). Hence, equation (3.59) can be rewritten to the following equation

$$\begin{pmatrix} [M] & [0] & [0] \\ [0] & [0] & [0] \end{pmatrix} \begin{Bmatrix} \{\ddot{q}_w\}_{global} \\ \{\ddot{v}\}_{global} \\ \{\ddot{\theta}\}_{global} \end{Bmatrix} + \begin{pmatrix} [K] & [K_{pb}] & -[K_{b\theta}] \\ [K_{bp}] & -[K_{pp}] & [K_{p\theta}] \end{pmatrix} \begin{Bmatrix} \{q_w\}_{global} \\ \{v\}_{global} \\ \{\theta\}_{global} \end{Bmatrix} = \begin{Bmatrix} \{Q\} \\ \{0\} \end{Bmatrix} \tag{3.60}$$

Equation (3.60) can further be written by taking the thermal strain effect and pyroelectric effect as force vectors on the right hand side as

$$\begin{pmatrix} [M] & [0] \\ [0] & [0] \end{pmatrix} \begin{Bmatrix} \{\ddot{q}_w\}_{global} \\ \{\ddot{v}\}_{global} \end{Bmatrix} + \begin{pmatrix} [K] & [K_{pb}] \\ [K_{bp}] & -[K_{pp}] \end{pmatrix} \begin{Bmatrix} \{q_w\}_{global} \\ \{v\}_{global} \end{Bmatrix} = \begin{Bmatrix} \{Q\} + [K_{b\theta}]\{\theta\}_{global} \\ -[K_{p\theta}]\{\theta\}_{global} \end{Bmatrix} \tag{3.61}$$

3.2.11.3 *Output voltage*

The output voltage from the thermoelectromechanical finite element equation can be obtained using the second part of equation (3.48) as

$$\left([K_{bp}] \quad -[K_{pp}] \right) \left\{ \begin{array}{c} \{q_w\}_{global} \\ \{v\}_{global} \end{array} \right\} = \left\{ -[K_{p\theta}]\{\theta\}_{global} \right\} \tag{3.62}$$

From equation (3.62) the voltage can be obtained as

$$\{v\}_{global} = \left([K_{pp}]^{-1}[K_{bp}]\{q_w\}_{global} \right) + \left([K_{pp}]^{-1}[K_{p\theta}]\{\theta\}_{global} \right) \tag{3.63}$$

Further, the output voltage for static electromechanical finite element equation can be obtained by putting the temperature vector, $\theta = 0$ in equation (3.63) as

$$\{v\}_{global} = [K_{pp}]^{-1}[K_{bp}]\{q_w\}_{global} \tag{3.64}$$

3.2.11.4 *Output power*

The equation (3.64) represents the piezo system and can be used to determine the motion of the system; however the equation doesn't contain any energy dissipation. As the model is intended for energy harvesting system which must be removing energy, this form will not hold good for the present need. Hence, to incorporate the energy dissipation term into the equation, Ohm's law is used, and a resistive element is added between the top and bottom surface of the piezoelectric patch. By incorporating the resistive element, the electrical boundary condition becomes

$$\{v\}_{global} = -R\{\dot{q}(t)\}_{global} \tag{3.65}$$

where, the term $\dot{q}(t)$ is the current output from the piezoelectric element and R is the external load resistance. Apart from this, the system should have some supplementary structural damping which needs to be taken into account. By using proportional damping method the damping ratio is predicted from the computed fundamental frequency as

$$[C] = \alpha\left([M]\right) + \beta\left([K]\right) \tag{3.66}$$

where, α and β are found out from the following equation

$$\zeta_i = \frac{\alpha}{2\omega_i} + \frac{\beta\omega_i}{2}, \quad i=1,\ 2,\ 3…n \tag{3.67}$$

Where, ζ_i is the damping ratio of the structure. Hence, incorporating equation (3.65) and equation (3.66) into equation (3.61), the resulting equation becomes

$$\left(\begin{bmatrix} [M] & [0] \\ [0] & [0] \end{bmatrix}\right)\left\{\begin{matrix} \{\ddot{q}_w\}_{global} \\ \{\ddot{v}\}_{global} \end{matrix}\right\} + \left(\begin{bmatrix} [C] & [0] \\ [0] & [0] \end{bmatrix}\right)\left\{\begin{matrix} \{\dot{q}_w\}_{global} \\ \{\dot{v}\}_{global} \end{matrix}\right\}$$

$$+ \left(\begin{bmatrix} [K] & [K_{pb}] \\ [K_{bp}] & -[K_{pp}] \end{bmatrix}\right)\left\{\begin{matrix} \{q_w\}_{global} \\ -R\{\dot{q}(t)\}_{global} \end{matrix}\right\} = \left\{\begin{matrix} \{Q\} + [K_{b\theta}]\{\theta\}_{global} \\ -[K_{p\theta}]\{\theta\}_{global} \end{matrix}\right\}$$
(3.68)

Equation (3.68) shows the model of energy harvesting system. The term $\dot{q}(t)$ provides the current output of the piezoelectric patch and can be used directly for output power through external load resistance R. Further, the global dynamic eletromechanical finite element equations are obtained by putting the temperature vector, $\theta = 0$ in equation (3.68) as

$$\left(\begin{bmatrix} [M] & [0] \\ [0] & [0] \end{bmatrix}\right)\left\{\begin{matrix} \{\ddot{q}_w\}_{global} \\ \{\ddot{v}\}_{global} \end{matrix}\right\} + \left(\begin{bmatrix} [C] & [0] \\ [0] & [0] \end{bmatrix}\right)\left\{\begin{matrix} \{\dot{q}_w\}_{global} \\ \{\dot{v}\}_{global} \end{matrix}\right\}$$

$$+ \left(\begin{bmatrix} [K] & [K_{pb}] \\ [K_{bp}] & -[K_{pp}] \end{bmatrix}\right)\left\{\begin{matrix} \{q_w\}_{global} \\ -R\{\dot{q}(t)\}_{global} \end{matrix}\right\} = \left\{\begin{matrix} \{Q\} \\ \{0\} \end{matrix}\right\}$$
(3.69)

3.2.11.5 *Electro-thermo-mechanical sensing of output power*

It is assumed that the deformed shape of the beam remains unaffected and there is an increase in bending stiffness due to the presence of a thin layer of the piezoelectric patch. For measuring the output power, the linear constitutive equations of the piezoelectric material have been employed across the thickness of the piezoelectric layer. Hence, the total charge on the electrode surface can be obtained as

$$Q_r = \int_A D_3 dA = \int_A \left(e_{31}\varepsilon_1 + \xi_{33}^S E_3 + p_3 \Delta\theta\right)dA$$
(3.70)

It should be emphasised that the produced charge, current and voltage are all functions of the time. The produced current, flowing out to the external impedance can be found using the charge developed on the piezoelectric patch. Again as the current is influenced by vibration frequency, its magnitude through the external impedance can be expressed as

$$I_r = \omega Q_r$$
(3.71)

where ω is the excitation frequency. For a pure load resistance, a linear relationship exists between voltage and current which can be written as

$$V = I_r R$$
(3.72)

Combining equations (3.70), (3.71) and (3.72), the amplitude of current flowing through the electric circuit becomes

$$I_r = \frac{bhe_{31}\omega\,[\psi(L_p) - \psi(0)] + 2bp_3\,\Delta\theta L_p}{2\left(1 + \dfrac{b\omega R\xi_{33}^s L_p}{t_p}\right)} \tag{3.73}$$

where, b and h represents the width and thickness of the beam respectively, Ψ is the slope of deflection of the beam, ω is the first natural frequency, R is the external load resistance and ΔT is the temperature difference. Hence, the output power from the piezolaminated system can be written as

$$P = I_r^2 R = \left[\frac{bhe_{31}\omega\,[\psi(L_p) - \psi(0)] + 2bp_3\,\Delta\theta L_p}{2\left(1 + \dfrac{b\omega R\xi_{33}^s L_p}{t_p}\right)}\right]^2 R \tag{3.74}$$

3.2.11.6 *Stress on the piezoelectric patch*

The piezoelectric patch is strained due to mechanical loading in the structure. Hence, a stress is induced in the patch which is an essential parameter for the design and analysis of the piezolaminated structure for preventing failure. For a beam of uniform cross section, the curvature (c) which was given as [132]

$$c = \frac{d^2 w}{dx^2} = \frac{d^2[N_w]}{dx^2}\{q_w\} \tag{3.75}$$

The average curvature of the piezoelectric patch can be written as

$$\lambda(x) = \frac{1}{L_p}\int_0^{L_p} \frac{d^2[N_w]}{dx^2}\{q_w\}dx \tag{3.76}$$

The average strain which is a function of average curvature can be obtained as

$$S(x,y) = -\lambda(x)(y - y_c) \tag{3.77}$$

where, y_c is the distance from the neutral axis of the PZT patch. By using the relation between the stress and strain, stress over the piezoelectric patch can be computed as

$$\sigma(x,y) = -\left(E_p(y - y_c)\frac{1}{L_p}\right) \times \int_0^{L_p} \frac{d^2[N_w]}{dx^2}\{q_w\}dx \tag{3.78}$$

3.2.12 State-space representation

This method is used to develop the uncoupled governing equations of motion of the system in terms of principal coordinates. It can be achieved by introducing a linear transformation between the generalized coordinates $q_w(t)$ and the principal coordinates $g(t)$ [133]. By using the transformation matrix, the displacement vector $q_w(t)$ can be approximated as

$$\{q_w(t)\}_{global} = [x(n)]\{g(t)\}_{global} \tag{3.79}$$

Where, $x(n)$ is represented as the modal matrix containing the eigen vectors representing the vibratory modes. The equation (3.61) can further be written as

$$[M]\{\ddot{q}_w\}_{global} + [K]\{q_w\}_{global} + [K_{pb}]\{v\}_{global} - [K_{b\theta}]\{\theta\}_{global} = \{Q\} \tag{3.80}$$

$$[K_{bp}]\{q_w\}_{global} - [K_{pp}]\{v\}_{global} + [K_{p\theta}]\{\theta\}_{global} = \{0\} \tag{3.81}$$

From the equation (3.81)

$$\{v\}_{global} = \left([K_{pp}]^{-1}[K_{p\theta}]\{\theta\}_{global}\right) + \left([K_{pp}]^{-1}[K_{bp}]\{q_w\}_{global}\right) \tag{3.82}$$

Now putting equation (3.82) into equation (3.80)

$$[M]\{\ddot{q}_w\}_{global} + [K]\{q_w\}_{global} + [K_{pb}]\left([K_{pp}]^{-1}[K_{p\theta}]\{\theta\}_{global} + [K_{pp}]^{-1}[K_{bp}]\{q_w\}_{global}\right) = \{Q\}$$
$$\Rightarrow [M]\{\ddot{q}_w\}_{global} + \left([K] + [K_{pb}][K_{pp}]^{-1}[K_{bp}]\right)\{q_w\}_{global} = \{Q\} - \left([K_{pb}][K_{pp}]^{-1}[K_{p\theta}]\right)\{\theta\}_{global} \tag{3.83}$$

Now incorporating structural damping of equation (3.66) into equation (3.83)

$$[M]\{\ddot{q}_w\}_{global} + [C]\{\dot{q}_w\}_{global} + \left([K] + [K_{pb}][K_{pp}]^{-1}[K_{bp}]\right)\{q_w\}_{global}$$
$$= \{Q\} - \left([K_{pb}][K_{pp}]^{-1}[K_{p\theta}]\right)\{\theta\}_{global} \tag{3.84}$$

The equation (3.84) can further be written as

$$[M]\{\ddot{q}_w\}_{global} + [C]\{\dot{q}_w\}_{global} + [K_1]\{q_w\}_{global} = \{F\} \tag{3.85}$$

where

$$[K_1] = [K] + ([K_{pb}][K_{pp}]^{-1}[K_{bp}]) \tag{3.86}$$

$$\{F\} = \{Q\} - ([K_{pb}][K_{pp}]^{-1}[K_{p\theta}])\{\theta\}_{global} \tag{3.87}$$

Now incorporating equation (3.79) into equation (3.85), we get

$$[M]\{\ddot{g}(t)\}_{global} + [C]\{\dot{g}(t)\}_{global} + [K_1]\{g(t)\}_{global} = x(n)^T\{F\} \tag{3.88}$$

Using state-space form, equation (3.88) can be expressed as

$$\{\dot{X}\} = [A]\{X\} + [B]\{u\} \tag{3.89}$$

where,

$$[A] = \begin{bmatrix} [0] & [I] \\ \left(-[M]^{-1}[K_1]\right) & \left(-[M]^{-1}[C]\right) \end{bmatrix} \qquad (3.90)$$

$$[B] = \begin{bmatrix} [0] \\ [-\{x(n)\}^T \{F\}] \end{bmatrix} \qquad (3.91)$$

$$\{\dot{X}\} = \begin{Bmatrix} \dot{g}(t) \\ \ddot{g}(t) \end{Bmatrix} \qquad (3.92)$$

$$\{X\} = \begin{Bmatrix} g(t) \\ \dot{g}(t) \end{Bmatrix} \qquad (3.93)$$

The terms *A, B, X* and *u* are the system matrix, input matrix, state vector and input vector, respectively. The output equation for sensor can be written as

$$\{y\} = [C_{output}]\{X\} \qquad (3.94)$$

Here, C_{output} is represented as the output matrix. The output matrix solely depends on the terms *x(n)* and K_{bp}.

Chapter 4

Nonlinear Formulation of Non-prismatic Axially FG Beams

4.1   Introduction

The use of non-prismatic beams shows an effective improvement of output power due to the uniform strain profiles compared to prismatic beams. These non-prismatic beams are not only selected to optimize the strength to weight ratio of the structure but also to meet the architectural and aesthetical needs. However, the geometric nonlinear effects due to the large deformation of such structures cannot be overlooked. In reality, no physical system is strictly linear and hence, linear models of physical systems have limitations of their own. In general, linear models are applicable only in a very restrictive domain like when the vibration amplitude is very small. Thus, to accurately identify and understand the dynamic behavior of a structural system under general loading conditions, it is essential that the nonlinearities present in the system should also be modeled and studied. Because nonlinearities have an influence on the vibrations of most of the mechanical structures, it is relevant to study their effects on the evolution of the oscillations with respect to certain parameters such as frequency of external excitation. With the inclusion of geometric nonlinear effects, an accurate estimation of voltage sensed by piezoelectric materials along with output power can be determined. This chapter is the extension of chapter 3 that includes the geometric nonlinear effects concerned with energy harvesting.

4.2   Mathematical Formulation for Vibration Energy Harvesting

The mathematical formulations involve the strain-displacement relationships of the

modelled beam, governing equation for output power and the solutions for the system of nonlinear equations. The details of the formulations have been presented in the following subsections.

4.2.1   Displacement field of the beam

The general form of assumed displacement field is expressed as

$$u(x,z) = u_0(x) + z\left[C_0 \frac{\partial w_0}{\partial x} + C_1\varphi_x(x)\right] + C_2 z^2 \psi_x(x) + C_3\left(\frac{z}{h}\right)^3\left[\varphi_x(x) + \frac{\partial w_0}{\partial x}\right]$$

$$v(x,z) = 0$$

$$w(x,z) = w_0(x)$$

(4.1)

where, *u*, *v* and *w* are the displacements along coordinate directions, longitudinal (*x*), lateral (*y*) and transverse (*z*), respectively. The terms $u_0(x)$ *and*, $w_0(x)$ denotes the displacement of a point on the midplane of an undeformed beam along axial (*x*) and transverse (*z*) directions, respectively. The terms $\phi_x(x)$ and $\Psi_x(x)$ are functions of *x* and *h* is the beam thickness. As our concern in this study is geometric nonlinearity based on Euler-Bernoulli beam assumptions, Poisson's effect and transverse shear strain are neglected. By substituting $C_0 = -1$, $C_1 = C_2 = C_3 = 0$, the general form of displacement has been modified to

$$u(x,z) = u_0(x) - z\frac{\partial w_0}{\partial x}$$

$$v(x,z) = 0$$

$$w(x,z) = w_0(x)$$

(4.2)

4.2.2   Shape functions

A beam element with three degrees of freedom per node with varying cross-sectional dimensions along the element axis is shown in Figure 4.1.
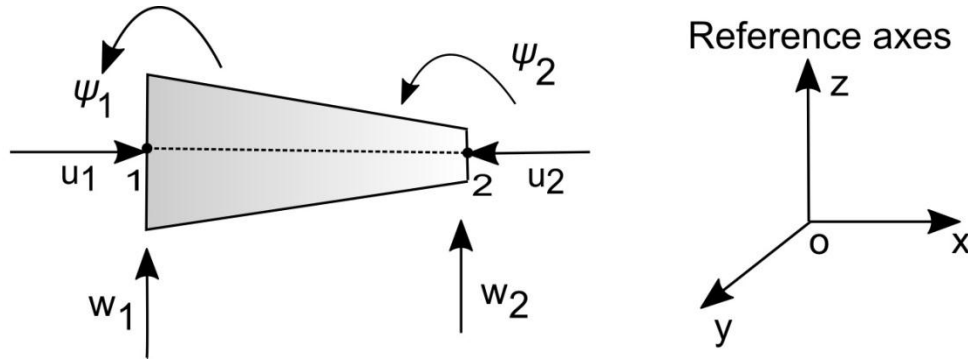
Figure 4.1 Nodal degrees of freedom of nonprismatic beam element.

Here, u_1, w_1 and ψ_1 are the axial, transverse and rotation degrees of freedom at node 1, respectively. Similarly u_2, w_2 and ψ_2 are the corresponding degrees of freedom at node 2. The axial and transverse displacement variation through the element length assumed be

$$u_0(x) = b_1 x + b_2$$
$$w_0(x) = a_1 x^3 + a_2 x^2 + a_3 x + a_4$$
$$(4.3)$$

where, the terms b_1, b_2, a_1, a_2, a_3 and a_4 are unknown constants which can be obtained using the boundary conditions. After applying the boundary conditions the displacement field could be interpolated in terms of degrees of freedom of nodes and shape functions based on the concept of FEM as

$$u_0(x) = [N_u]\{q_u\}$$
$$\text{and } w_0(x) = [N_w]\{q_w\}$$
$$(4.4)$$

where, N_u and N_w are the Lagrange and the Hermite cubic interpolation or shape functions, and q_u, q_w are the elemental nodal degrees of freedoms respectively. The accuracy of the result depends on how well these shape functions are selected. These interpolation functions for a beam element can be written as

$$[N_u] = [N_{1u} \quad N_{2u}] \text{ and}$$
$$[N_w] = [N_{1w} \quad N_{2w} \quad N_{3w} \quad N_{4w}]$$
where,

$$N_{1u} = \frac{L_e - x}{L_e}, \quad N_{2u} = \frac{x}{L_e}$$

$$N_{1w} = 1 - \frac{3x^2}{L_e} + \frac{2x^3}{L_e^3}, \quad N_{2w} = x - \frac{2x^2}{L_e} + \frac{x^3}{L_e^2}$$

$$N_{3w} = \frac{3x^2}{L_e^2} - \frac{2x^3}{L_e^3}, \quad N_{4w} = -\frac{x^2}{L_e} + \frac{x^3}{L_e^2}$$

$$(4.5)$$

Here L_e represents length of the beam element. The elemental nodal displacement vector can be represented in matrix form as

$$\{q_u\} = \begin{Bmatrix} u_1 \\ u_2 \end{Bmatrix} \ \ and \ \{q_w\} = \begin{Bmatrix} v_1 \\ \psi_1 \\ v_2 \\ \psi_2 \end{Bmatrix}$$

(4.6)

Again

$$\{q\} = \begin{bmatrix} \{q_u\} \\ \{q_w\} \end{bmatrix}$$

4.2.3   Strain-Displacement relationships

The general form of strain-displacement relations can be represented as

$$\varepsilon_{ij} = \frac{1}{2}\left(\frac{\partial u_i}{\partial x_j} + \frac{\partial u_j}{\partial x_i}\right) + \frac{1}{2}\left(\frac{\partial u_m}{\partial x_i} + \frac{\partial u_m}{\partial x_j}\right) \quad i,j,m = 1, 2, 3$$

(4.7)

where, the deformation u_1, u_2, u_3 are u_0, v_0, w_0, respectively, the directions x_1, x_2, x_3 are x, y, z, respectively and the strain components ε_{11}, ε_{22}, ε_{33}, ε_{13}, ε_{23}, ε_{12} are ε_1, ε_2, ε_3, ε_4, ε_5, ε_6, respectively. Since the modelled beam length is too high compared to the cross-sectional dimensions of the beam, the shear strains are assumed to be zero. Moreover, according to Von-Karman hypothesis, omitting the large strain components but retaining the square of the rotation of normal transverse line in the beam, the modified strain becomes

$$\varepsilon_1 = \frac{\partial u_0(x)}{\partial x} - z\frac{\partial^2 w_0(x)}{\partial x^2} + \frac{1}{2}\left(\frac{\partial w_0(x)}{\partial x}\right)^2$$

(4.8)

Equation (4.8) can be written in matrix form as

$$\begin{aligned} \varepsilon_1 &= \begin{Bmatrix} \dfrac{\partial u_0(x)}{\partial x} \\ -z\dfrac{\partial^2 w_0(x)}{\partial x^2} \end{Bmatrix} + \begin{Bmatrix} \dfrac{1}{2}\left(\dfrac{\partial w_0(x)}{\partial x}\right)^2 \\ 0 \end{Bmatrix} \\ &= \begin{Bmatrix} \varepsilon_l^p \\ \varepsilon_l^b \end{Bmatrix} + \begin{Bmatrix} \varepsilon_{nl}^p \\ 0 \end{Bmatrix} \\ &= \{\varepsilon_l\} + \{\varepsilon_{nl}\} \end{aligned}$$

(4.9)

In equation (4.9), ε_1 is divided into linear (ε_l) and geometrically nonlinear (ε_{nl}) strains. The linear strain is further subdivided into linear membrane strain ε_l^p and bending strain ε_l^b. Using equation (4.4), the terms of strain can be expressed as

$$\varepsilon_l^p = [D_u]\{q_u\} \tag{4.10}$$

$$\varepsilon_l^b = -z[B_w]\{q_w\} \tag{4.11}$$

And, the geometric nonlinear membrane strain

$$
\begin{aligned}
\varepsilon_{nl}^p &= \frac{1}{2}\left[\frac{\partial w_0(x)}{\partial x}\right]^2 \\
&= \frac{1}{2}\left[\frac{\partial w_0(x)}{\partial x}\right]\left[\frac{\partial N_w}{\partial x}\right]\{q_w\} \\
&= \frac{1}{2}[A_{nw}][G_{nw}]\{q_w\} \\
&= [B_{nw}]\{q_w\}
\end{aligned}
\tag{4.12}
$$

Here, $[A_{nw}]$ depends on the displacement vector of the deformed configuration structure and $[G_{nw}]$ purely based on the derivatives of shape functions.

4.2.4 Governing equation

The non-prismatic piezolaminated axially FG cantilever beam is shown in Figure 3.4 of Chapter 3. The piezoelastic constitutive equation and the electric potential of the piezoelectric patch has been discussed in Chapter 3 (sections 3.2.8 and 3.2.9).The detailed static and dynamic formulations considering geometric nonlinearity for the model are presented in the following sections.

4.2.4.1 Static nonlinear finite element equation

The variation of total potential energy of the element is given by

$$\delta\Pi = \int_{t_1}^{t_2} [\delta (T_p - W)\, dt = 0 \tag{4.13}$$

where, T_p is the total internal potential energy consisting of elastic strain energy of the structure (T_{es}), electric potential energy of the piezoelectric patch (T_{ep}) and the internal energy due to thermal fields (T_{et}).

$$T_p = T_{es} + T_{ep} \tag{4.14}$$

The external work done W consists of work done due to applied mechanical force and the applied electrical charges. The terms used in equation (4.13) can be deduced as follows.

a. Elastic strain energy of the structure

$$T_{es} = \frac{1}{2} \int_V \{\varepsilon_1\}^T \sigma_1 dV$$

$$= \frac{1}{2} \int_V \{\varepsilon_1\}^T (C_{11}^E \varepsilon_1 - e_{31} E_3) \, dV$$

$$= \frac{1}{2} \int_V [\{\varepsilon_l\} + \{\varepsilon_{nl}\}]^T C_{11}^E [\{\varepsilon_l\} + \{\varepsilon_{nl}\}] \, dV - \frac{1}{2} \int_{V_p} [\{\varepsilon_l\} + \{\varepsilon_{nl}\}]^T e_{31} E_3 \, dV$$

$$= \frac{1}{2} \int_V \{\varepsilon_l\}^T C_{11}^E \{\varepsilon_l\} \, dV + \frac{1}{2} \int_V \{\varepsilon_l\}^T C_{11}^E \{\varepsilon_{nl}\} \, dV + \frac{1}{2} \int_V \{\varepsilon_{nl}\}^T C_{11}^E \{\varepsilon_l\} \, dV$$

$$+ \frac{1}{2} \int_V \{\varepsilon_{nl}\}^T C_{11}^E \{\varepsilon_{nl}\} \, dV - \frac{1}{2} \int_V \{\varepsilon_l\}^T e_{31} E_3 \, dV - \frac{1}{2} \int_V \{\varepsilon_{nl}\}^T e_{31} E_3 \, dV$$

$$= \frac{1}{2} \int_V \left\{ \begin{matrix} \{q_u\}^T \\ \{q_w\}^T \end{matrix} \right\} \left\{ \begin{matrix} [D_u]^T \\ -z[B_w]^T \end{matrix} \right\} C_{11}^E \left\{ \begin{matrix} [D_u] \\ -z[B_w] \end{matrix} \right\} \left\{ \begin{matrix} \{q_u\} \\ \{q_w\} \end{matrix} \right\} dV$$

$$+ \frac{1}{2} \int_V \left\{ \begin{matrix} \{q_u\}^T \\ \{q_w\}^T \end{matrix} \right\} \left\{ \begin{matrix} [D_u]^T \\ -z[B_w]^T \end{matrix} \right\} C_{11}^E \left\{ \begin{matrix} [B_{nw}]\{q_w\} \\ 0 \end{matrix} \right\} dV$$

$$+ \frac{1}{2} \int_V \left\{ \begin{matrix} [B_{nw}]^T \{q_w\}^T \\ 0 \end{matrix} \right\} C_{11}^E \left\{ \begin{matrix} [D_u] \\ -z[B_w] \end{matrix} \right\} \left\{ \begin{matrix} \{q_u\} \\ \{q_w\} \end{matrix} \right\} dV$$

$$+ \frac{1}{2} \int_V \left\{ \begin{matrix} [B_{nw}]^T \{q_w\}^T \\ 0 \end{matrix} \right\} C_{11}^E \left\{ \begin{matrix} [B_{nw}]\{q_w\} \\ 0 \end{matrix} \right\} dV$$

$$+ \frac{1}{2} \int_V \left\{ \begin{matrix} \{q_u\}^T \\ \{q_w\}^T \end{matrix} \right\} \left\{ \begin{matrix} [D_u]^T \\ -z[B_w]^T \end{matrix} \right\} e_{31} [B_v] dV + \frac{1}{2} \int_V \left\{ \begin{matrix} [B_{nw}]^T \{q_w\}^T \\ 0 \end{matrix} \right\} e_{31} [B_v]\{v\} dV$$

$$\text{(4.15)}$$

$$= \frac{1}{2} \int_{L_e} \left\{ \begin{matrix} \{q_u\}^T \\ \{q_w\}^T \end{matrix} \right\} \left[\begin{matrix} [D_u]^T \\ [B_w]^T \end{matrix} \right] \left[\begin{matrix} A_{11} & 0 \\ 0 & D_{11} \end{matrix} \right] \left[\begin{matrix} [D_u] \\ [B_w] \end{matrix} \right] \left\{ \begin{matrix} \{q_u\} \\ \{q_w\} \end{matrix} \right\} dx$$

$$+ \frac{1}{2} \int_{L_e} \left\{ \begin{matrix} \{q_u\}^T \\ \{q_w\}^T \end{matrix} \right\} \left[\begin{matrix} [D_u]^T \\ [B_w]^T \end{matrix} \right] \left[\begin{matrix} A_{11} & 0 \\ 0 & D_{11} \end{matrix} \right] \left[\begin{matrix} [B_{nw}]\{q_w\} \\ 0 \end{matrix} \right] dx$$

$$+ \frac{1}{2} \int_{L_e} \left\{ \begin{matrix} [B_{nw}]^T \{q_w\}^T \\ 0 \end{matrix} \right\} \left[\begin{matrix} A_{11} & 0 \\ 0 & D_{11} \end{matrix} \right] \left[\begin{matrix} [D_u] \\ [B_w] \end{matrix} \right] \left\{ \begin{matrix} \{q_u\} \\ \{q_w\} \end{matrix} \right\} dx$$

$$+ \frac{1}{2} \int_{L_e} \left\{ \begin{matrix} [B_{nw}]^T \{q_w\}^T \\ 0 \end{matrix} \right\} \left[\begin{matrix} A_{11} & 0 \\ 0 & D_{11} \end{matrix} \right] \left[\begin{matrix} [B_{nw}]\{q_w\} \\ 0 \end{matrix} \right] dx$$

$$+ \frac{1}{2} \int_{L_e} \left\{ \begin{matrix} \{q_u\}^T \\ \{q_w\}^T \end{matrix} \right\} \left\{ \begin{matrix} [D_u]^T \\ -z[B_w]^T \end{matrix} \right\} e_{31} A_p(x) [B_v]\{v\} dx + \frac{1}{2} \int_{L_e} \left\{ \begin{matrix} [B_{nw}]^T \{q_w\}^T \\ 0 \end{matrix} \right\} e_{31} A_p(x) [B_v]\{v\} dx$$

$$= \frac{1}{2}\{q_u\}^T\left[\int_{L_e}[D_u]^T A_{11}[D_u]dx\right]\{q_u\} + \frac{1}{2}\{q_w\}^T\left[\int_{L_e}[B_w]^T D_{11}[B_w]dx\right]\{q_w\}$$

$$+ \frac{1}{2}\{q_u\}^T\left[\int_{L_e}[D_u]^T A_{11}[B_{nw}]dx\right]\{q_w\} + \frac{1}{2}\{q_w\}^T\left[\int_{L_e}[B_{nw}]^T A_{11}[D_u]dx\right]\{q_u\}$$

$$+ \frac{1}{2}\{q_w\}^T\left[\int_{L_e}[B_{nw}]^T A_{11}[B_{nw}]dx\right]\{q_w\} + \frac{1}{2}\{q_u\}^T\left[\int_{L_e}[D_u]^T e_{31}A_p(x)[B_v]\right]\{v\}$$

$$+ \frac{1}{2}\{q_w\}^T\left[\int_{L_e}(-z)[B_w]^T e_{31}A_p(x)[B_v]\right]\{v\} + \frac{1}{2}\{q_w\}^T\left[\int_{L_e}[B_{nw}]^T e_{31}A_p(x)[B_v]\right]\{v\}$$

$$= \frac{1}{2}\{q_u\}^T[K_{1p}^e]\{q_u\} + \frac{1}{2}\{q_w\}^T[K_{1b}^e]\{q_w\} + \frac{1}{2}\{q_u\}^T[K_2^e]\{q_w\} + \frac{1}{2}\{q_w\}^T[K_3^e]\{q_u\}$$

$$+ \frac{1}{2}\{q_w\}^T[K_4^e]\{q_w\} + \frac{1}{2}\{q_u\}^T[K_{1pb}^e]\{v\} + \frac{1}{2}\{q_w\}^T[K_{2pb}^e]\{v\} + \frac{1}{2}\{q_w\}^T[K_{3pb}^e]\{v\}$$

b. Electric potential energy of the piezoelectric patch

$$T_{ep} = -\frac{1}{2}\int_{V_p} E_3^T D_3 dV$$

$$= -\frac{1}{2}\int_{V_p} E_3^T\left(e_{31}\varepsilon_1 + \xi_{33}^S E_3\right)dV$$

$$= -\frac{1}{2}\int_{V_p} E_3^T e_{31}\varepsilon_1 dV_p - \frac{1}{2}\int_{V_p} E_3^T \xi_{33}^S E_3 dV_p$$

$$= -\frac{1}{2}\int_{V_p} E_3^T e_{31}[\{\varepsilon_l\} + \{\varepsilon_{nl}\}]dV_p - \frac{1}{2}\int_{V_p} E_3^T \xi_{33}^S E_3 dV_p$$

$$= -\frac{1}{2}\int_{V_p} E_3^T e_{31}\{\varepsilon_l\}dV_p - \frac{1}{2}\int_{V_p} E_3^T e_{31}\{\varepsilon_{nl}\}dV_p - \frac{1}{2}\int_{V_p} E_3^T \xi_{33}^S E_3 dV_p$$

$$= \frac{1}{2}\left[\int_{L_e}[B_v]^T\{v\}^T e_{31}A_p(x)\begin{Bmatrix}[D_u]\\-z[B_w]\end{Bmatrix}\begin{Bmatrix}\{q_u\}\\\{q_w\}\end{Bmatrix}dx\right] \qquad (4.16)$$

$$+ \frac{1}{2}\left[\int_{L_e}[B_v]^T\{v\}^T e_{31}A_p(x)\begin{Bmatrix}[B_{nw}]\{q_w\}\\0\end{Bmatrix}dx\right]$$

$$- \frac{1}{2}\left[\int_{L_e}[B_v]^T\{v\}^T \xi_{33}^S A_p(x)[B_v]\{v\}dx\right]$$

$$= \frac{1}{2}\{v\}^T\left[\int_{L_e}[B_v]^T e_{31}A_p(x)[D_u]dx\right]\{q_u\} + \frac{1}{2}\{v\}^T\left[\int_{L_e}(-z)[B_v]^T e_{31}A_p(x)[B_w]dx\right]\{q_w\}$$

$$+ \frac{1}{2}\{v\}^T\left[\int_{L_e}[B_v]^T e_{31}A_p(x)[B_{nw}]dx\right]\{q_w\} - \frac{1}{2}\{v\}^T\left[\int_{L_e}[B_v]^T \xi_{33}^S A_p(x)[B_v]dx\right]\{v\}$$

$$= \frac{1}{2}\{v\}^T[K_{1bp}^e]\{q_u\} + \frac{1}{2}\{v\}^T[K_{2bp}^e]\{q_w\} + \frac{1}{2}\{v\}^T[K_{3bp}^e]\{q_w\} - \frac{1}{2}\{v\}^T[K_{pp}^e]\{v\}$$

Hence, the total internal potential energy is given by

69

$$T_p = \frac{1}{2}\{q_u\}^T[K_{1p}^e]\{q_u\} + \frac{1}{2}\{q_w\}^T[K_{1b}^e]\{q_w\} + \frac{1}{2}\{q_u\}^T[K_2^e]\{q_w\} + \frac{1}{2}\{q_w\}^T[K_3^e]\{q_u\}$$

$$+ \frac{1}{2}\{q_w\}^T[K_4^e]\{q_w\} + \frac{1}{2}\{q_u\}^T[K_{1pb}^e]\{v\} + \frac{1}{2}\{q_w\}^T[K_{2pb}^e]\{v\} + \frac{1}{2}\{q_w\}^T[K_{3pb}^e]\{v\} \quad (4.17)$$

$$+ \frac{1}{2}\{v\}^T[K_{1bp}^e]\{q_u\} + \frac{1}{2}\{v\}^T[K_{2bp}^e]\{q_w\} + \frac{1}{2}\{v\}^T[K_{3bp}^e]\{q_w\} - \frac{1}{2}\{v\}^T[K_{pp}^e]\{v\}$$

Now, the work done by the external forces and electric charges can be obtained as

$$W = \int_A \{q_w\}^T \{q(x,y)\}dA - \int_A \{v\}^T \{g(x,y)\}dA$$

$$= \{q_w\}^T \{Q^e\} + \{v\}^T \{G^e\} \quad (4.18)$$

where, A_{11}, B_{11} and D_{11} are the extension, coupling and bending coefficients given by

$$c_{11}^E = \begin{bmatrix} A_{11} & B_{11} \\ B_{11} & D_{11} \end{bmatrix}$$

$$A_{11}, B_{11}, D_{11} = \int_A (1, z, z^2) c_{11}^E dA \quad (4.19)$$

In the present formulations the terms used are given by

$$A_{11} = \int_A c_{11}^E dA = c_{11}^E A(x)$$

$$B_{11} = \int_A c_{11}^E z\, dA = 0 \quad (4.20)$$

$$D_{11} = \int_A c_{11}^E z^2 dA = c_{11}^E I(x)$$

Hence, equation (4.19) becomes

$$c_{11}^E = \begin{bmatrix} A_{11} & 0 \\ 0 & D_{11} \end{bmatrix} \quad (4.21)$$

Now, substituting the first variation of equations (4.17) and (4.18) in equation (4.13)

$$\partial\Pi = \int_{t_1}^{t_2} \begin{bmatrix} \{\delta q_u\}^T[K_{1p}^e]\{q_u\} + \{\delta q_w\}^T[K_{1b}^e]\{q_w\} \\ + \{\delta q_u\}^T[K_2^e]\{q_w\} \\ + \{\delta q_w\}^T[K_3^e]\{q_u\} + \{\delta q_w\}^T[K_4^e]\{q_w\} + \{\delta q_u\}^T[K_{1pb}^e]\{v\} \\ + \{\delta q_w\}^T[K_{2pb}^e]\{v\} + \{\delta q_w\}^T[K_{3pb}^e]\{v\} + \{\delta v\}^T[K_{1bp}^e]\{q_u\} \\ + \{\delta v\}^T[K_{2bp}^e]\{q_w\} + \{\delta v\}^T[K_{3bp}^e]\{q_w\} \\ - \{\delta v\}^T[K_{pp}^e]\{v\} - \{\delta q_w\}^T\{Q^e\} - \{\delta v\}^T\{G^e\} \end{bmatrix} dt = 0$$

$$\Rightarrow \int_{t_1}^{t_2} \begin{bmatrix} \{\delta q_u\}^T \left[[K_{1p}^e]\{q_u\} + [K_2^e]\{q_w\} + [K_{1pb}^e]\{v\}\right] \\ + \{\delta q_w\}^T \left[[K_{1b}^e]\{q_w\} + [K_3^e]\{q_u\} + [K_4^e]\{q_w\} + [K_{2pb}^e]\{v\} + [K_{3pb}^e]\{v\} - \{Q^e\}\right] \\ + \{\delta v\}^T \left[[K_{1bp}^e]\{q_u\} + [K_{2bp}^e]\{q_w\} + [K_{3bp}^e]\{q_w\} - [K_{pp}^e]\{v\} - \{G^e\}\right] \end{bmatrix} = 0$$

(4.22)

From equation (4.22), the system of equations for an element can be obtained as

$$[K_{1p}^e]\{q_u\} + [K_2^e]\{q_w\} + [K_{1pb}^e]\{v\} = 0 \tag{4.23}$$

$$[K_{1b}^e]\{q_w\} + [K_3^e]\{q_u\} + [K_4^e]\{q_w\} + [K_{2pb}^e]\{v\} + [K_{3pb}^e]\{v\} - \{Q^e\} = 0 \tag{4.24}$$

$$[K_{1bp}^e]\{q_u\} + [K_{2bp}^e]\{q_w\} + [K_{3bp}^e]\{q_w\} - [K_{pp}^e]\{v\} - \{G^e\} = 0 \tag{4.25}$$

where,

$$[K_{1p}^e] = [K_{1p}^e]_{beam} + [K_{1p}^e]_{piezo} \tag{4.26}$$

$$[K_{1b}^e] = [K_{1b}^e]_{beam} + [K_{1b}^e]_{piezo} \tag{4.27}$$

$$[K_{1p}^e]_{beam} = \int_{L_e}[D_u]^T A_{11}[D_u]dx = \int_{L_e}[D_u]^T \left(c_{11}^E\right)_b A_b(x)[D_u]dx \tag{4.28}$$

$$[K_{1p}^e]_{piezo} = \int_{L_e}[D_u]^T A_{11}[D_u]dx = \int_{L_e}[D_u]^T \left(c_{11}^E\right)_p A_p(x)[D_u]dx \tag{4.29}$$

$$[K_{1b}^e]_{beam} = \int_{L_e}[B_w]^T D_{11}[B_w]\,dx = \int_{L_e}[B_w]^T \left(c_{11}^E\right)_b I_b(x)[B_w]\,dx \tag{4.30}$$

$$[K_{1b}^e]_{piezo} = \int_{L_e}[B_w]^T D_{11}[B_w]dx = \int_{L_e}[B_w]^T \left(c_{11}^E\right)_p I_p(x)[B_w]dx \tag{4.31}$$

$$[K_2^e] = \int_{L_e}[D_u]^T A_{11}[B_{nw}]dx = \int_{L_e}[D_u]^T \left(c_{11}^E\right)_b A_b(x)[A][G]dx \tag{4.32}$$

$$[K_3^e] = \int_{L_e}[B_{nw}]^T A_{11}[D_u]dx = \int_{L_e}[A]^T [G]^T \left(c_{11}^E\right)_b A_b(x)[D_u]dx \tag{4.33}$$

$$[K_4^e] = \int_{L_e}[B_{nw}]^T A_{11}[B_{nw}]dx = \int_{L_e}[A]^T [G]^T \left(c_{11}^E\right)_b A_b(x)[A][G]\,dx \tag{4.34}$$

$$[K_{1pb}^e] = \int_{L_e}[D_u]^T e_{31}A_p(x)[B_v]dx \tag{4.35}$$

$$[K_{2pb}^e] = -\int_{L_e} z[B_w]^T e_{31} A_p(x)[B_v]dx \tag{4.36}$$

$$[K_{3pb}^e] = \int_{L_e} [B_{nw}]^T e_{31} A_p(x)[B_v]dx = \int_{L_e} [A]^T [G]^T e_{31} A_p(x)[B_v]dx \tag{4.37}$$

Similarly,

$$
\begin{aligned}
[K_{1bp}^e] &= [K_{1pb}^e]^T \\
[K_{2bp}^e] &= [K_{2pb}^e]^T \\
[K_{3bp}^e] &= [K_{3pb}^e]^T
\end{aligned}
\tag{4.38}
$$

After assembling the elemental stiffness matrices of piezoelastic beam the global set of equations become

$$
\begin{pmatrix}
[K_{1p}] & [K_2] & [K_{1pb}] \\
[K_3] & [K_{1b}]+[K_4] & [K_{2pb}]+[K_{3pb}] \\
[K_{1bp}] & [K_{2bp}]+[K_{3bp}] & -[K_{pp}]
\end{pmatrix}
\begin{Bmatrix}
\{q_u\}_{global} \\
\{q_w\}_{global} \\
\{v\}_{global}
\end{Bmatrix}
=
\begin{Bmatrix}
\{0\} \\
\{Q\} \\
\{G\}
\end{Bmatrix}
\tag{4.39}
$$

The modelled beam in electrical domain is assumed to be open-circuited for the analysis. For open circuit, the differences in electrical potential between the electrodes are unknown considering charge equal to zero (*G =0*) which leads to the following equation as

$$
\begin{pmatrix}
[K_{1p}] & [K_2] & [K_{1pb}] \\
[K_3] & [K_{1b}]+[K_4] & [K_{2pb}]+[K_{3pb}] \\
[K_{1bp}] & [K_{2bp}]+[K_{3bp}] & -[K_{pp}]
\end{pmatrix}
\begin{Bmatrix}
\{q_u\}_{global} \\
\{q_w\}_{global} \\
\{v\}_{global}
\end{Bmatrix}
=
\begin{Bmatrix}
\{0\} \\
\{Q\} \\
\{0\}
\end{Bmatrix}
\tag{4.40}
$$

4.2.4.2 Dynamic nonlinear finite element equation

The dynamic equations of motion of the modelled system can be represented using Hamilton's principle as

$$\delta \Pi = \int_{t_1}^{t_2} [\delta (T_k - T_p + W)]\, dt = 0 \tag{4.41}$$

The equation (4.41) can further be represented as

$$\delta \Pi = \int_{t_1}^{t_2} [\delta T_k - \delta(T_{es} + T_{ep}) + \delta W)] \, dt = 0$$

$$\Rightarrow \int_{t_1}^{t_2} \delta T_k \, dt - \int_{t_1}^{t_2} \delta(T_{es} + T_{ep}) \, dt + \int_{t_1}^{t_2} \delta W \, dt = 0$$

(4.42)

The terms used in equation (4.42) can be obtained as follows:

Part 1. The kinetic energy of the system is

$$T_k = \int_V \frac{1}{2} \{\dot{u}_0\}^T \rho(x) \{\dot{u}_0\} dV + \int_V \frac{1}{2} \{\dot{w}_0\}^T \rho(x) \{\dot{w}_0\} dV$$

$$\int_{t_1}^{t_2} \delta T_k \, dt = \int_{t_1}^{t_2} \delta \left[\int_V \frac{1}{2} \{\dot{u}_0\}^T \rho(x) \{\dot{u}_0\} dV + \int_V \frac{1}{2} \{\dot{w}_0\}^T \rho(x) \{\dot{w}_0\} dV \right] dt$$

$$= -\int_{t_1}^{t_2} \left[\int_V \{\delta u_0\}^T \rho(x) \{\ddot{u}_0\} dV + \int_V \{\delta w_0\}^T \rho(x) \{\ddot{w}_0\} dV \right] dt$$

$$= -\int_{t_1}^{t_2} \{\delta q_u\}^T \left[\int_V [N_u]^T \rho(x) [N_u] dV \right] \{\ddot{q}_u\} \, dt$$

$$\qquad -\int_{t_1}^{t_2} \{\delta q_w\}^T \left[\int_V [N_w]^T \rho(x) [N_w] dV \right] \{\ddot{q}_w\} \, dt$$

(4.43)

$$= -\int_{t_1}^{t_2} \{\delta q_u\}^T [M_{1p}^e] \{\ddot{q}_u\} dt - \int_{t_1}^{t_2} \{\delta q_w\}^T [M_{1b}^e] \{\ddot{q}_w\} \, dt$$

Part 2. The total electromechanical enthalpy of the system is

$$\int_{t_1}^{t_2} \delta T_p \, dt = \int_{t_1}^{t_2} \delta (T_{es} + T_{ep}) dt$$

$$= \int_{t_1}^{t_2} \begin{bmatrix} \{\delta q_u\}^T [K_{1p}^e]\{q_u\} + \{\delta q_w\}^T [K_{1b}^e]\{q_w\} + \{\delta q_u\}^T [K_2^e]\{q_w\} \\ + \{\delta q_w\}^T [K_3^e]\{q_u\} + \{\delta q_w\}^T [K_4^e]\{q_w\} + \{\delta q_u\}^T [K_{1pb}^e]\{v\} \\ + \{\delta q_w\}^T [K_{2pb}^e]\{v\} + \{\delta q_w\}^T [K_{3pb}^e]\{v\} + \{\delta v\}^T [K_{1bp}^e]\{q_u\} \\ + \{\delta v\}^T [K_{2bp}^e]\{q_w\} + \{\delta v\}^T [K_{3bp}^e]\{q_w\} \\ - \{\delta v\}^T [K_{pp}^e]\{v\} \end{bmatrix} dt$$

(4.44)

Part 3. The work done by the external force is

$$\int_{t_1}^{t_2} \delta W dt = \int_{t_1}^{t_2} \delta \left[\int_A \{q_w\}^T \{q(x,y)\} dA - \int_A \{v\}^T \{g(x,y)\} dA \right] dt$$

$$= \int_{t_1}^{t_2} \left[\int_A \{\delta q_w\}^T \{q(x,y)\} dA - \int_A \{\delta v\}^T \{g(x,y)\} dA \right] dt \tag{4.45}$$

$$= \{\delta q_w\}^T \{Q^e\} + \{\delta v\}^T \{G^e\}$$

Now substituting equations (4.43)-(4.45) in equation (4.42) , the resulting equation becomes

$$\int_{t_1}^{t_2} \begin{bmatrix} \{\delta q_u\}^T \left[-[M_{1p}^e]\{\ddot{q}_u\} - [K_{1p}^e]\{q_u\} - [K_2^e]\{q_w\} - [K_{1pb}^e]\{v\} \right] \\[2mm] + \{\delta q_w\}^T \begin{bmatrix} -[M_{1b}^e]\{\ddot{q}_w\} - [K_{1b}^e]\{q_w\} - [K_3^e]\{q_u\} \\ -[K_4^e]\{q_w\} - [K_{2pb}^e]\{v\} - [K_{3pb}^e]\{v\} + \{Q^e\} \end{bmatrix} \\[2mm] + \{\delta v\}^T \begin{bmatrix} -[K_{1bp}^e]\{q_u\} - [K_{2bp}^e]\{q_w\} - [K_{3bp}^e]\{q_w\} + [K_{pp}^e]\{v\} \\ + \{G^e\} \end{bmatrix} \end{bmatrix} = 0 \tag{4.46}$$

From equation (4.46), it is observed that the partial differentiation of q_u, q_w and v can be of any arbitrary value rather than zero. Therefore, the equation (4.46) is valid only if

$$[M_{1p}^e]\{\ddot{q}_u\} - [K_{1p}^e]\{q_u\} - [K_2^e]\{q_w\} - [K_{1pb}^e]\{v\} = 0 \tag{4.47}$$

$$[M_{1b}^e]\{\ddot{q}_w\} + [K_{1b}^e]\{q_w\} + [K_3^e]\{q_u\} + [K_4^e]\{q_w\} + [K_{2pb}^e]\{v\} + [K_{3pb}^e]\{v\} = \{Q^e\} \tag{4.48}$$

$$[K_{1bp}^e]\{q_u\} + [K_{2bp}^e]\{q_w\} + [K_{3bp}^e]\{q_w\} - [K_{pp}^e]\{v\} = \{G^e\} \tag{4.49}$$

The equations (4.47)-(4.49) represent the dynamic equation of motion of one element. Further, the equations (4.47)-(4.49) can be represented in matrix form as

$$\begin{pmatrix} [M_{1p}^e] & [0] & [0] \\ [0] & [M_{1b}^e] & [0] \\ [0] & [0] & [0] \end{pmatrix} \begin{Bmatrix} \{\ddot{q}_u\} \\ \{\ddot{q}_w\} \\ \{\ddot{v}\} \end{Bmatrix} + \begin{pmatrix} [K_{1p}^e] & [K_2^e] & [K_{1pb}^e] \\ [K_3^e] & [K_{1b}^e]+[K_4^e] & [K_{2pb}^e]+[K_{3pb}^e] \\ [K_{1bp}^e] & [K_{2bp}^e]+[K_{3bp}^e] & -[K_{pp}^e] \end{pmatrix} \begin{Bmatrix} \{q_u\} \\ \{q_w\} \\ \{v\} \end{Bmatrix} = \begin{Bmatrix} \{0\} \\ \{Q^e\} \\ \{G^e\} \end{Bmatrix} \tag{4.50}$$

After assembling the elemental matrices the global set of equations can be obtained and can be written as

$$\begin{pmatrix} [M_{1p}] & [0] & [0] \\ [0] & [M_{1b}] & [0] \\ [0] & [0] & [0] \end{pmatrix} \begin{Bmatrix} \{\ddot{q}_u\}_{global} \\ \{\ddot{q}_w\}_{global} \\ \{\ddot{v}\}_{global} \end{Bmatrix}$$

$$+ \begin{pmatrix} [K_{1p}] & [K_2] & [K_{1pb}] \\ [K_3] & [K_{1b}]+[K_4] & [K_{2pb}]+[K_{3pb}] \\ [K_{1bp}] & [K_{2bp}]+[K_{3bp}] & -[K_{pp}] \end{pmatrix} \begin{Bmatrix} \{q_u\}_{global} \\ \{q_w\}_{global} \\ \{v\}_{global} \end{Bmatrix} = \begin{Bmatrix} \{0\} \\ \{Q\} \\ \{G\} \end{Bmatrix} \tag{4.51}$$

For open circuit condition, the differences in electrical potential between the electrodes are unknown considering charge equal to zero (*G=0*). Hence, the equation (4.51) can be deduced to the following equation:

$$
\begin{pmatrix} [M_{1p}] & [0] & [0] \\ [0] & [M_{1b}] & [0] \\ [0] & [0] & [0] \end{pmatrix} \begin{Bmatrix} \{\ddot{q}_u\}_{global} \\ \{\ddot{q}_w\}_{global} \\ \{\ddot{v}\}_{global} \end{Bmatrix}
$$

$$
+ \begin{pmatrix} [K_{1p}] & [K_2] & [K_{1pb}] \\ [K_3] & [K_{1b}]+[K_4] & [K_{2pb}]+[K_{3pb}] \\ [K_{1bp}] & [K_{2bp}]+[K_{3bp}] & -[K_{pp}] \end{pmatrix} \begin{Bmatrix} \{q_u\}_{global} \\ \{q_w\}_{global} \\ \{v\}_{global} \end{Bmatrix} = \begin{Bmatrix} \{0\} \\ \{Q\} \\ \{0\} \end{Bmatrix}
$$

(4.52)

4.2.4.3 Output voltage

Equation (4.40) represents the static piezo electro-mechanical system with geometric nonlinear parameters, which can be represented as

$$
\begin{pmatrix} [K_{1p}] & [K_2] \\ [K_3] & [K_{1b}]+[K_4] \end{pmatrix} \begin{Bmatrix} \{q_u\}_{global} \\ \{q_w\}_{global} \end{Bmatrix} + \begin{pmatrix} [K_{1pb}] \\ [K_{2pb}]+[K_{3pb}] \end{pmatrix} \{v\}_{global} = \begin{Bmatrix} \{0\} \\ \{Q\} \end{Bmatrix}
$$

$$
\begin{pmatrix} [K_{1bp}] & [K_{2bp}]+[K_{3bp}] \end{pmatrix} \begin{Bmatrix} \{q_u\}_{global} \\ \{q_w\}_{global} \end{Bmatrix} - [K_{pp}]\{v\}_{global} = \{0\}
$$

(4.53)

From the second part of the equation (4.53), the output voltage can be obtained as

$$
\{v\}_{global} = [K_{pp}]^{-1} \begin{pmatrix} [K_{1bp}] & [K_{2bp}]+[K_{3bp}] \end{pmatrix} \begin{Bmatrix} \{q_u\}_{global} \\ \{q_w\}_{global} \end{Bmatrix}
$$

(4.54)

4.2.4.4 Output power

The equation (4.52) represents the piezo electro-mechanical system which can be used to determine the motion of the beam; however the equation doesn't contain any energy dissipation. Since the model is intended for energy harvesting system which must focus on scavenging energy, this form will not hold good for the present need. Hence, to incorporate the energy dissipation term into the equation, Ohm's law is used, and a resistive element is added between the top and bottom surface of the piezoelectric patch. By incorporating equation (3.65) into equation (4.52), the equation becomes

$$\begin{pmatrix} [M_{1p}] & [0] & [0] \\ [0] & [M_{1b}] & [0] \\ [0] & [0] & [0] \end{pmatrix} \begin{Bmatrix} \{\ddot{q}_u\}_{global} \\ \{\ddot{q}_w\}_{global} \\ \{\ddot{v}\}_{global} \end{Bmatrix}$$

$$+ \begin{pmatrix} [K_{1p}] & [K_2] & [K_{1pb}] \\ [K_3] & [K_{1b}]+[K_4] & [K_{2pb}]+[K_{3pb}] \\ [K_{1bp}] & [K_{2bp}]+[K_{3bp}] & -[K_{pp}] \end{pmatrix} \begin{Bmatrix} \{q_u\}_{global} \\ \{q_w\}_{global} \\ R\{\dot{q}(t)\}_{global} \end{Bmatrix} = \begin{Bmatrix} \{0\} \\ \{Q\} \\ \{0\} \end{Bmatrix} \qquad (4.55)$$

Equation (4.55) shows the model of energy harvesting system. The term $\dot{q}(t)$ provides the current output of the piezoelectric patch and can be used directly for output power through external load resistance *R*.

4.2.4.5 Electro-mechanical sensing of output power

For measuring the output power, the linear constitutive equations of the piezoelectric material have been employed across the thickness of the piezoelectric layer. Hence, the total charge on the electrode surface can be obtained as

$$Q_r = \int_A D_3 \, dA = \int_A \left(e_{31} \varepsilon_1 + \xi_{33}^S E_3 \right) dA \qquad (4.56)$$

It should be emphasised that the produced charge, current and voltage are all functions of time. The produced current, flowing out to the external impedance can be found using the charge developed on the piezoelectric patch. Again as the current is influenced by vibration frequency, its magnitude through the external impedance can be expressed as

$$I_r = \omega Q_r \qquad (4.57)$$

where ω is the vibration frequency. For a pure load resistance, a linear relationship exists between voltage and current which can be written as

$$V = I_r R \qquad (4.58)$$

Combining equations (4.56), (4.57) and (4.58), the amplitude of current flowing through the electric circuit becomes

$$I_r = \frac{bhe_{31}\omega\,[\psi(L_p) - \psi(0)]}{2\left(1 + \dfrac{b\omega R \xi_{33}^s L_p}{t_p}\right)} \qquad (4.59)$$

where, *b* and *h* represents the width and thickness of the beam. Ψ is the slope of deflection of the beam, ω is the first natural frequency and *R* is the external load resistance. Hence, the output power from the piezolaminated system can be written as

$$P = I_r^2 R = \left[\frac{bhe_{31}\omega\,[\psi(L_p) - \psi(0)]}{2\left(1 + \dfrac{b\omega R \xi_{33}^s L_p}{t_p}\right)} \right]^2 R \tag{4.60}$$

4.2.5   Nonlinear system of equations

The non-linear equation (4.55) in the time domain can be solved using Newmark method in conjunction with an iteration method, i.e. Newton-Raphson method. By using such method, the nonlinear differential equations of motion can be reduced to a set of non-linear algebraic equations [134]. The nonlinear equation (4.55) can be written in the form of

$$[K_{eff}]^{t+\Delta t}\{q\}_{global} = \{Q_{eff}\}^{t+\Delta t} \tag{4.61}$$

where, K_{eff} and Q_{eff} are the effective global stiffness matrix consisting of nonlinear terms and effective global load vector, respectively which can be written as

$$[K_{eff}] = \left(\begin{bmatrix} [K_{1p}] \\ +[K_{1pb}][K_{pp}]^{-1}[K_{1bp}] \end{bmatrix} \begin{bmatrix} [K_2] \\ +[K_{1pb}][K_{pp}]^{-1}\{[K_{2bp}]+[K_{3bp}]\} \end{bmatrix} \\ \begin{bmatrix} [K_3] \\ +\{[K_{2pb}]+[K_{3pb}]\}[K_{pp}]^{-1}[K_{1bp}] \end{bmatrix} \begin{bmatrix} \{[K_{1b}]+[K_4]\} \\ +\{[K_{2pb}]+[K_{3pb}]\}[K_{pp}]^{-1}\{[K_{2bp}]+[K_{3bp}]\} \end{bmatrix} \right) \\ + a_0 \begin{pmatrix} [M_{1p}] & [0] \\ [0] & [M_{1b}] \end{pmatrix} \tag{4.62}$$

$$\{Q_{eff}\}^{t+\Delta t} = \{Q\}^{t+\Delta t} + \begin{pmatrix} [M_{1p}] & [0] \\ [0] & [M_{1b}] \end{pmatrix} \left\{ a_0 \{q\}_{global}^t + a_1 \{\dot{q}\}_{global}^t + a_2 \{\ddot{q}\}_{global}^t \right\}$$

The terms $a_0,\ a_1$, and a_2 are represented as [135]

$$a_0 = \frac{1}{\alpha\Delta t^2}\,;\, a_1 = \frac{1}{\alpha\Delta t}\,;\, a_2 = \frac{1}{2\alpha} - 1;\ \ \alpha = 0.25 \tag{4.63}$$

Since the effective stiffness matrix is nonlinear, an iterative solution procedure, i.e. Newton-Raphson method has been adopted for any fixed time having s[th] iteration. In Newton-Raphson method, the linearized element equation is of the form

$$\{q\}_{global}^s = \{q\}_{global}^{s-1} - \left(\left\{[T]^{s-1}\right\}^{-1}\left\{[R]^{s-1}\right\} \right) \tag{4.64}$$

where, the terms R and T denote the residual and tangent stiffness matrix and can be written as

$$\left\{ [R]^{(s-1)} \right\} = \left([K_{eff}]^{(s-1)} \right) \{q\}_{global}^{s-1} - \{Q_{eff}\} \tag{4.65}$$

$$\begin{aligned} \left\{ [T]^{s-1} \right\} &= \frac{\partial \left\{ [R]^{(s-1)} \right\}}{\partial \{q\}_{global}^{s-1}} \\ &= \left([K_{eff}]^{(s-1)} \right) + \frac{\partial \left([K_{eff}]^{(s-1)} \right)}{\partial \{q\}_{global}^{s-1}} \{q\}_{global}^{s-1} \end{aligned} \tag{4.66}$$

In Newton-Raphson method, the first iteration can be calculated using linear stiffness matrix, by assuming $q_{global}^{s-1} = 0$ and q_{global}^{s} is calculated using equation (4.64). The residual is then calculated and the iteration process is repeated till a sufficient residual is reached. The exact solution can be obtained when the residual becomes zero.

Chapter 5

Genetic Algorithm for Optimal Power Harvesting

This chapter describes a constrained real coded genetic algorithm (GA) based optimization technique to determine the best set of design variables for obtaining maximum output power from non-prismatic axially FG beam with temperature gradient and nonlinear non-prismatic axially FG beam.

5.1 Genetic algorithm

The conventional optimization techniques possess many drawbacks for which it cannot be implemented in regular basis in many practical problems. Some of the drawbacks are as follows:

(i) Convergence depends on the initial solution.
(ii) A separate algorithm is required for each problem.
(iii) Inefficient for problems with discrete search spaces.
(iv) Inefficient for simultaneous used for parallel machines.

In order to overcome these limitations genetic algorithms (GAs) shows a significant alternative for conventional techniques in real optimization problems. Further the computational time spent in evaluating solutions with multiple processors can be reduced substantially.

The GA is an optimization technique established on the concepts of natural evolution. It operates on population-based techniques considering the principle of survival of the fittest to yield the best approximated result. At each generation of GA, a new set of the chromosome is formed according to their appropriateness in the problem domain

reproducing them using operators like crossover, mutation, lent from natural genetics.
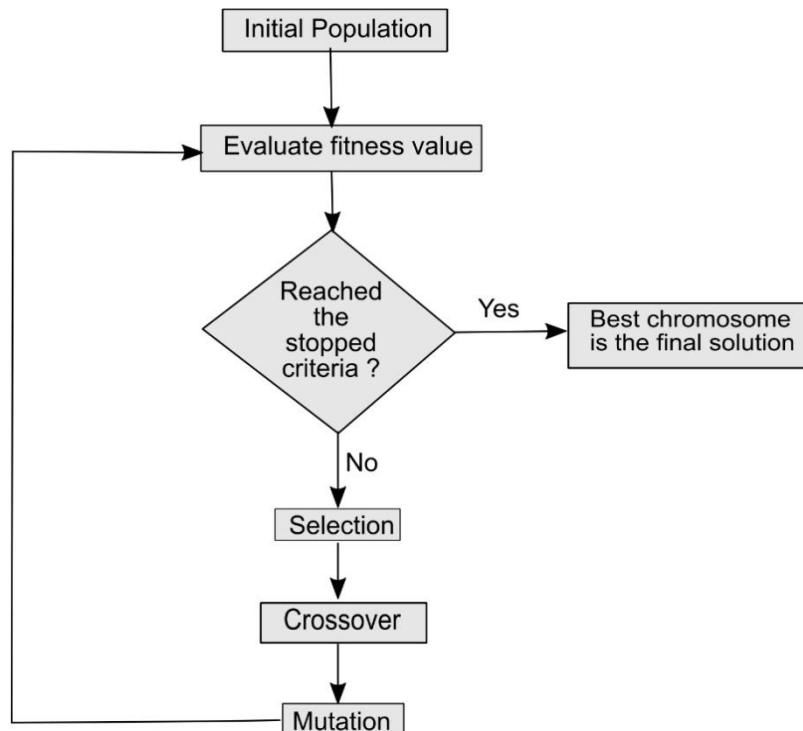
Figure 5.1 A frame work of genetic algorithm used for the parametric optimization

This process leads to the progression of the population of individuals that is best appropriate to their environment than the individuals created by natural adaption. The framework of the basic genetic procedure is shown in Figure 5.1. A simple genetic algorithm contains three operators namely reproduction, crossover and mutation. Individuals are generated randomly from the initial population which are evaluated according to a fitness function or objective function. Then, the reproduction operation is carried out by selecting individuals based on their relative fitness. The individuals with higher fitness values are selected for a greater number of times, in proportion to their relative fitness. Reproduction alone cannot introduce any different individuals into a population. Therefore, the crossover and mutation operations are performed to generate new individuals.

The crossover operator is supposed to be the main search operator and behaves in twofold operation. Primarily, random strings signifying the design variables are searched thoroughly. The favourable portions of these strings are then combined to form potentially better strings. Thus, the crossover operation is performed between two strings that are

called as parents. Two new strings are formed by the exchange of substrings between the parents and are called as children. The produced children might or might not be fit than the parents, depending on whether the crossing site falls in an appropriate place. Hence, every crossover might not create better solutions. If low-fitness children are created, they will be eliminated in the next reproduction operation and hence, will have a short life. On the other hand, if high fitness children are produced, they are likely to increase in number in the next reproduction operation. Thus, this operation tends to enable the evolutionary process to move toward promising regions of the search space.

In a binary coded genetic algorithm, the string length influences the precision. For higher precision, greater requirements of the string length and population size is needed, thereby increasing the computational complexity. Moreover, a fixed coding scheme is used to code the design variables and their corresponding limits. These variable bounds must be used such that they bracket the optimum variables. In many problems, such information is not known previously. Hence, a real coded genetic algorithm has been developed where the real parameters are used directly and optimization is easier than for binary coded GAs. In the present study to find the design variables for optimal harvesting of power, a real coded GA based constrained technique has been implemented.

5.2 Real-coded genetic algorithm

Real-coded genetic algorithm (GA) possesses a lot of advantages than its binary coded counterpart while dealing with continuous search spaces with large dimensions. It can deal with large domains without sacrificing precision as the binary implementation did. Moreover, the computational complexity is less in real coded GA compared to binary coded GA. In a real coded GA, the number of parents used in perturbation is the main criteria to distinguish between the crossover and mutation operations. The operator is mutation if only one parent is used and crossover if more than one parent is used. Hence, real-coded GA has been used in the present work to find the optimum parameters that give a maximum harvested power. In the present study, a real-coded GA along with simulated binary crossover (SBX) and parameter based mutation [136] has been involved to maximize the output power.

5.3 Mathematical formulation

The mathematical formulation involves the real coded GA based optimization scheme to maximize the output power for non-prismatic axially FG beam with temperature gradient and another non-prismatic axially FG beam with geometric nonlinear effects. The following section depict the detailed formulation for optimising the output power.

5.3.1 Genetic algorithm approach for optimal output power of nonprismatic axially FG beam under thermo-mechanical loading

As far as the present mathematical formulation is concerned, the output power depends on geometric, mechanical properties, boundary conditions, nature of the applied force of the beam and the piezolaminated patch. From the formulation, it is perceived that the output power is primarily a function of slope of the piezolaminated patch, which is further influenced by c_b and c_h. The output power depends on the thickness of the piezoelectric patch (t_p) and the load resistance (R) as well. Apart from this, the first natural frequency also depends on the positive integer constant (k) and power gradient index (np) of axially FG beam. Set of these parameters has different values, to generate more power. To obtain the best combination of the above parameters, a search algorithm is required within the safe design of the piezolaminated beam. In the present study, a constrained optimization problem has been proposed to maximize the output power within the allowable stresses of the beam, PZT material and the voltage of the PZT material. The objective function (i.e. obtained power) can be written as

$$Maximize \ P_1 = \left[\frac{g_1\varphi + g_3}{2\left(1 + \frac{g_2 R}{t_p}\right)}\right]^2 R$$

$$subjected\,to\ (\sigma_{induced})_{beam} < (\sigma_{allowable})_{beam}, (\sigma_{induced})_{PZT} < (\sigma_{allowable})_{PZT} \tag{5.1}$$

$$and \quad (V_{induced})_{PZT} < (V_{allowable})_{PZT}$$

$$where, \ g_1 = bh\omega e_{31} \ , \ g_2 = bL_p\omega\xi_{33}., \ g_3 = 2bp_3 L_p\Delta\theta$$

$$and \quad \varphi = \varphi(L_p) - \varphi(0)$$

The term $\sigma_{induced}$ and $V_{induced}$ are the stress and open circuit voltage of PZT material, respectively. The allowable stress for beam material and PZT material are considered as 550 MPa and 14 MPa, respectively [137]. The allowable voltage of piezo-ceramic material is around 500-1000 V per 1 mm piezo thickness [138]. For the present analysis, six parameters are selected for the optimization process which mostly influence the harvested power such as: width taper (c_b), height taper (c_h), electrical resistance (R), thickness of piezoelectric patch (t_p), positive integer constant (k) and power gradient index (np). The fitness function for this problem can be written as

$$H(u) = \begin{cases} P_1(u) & if\ (\sigma_{induced})_{beam} < (\sigma_{allowable})_{beam} \ ;\ (\sigma_{induced})_{PZT} < (\sigma_{allowable})_{PZT} \ ; \\ & \&\ (V_{induced})_{PZT} < (V_{allowable})_{PZT} \\ P_1(u)\alpha & otherwise \end{cases} \tag{5.2}$$

where, H is the fitness function, u is the optimization parameters vector and P_1 is the power harvested from the non-prismatic axially FG beam under thermo-mechanical loading. The term α represents as the penalty for this algorithm and is taken as 10^{-8} which is used in the case of constrained violation. The algorithm is sustained for some generations until the fitness reaches the optimum value and there is also no change in fitness for a large number of generations. In the present work, the real coded genetic algorithm consists of the Roulette wheel selection, simulated binary crossover (SBX) and parameter based mutation operators. The following section give the brief description of these parameters.

Simulated binary crossover

A probability distribution function has been considered for the parent solution to create two child solutions as

$$p(z) = \begin{cases} 0.5(\psi+1)z^\psi & if\ z \le 1 \\ 0.5(\psi+1)/z^{\psi+2} & otherwise \end{cases} \tag{5.3}$$

where,

$$z = \left| \frac{c^{(2)} - c^{(1)}}{p^{(2)} - p^{(1)}} \right| \tag{5.4}$$

The terms $c^{(1)}$, $c^{(2)}$ are the child solutions and $p^{(1)}$, $p^{(2)}$ are the parent solutions. The term Ψ is the parameter that controls the spread of child solutions. A self-adaptive method for updating the Ψ parameter has been considered [139]. The general procedure adopted for the parent solution and child solution are as follows:

(a) A random number *m* is generated between 0 and 1.

(b) The polynomial probability distribution is used for parameter $\bar{z}$ which can be written as

$$\bar{z} = \begin{cases} (\beta m)^{\frac{1}{\psi+1}} & \text{if } m \leq \dfrac{1}{\beta} \\[2ex] (0.5 - \beta m)^{\frac{1}{\psi+1}} & \text{otherwise} \end{cases} \tag{5.5}$$

where

$$\beta = 2 - z^{-(\psi+1)} \tag{5.6}$$

and *z* is calculated as

$$z = 1 + \frac{2}{p^{(u)} - p^{l}} \min\left[\left(p^{(1)} - p^{(l)}\right), \left(p^{(u)} - p^{(2)}\right)\right] \tag{5.7}$$

Here, $p^{(u)}$ and $p^{(l)}$ are the upper and lower bound of a variable, respectively. The child solutions are calculated as follows:

$$c^{(1)} = \frac{1}{2}[(a^{(1)} + a^{(2)}) - \bar{z}|a^{(2)} - a^{(1)}|]$$

$$c^{(2)} = \frac{1}{2}[(a^{(1)} + a^{(2)}) + \bar{z}|a^{(2)} - a^{(1)}|] \tag{5.8}$$

Parameter based mutation operator

In the vicinity of parent solution, a polynomial probability distribution has been used to create the child solution. The procedure adopted has been presented below:

(a) A random number *m* is generated between 0 and 1.

(b) The parameter *δ* is calculated as follows

$$\delta = \begin{cases} \left[2m + (1 - 2m)(1 - \alpha)^{\lambda+1}\right]^{\frac{1}{\lambda+1}} - 1 & \text{if } m \leq 0.5 \\[2ex] 1 - \left[2(1 - m) + 2(m - 0.5)(1 - \alpha)^{\lambda+1}\right]^{\frac{1}{\lambda+1}} & \text{otherwise} \end{cases} \tag{5.9}$$

where,

$$\alpha = \frac{\min\left[(p - p^{(l)}), (p^{(u)} - p)\right]}{(p^{(u)} - p^{(l)})} \tag{5.10}$$

The term *λ* is the mutation distribution index and has positive value.

(c) The mutated child is calculated as

$$c = p + \delta \Delta_{max} \tag{5.11}$$

where, Δ_{max} is the maximum perturbation allowed in the parent solution. By using $\Delta_{max} = p^{(u)} - p^{(l)}$, the normalised perturbation can be calculated as

$$\frac{(c-p)}{p^u - p^l} \tag{5.12}$$

Thus, to obtain the mutation effect of 1%, perturbation λ has been taken as 100.

5.3.2 Genetic algorithm approach for optimal output power of nonlinear nonprismatic axially FG beam under mechanical loading

For a nonprismatic nonlinear axially FG beam under mechanical loading the objective function can be written similar to equation (5.1).Therefore the objective function can be written as

$$Maximize\ P_2 = \left[\frac{z_1\varphi}{2\left(1 + \dfrac{z_2 R}{t_p}\right)}\right]^2 R$$

$$subjected\ to\ (\sigma_{induced})_{beam} < (\sigma_{allowable})_{beam}, (\sigma_{induced})_{PZT} < (\sigma_{allowable})_{PZT}\ and \tag{5.13}$$

$$(V_{induced})_{PZT} < (V_{allowable})_{PZT}$$

where, $z_1 = bh\omega e_{31}$ and $z_2 = bL_p\omega\xi_{33}$.
$$\varphi = \varphi(L_p) - \varphi(0)$$

The used symbols have their usual meanings. The fitness function for this problem is derived as:

$$G(u) = \begin{cases} P_2(u) & if\ (\sigma_{induced})_{beam} < (\sigma_{allowable})_{beam}\ ;\ (\sigma_{induced})_{PZT} < (\sigma_{allowable})_{PZT}\ ; \\ & \&\ (V_{induced})_{PZT} < (V_{allowable})_{PZT} \\ P_2(u)\alpha & otherwise \end{cases} \tag{5.14}$$

where, G is the fitness function, u is the optimization parameters vector and P_2 is the power harvested from the nonlinear nonprismatic axially FG beam. The term α represents the penalty for this algorithm taken as 10^{-8} and which is used in case of constrained violation. The algorithm is sustained for some generations until the fitness reaches the optimum value and there is also no change in fitness for a large number of generations. In the present work, the real coded genetic algorithm consists of the Roulette wheel

selection, simulated binary crossover (SBX) and parameter based mutation operators, are similarly used.

Chapter 6

Thermo-Electro-Mechanical Responses of Non-prismatic Axially FG Beam Structures

This chapter initially presents the validation of the developed computer code in MATLAB platform which is capable of finite element analysis of non-prismatic axially FG beam subjected to thermo-electro-mechanical loading. After validation of the developed MATLAB code various coupled thermo-electro-mechanical responses of the modelled structures have been analysed under thermal loading.

6.1 Validation of the present formulation

Based on the finite element formulations discussed in chapter 3, a finite element code has been developed for thermo-electro-mechanical analysis of non-prismatic axially FG piezolaminated beam for three different profile cross-sections (linear, parabolic and cubic profiles). Further, a code has been developed for optimal harvesting of power from the mathematical formulations described in chapter 5 for the said profile cross-sections. These two codes integration leads to design and analysis of non-prismatic axially FG piezolaminated beam for optimal harvesting of power.

6.1.1   Structural validation

To verify the present developed code, the static and free vibration analyses have been carried out for both prismatic and non-prismatic homogeneous beams. The results have been presented in the following subsections.

6.1.1.1 Prismatic homogeneous beam

The present developed code is validated by considering a homogeneous cantilever
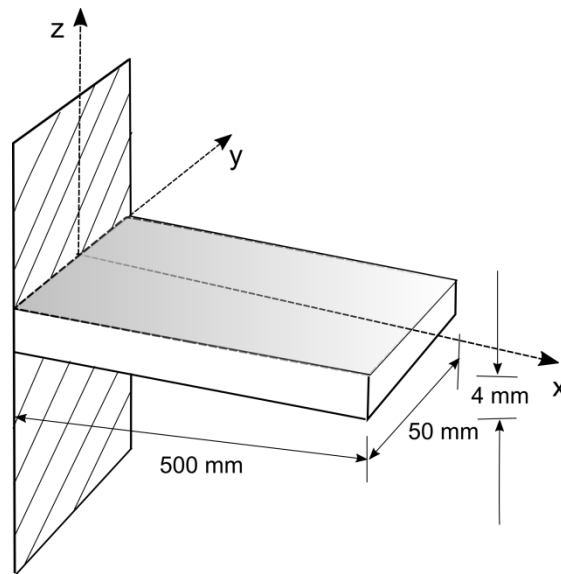
Figure 6.1 Schematic view of a rectangular homogeneous beam

beam rectangular cross section as shown in Figure 6.1. The dimensions of the beam are (500×50×4) mm. Material properties are taken as: Modulus of elasticity (*E*) = 210 GPA, material density (*ρ*) = 7850 kg/m³ and Poisson's ratio (*μ*) = 0.3. The beam is divided into several numbers of equal finite elements. The convergence results of the beam are presented in Table 6.1.

Table 6.1 Convergence result of natural frequencies of cantilever beam

Natural frequency (rad/sec)	Present code (n=6)	Present code (n=8)	Present code (n=10)	Present code (n=12)
ω_1	85.10	84.76	84.26	84.26
ω_2	528.95	528.58	528.07	528.07
ω_3	1479.12	1478.89	1478.62	1478.62
ω_4	2898.76	2898.22	2897.51	2897.51

where, *n* is the number of finite elements. Table 6.1 reveals that for 10 finite numbers of elements the natural frequencies are converged. Hence, for further analysis the number of beam elements has been taken as 10. Further, the exact solution for first four natural frequencies with Euler-Bernoulli beam assumptions has been found out as [140]

$$\omega = \left(\beta L_b\right)^2 \sqrt{\frac{EI}{\rho A L_b^4}} \qquad (6.1)$$

where, *EI*=Flexural rigidity, *ρA*=Mass per unit length, L_b=length of the beam and the values of 'βL_b' for first four natural frequencies are 1.875, 4.694, 7.854 and 10.995

respectively. The first four natural frequencies are calculated by using the developed code and compared with the results obtained using equation (6.1) shown in Table 6.2.

Table 6.2 Comparison of first four natural frequencies of homogeneous cantilever beam

Natural frequency(rad/sec)	Present code	Exact [140]	% of error
ω_1	84.26	84.3	0.047
ω_2	528.07	528.36	0.054
ω_3	1478.62	1479.21	0.039
ω_4	2897.51	2896.3	0.041

From the above table a comparable result can be seen using the developed code.

6.1.1.2 Non-prismatic homogeneous beam

In this section a non-prismatic (taper (*c*) =0.0, 0.2) homogeneous cantilever beam of rectangular cross section is considered for structural validation of present formulation as shown in Figure 6.2.
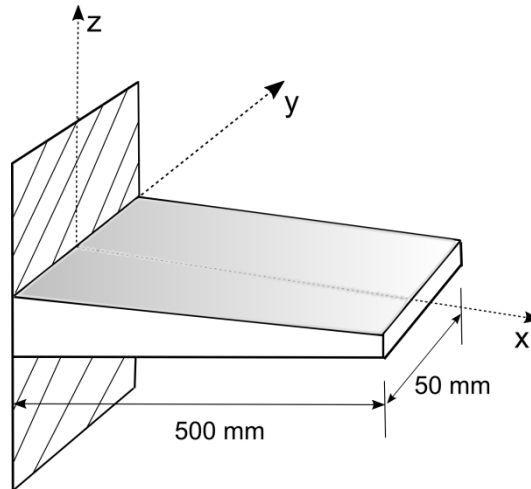
Figure 6.2 A homogeneous nonprismatic (*c*=0.0, 0.2) cantilever beam.

The first four non-dimensional fundamental frequencies are calculated by using the current developed computer code and compared with the existing results as listed in Table 6.3. The present results are corroborated with the existing one as obtained [93]. In order to facilitate the presentation of results, the nondimensional fundamental frequency can be introduced as

$$\overline{\omega} = \omega \sqrt{\frac{\rho_0 A_0 L_b^4}{E_0 I_0}} \tag{6.2}$$

The subscript 0 designates the value of parameters at the fixed end of the beam.

Table 6.3 Nondimensional natural frequencies of a nonprismatic homogeneous cantilever beam

Mode	Shahba, et al. [93]			present code		
	No of elements			No of elements		
	20	25	30	20	25	30
c=0.0						
ϖ_1	3.22	3.22	3.22	3.17	3.18	3.19
ϖ_2	14.47	14.47	14.47	14.34	14.34	14.35
ϖ_3	31.56	31.54	31.5	31.44	31.38	31.34
ϖ_4	48.09	48.03	47.91	48.13	47.92	47.8
c=0.2						
ϖ_1	3.33	3.33	3.33	3.18	3.19	3.19
ϖ_2	14.29	14.29	14.29	14.37	14.36	14.36
ϖ_3	30.79	30.76	30.74	31.49	31.41	31.37
ϖ_4	48.05	47.94	47.88	48.17	47.94	47.82

Table 6.3, shows that the present results are in good agreement with the available existing results.

6.1.2   Electromechanical validation
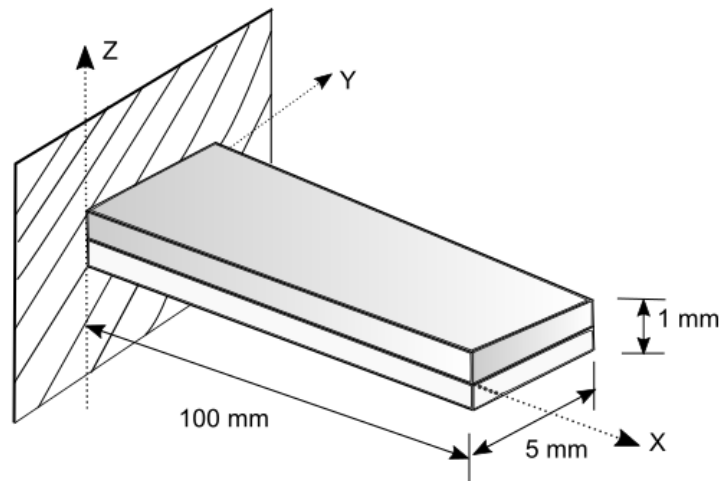
Figure 6.3 Schematic view of a bimorph beam

To verify the accuracy of present coupled electro-mechanical code, the results obtained have been validated with the existing published results [141]. For this case a bimorph cantilever beam (shown in Figure 6.3) made up of two PVDF layers has been considered. The material properties used has been shown in Table 6.4.

Table 6.4 Material properties of the bimorph beam

Properties	PZT
ρ (kg/m^3)	1800
E (Gpa)	2
e_{31} (C/m^2)	0.0462
ε_{33} (nF)	0.1062

The bimorph beam is exposed to an external voltage. The internal stresses induced causes a bending moment which powers the bimorph beam to bend. The dimensions of the beam are (100×5×1) mm. The bimorph beam is discretized into five finite elements. Table 6.5 shows that the results obtained using the present code are in good agreement with those available in published literature [141].

Table 6.5 Transverse deflection of piezoelectric bimorph actuator

Distance(mm)from fixed end	Deflection(μm) Hwang and Park [141]	Deflection(μm) present code	% of error
20	0.0131	0.0139	5.75
40	0.0545	0.0554	1.62
60	0.1200	0.1247	3.76
80	0.2180	0.2218	1.71
100	0.3400	0.3465	2.74

The percentage of errors between the present and existing results is less.

6.1.3   Validation of Piezothermoelastic behavior of a piezolaminated beam

The piezothermoelastic behavior of a cantilever piezolaminated graphite/epoxy beam is studied and compared with presently developed code. The piezolaminated model considered (Figure 6.4, L=0.5 m, t_b=0.01 m, b=0.01 m, and t_p=0.001 m) is a graphite/epoxy beam sandwiched between two PZT layers is shown in Figure 6.4. The material properties of the structure have been listed in Table 6.6 [106].
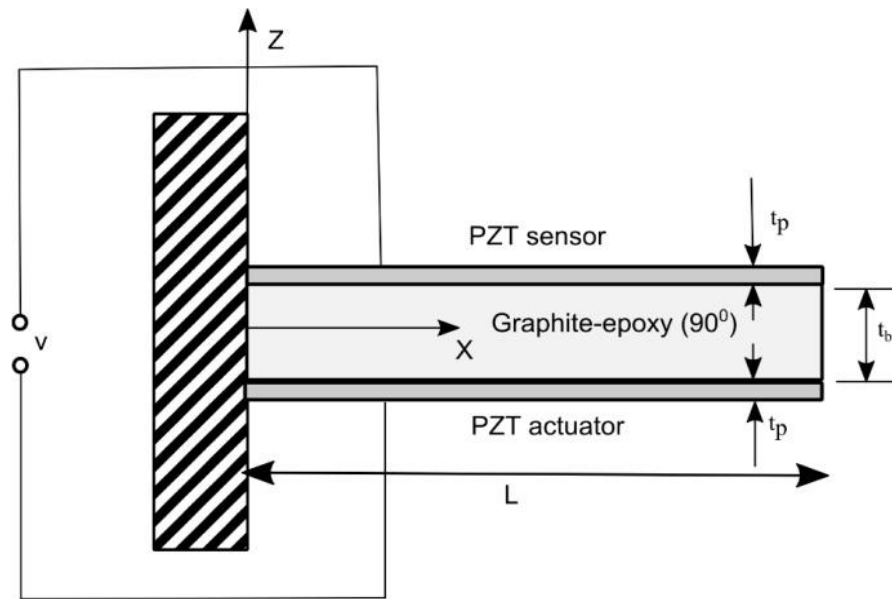
Figure 6.4 Piezolaminated cantilever composite beam

Table 6.6 Material Properties of Graphite-epoxy and PZT

Properties	PZT	Graphite-epoxy
E (GPa)	60	180
υ	0.33	0.33
G(GPa)	22.5	8
α	0.012×10^{-4}	2.4×10^{-8}
ε_{33} (nFm^{-1})	15	-
d_{31}(CN^{-1})	-17.5×10^{-11}	-
p_3 (CK^{-1}m^{-2})	-2.5×10^{-5}	-
ρ (Kg/m^3)	7750	1600

For analysis and validation, the piezothermoelastic effect of the sensor due to thermal excitation and the deflection due to the thermal gradient is taken into account. First of all the beam with PZT patch is placed in a temperature field, and then the beam temperature reaches quickly to a steady state. The PZT layer is assumed with a single electrode at its surface. By using equation (3.63), it can be observed that the variation of temperature can induce a voltage in the PZT sensor which is termed as the pyroelectric effect. Apart

from this, the thermally induced deformation can also induce a signal. This piezothermoelastic effect (i.e. both pyroelectric and thermal strain effect) has been studied and the validated results are shown in Figure 6.5 and Figure 6.6.
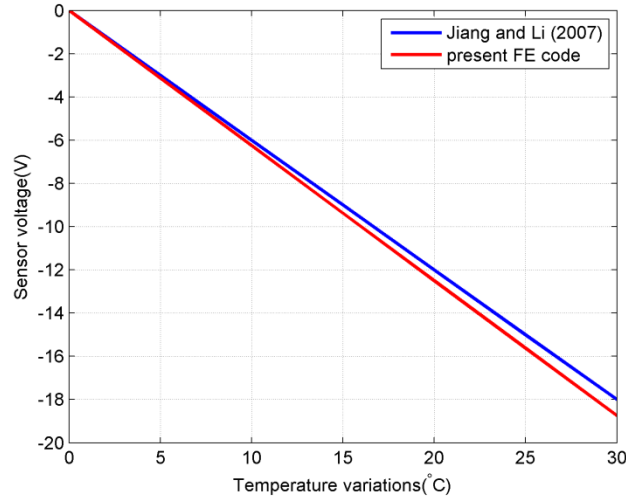
Figure 6.5 Sensor voltage generated due to pyroelectric effect
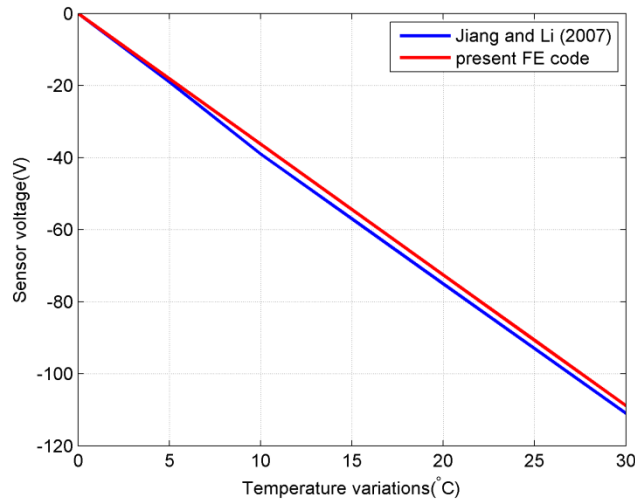
Figure 6.6 Sensor voltage generated due to thermal strain effect.

Next, thermally induced deflection of the piezolaminated beam has been studied. A temperature gradient has been applied such that the temperature of the bottom surface is higher than the top surface of the piezolaminated beam. Owing to the temperature gradient the centre line of the beam deflects upward. Figure 6.7 shows the validated results for deflection of centre line of the beam subjected to 5, 10, 20 and 50^0C temperature gradient [106].
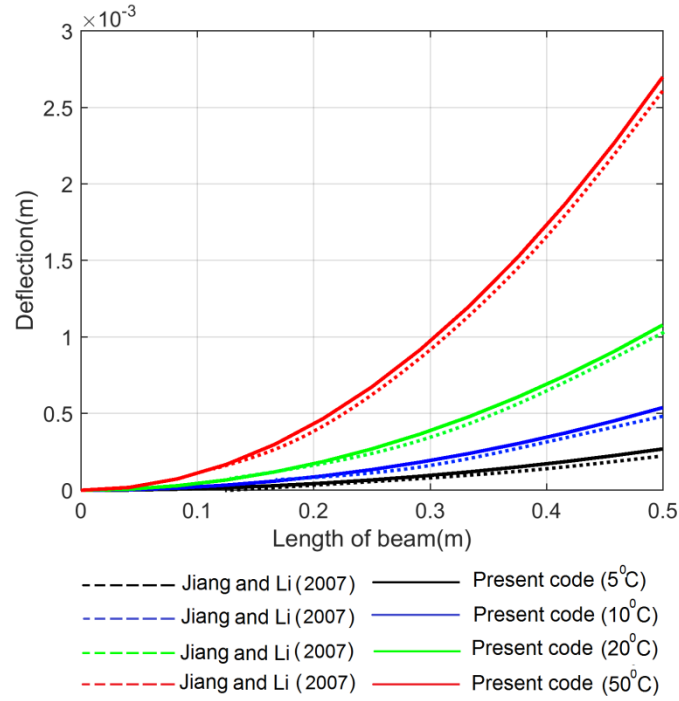
Figure 6.7 Comparison of deflection due to thermal gradient for 5, 10, 20,50^{0}C

In the case of thermal loading, the temperature at the top surface has been taken as 100^{0}C and the bottom surface temperature as 0^{0}C.

6.1.4   Experimental validation of the present formulation
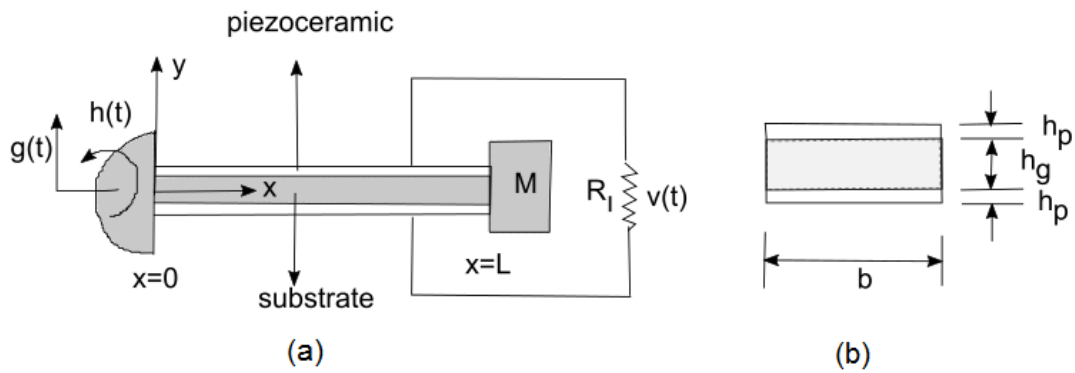
Figure 6.8 Bimorph cantilever configuration(a) with piezoceramic layers (b) cross sectional view

The present formulation of the harvester is validated with the available experimental results [36]. For this type of validation, a rectangular cantilever bimorph energy harvester

with a tip mass under base excitation is considered as shown in Figure 6.8. Figure 6.9 (a-b) show the computed results of the voltage and current frequency response function (FRF) using the present formulation. Figure 6.9 (a-b) show that the present results are in close agreement with the previously published experimental results [36].
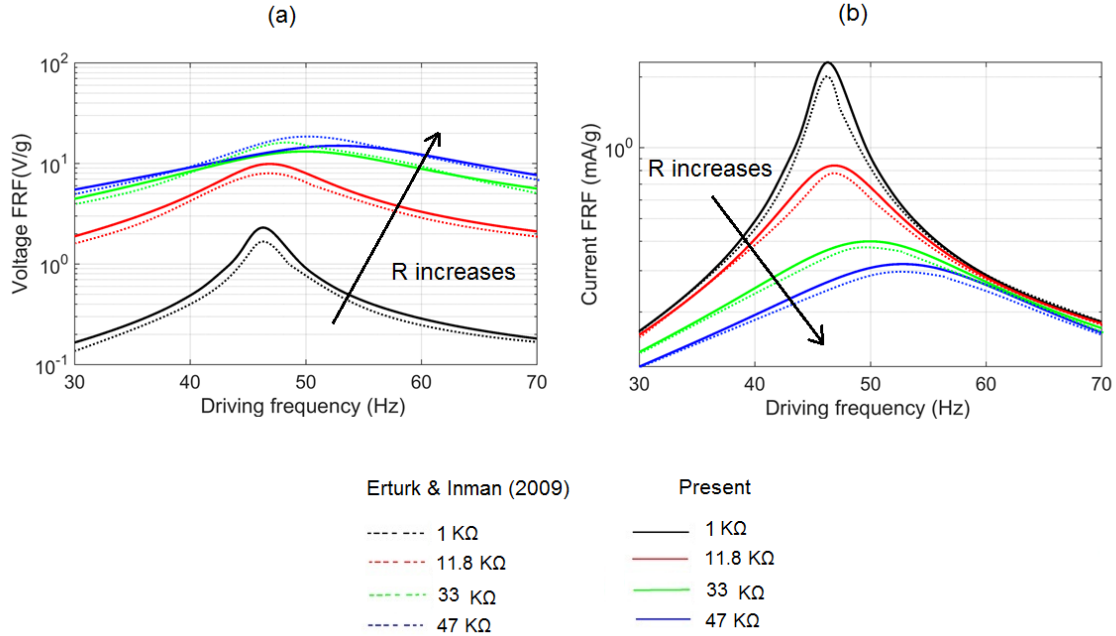
Figure 6.9 Comparison of voltage FRF for load resistances 1, 11.8 and 33 kΩ.

6.2 Responses of prismatic and nonprismatic homogeneous beam

Three cases of piezolaminated cantilever beam under the simultaneous action of an impulse load at the free end and thermal load has been analysed to study the output responses such as displacement, voltage, and power

The cross-sectional dimensions of the beam near the clamped end has been taken as b_0 = 0.05 m and t_0 = 0.004 m. The piezoelectric patch with a length (L_p) 0.05 m and thickness (t_p) 0.0005 mm has been attached near the clamped end of the beam of length 0.5m as shown in Figure 6.10. The piezolaminated beam has been subjected to an impulse load of 1N at the free end for duration of 4 s. In the case of thermal loading, the temperature at the top surface has been taken as 100^0C and the bottom surface

temperature as 0^0C. Based on the methodology discussed in chapter 4, various responses for all the proposed modelled beams have been illustrated in the subsequent sections.
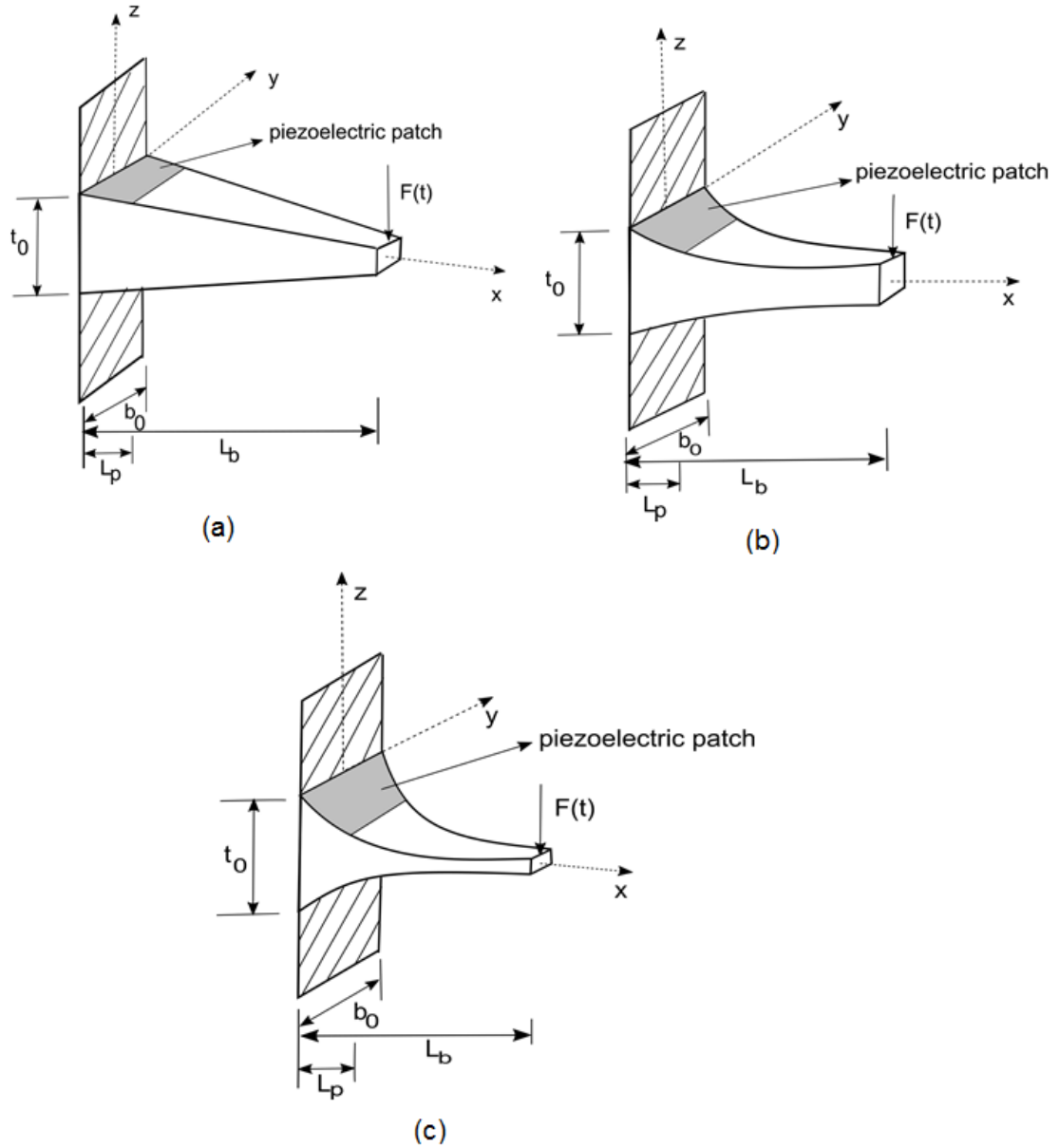
Figure 6.10 Modelled profile beams (a) Linear (b) parabolic (c) Cubic with piezoelectric patch.

The mechanical, electrical and thermal properties used in the present study for all cases have been listed in Table 6.7.

Table 6.7 Material properties of beam and PZT

Properties	Steel beam	PZT
E_0(GPa)	210	0.0606
μ_0	0.3	0.3
G_0(Gpa)	80.7	0.0234
ρ_0(Kg m^{-3})	7850	7500
e_{31}(C m^{-2})	-	16.6
ε_{33}(nFm^{-1})	-	25.55
α(^{0}C^{-1})	2.4×10^{-8}	3×10^{-6}
p_3(CK^{-1}m^{-2})	-	-23×10^{-4}

This section depicts the frequency and time domain analysis of tip displacement, frequency, output voltage and output power responses of homogeneous prismatic and three cases of modelled non-prismatic beams (Case (A), Case (B) and Case (C)). This comparison helps in predicting for enhancement of output power of the proposed modelled beams.

6.2.1   Frequency domain analysis

In frequency domain analysis the frequency, output voltage and power responses of the homogeneous prismatic and modelled non-prismatic beams (such as Case (A), Case (B) and Case (C)) are compared in the subsequent sections.

6.2.1.1 Frequency responses

The amplitude of motion is the most important parameter for energy harvesting from vibration analysis. From the mathematical formulation for energy harvesting described in equation (3.73), it is observed that the output power of a piezolaminated beam is directly related to the slope of the beam. Beams undergoing large deflection could produce more slopes, and hence, more power will be generated. A comparison has been carried out for frequency responses for homogeneous prismatic and homogeneous non-prismatic modelled beams for three different cross section profiles (Cases (A), (B) and (C)) shown in Figure 6.11 (a-d) with arbitrary taper values 0.1 and 0.3.
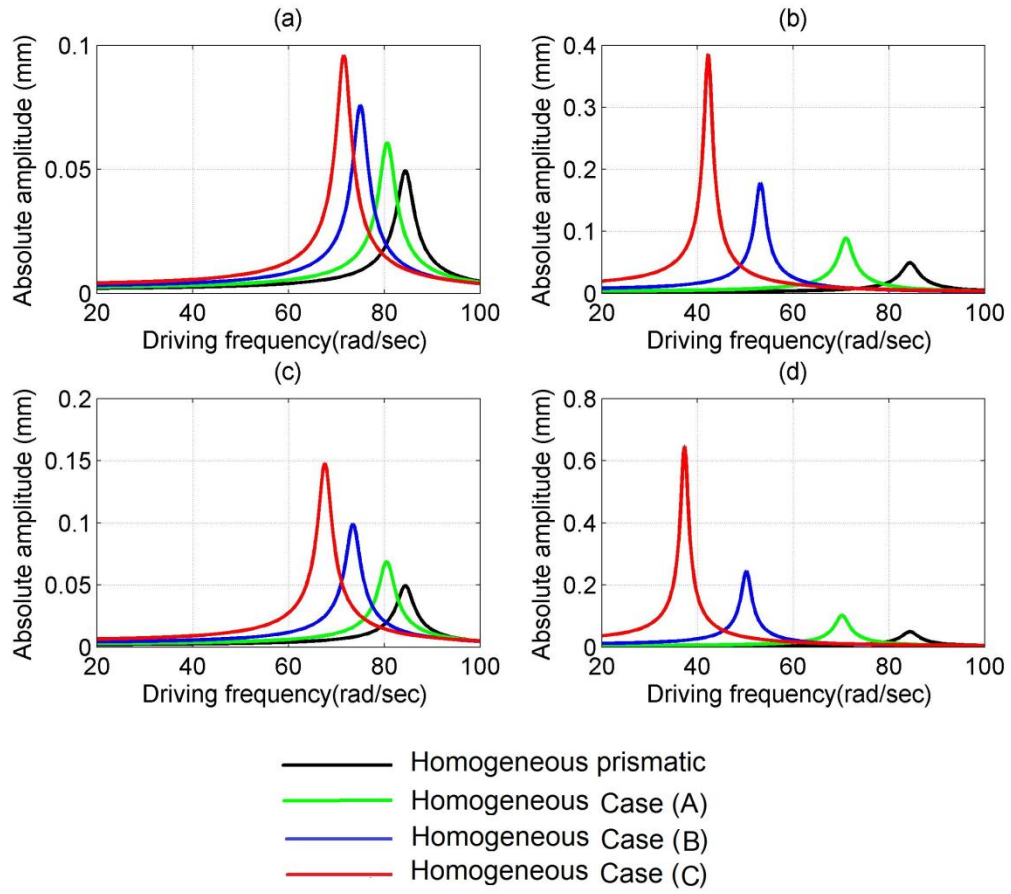
Figure 6.11 Frequency responses of homogeneous prismatic beam (c_b=0.0, c_h=0.0) and nonprismatic beam for (a) c_b=0.1, c_h=0.1 (b) c_b=0.1, c_h=0.3 (c) c_b=0.3, c_h=0.1 and (d) c_b=0.3, c_h=0.3

The modelled beam is subjected to a sinusoidal excitation at the free end. From Figure 6.11 (a-d), it can be observed that the amplitude ratios for homogeneous non-prismatic beams are more compared to homogeneous prismatic beam for all value of tapers. Further, the amplitude ratio of homogeneous Case (C) is more compared to homogeneous Case (A) and (B) for all cases of tapers.

6.2.1.2 Voltage responses
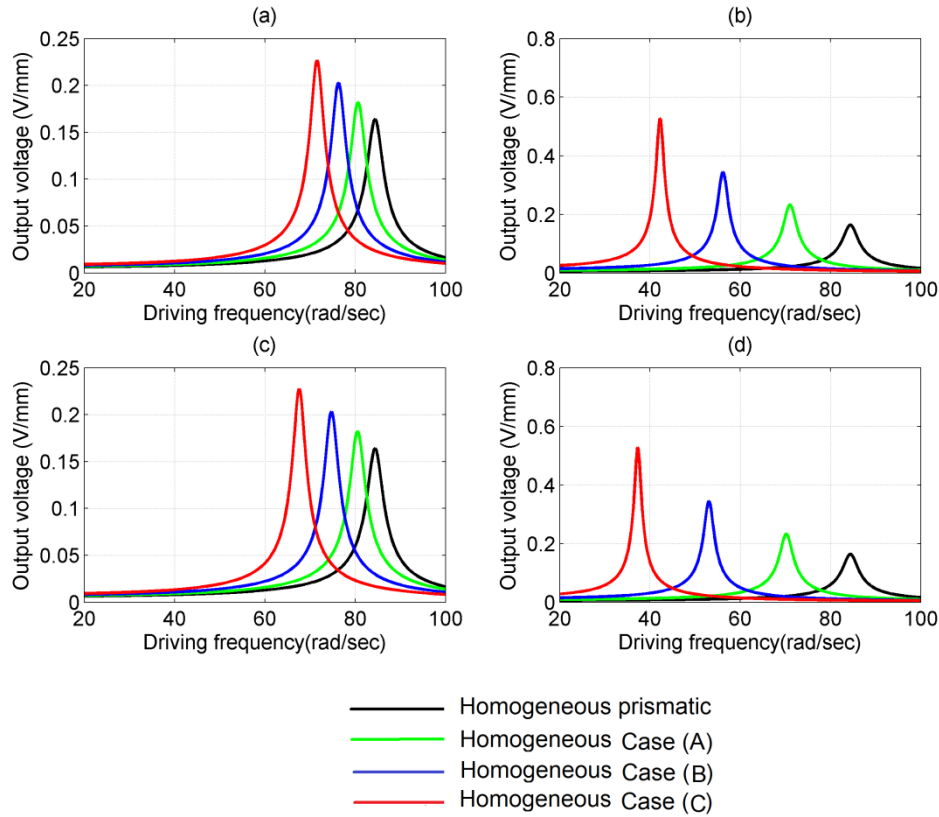
Figure 6.12 Voltage responses of homogeneous prismatic beam (c_b=0.0, c_h=0.0) and nonprismatic beam for (a) c_b=0.1, c_h=0.1 (b) c_b=0.1, c_h=0.3 (c) c_b=0.3, c_h=0.1 and (d) c_b=0.3, c_h=0.3

Voltage is generated in the piezoelectric patch due to vibration of the beam. This generated voltage is responsible for current flow through the electric circuit power generation. Again the amplitude of generated voltage depends on cross section profile of the beam. This section provides a comparative study of voltage responses of homogeneous prismatic beam and homogeneous nonprismatic modelled beams (Cases (A), (B) and (C)). The piezoelectric patch is attached at the clamped end of the beam where it experiences a maximum value of strain. As the beam vibrates due to the external sinusoidal excitation at the free end, the charge gets accumulated over the surface of the piezoelectric patch from which the voltage can be calculated. Figure 6.12 (a-d) represent the voltage responses for vibration of the beam excited in first vibration mode with arbitrary taper values of 0.1 and 0.3 respectively. From the Figure 6.12 (a-d), it has been observed from the results that more voltage can be obtained for homogeneous nonprismatic beams (Cases (A), (B) and (C)) compared to homogeneous prismatic beam

for different values of taper. Further, the voltage amplitude of homogeneous Case (C) beam is more compared to homogeneous Case (A) and (B) for all values of tapers.

6.2.1.3 Output power responses
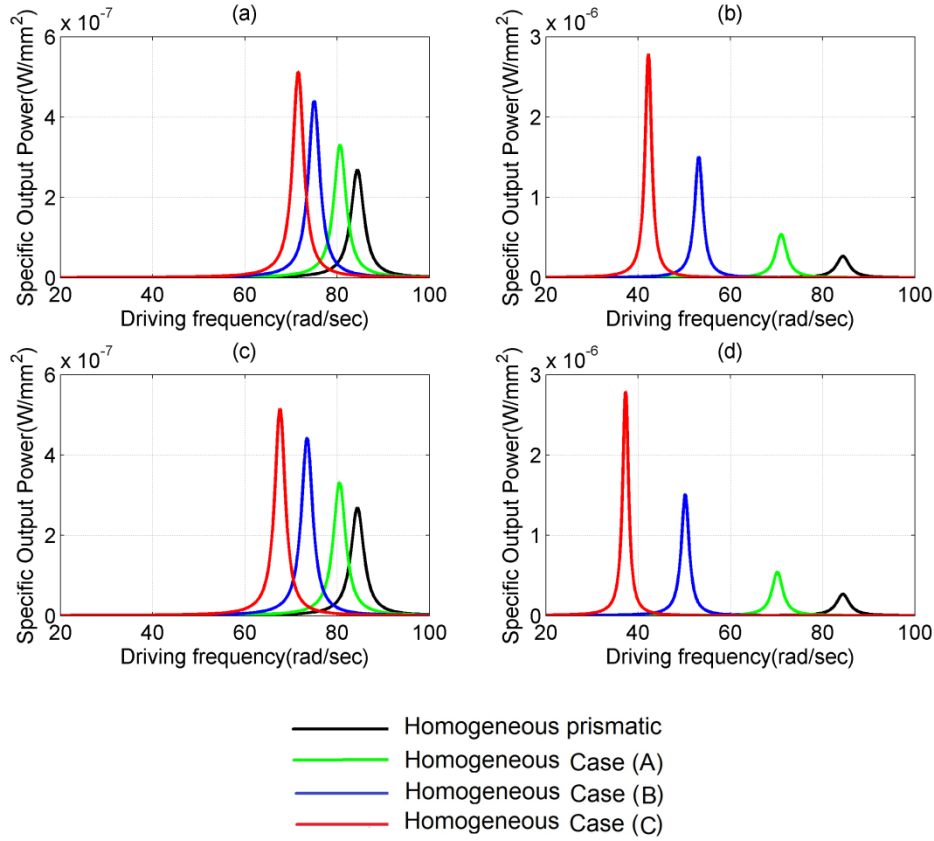
Figure 6.13 Variation of specific output power with driving frequency of homogeneous prismatic beam (c_b=0.0, c_h=0.0) and nonprismatic beam for (a) c_b=0.1, c_h=0.1 (b) c_b=0.1, c_h=0.3 (c) c_b=0.3, c_h=0.1 and (d) c_b=0.3, c_h=0.3

The specific output power frequency response function (FRF) of Cases (A), (B) and (C) subjected to a sinusoidal excitation at the free end are shown in Figure 6.13 (a-d) with different values of c_b and c_h (0.1 and 0.3). From Figure 6.13 (a -b), it is observed that homogeneous non-prismatic beam (Cases (A), (B) and (C)) generates more than 20%, 60% and 90% of specific output power for taper values of c_b = 0.1 and c_h = 0.1 compared to the homogeneous prismatic beam, respectively. Further, Case (B) and Case (C) generate 30% and 50% more specific output power compared to Case (A), whereas Case (C) generates more than 15% of output power compared to Case (B) for the same

values of tapers. However, the increase in percentage is 100%, 400% and 800% more in Cases (A), (B) and (C) with increase in c_h to 0.3 compared to homogeneous prismatic beam. Further, no commendable variation in specific output power is ascertained in Cases (A), (B) and (C) for further variation of c_b and c_h as shown in Figure 6.13 (c-d). It is also observed that with increase in c_h in all cases of non-prismatic beams 90% more specific output power can be generated compared to increase in c_b. Further, for a given variation in c_h, Case (C) generates 80% and 60% more specific output power compared to Cases (A) and (B), respectively.
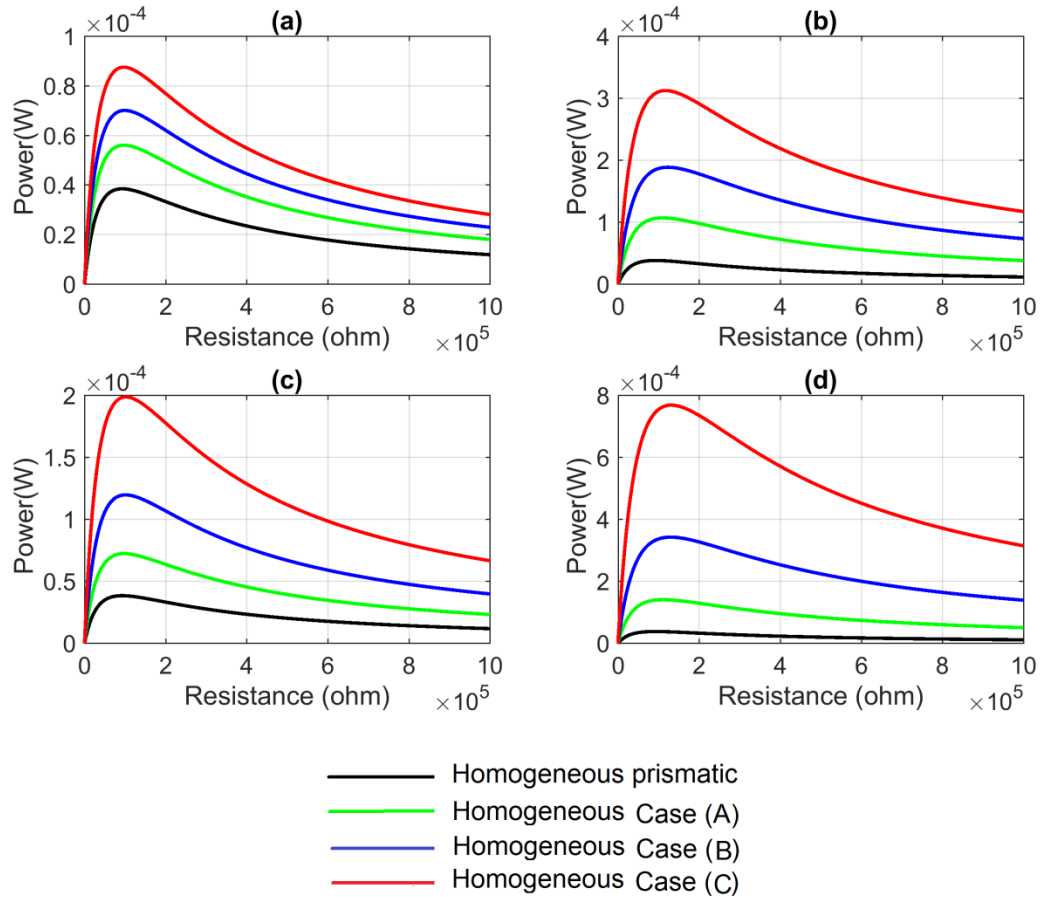
Figure 6.14 Variation of output power with external load resistance of homogeneous prismatic beam (c_b=0.0, c_h=0.0) and homogeneous nonprismatic beam for (a) c_b=0.1, c_h=0.1 (a) c_b=0.1, c_h=0.3 (a) c_b=0.3, c_h=0.1 and (a) c_b=0.3, c_h=0.3

Further, the output power from the piezolaminated beam has been found by assuming the beam to be excited at the first fundamental frequency. The electrical circuit which is connected to the top and bottom surface of the piezoelectric patch is modelled by an equivalent resistance *R*. As the beam vibrates, voltage is generated across the

piezoelectric material which is responsible for the flow of current in the circuit. This current when flows through the load resistance power is generated. Apart from the frequency and amplitude of vibration, the output power generated also depends on load resistance. The effect of load resistance on output power is discussed by comparing homogeneous prismatic beam and homogeneous non-prismatic beams (Cases (A), (B) and (C)). The variables of the system are functions of external resistance which gives maximum output power. According to the application, the requirement of resistance is determined, and the variables of the system can be designed to reach maximum power. Figure 6.14 (a-d) show the variation of output power with external load resistance for homogeneous prismatic beam and homogeneous non-prismatic beams (such as Cases (A), (B) and (C)). From Figure 6.14 (a) and (b), it is observed that the output power for Case (C) is 0.087 mW, and that of Case (B) and (A) the values are 0.07 mW and 0.056 mW for taper values of c_b = 0.1 and c_h = 0.1. The optimum resistance for Case (C) is 96.767 kΩ, for Case (B) and Case (A) the optimum resistances are 99.038 kΩ and 97.060 kΩ respectively. When the height taper increases to 0.3 the power increases to 0.312 mW with optimum resistance of 117.275 kΩ in Case (C). For Case (B) the output power is 0.188 mW with optimum resistance of 123.056 kΩ and for Case (A) the output power is 0.107 mW with optimum resistance of 110.178 kΩ. It indicates with an increase in height taper the output power increases near about 258% in Case (C), whereas in Case (B) and Case (A) the output power increases near about 168% and 90%, respectively. Similarly, there is an increase in optimum resistance as the height taper increases. Again from Figure 6.14 (c) and (d) for taper values of c_b = 0.3 and c_h = 0.1, the output power for Case (C) is 0.198 mW with optimum resistance of 101.881 kΩ. For Case (B) the output power is 0.119 mW with optimum resistance 101.078 kΩ. Again for Case (A) the output power is 0.072 mW with optimum resistance of 97.190 kΩ. As the height taper increases to 0.3, the output power increases to 0.769 mW in Case(C) whereas in Case (B) and Case (A) the values are 0.343 mW and 0.141 mW, respectively. The optimum resistance for Case (C) is (131.097 kΩ) more than Case (B) (129.948 kΩ) and Case (A) (111.462 kΩ), respectively. The output power attains a maximum value for particular value of resistance. The output power attains a maximum value for particular value of resistance and beyond that the output power decreases with increase in resistance. Again the results of the analysis reveals that increase in c_h produces 40% more power as compared to increase in c_b.

6.2.2   Time domain analysis

In time domain analysis the tip displacement, output voltage and power responses of the homogeneous prismatic and modelled non-prismatic beams (such as Case (A), Case (B) and Case (C)) are compared for different taper values in the subsequent sections.

6.2.2.1 Tip displacement response

Figure 6.15 Tip displacement responses of homogeneous prismatic beam (c_b=0.0, c_h=0.0) and nonprismatic beam for (a) c_b=0.1, c_h=0.1 (b) c_b=0.1, c_h=0.3 (c) c_b=0.3, c_h=0.1 and (d) c_b=0.3, c_h=0.3

The tip displacement response in time domain of homogeneous prismatic (c_b=0.0, c_h=0.0) and non-prismatic beams (Case (A), Case (B) and Case (C)) with tapers 0.1 and 0.3 are presented in Figure 6.15 (a-d). The tip displacement has been simulated for a time period of 2 sec. In Figure 6.15(a-d), at t=0.05 sec the peak amplitude of homogeneous prismatic beam is around 0.453e-3 mm. As time progresses the tip displacement dies out substantially. For same time period it appears that peak amplitude

of homogeneous Case (A), (B) and (C) beams are 0.539e-3 mm, 0.644e-3 mm and 0.769e-3 mm for c_b=0.1 and c_h=0.1, respectively. When c_h increased to 0.3, the peak amplitude of Case (C) is 2.1 mm whereas for Case (A) and (B) the values are 0.71e-3 mm and 1.2e-3 mm. Similarly, the peak amplitude for Case (C) is 1.1e-3 mm, whereas the values for Case (A) and Case (B) are 0.608e-3 mm and 0.825e-3 mm, respectively. When c_b increases to 0.3, the peak amplitudes for Case (A), (B) and (C) are shifted to 0.805e-3 mm, 1.6e-3 mm and 3.2e-3 mm, respectively. From this analysis, it is observed that tip displacement shows a decreasing trend for all cases of tapers with increase in time. The peak amplitude of Case (C) is more compared to Case (A) and (B) for a given taper. Further, increase in c_h has predominant effect in the response than increase in c_b for the proposed nonprismatic beams.

6.2.2.2 Output voltage response
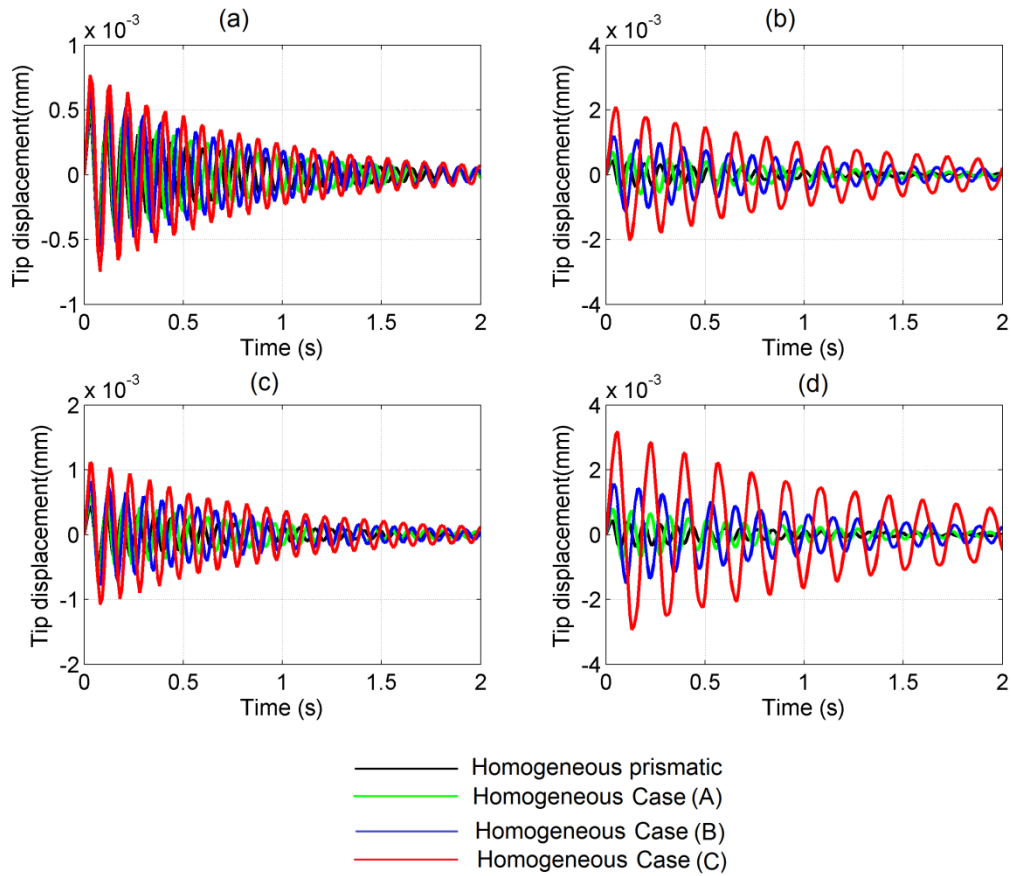

Figure 6.16 Output voltage responses of homogeneous prismatic beam (c_b=0.0, c_h=0.0) and nonprismatic beam for (a) c_b=0.1, c_h=0.1 (b) c_b=0.1, c_h=0.3 (c) c_b=0.3, c_h=0.1 and (d) c_b=0.3, c_h=0.3

The output voltage responses in time domain of homogeneous prismatic (c_b=0.0, c_h=0.0) and the proposed non-prismatic beams (Case (A), Case (B) and Case (C)) with arbitrarily taken tapers (0.1 and 0.3) are shown in Figure 6.16 (a-d). The output voltage has been simulated for a time period of 2 sec. As time progresses the amplitude of voltage dies out substantially. This might be due to the presence of internal damping along with the electrical circuit with external load resistance attached to the system. In Figure 6.16 (a), at t = 0.05 sec the peak amplitude of voltage for homogeneous prismatic beam is around 20.0067 V/m. For same time period it appears that peak voltage amplitude of homogeneous Case (A), (B) and (C) beams are 0.0215 V/mm, 0.0229 V/mm and 0.0281 V/mm for c_b=0.1 and c_h=0.1, respectively. When c_h increased to 0.3, the peak voltage amplitude of Case (C) is also increased to 0.0384 V/mm whereas for Case (A) and (B) the values are 0.0244 V/mm and 0.0288 V/mm as shown in Figure 6.16 (b). Similarly, when c_b increases to 0.3 the peak amplitude of Case (C) is 0.0228 V/mm, whereas the values for Case (A) and Case (B) are 0.0215 V/mm and 0.0225 V/mm, shown in Figure 6.16 (c). From Figure 6.16 (d) when c_b=0.3 and c_h=0.3, the peak amplitudes for Case (A), (B) and (C) are shifted to 0.0246 V/mm, 0.0297 V/mm and 0.394 V/mm, respectively. From this analysis, it is observed that peak voltage shows a decreasing trend for all cases of tapers with increase in time. For a given tapers, the peak voltage of Case (C) is more compared to Case (A) and (B) beams.
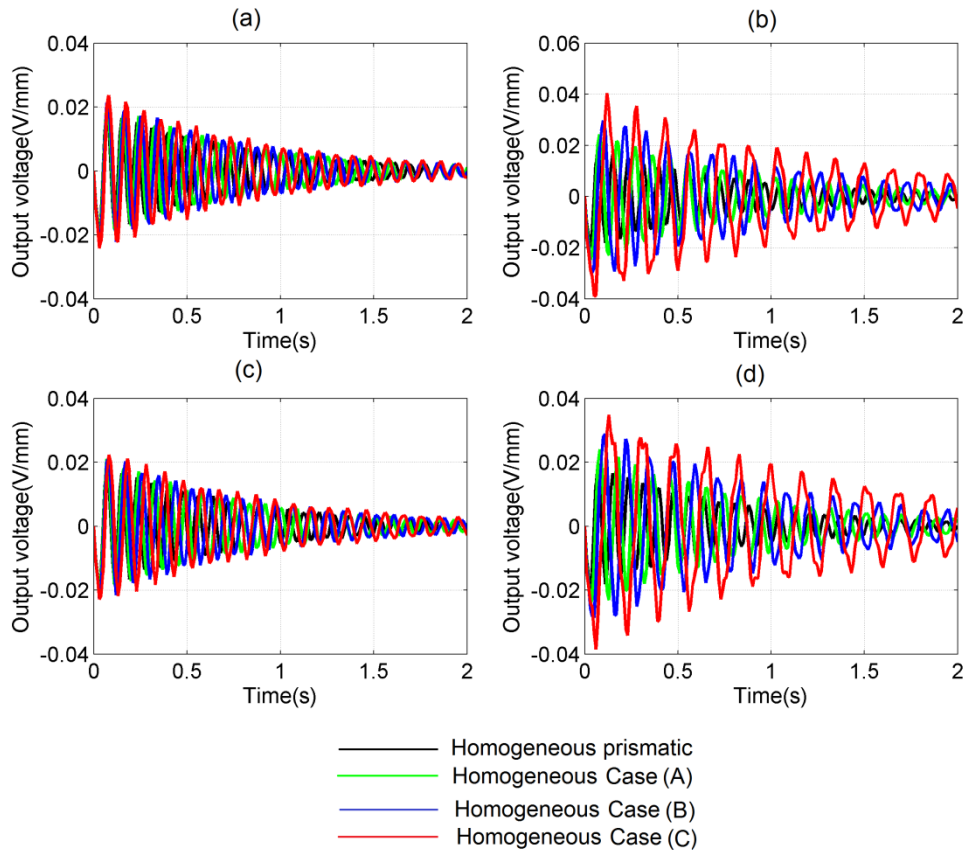
6.2.2.3 Output power response
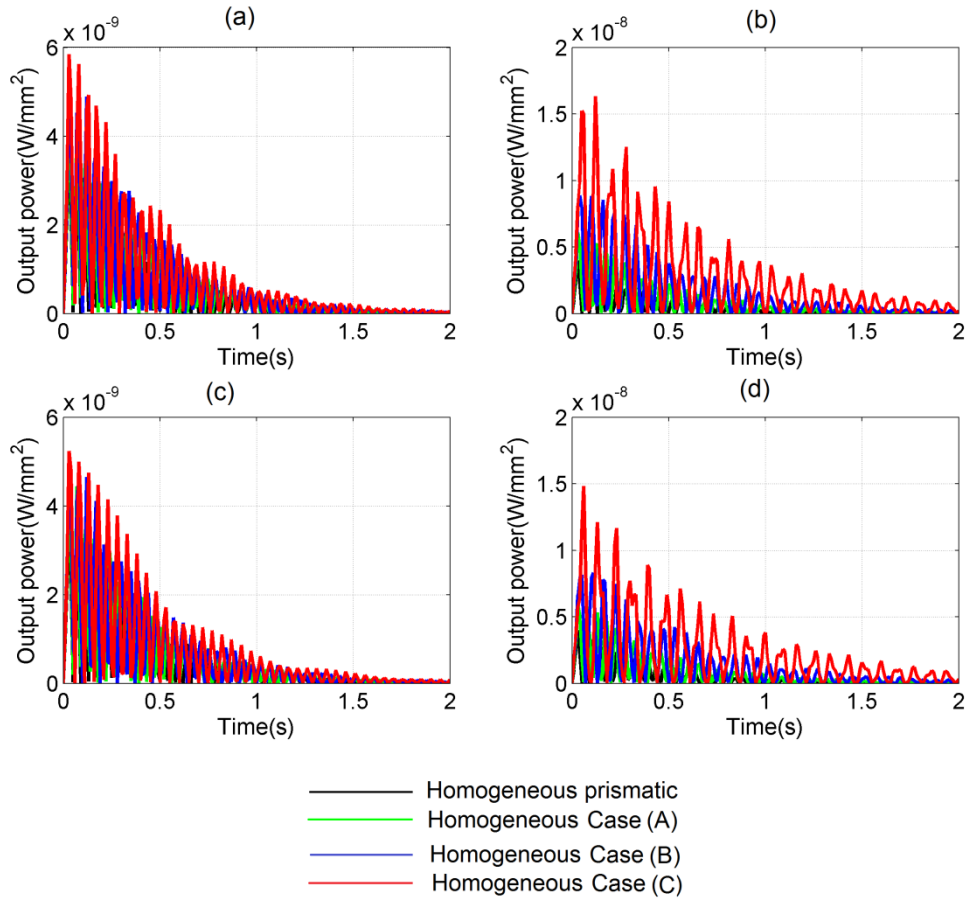
Figure 6.17 Output power responses of homogeneous prismatic beam (c_b=0.0, c_h=0.0) and nonprismatic beam for (a) c_b=0.1, c_h=0.1 (b) c_b=0.1, c_h=0.3 (c) c_b=0.3, c_h=0.1 and (d) c_b=0.3, c_h=0.3

The output power responses in time domain of homogeneous prismatic (c_b=0.0, c_h=0.0) and non-prismatic beams (Case (A), Case (B) and Case (C)) with tapers 0.1 and 0.3 are shown in Figure 6.17 (a-d). The output power has been simulated for a time period of 2 sec. As time progresses the output power dies out substantially. In Figure 6.17 (a), at t= 0.03 sec the peak output power for homogeneous prismatic beam is around 4 mW. For same time period it appears that peak output power of homogeneous Case (A), (B) and (C) beams are 4.6e-9 W/mm^2, 5.3 e-9 W/mm^2 and 5.8 e-9 W/mm^2 for c_b=0.1 and c_h=0.1, respectively. When c_h increased to 0.3, the peak output power of Case (C) is increased to 15.2 e-9 W/mm^2 whereas for Case (A) and (B) the values are 5.6 e-9 W/mm^2 and 8.3 e-9 W/mm^2, shown in Figure 6.17 (b). Similarly, when c_b increases to 0.3 the peak power for

Case (C) is 5.2 e-9 W/mm^2, whereas the values for Case (A) and Case (B) are 4.2 e-9 W/mm^2 and 5.1e-9 W/mm^2, shown in Figure 6.17 (c). From Figure 6.17 (d) when c_b=0.3 and c_h=0.3, the peak values for Case (A), (B) and (C) are shifted to 5.9 e-9 W/mm^2, 8.9 e-9 W/mm^2 and 14.9 e-9 W/mm^2, respectively. It reveals that peak output power shows a decreasing trend for all cases of tapers with increase in time. The peak output power of Case (C) is more compared to Case (A) and (B) for a given taper values. Further increase in c_h has predominant effect on output power over increase in c_b for all cases of proposed beams.

6.3 Variation of material properties

The variations of FG properties (such as density (ρ), Young's modulus (E), Poisson's ratio (υ) and coefficient of thermal expansion (α)) with temperature have been presented in Figure 6.18 (a-d) by using the equation (3.1). The various material properties used in the analysis are presented in the Table 6.8 [131].

Table 6.8 Material properties of the beam

Properties	Y_0	Y_{-1}	Y_1	Y_2	Y_3
ρ (Kg/m^3)	7850	0	0	0	0
E (N/m^2)	210e9	0	3.079e-4	-6.534e-7	0
Y	0.3	0	-2.002e-4	3.797e-7	0
α (/^{0}c)	12e-6	0	8.086e-4	0	0
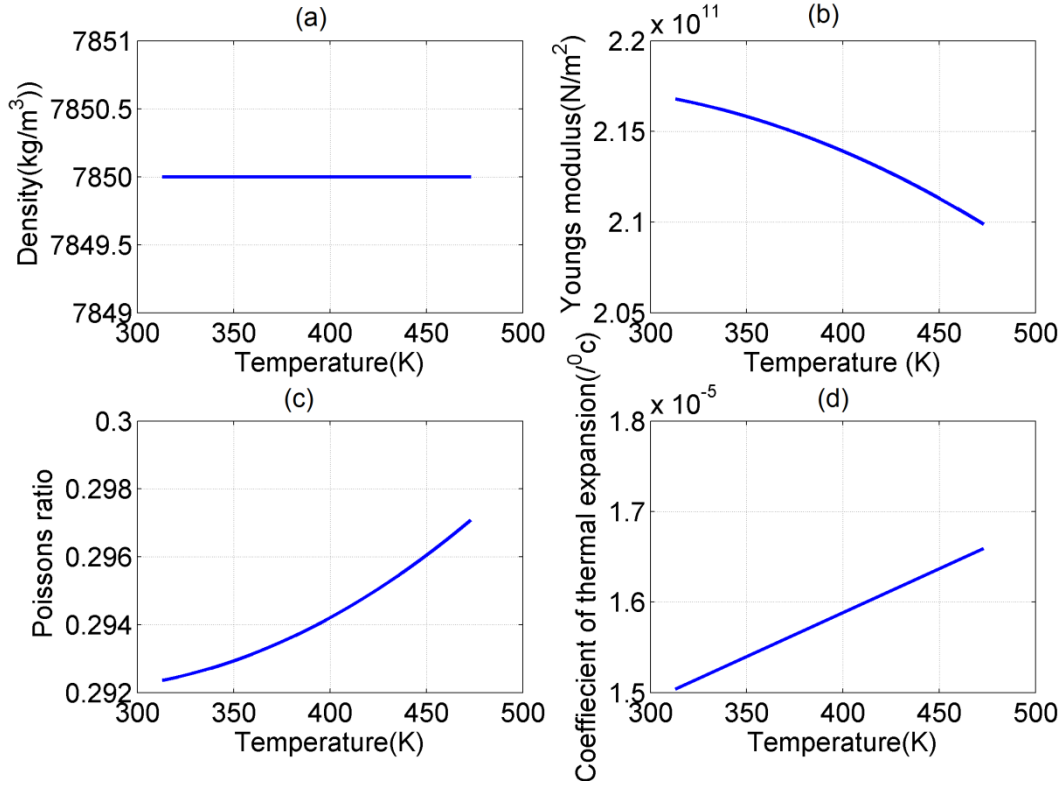
Figure 6.18 Variation of (a)Young's modulus (b) density (c) Poisson's ratio and (d) coefficient of thermal expansion with temperature.

From the Figure 6.18 (a-d), it is observed that with increase in temperature the density remains constant; Young's modulus of the beam decreases, Poisson's ratio increases and coefficient of thermal expansion also increases, respectively. The variations of FG properties in the axial direction are presented in Figure 6.19 (a-d) by using equation (3.1). The values of *np* have been arbitarily taken as 0, 0.5, 1, 5 and 10, and the values of *T and k* has been arbitrarily taken as $50^0 C$ and 2, respectively. From Figure 6.19 (a-d), it is observed that the FG properties of the beam continuously decrease towards the tip of the cantilever beam with an increase in *np*.
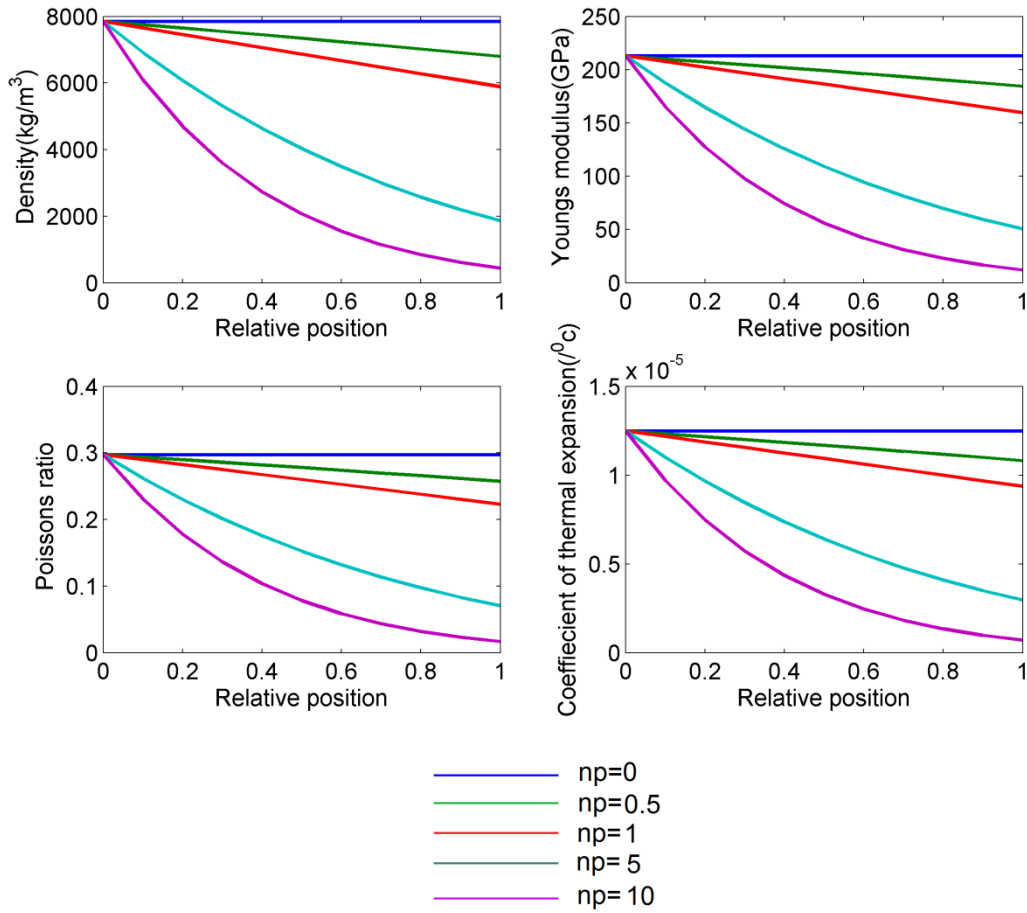
Figure 6.19 Variation of density, Young's modulus, Poisson's ratio and coefficient of thermal expansion of an axially FG beam with different power gradient index.

Again, it is obvious from the Figure 6.19 (a-d) that as the power gradient index increases (> 10); the material properties approach to zero. Therefore, for further analysis, the power gradient index is assumed to be less than or equal to 10.

6.4 Effect of tapers and axially FG properties on the harvested energy

In order to study the superimposing effects due to simultaneous variation of axially FG properties and axially varying cross-section of the beam, the prevailing effect has been analysed and presented in this section. For this case, arbitrarily varying parameters (c_b=0.1, c_h=0.1, np=2 and k=1) have been used to find the individual dominant effect of

109

axially FG properties and changes of cross section of the beam. Figure 6.20 (a-d) show the comparison of various responses (such as static deflection, frequency response, and output voltage and power responses) of axially FG and nonprismatic (Case (A), (B) and (C)) beam.
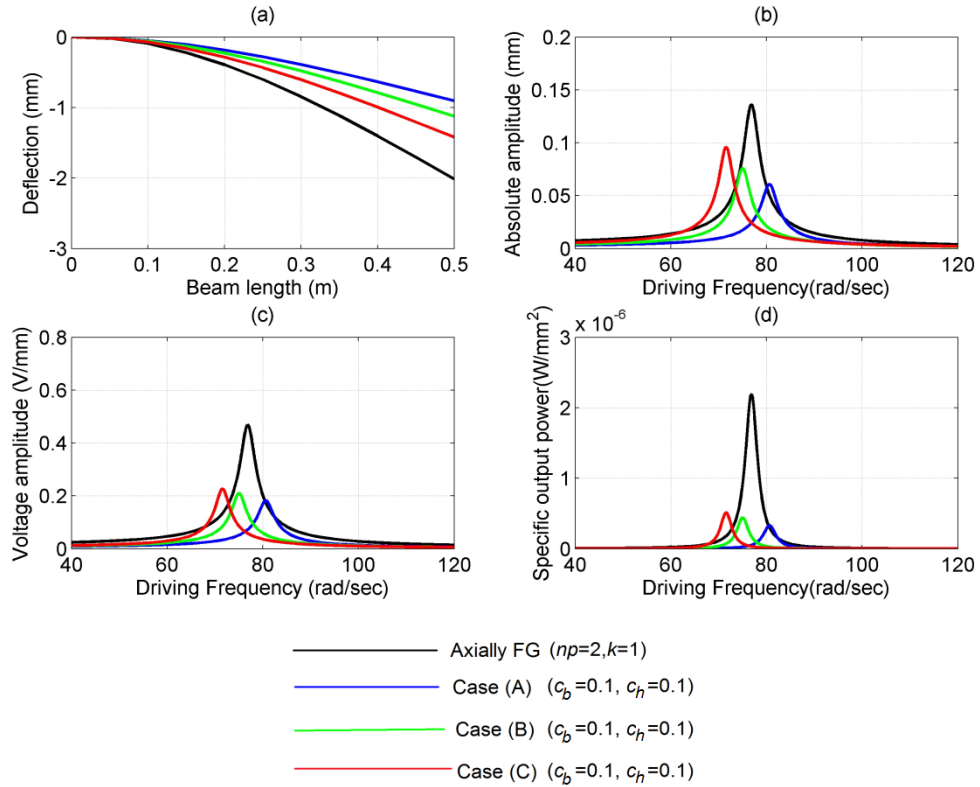
Figure 6.20 Effect of axially FG and nonprismatic beams on (a) static deflection (b) frequency (c) output voltage and (d) output power responses.

From Figure 6.20 (a-d), it is observed that the static deflection of axially FG beam is 30% more compared to the nonprismatic beam. It is also observed that the absolute amplitude, output voltage amplitude and specific output power of axially FG beam are 30%, 50% and 150% more than nonprismatic beam. Therefore it is perceived that, axially FG beam has more prevailing effect than that of nonprismatic piezolaminated beam.
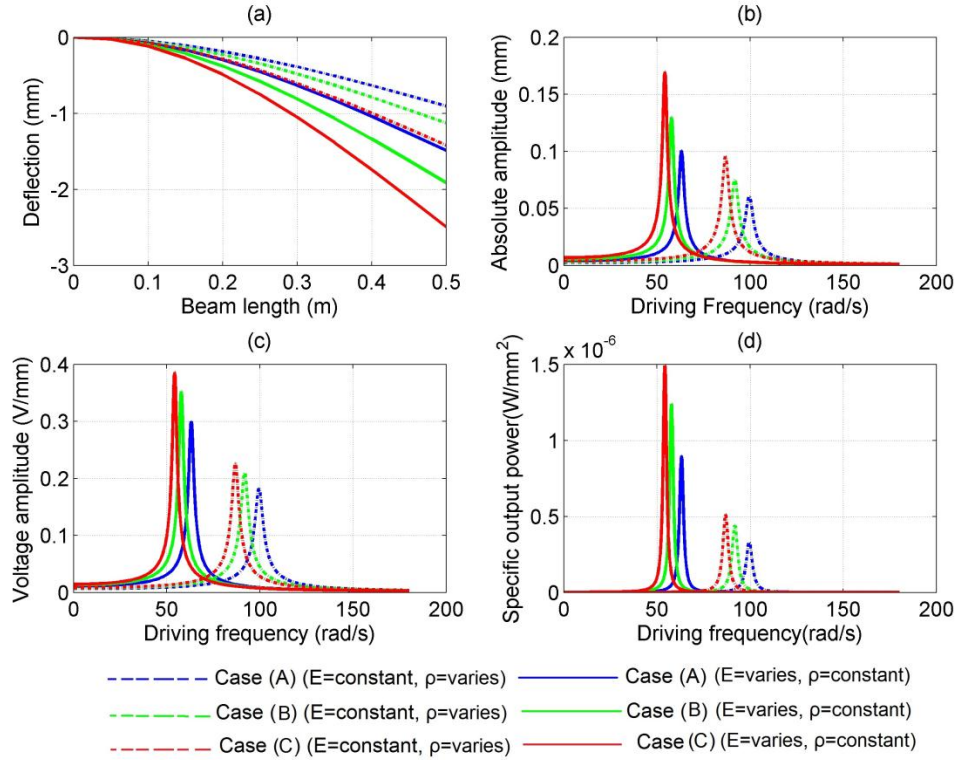
Figure 6.21 Effect of material properties on (a) static deflection (b) frequency (c) output voltage and (d) output power responses of nonprismatic beams with $np=2$, $k=1$, $c_b=0.1$ and $c_h=0.1$.

Furthermore, a comparison has been carried out to study the prevailing effect of material properties (such as E and ρ) on output responses i.e., static deflection, frequency, output voltage and output power. For this purpose two conditions have been considered in the analysis. Firstly, keeping E constant and varying ρ in axial direction and keeping ρ constant and varying E in axial direction for a given average temperature with power law using equation (3.1). Figure 6.21 (a-d) show the comparison of various responses for the above two cases, of proposed cross-section profile beams using arbitrarily varying parameters. From Figure 6.21 (a-d) it is observed that variation of E in axial direction has more prevailing effect than that of variation of ρ in same direction.

6.5 Responses of homogeneous and axially functionally graded non-prismatic beam

This section presents the dynamic analysis in both frequency and time domain responses i.e., frequency, output voltage and output power of homogeneous and axially functionally graded (FG) modelled nonprismatic beams (Case (A), Case (B) and Case (C)) for different tapers.

6.5.1   Frequency domain analysis

In frequency domain analysis, the frequency, output voltage and power responses of the homogeneous and modelled axially FG non-prismatic beams (such as Case (A), Case (B) and Case (C)) are compared in the subsequent sections.

6.5.1.1 Frequency response

Figure 6.22 Frequency responses of homogeneous and axially FG nonprismatic (Case (A),Case (B) and Case (C)) beams for (a) c_b=0.1, c_h=0.1 (b) c_b=0.1, c_h=0.3 (c) c_b=0.3, c_h=0.1 and (d) c_b=0.3, c_h=0.3

This section provides a comparative study of frequency responses between homogeneous and proposed axially FG piezolaminated beam subjected to sinusoidal excitation at the free end. Figure 6.22 (a-d) depict the comparison for different values of c_b and c_h (such as 0.1, 0.3). From Figure 6.22 (a-d), it is evident that the amplitude ratio of axially FG ($np= 2$, $k= 2$) beam for a given range of driving frequencies is substantially more compared to homogeneous beam of same dimensions in all cases of cross-sections of beam. It is also observed that axially FG Case (C) piezolaminated beam produce more amplitude ratio compared to axially FG Case (A) and Case (B) piezolaminated beams for all cases of taper.

6.5.1.2 Voltage response
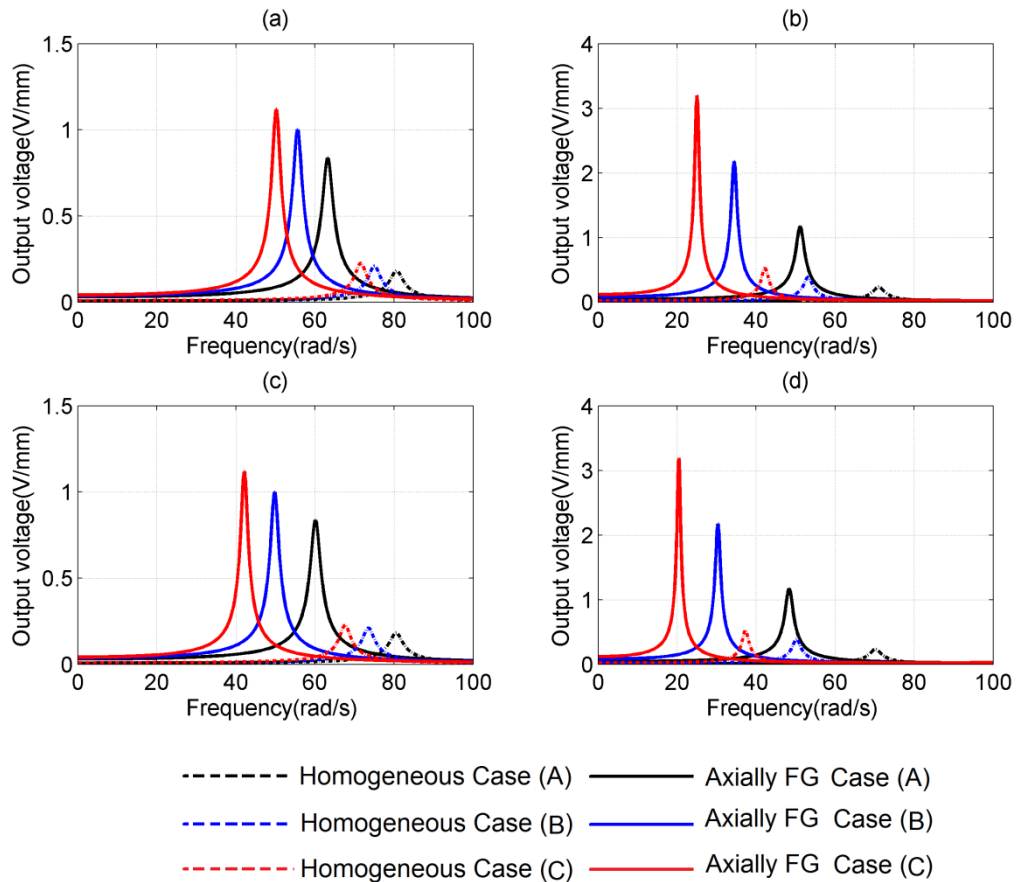
Figure 6.23 Voltage responses of homogeneous and axially FG nonprismatic (Case (A),Case (B) and Case (C)) beams for (a) c_b=0.1, c_h=0.1 (b) c_b=0.1, c_h=0.3 (c) c_b=0.3, c_h=0.1 and (d) c_b=0.3, c_h=0.3

This section provides a comparative study of output voltage between homogeneous and proposed axially FG piezolaminated beam subjected to sinusoidal excitation (magnitude 1 N) at the free end. Figure 6.23 (a-d) depict the comparison for different values of c_b and c_h (such as 0.1, 0.3). From Figure 6.23 (a-d), it is evident that the voltage amplitude of axially FG ($np= 4$, $k= 1$) beam for a given range of driving frequencies is 90% more compared to homogeneous beam of same dimensions in all cases of cross-sections of beam. It is also observed that axially FG Case (C) piezolaminated beam generates 5% and 10% more voltage compared to axially FG Case (A) and Case (B) piezolaminated beam for all cases of tapers.

6.5.1.3 Output power responses

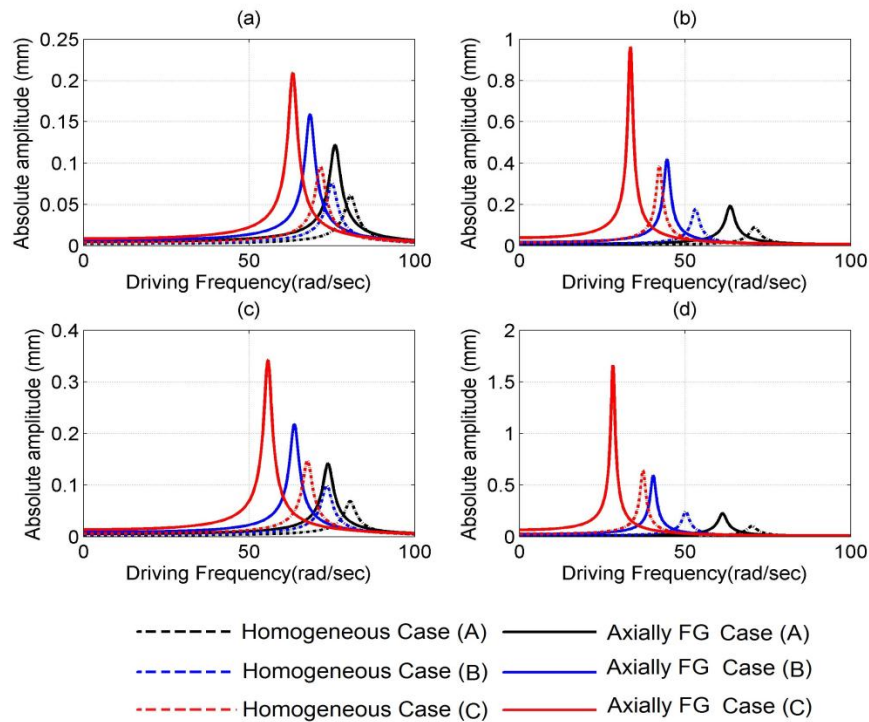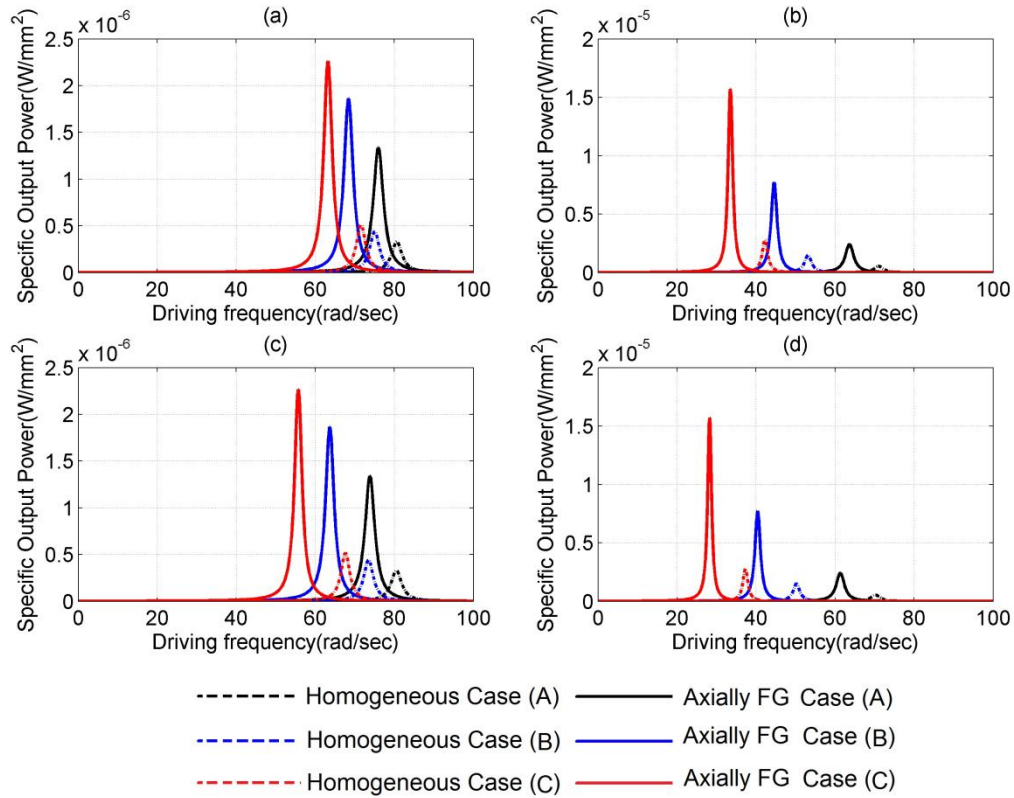Figure 6.24 Variation of specific output power with driving frequency of homogeneous and axially FG nonprismatic (Case (A),Case (B) and Case (C)) beams for (a) c_b=0.1, c_h=0.1 (b) c_b=0.1, c_h=0.3 (c) c_b=0.3, c_h=0.1 and (d) c_b=0.3, c_h=0.3

The specific output power FRF of Cases (A), (B) and (C) piezolaminated beams subjected to a sinusoidal excitation at the free end are shown in Figure 6.24 (a-d) with

different values of c_b and c_h (0.1 and 0.3). From Figure 6.24 (a-d), it is observed that non-prismatic axially FG beam generates 300% more specific output power for all taper values of c_b and c_h compared to the homogeneous non-prismatic beam in all cases of cross section profiles respectively. Further, it is observed that axially FG Case (C) piezolaminated beam generates more than 35% and 15% specific output power compared to axially FG Case (A) and Case (B) piezolaminated beam for all cases of tapers.
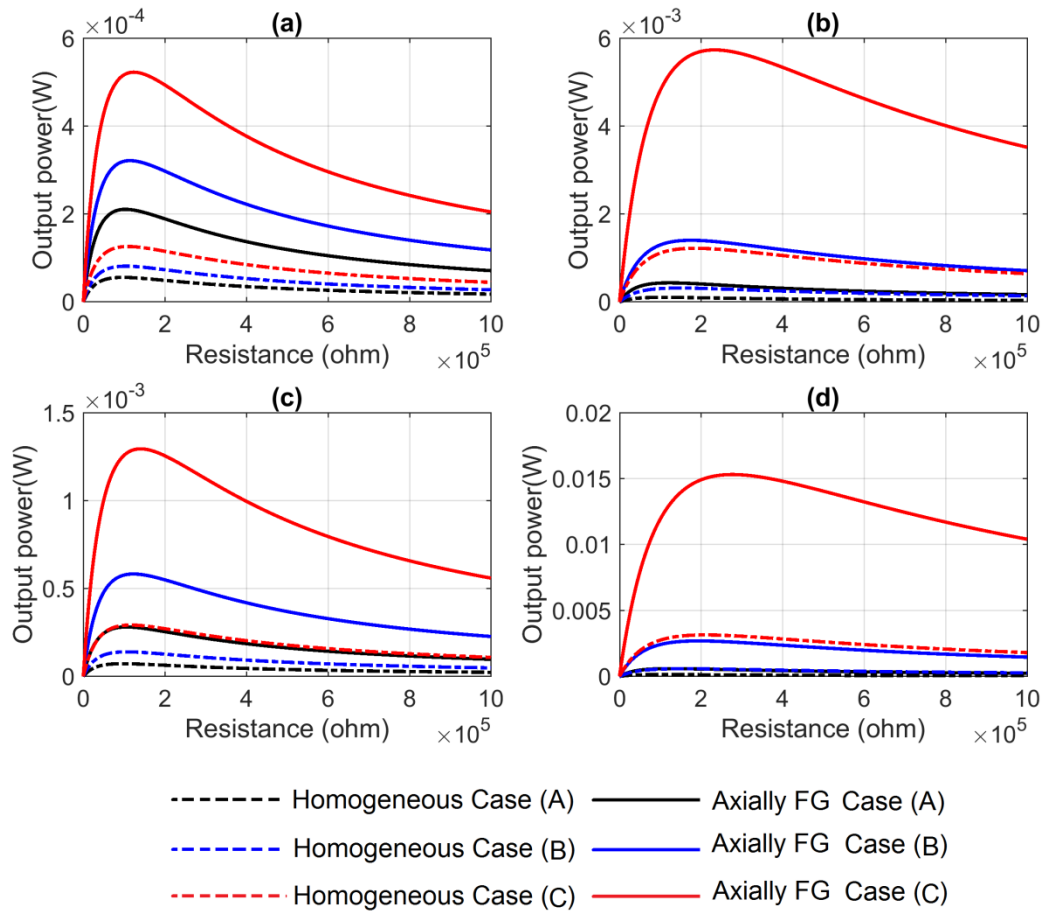
Figure 6.25 Variation of output power with external load resistance of homogeneous and axially FG nonprismatic (Case (A),Case (B) and Case (C)) beams for (a) c_b=0.1, c_h=0.1 (a) c_b=0.1, c_h=0.3 (a) c_b=0.3, c_h=0.1 and (a) c_b=0.3, c_h=0.3

Figure 6.25 (a-d) shows the variation of output power with external load resistance for homogeneous and axially FG non-prismatic (such as Cases (A), (B) and (C)) piezolaminated beams. From Figure 6.25 (a) and (b), it is observed that the output power of homogeneous Case (C) is 0.127 mW, whereas the output power of axially FG Case

(C) is 0.523 mW for taper values of c_b = 0.1 and c_h = 0.1, respectively. However, for the same values of c_b and c_h, the output power of homogeneous and axially FG Case (A) and Case (B) are 0.056 mW, 0.211 mW and 0.082 mW, 0.322 mW, respectively. The optimum resistance for homogeneous and axially FG Case (C) is 109.346 kΩ and 123.816 kΩ, respectively, whereas the optimum resistance for homogeneous and axially FG Case (A) and Case (B) are 97.062 kΩ, 103.022 kΩ and 104.315 kΩ, 114.400 kΩ, respectively. When c_h increases to 0.3 the output power of homogeneous and axially FG Case (C) increases to 1.2 mW and 5.7 mW, respectively, with the optimum resistance of 233.629 kΩ and 185.291 kΩ, respectively. Similarly ,the output power of homogeneous and axially FG Case (A) and (B) increases to 0.107 mW, 0.438 mW and 0.32 mW, 1.4 mW with optimum resistance of 110.18 kΩ, 122.973 kΩ and 147.231 kΩ, 175.581 kΩ, respectively. This indicates axially FG beams generate more power compared to the homogenous beam for a given values of c_b and c_h. Further, with an increase in c_h, the output power of axially FG Case (C) increases 80% more, whereas in Case (A) and Case (B), the output power increases 15% and 50% more, respectively. The Figure 6.25 (c) represents the variation of power when c_b changes to 0.3. From Figure 6.25 (c), it can be observed that, the output power of homogeneous and axially FG Case (C) changes to 0.292 mW and 1.3 mW with the optimum resistance of 115.741 kΩ and 140.511 kΩ, respectively. Similarly, the output power of homogeneous and axially FG Case (A) and (B) increases to 0.073 mW, 0.281 mW and 0.140 mW, 0.583 mW with optimum resistance of 97.192 kΩ ,106.008 kΩ and 106.499 kΩ, 122.916 kΩ, respectively. Further from Figure 6.25 (d), when c_h increases to 0.3, the output power of homogeneous and axially FG Case (C) changes to 3.2 mW and 15.3 mW with the optimum resistance of 209.841 kΩ and 277.219 kΩ, respectively. Similarly, the output power of homogeneous and axially FG Case (A) and (B) changes to 0.141 mW ,0.594 mW and 0.587 mW, 2.7 mW with optimum resistance of 111.464 kΩ ,127.598 kΩ and 155.839 kΩ, 193.694 kΩ, respectively. From the analysis, it is observed that with increase in c_h more power can be achieved compared to increase in c_b in axially FG beam. It is also observed that with simultaneous increase in c_b and c_h more output power can be scavenged in axially FG beams compared to homogeneous beams. Nevertheless, axially FG Case (C) generates 90% more power compared to case (A) and Case (B).

6.5.2   Time domain analysis

In time domain analysis, the tip displacement, output voltage and power responses of the homogeneous and modelled axially FG non-prismatic piezolaminated beams (Case (A), Case (B) and Case (C)) are compared for different taper values in the subsequent sections.

6.5.2.1 Tip displacement response

Figure 6.26 Tip displacement responses of homogeneous and axially FG Case(A) beam for (a) c_b=0.1, c_h=0.1 (b) c_b=0.1, c_h=0.3 (c) c_b=0.3, c_h=0.1 and (d) c_b=0.3, c_h=0.3

Figure 6.27 Tip displacement responses of homogeneous and axially FG Case(B) beam for (a) c_b=0.1, c_h=0.1 (b) c_b=0.1, c_h=0.3 (c) c_b=0.3, c_h=0.1 and (d) c_b=0.3, c_h=0.3
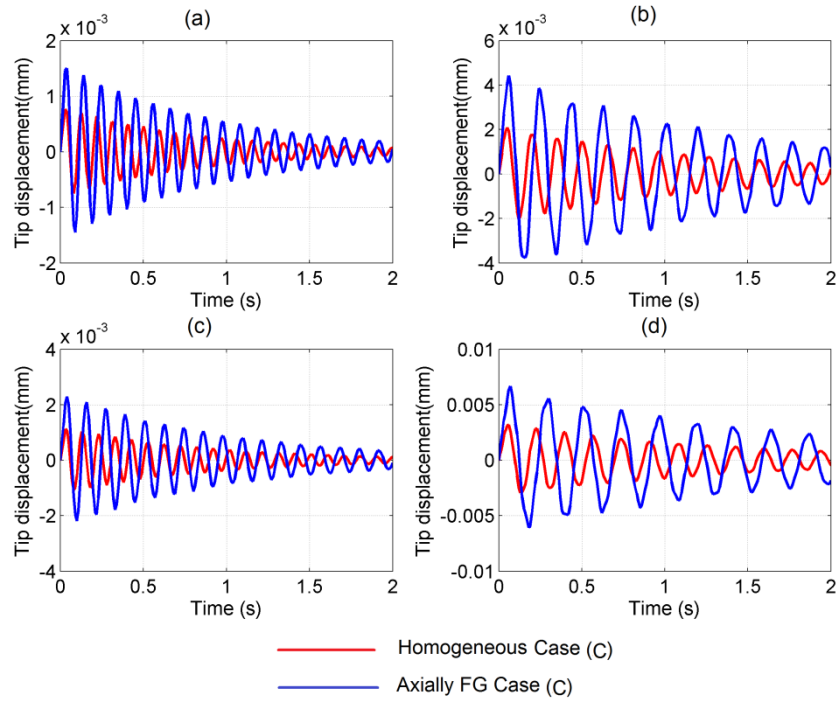
Figure 6.28 Tip displacement responses of homogeneous and axially FG Case(C) beam for (a) c_b=0.1, c_h=0.1 (b) c_b=0.1, c_h=0.3 (c) c_b=0.3, c_h=0.1 and (d) c_b=0.3, c_h=0.3

The tip displacement responses of homogeneous and axially FG (Case (A), Case (B) and Case (C)) piezolaminated beam in time domain with tapers (0.1 and 0.3) are presented in Figure 6.26 (a-d)-Figure 6.28 (a-d). The displacement response has been simulated for a time period of 2 sec. In Figure 6.28 (a) at time t=0.07 sec, the peak amplitude of homogeneous and axially FG Case (C) beams are 0.7e-3 mm and 1.5e-3 mm respectively for c_b=0.1 and c_h=0.1. As the time progresses the peak amplitude decreases substantially. Similarly, the values of homogeneous and axially FG Case (A) and (B) are 0.5e-3 mm, 1e-3 mm and 0.6e-3 mm, 1.2e-3 mm, shown in Figure 6.26 and Figure 6.27 (a), respectively. It is seen that the peak displacements for all cases of axially FG beam increases than corresponding homogeneous cases. When c_h increases to 0.3, the peak displacements of axially FG Case (A), (B) and (C) beams are found as 1.4e-3 mm, 2.4e-3 mm and 4.4e-3 mm as shown in Figure 6.26- Figure 6.28 (b). Further, increase in c_b to 0.3, the peak displacements of axially FG Case (A), (B) and (C) are found as 1.2e-3 mm, 1.6e-3 mm and 2.3e-3 mm presented in Figure 6.26- Figure 6.28 (c). From Figure 6.26- Figure 6.28 (d), when c_b=0.3 and c_h=0.3, the peak displacements of axially FG Case (A), (B) and (C) are shifted to 1.6e-3 mm, 3.3e-3 mm and 6.7e-3 mm. This shows an increase in 97%, 100% and 102% of peak displacements of axially FG nonprismatic beams compared to corresponding homogeneous cases.

6.5.2.2 Output voltage response

Figure 6.29 Output voltage responses of homogeneous and axially FG Case(A) beam for (a) c_b=0.1, c_h=0.1 (b) c_b=0.1, c_h=0.3 (c) c_b=0.3, c_h=0.1 and (d) c_b=0.3, c_h=0.3
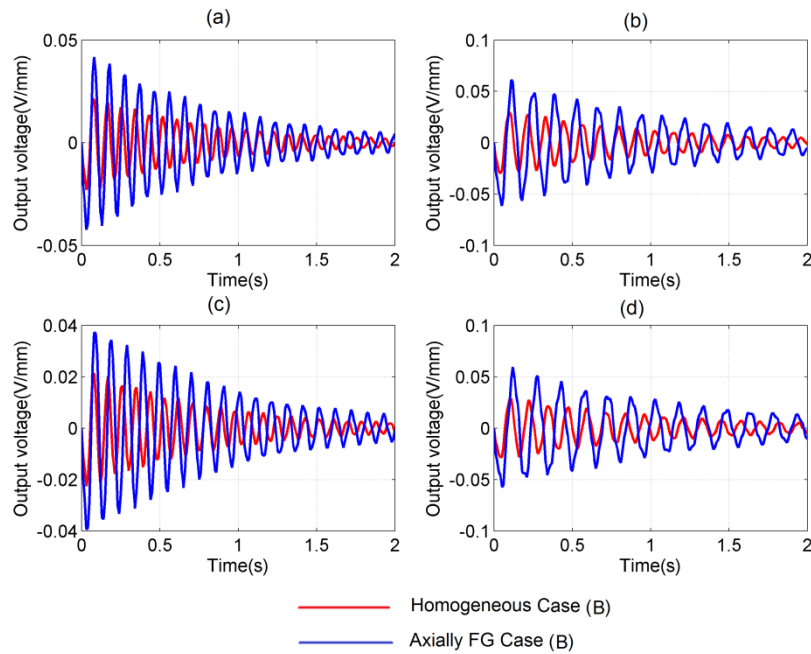
Figure 6.30 Output voltage responses of homogeneous and axially FG Case(B) beam for (a) c_b=0.1, c_h=0.1 (b) c_b=0.1, c_h=0.3 (c) c_b=0.3, c_h=0.1 and (d) c_b=0.3, c_h=0.3
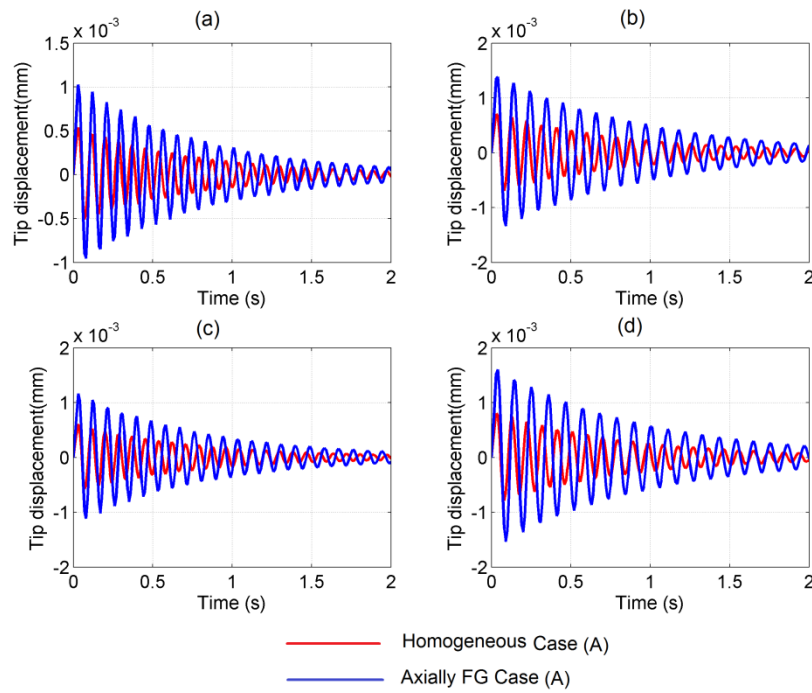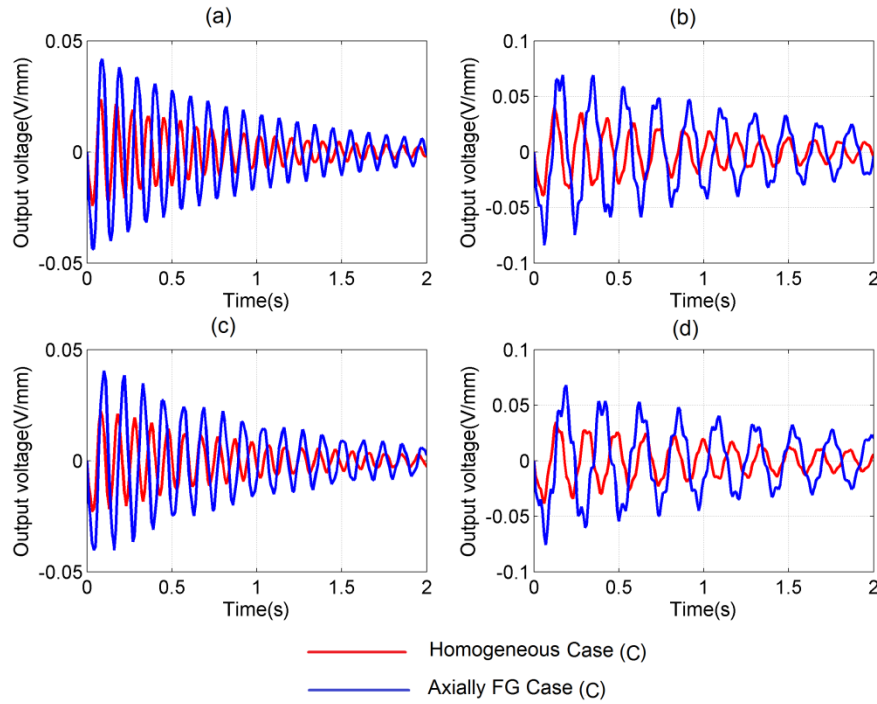
Figure 6.31 Output voltage responses of homogeneous and axially FG Case(C) beam for (a) c_b=0.1, c_h=0.1 (b) c_b=0.1, c_h=0.3 (c) c_b=0.3, c_h=0.1 and (d) c_b=0.3, c_h=0.3
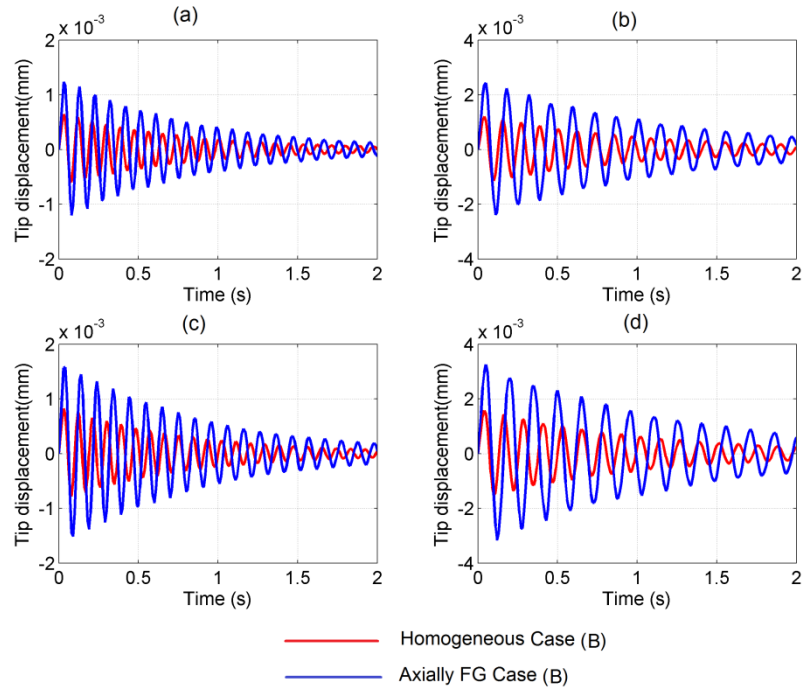
The output voltage responses in time domain of homogeneous and axially FG non-prismatic (Case (A), Case (B) and Case (C)) piezolaminated beams with tapers (0.1 and 0.3) are presented in Figure 6.29- Figure 6.31 (a-d). The output voltage responses have been simulated for a time period of 2 sec. In Figure 6.29 (a) at time t=0.05 Sec, the peak output voltage of homogeneous and axially FG Case (C) beam are 0.0242 V/mm and 0.0438 V/mm respectively for c_b=0.1 and c_h=0.1. With increase in time period the maximum value of output voltage decreases gradually. Similarly, the values of homogeneous and axially FG Case (A) and (B) are 0.0215 V/mm, 0.0404 V/mm and 0.0229 V/mm, 0.0423 V/mm, shown in Figure 6.30 and Figure 6.31 (a), respectively. It is observed that the peak output voltages for all cases of axially FG beam increases than homogeneous one. When c_h increases to 0.3, the peak voltages of axially FG Case (A), (B) and (C) beam are found as 0.0454 V/mm, 0.0614 V/mm and 0.0756 V/mm shown in Figure 6.29- Figure 6.31 (b). When c_b increases to 0.3, the peak voltages of axially FG Case (A), (B) and (C) are found as 0.0394 V/mm, 0.0393 V/mm and 0.0404 V/mm shown in Figure 6.29- Figure 6.31 (c). Further, from Figure 6.29- Figure 6.31 (d), when c_b=0.3 and c_h=0.3, the peak voltages of axially FG Case (A), (B) and (C) are changed to 0.0456 V/mm, 0.0614 V/mm and 0.0782 V/mm. This shows an increase in 90%, 102% and 106%

121

of peak output voltages of axially FG nonprismatic beams compared to corresponding homogeneous ones.

6.5.2.3 Output Power responses
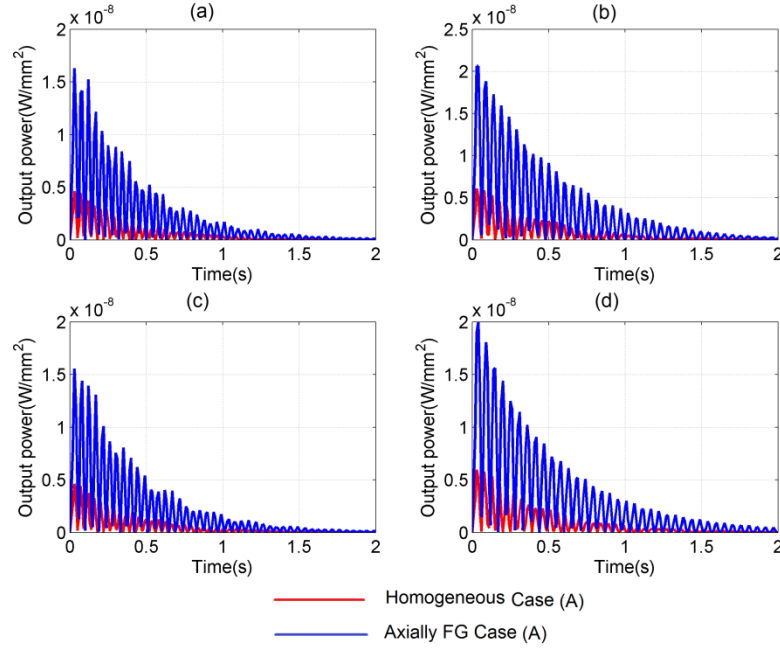
Figure 6.32 Output power responses of homogeneous and axially FG Case(A) beam for (a) c_b=0.1, c_h=0.1 (b) c_b=0.1, c_h=0.3 (c) c_b=0.3, c_h=0.1 and (d) c_b=0.3, c_h=0.3
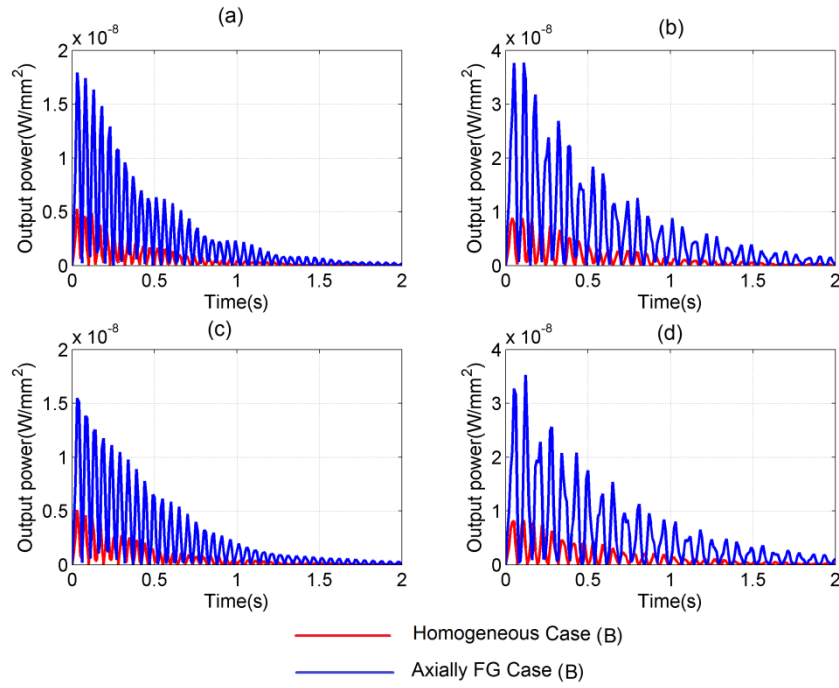
Figure 6.33 Output power responses of homogeneous and axially FG Case(B) beam for (a) c_b=0.1, c_h=0.1 (b) c_b=0.1, c_h=0.3 (c) c_b=0.3, c_h=0.1 and (d) c_b=0.3, c_h=0.3
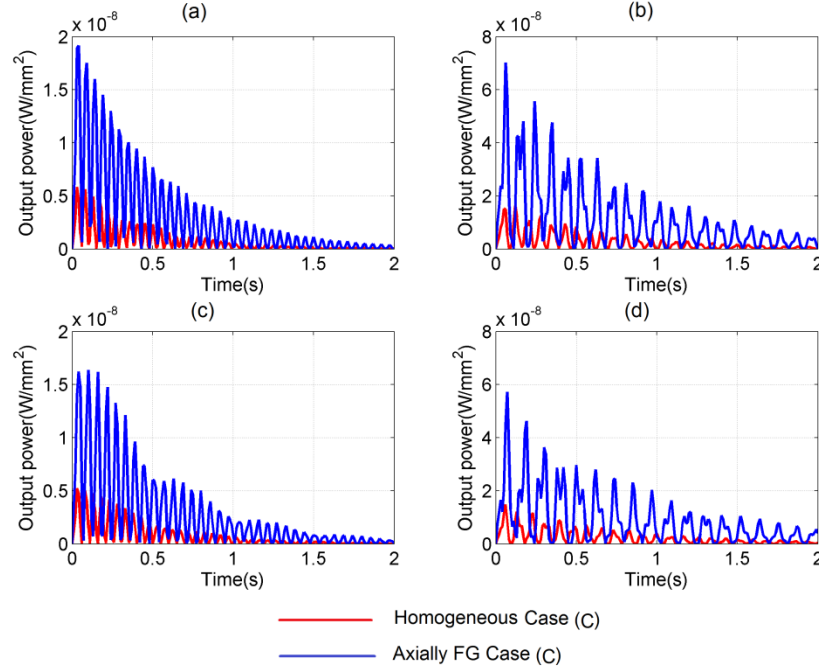
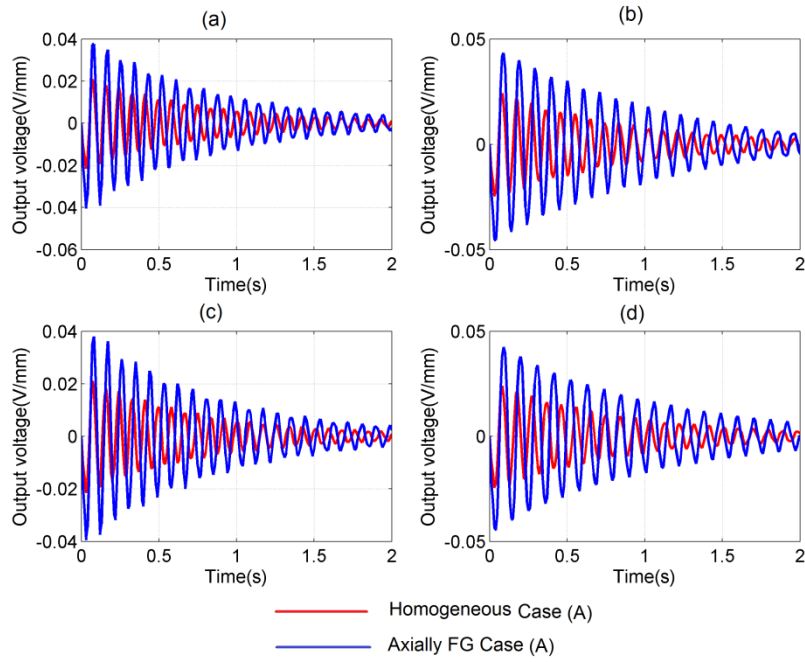

Figure 6.34 Output power responses of homogeneous and axially FG Case(C) beam for (a) c_b=0.1, c_h=0.1 (b) c_b=0.1, c_h=0.3 (c) c_b=0.3, c_h=0.1 and (d) c_b=0.3, c_h=0.3

The time history of output power of homogeneous and axially FG nonprismatic beam (Case (A), Case (B) and Case (C)) with arbitrarily taken tapers (0.1 and 0.3) are presented in Figure 6.32- Figure 6.34 (a-d). The output power responses have been simulated for a time period of 2 sec. In Figure 6.32 (a) at time t=0.08 Sec, the peak output power of homogeneous and axially FG Case (C) beam are 5.8e-9 W/mm^2 and 19.2e-9 W/mm^2 for c_b=0.1 and c_h=0.1. With increase in time the peak values of output power decreases substantially. Similarly, the values of homogeneous and axially FG Case (A) and (B) are 4.6e-9 W/mm^2, 16.3e-9 W/mm^2 and 5.3e-9 W/mm^2, 17.9e-9 W/mm^2, shown in Figure 6.33 and Figure 6.34 (a), respectively. It is observed that the peak output power for all cases of axially FG beam increases than homogeneous beam. When c_h increases to 0.3, the peak output power of axially FG Case (A), (B) and (C) beams are found as 20.6e-9 W/mm^2, 37.7e-9 W/mm^2 and 70.3e-9 W/mm^2 shown in Figure 6.32- Figure 6.34 (b). Further, with increase in c_b to 0.3, the peak output power of axially FG Case (A), (B) and (C) are found as 15.6e-9 W/mm^2, 15.5e-9W/mm^2 and 16.4e-9 W/mm^2 as shown in Figure 6.32- Figure 6.34 (c). Figure 6.32- Figure 6.34 (d) demonstrate that when c_b=0.3 and c_h=0.3, the peak output power of axially FG Case (A), (B) and (C) are changes to 20.6e-9 W/mm^2, 41.5e-9 W/mm^2 and 59.3e-9 W/mm^2. This indicates axially FG nonprismatic beams generate more output power compared to homogeneous nonprismatic beams. Further, with increase in c_h more output power can be obtained in Case (C) than Case (A) and Case (B) beams.

6.6 Responses of axially functionally graded non-prismatic beam without and with thermo-mechanical loading.

In this section, the proposed axially FG non-prismatic (Case (A), Case (B) and Case (C)) piezolaminated beam is subjected to mechanical loading of magnitude 1N along with thermal loading (θ_t= 100^{0}C and θ_b= 0^{0}C). The analysis is carried out without and with pyroelectric effect.

6.6.1   Static analysis

Figure 6.35 Deflection of axially FG nonprismatic (Case (A),Case (B) and Case (C)) beams under mechanical and thermo-mechanical loading without pyroelectric effect for (a) c_b=0.1, c_h=0.1 (b) c_b=0.1, c_h=0.3 (c) c_b=0.3, c_h=0.1 and (d) c_b=0.3, c_h=0.3

Figure 6.36 Deflection of axially FG nonprismatic (Case (A),Case (B) and Case (C)) beams under mechanical and thermo-mechanical loading with pyroelectric effect for (a) c_b=0.1, c_h=0.1 (b) c_b=0.1, c_h=0.3 (c) c_b=0.3, c_h=0.1 and (d) c_b=0.3, c_h=0.3

Figure 6.35 (a-d) and Figure 6.36 (a-d) show the beam deflection for all cases of axially FG nonprismatic piezolaminated beams under mechanical loading and thermo-mechanical loading without and with pyroelectric effect for tapers 0.1 and 0.3. The values of *np* and *k* are arbitrarily taken as 4 and 1, respectively. From Figure 6.35 (a-d) and Figure 6.36 (a-d), it is observed that under thermo-mechanical loading, the deflection of beam in each case of axially FG non-prismatic beams increased by 70% more than that for only mechanical loading. Further it has been observed that in Case (C), the deflection is more under thermo-mechanical loading than Case (A) and Case (B) for all cases of tapers. This is due to the fact that as the beam is kept under thermo-mechanical loading, the stiffness reduces. Hence more deflection of the beam can be obtained. From Figure 6.35 (a-d) and Figure 6.36 (a-d), it has also been observed that no significant variation has been found in the responses with and without pyroelectric effect.

6.6.2   Frequency domain analysis

In section 6.6.1, as it is observed that no significant variation exists without and with pyroelectric effect, hence further analyses have been carried out under thermo-mechanical loading with pyroelectric effect. In frequency domain analysis the frequency, output voltage and power responses of the axially FG modelled non-prismatic (Case (A), Case (B) and Case (C)) beams subjected to with and without thermal loading are discussed in the subsequent sections.

6.6.2.1 Frequency responses

Figure 6.37 Frequency responses of axially FG nonprismatic (Case (A),Case (B) and Case (C)) beams under mechanical and thermo-mechanical loading considering pyroelectric effect for (a) c_b=0.1, c_h=0.1 (b) c_b=0.1, c_h=0.3 (c) c_b=0.3, c_h=0.1 and (d) c_b=0.3, c_h=0.3.

This section provides a comparative study of frequency responses of proposed axially FG non-prismatic (Case (A), Case (B) and Case (C)) piezolaminated beams under mechanical loading and thermo-mechanical loading with pyroelectric effect. Figure 6.37 (a-d) depict the comparison of frequency responses for arbitrarily chosen values of c_b and c_h (such as 0.1, 0.3). From Figure 6.37 (a-d), it is evident that the amplitude ratio of axially FG (np= 2, k= 1) beam under thermo-mechanical loading, for a given range of driving frequencies is 60% more compared to only mechanical loading for all cases of cross-sections of beam. It is also observed that axially FG Case (C) under thermo-mechanical loading produce more amplitude ratio compared to axially FG Case (A) and Case (B) for all cases of tapers.

6.6.2.2 Voltage response
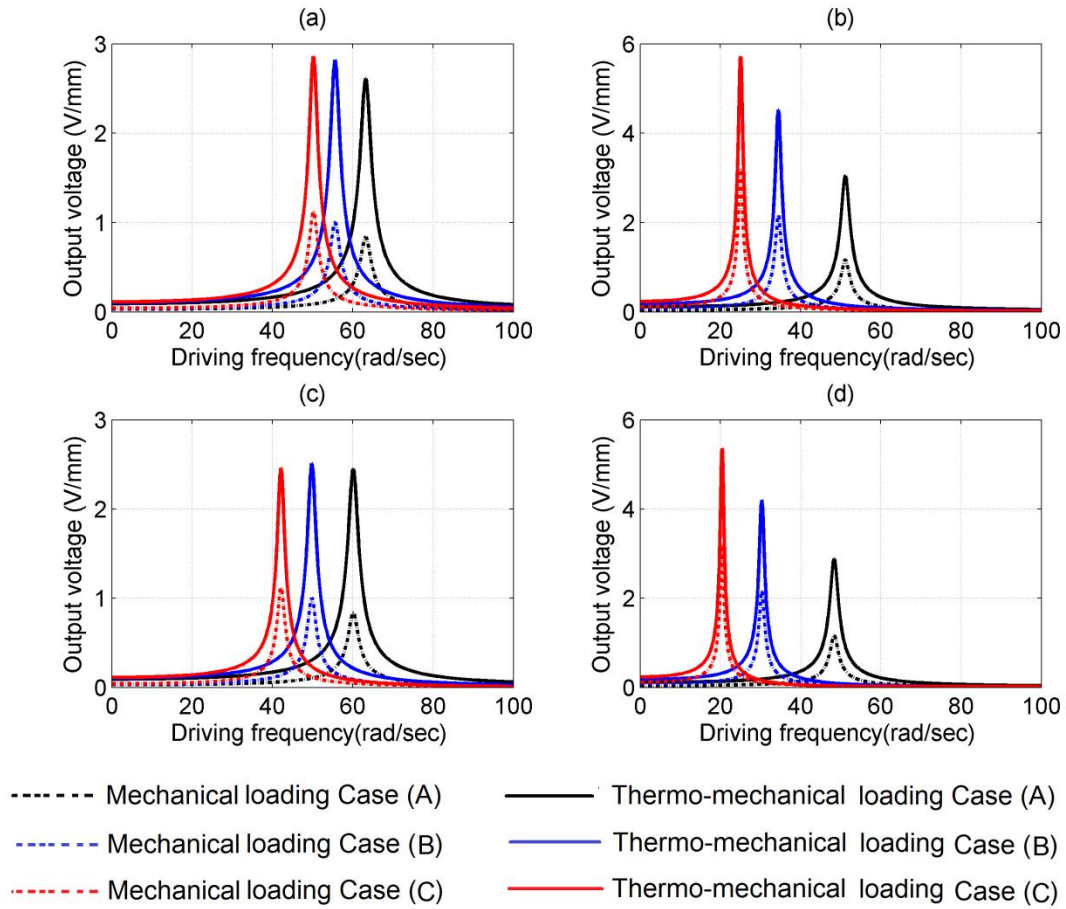
Figure 6.38 Voltage responses of axially FG nonprismatic (Case (A),Case (B) and Case (C)) beams under mechanical and thermo-mechanical loading considering pyroelectric effect for (a) c_b=0.1, c_h=0.1 (b) c_b=0.1, c_h=0.3 (c) c_b=0.3, c_h=0.1 and (d) c_b=0.3, c_h=0.3.

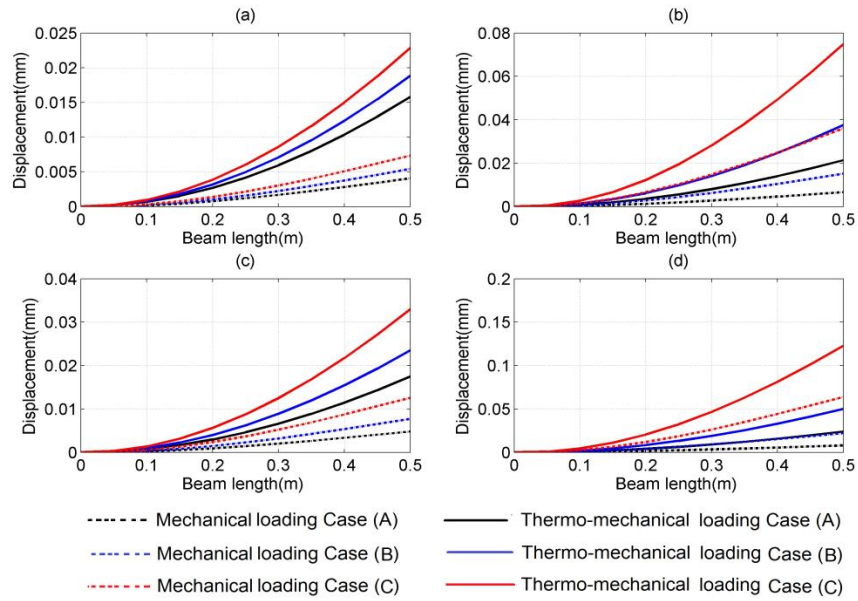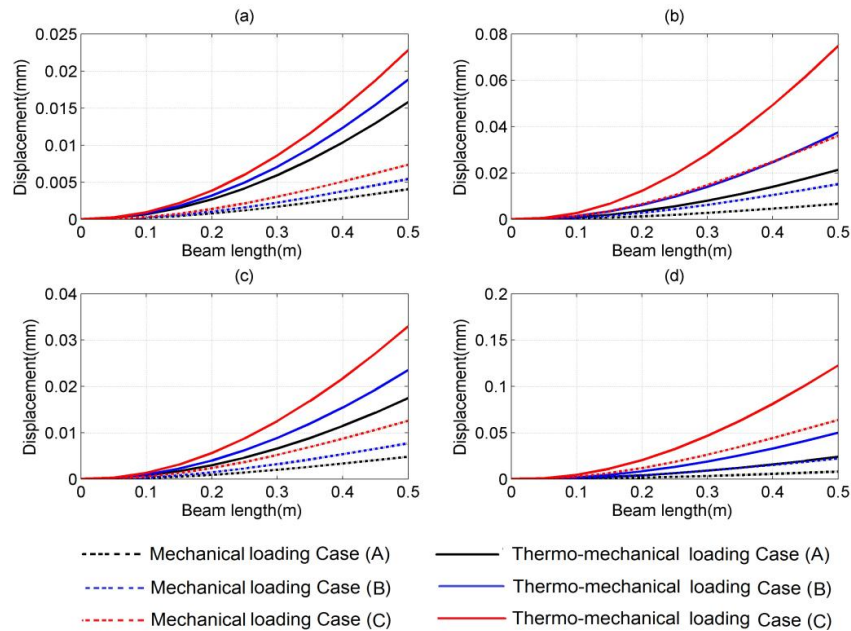Figure 6.38 (a-d) depict the comparative study of output voltage responses of proposed axially FG non-prismatic (Case (A), Case (B) and Case (C)) piezolaminated beams under mechanical and thermo-mechanical loading with pyroelectric effect. The analyses are carried out for different values of c_b and c_h (such as 0.1, 0.3). From Figure 6.38 (a-d), it is evident that the voltage amplitude of axially FG (np= 2, k= 1) beam under thermo-mechanical loading with pyroelectric effect for a given range of driving frequencies is 65% more compared to only mechanical loading in all cases of cross-sections of beam. It is also observed that axially FG Case (C) under thermo-mechanical loading generates more voltage compared to axially FG Case (A) and Case (B) for all cases of tapers.

6.6.2.3 Output Power responses
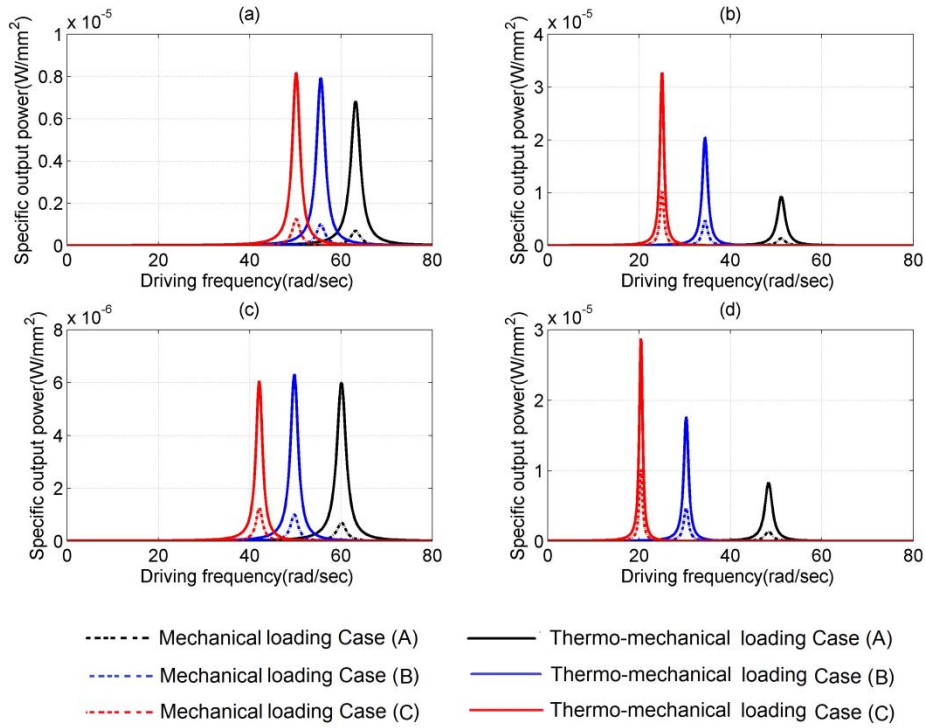
Figure 6.39 Variation of specific output power of axially FG nonprismatic (Case (A),Case (B) and Case (C)) beams under mechanical and thermo-mechanical loading considering pyroelectric effect for (a) c_b=0.1, c_h=0.1 (b) c_b=0.1, c_h=0.3 (c) c_b=0.3, c_h=0.1 and (d) c_b=0.3, c_h=0.3.

The specific output power FRFs of all cases under mechanical and thermo-mechanical loading have been shown in Figure 6.39 (a-d) with different values of c_b and c_h (0.1 and 0.3), respectively. From Figure 6.39 (a-d), it has been observed that non-prismatic axially FG beam under thermo-mechanical loading generates 70% more specific output power for all taper values of c_b and c_h than mechanical loading only in all cases of cross section profiles. This is due to the fact that under thermo-mechanical loading, the beam is thermally poled, which produces more deflection than mechanical loading only. Consequently, more voltage and power can be obtained from the modelled beams.

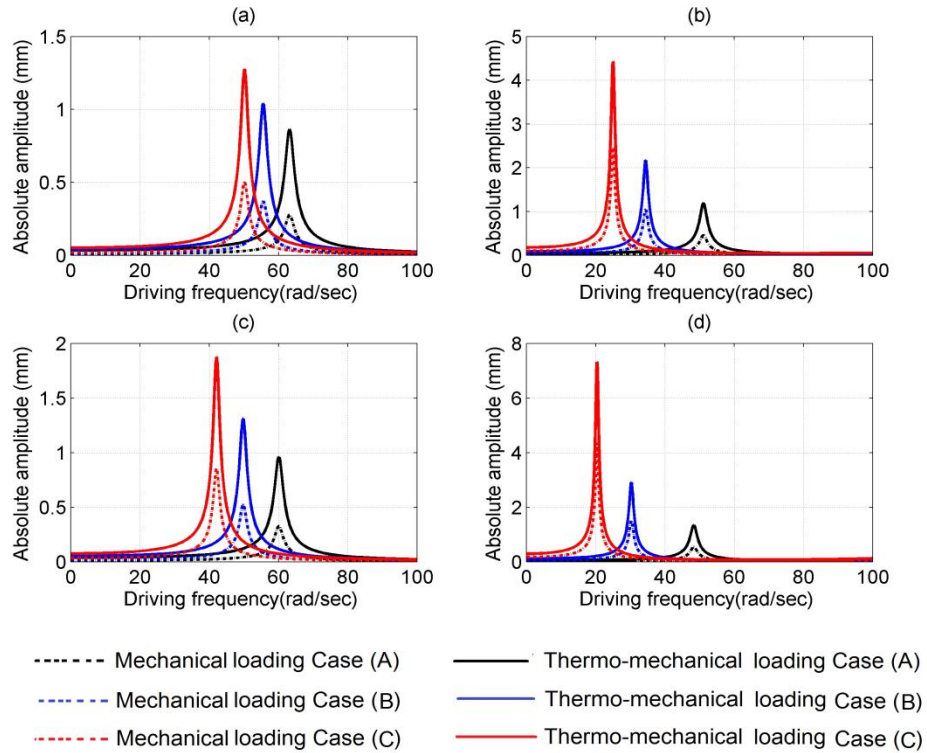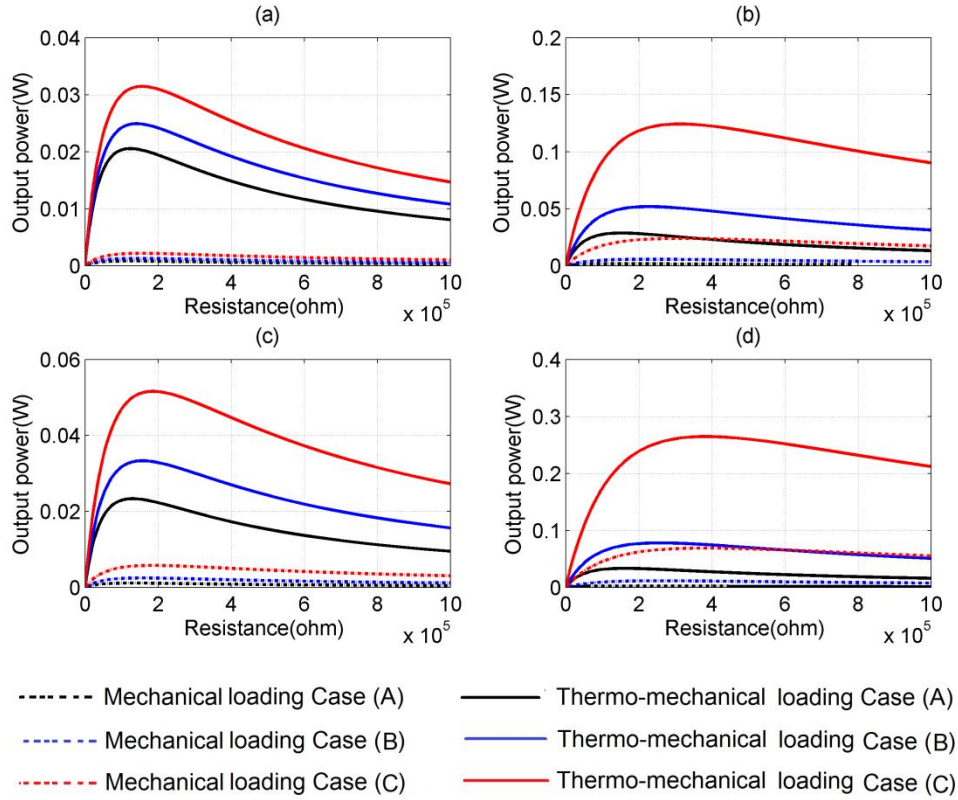Figure 6.40 Variation of output power with external load resistance of axially FG nonprismatic (Case (A),Case (B) and Case (C)) beams under mechanical and thermo-mechanical loading considering pyroelectric effect for (a) c_b=0.1, c_h=0.1 (b) c_b=0.1, c_h=0.3 (c) c_b=0.3, c_h=0.1 and (d) c_b=0.3, c_h=0.3.

Figure 6.40 (a-d) show the variation of output power with external load resistance for axially FG non-prismatic (Cases (A), (B) and (C)) piezolaminated beams under mechanical and thermo-mechanical loading with pyroelectric effect. From Figure 6.40 (a) and (b), it is observed that the output power of axially FG Case (C) under thermo-mechanical loading is 31.4566 mW, whereas with mechanical loading is 2.1650 mW for taper values of c_b = 0.1 and c_h = 0.1. However, for the same values of c_b and c_h the output power of axially FG Case (A) and Case (B) for mechanical and thermo-mechanical loading are 0.8219 mW, 20.5476 mW and 1.2851 mW, 24.9095 mW, respectively. When, c_h increases to 0.3 the output power of axially FG Case (C) increases to 23.8718 mW and 124.2968 mW for mechanical and thermo-mechanical loading respectively. Similarly, the output power of axially FG Case (A) and (B) increases to 1.7698 mW, 28.6321 mW and, 5.6237 mW, 51.8313 mW for mechanical and thermo-mechanical loading, respectively. This indicates axially FG beams under thermo-mechanical loading with pyroelectric effect

generates more power compared to mechanical loading only for given values of c_b and c_h. The Figure 6.40 (c) represents the variation of power when c_b changes to 0.3. In Figure 6.40 (c) the output power of axially FG Case (C) changes to 5.7781 mW and 51.5955 mW while the output power of axially FG Case (A) and (B) increases to 1.1344 mW, 23.3387 mW and 2.4750 mW, 33.3304 mW under mechanical and thermo-mechanical loading, respectively. When c_h increases to 0.3, the output power of axially FG Case (C) changes to 68.9079 mW and 264.6845 mW while the output power of axially FG Case (A) and (B) changes to 2.4779 mW, 33.3757 mW and 11.5134 mW, 78.0562 mW under mechanical and thermo-mechanical loading respectively. From the analysis, it is observed that in axially FG beam under thermo-mechanical loading, with increase in c_h, more power can be obtained than increase in c_b. It is also observed that simultaneous increase in c_b and c_h, more output power can be scavenged in axially FG beams under thermo-mechanical loading compared to mechanical loading only.

6.6.3   Time domain analysis

In time domain analysis, the tip displacement, output voltage and output power of the axially FG nonprismatic (Case (A), Case (B) and Case (C)) piezolaminated beam under mechanical and thermo-mechanical loading with pyroelectric effect have been compared and presented for different taper values in the subsequent sections.

6.6.3.1 Tip displacement response
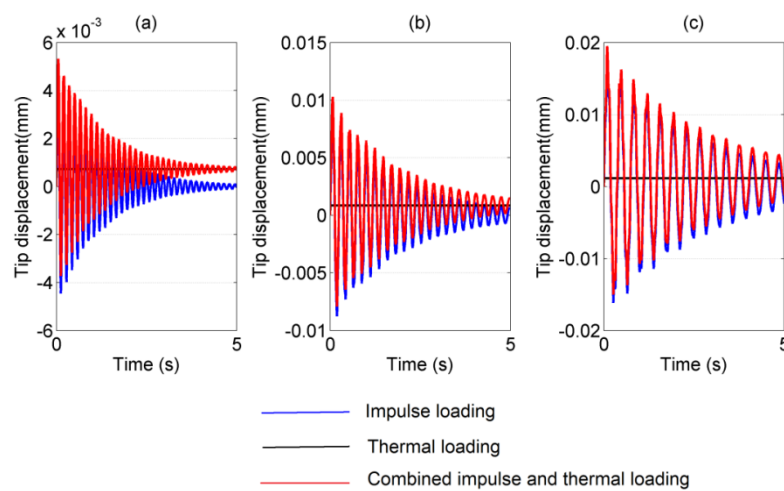
Figure 6.41 Tip displacement responses of axially FG piezolaminated beams with pyroelectric effect for c_b=0.3, c_h=0.3 of (a) Case (A) (b) Case (B) and (c) Case (C).

The tip displacement responses of axially FG beams (Case (A), Case (B) and Case (C)) with pyroelectric effect in time domain for c_b= 0.3 and c_h=0.3 have been shown in Figure 6.41 (a-c). The transverse tip displacement has been simulated for a time period of 5 sec. The amplitude decreases substantially with increase in time. From Figure 6.41 (a), the peak amplitude of Case (A) under impulse loading is 4.6e-3 mm whereas under thermo mechanical loading it is 5.3e-3 mm. Similarly, the amplitude values for Case (B) and (C) are 9.4e-3 mm, 10.3e-3 mm and 18.3e-3 mm, 19.5e-3 mm as shown in Figure 6.41 (b) and (c) respectively. From the figures it is observed that there is an increase in 15%, 10% and 7% of peak amplitudes for Case (A), (B) and (C) under thermo mechanical loading compared to impulse loading. Again, Case (C) beam has got more peak amplitude than Case (A) and (B) beams under thermo mechanical loading for a given value of taper.

6.6.3.2 Output voltage response

Here the output voltage responses for all cases of beams are discussed. The axially FG (Case (A), Case (B) and Case (C)) piezolaminated beams with pyroelectric effect in concern with time domain for c_b= 0.3 and c_h=0.3 have been presented in Figure 6.42 (a-c). The voltages have been simulated for a time period of 5 sec. The peak amplitude for output voltage of Case (A) under impulse loading is 0.1349 V/mm whereas for thermo mechanical loading it is 0.2667 V/mm. The results are shown in Figure 6.42 (a). Similar results are found for Case (B) and (C) beams. The results for Case (B) and (C) are 0.1761 V/mm, 0.3687 V/mm and 0.2197 V/mm, 0.4737 V/mm as shown in Figure 6.42 (b) and (c) respectively. It is found that there are 97%, 109% and 115% increase in peak output voltage for Case (A), (B) and (C) beams under thermo mechanical loading compared to impulse load. For a given taper, Case (C) beam has more peak output voltage than Case (A) and (B) beams under thermo mechanical loading.
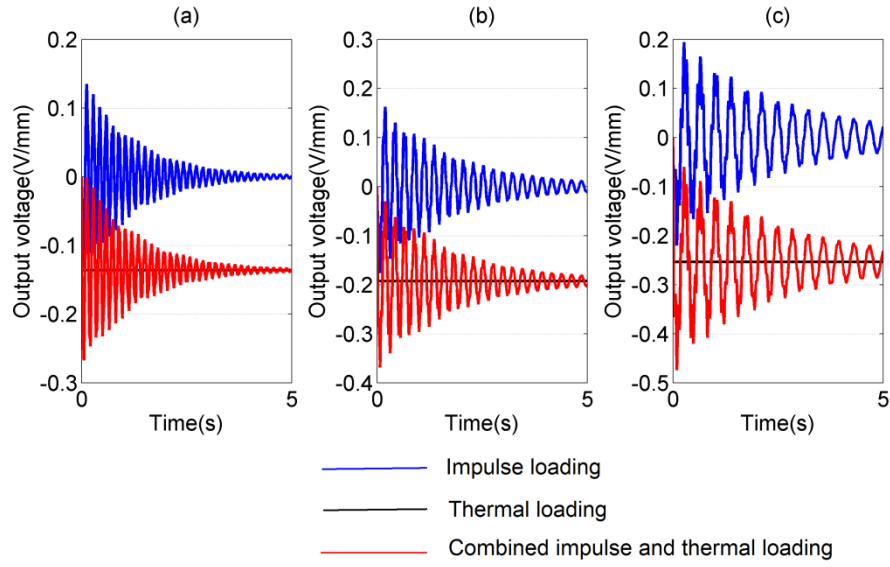
Figure 6.42 Output voltage responses of axially FG piezolaminated beams with pyroelectric effect for c_b=0.3, c_h=0.3 of (a) Case (A) (b) Case (B) and (c) Case (C).

6.6.3.3 Output Power responses
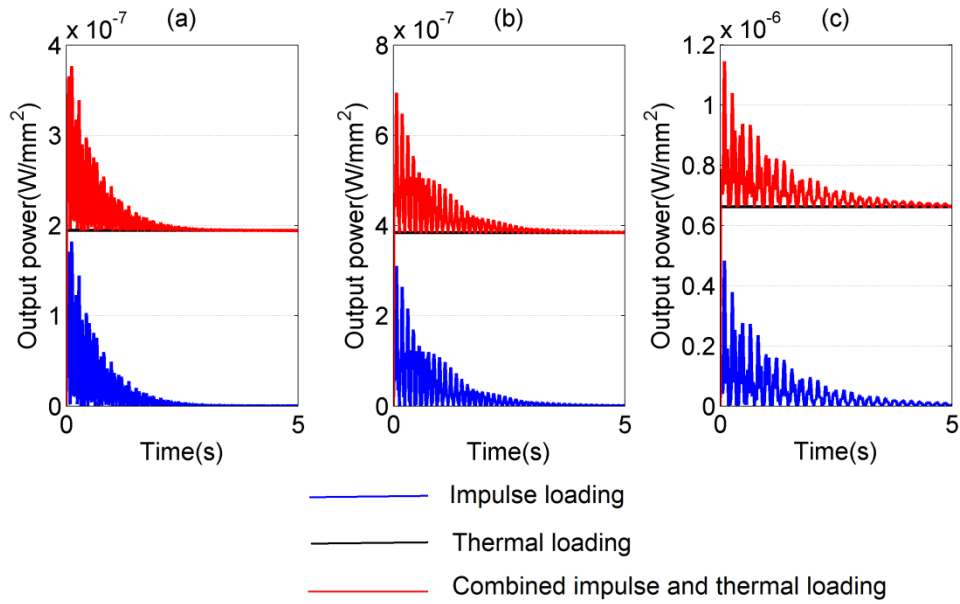
Figure 6.43 Output power responses of axially FG piezolaminated beams with pyroelectric effect for c_b=0.3, c_h=0.3 of (a) Case (A) (b) Case (B) and (c) Case (C).

The output power of axially FG (Case (A), Case (B) and Case (C)) piezolaminated beam with pyroelectric effect in time domain with c_b= 0.3 and c_h=0.3 have been simulated and presented in Figure 6.43 (a-c). Here the output powers have been simulated for a time period of 5 sec. The peak output power of Case (A) under impulse loading is 18.2e-8

W/mm^2 and under thermo mechanical loading it is 37.7e-8 W/mm^2 as presented in Figure 6.43 (a). The corresponding values for Case (B) and (C) are 31e-8 W/mm^2, 69.4e-8 W/mm^2 and 48.3e-8 W/mm^2, 114.5e-8 W/mm^2 shown in Figure 6.43 (b) and (c) respectively. It is noticed that there is 107%, 123% and 137% increase in peak output power for Case (A), (B) and (C) under thermo mechanical loading compared to impulse load. Again, Case (C) beam generates more peak output power than Case (A) and (B) beams under thermo mechanical loading for a given value of taper.

6.7 Responses of axially functionally graded non-prismatic beam under thermo-mechanical loading without and with temperature dependent material properties.

In this section, the proposed axially FG non-prismatic (Case (A), Case (B) and Case (C)) piezolaminated beam is subjected to mechanical loading of magnitude 1N along with thermal loading (θ_t= 100^{0}C and θ_b= 0^{0}C). The material properties of the beam vary axially with position from fixed end to the tip of the beam along with average temperature using equation (3.1). The various material properties used in the analysis have been presented in Table 6.8.

6.7.1   Static analysis
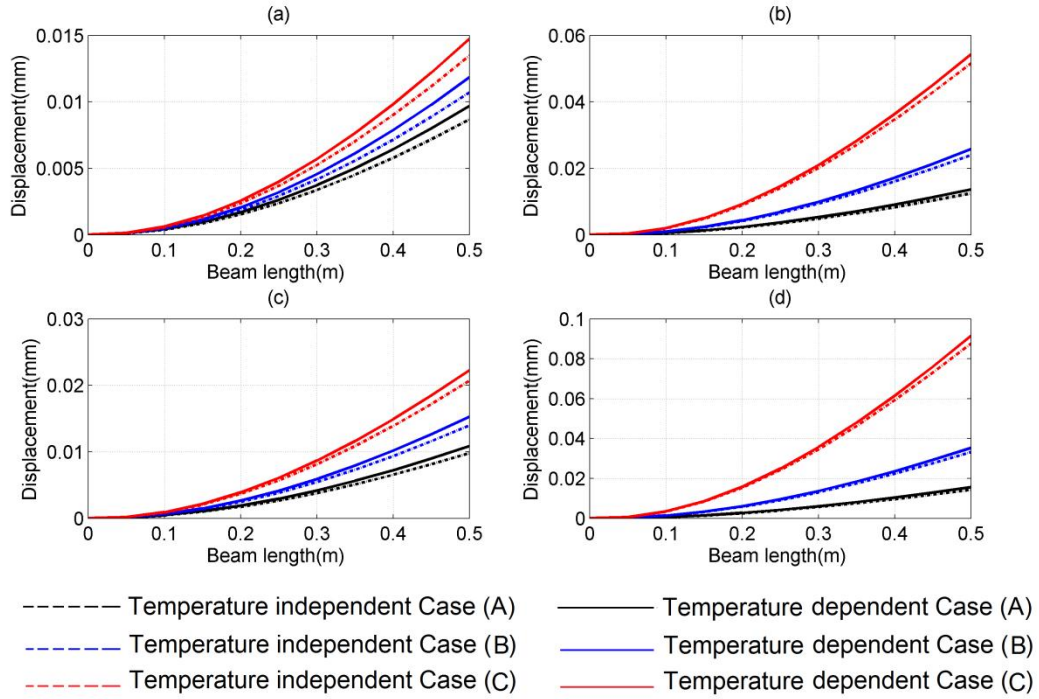
Figure 6.44 Deflection of axially FG nonprismatic (Case (A),Case (B) and Case (C)) beams under thermo-mechanical loading with temperature independent and dependent material properties for (a) c_b=0.1, c_h=0.1 (b) c_b=0.1, c_h=0.3 (c) c_b=0.3, c_h=0.1 and (d) c_b=0.3, c_h=0.3

Figure 6.44 (a-d) show the beam deflection for all cases of axially FG nonprismatic piezolaminated beams subjected to thermo-mechanical loading with temperature dependent and independent material properties (such as ρ, E, υ and α) for tapers 0.1 and 0.3. The average temperature has been considered as 50^0C for all cases of modelled beams. From Figure 6.44 (a-d), it has been observed that due to thermo-mechanical loading, the static deflection of the beam with temperature dependent material properties shows 6% more than temperature independent material properties.

6.7.2   Frequency domain analysis

In frequency domain analysis the frequency, output voltage and power responses of the axially FG modelled non-prismatic (Case (A), Case (B) and Case (C)) beams with thermo-mechanical loading with temperature independent and dependent material

properties have been discussed in the subsequent sections. For the analysis, the average temperature has been considered as 50^0C.

6.7.2.1 Frequency responses

Figure 6.45 Frequency responses of axially FG nonprismatic (Case (A),Case (B) and Case (C)) beams under thermo-mechanical loading for (a) c_b=0.1, c_h=0.1 (b) c_b=0.1, c_h=0.3 (c) c_b=0.3, c_h=0.1 and (d) c_b=0.3, c_h=0.3.

This section provides a comparative study of frequency responses of proposed axially FG non-prismatic (Case (A), Case (B) and Case (C)) piezolaminated beams under thermo-mechanical loading with temperature independent and dependent material properties. Figure 6.45 (a-d) depicts the comparison of frequency responses for arbitrarily chosen values of c_b and c_h (such as 0.1, 0.3). From Figure 6.45 (a-d), it is evident that the amplitude ratio of axially FG (np= 4, k= 1) beam under thermo-mechanical loading with temperature dependent material properties shows 60% more than temperature independent material properties for all cases of cross-sections of beam. It is also observed that axially FG Case (C) under thermo-mechanical loading with temperature

dependent material properties produce more amplitude ratio than temperature independent material properties of Case (A) and Case (B) for all cases of tapers.

6.7.2.2 Voltage response
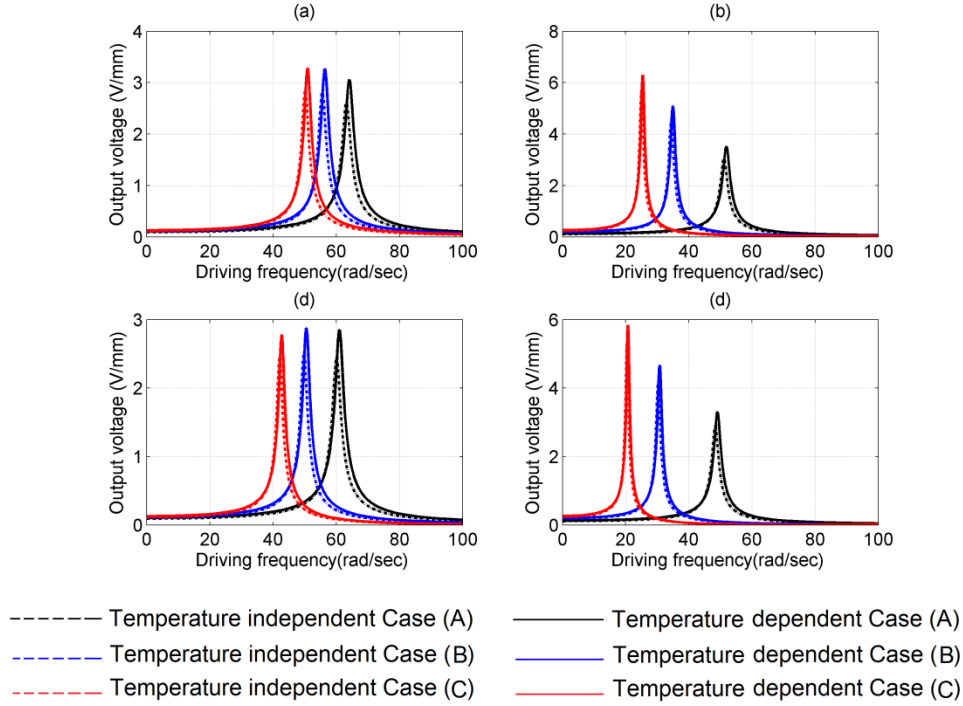
Figure 6.46 Voltage responses of axially FG nonprismatic (Case (A),Case (B) and Case (C)) beams under thermo-mechanical loading for (a) c_b=0.1, c_h=0.1 (b) c_b=0.1, c_h=0.3 (c) c_b=0.3, c_h=0.1 and (d) c_b=0.3, c_h=0.3.

Figure 6.46 (a-d) depict the comparative study of output voltage responses of proposed axially FG non-prismatic (Case (A), Case (B) and Case (C)) piezolaminated beams under thermo-mechanical loading with temperature independent and dependent material properties. The analyses have been carried out for different values of c_b and c_h (such as 0.1, 0.3), respectively. It is evident that the voltage amplitude of axially FG (np= 4, k= 1) beam under thermo-mechanical loading with temperature dependent material properties shows 65% more than temperature independent material properties for all cases of cross-sections of beam shown in Figure 6.46 (a-d). It is also observed that axially FG Case (C) under thermo-mechanical loading with temperature dependent material properties

produce more amplitude ratio than temperature independent material properties of Case (A) and Case (B) for all cases of tapers.

6.7.2.3 Output power response
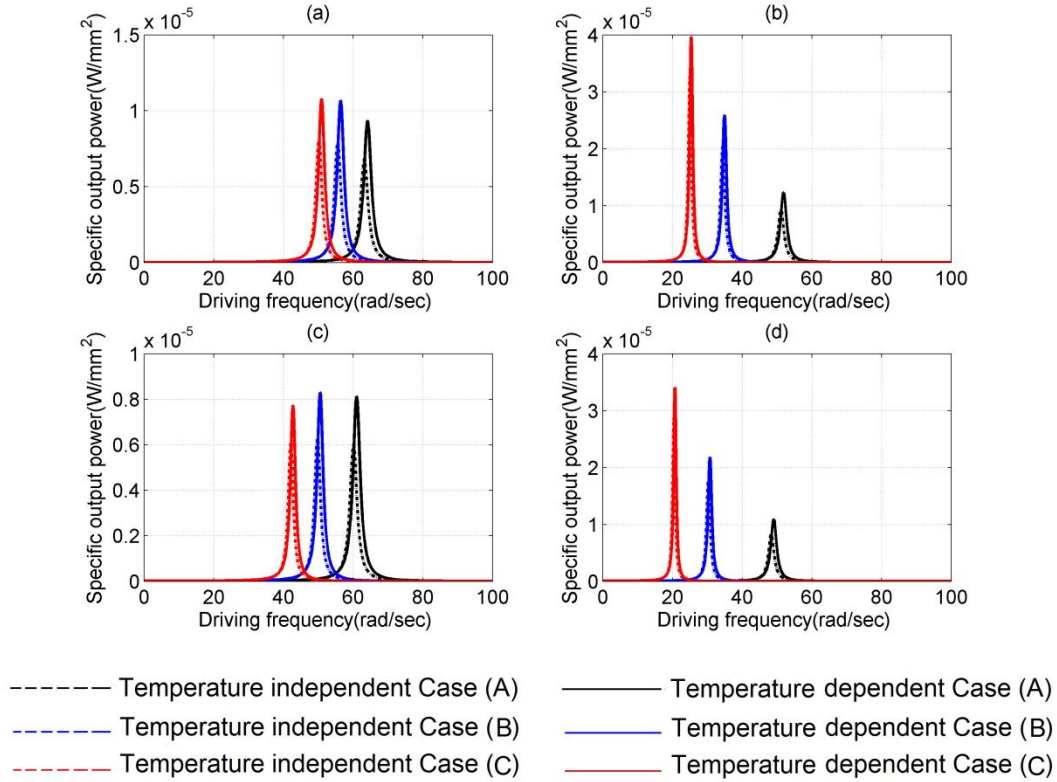
Figure 6.47 Variation of specific output power of axially FG nonprismatic (Case (A),Case (B) and Case (C)) beams under thermo-mechanical loading for (a) c_b=0.1, c_h=0.1 (b) c_b=0.1, c_h=0.3 (c) c_b=0.3, c_h=0.1 and (d) c_b=0.3, c_h=0.3

The specific output power FRF of all cases under thermo-mechanical loading with temperature independent and dependent material properties are shown in Figure 6.47 (a-d) with different values of c_b and c_h (0.1 and 0.3). The non-prismatic axially FG beam under thermo-mechanical loading with temperature dependent material properties generates 70% more specific output power for all taper values of cb and ch than temperature independent material properties for all cases of cross section profiles. Further, it is predicted that axially FG Case (C) under thermo-mechanical loading with temperature dependent material properties generates 25% and 15% more specific output power than temperature independent material properties for all cases of tapers.

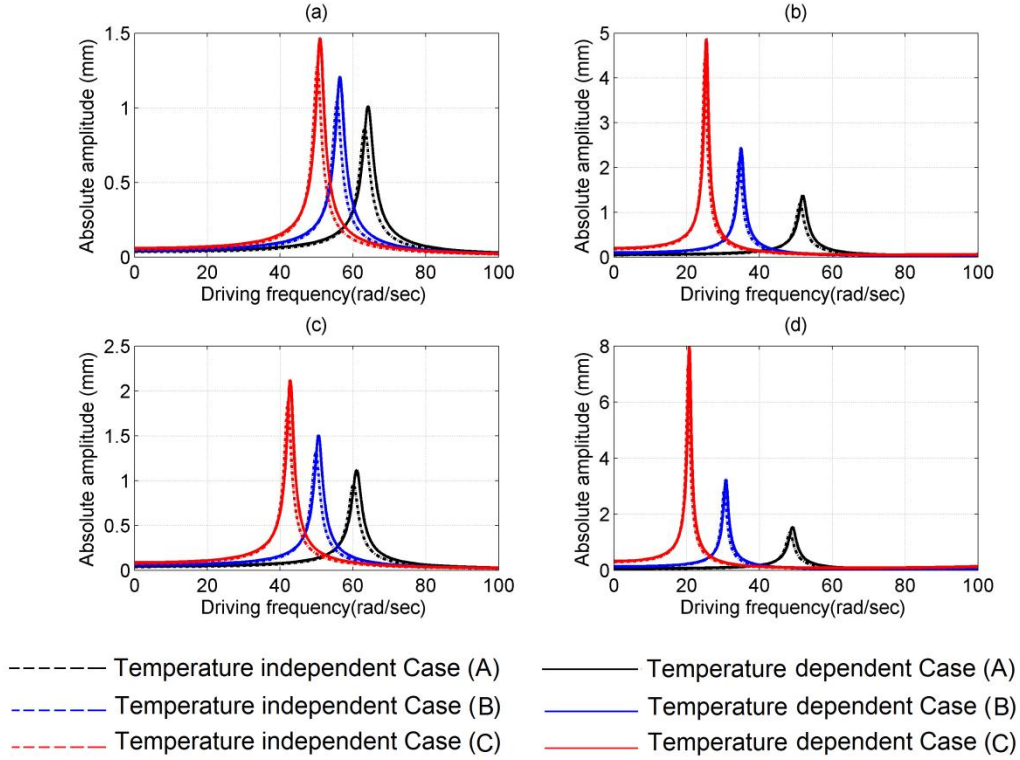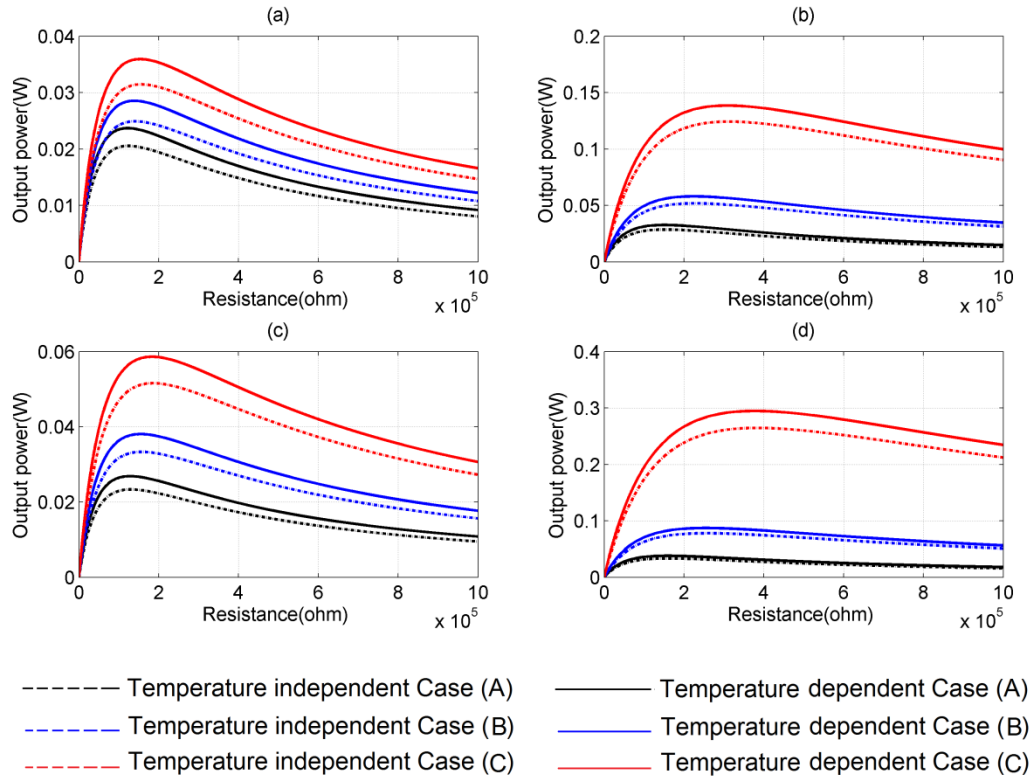Figure 6.48 Variation of output power with external load resistance of axially FG nonprismatic (Case (A),Case (B) and Case (C)) beams under thermo-mechanical loading for (a) c_b=0.1, c_h=0.1 (b) c_b=0.1, c_h=0.3 (c) c_b=0.3, c_h=0.1 and (d) c_b=0.3, c_h=0.3

Figure 6.48 (a-d) show the variation of output power with external load resistance for axially FG non-prismatic (Cases (A), (B) and (C)) piezolaminated beams subjected to mechanical and thermo-mechanical loading with pyroelectric effect. The output power of axially FG Case (C) under thermo-mechanical loading with temperature dependent material properties is 35.9363 mW, whereas with temperature independent material properties is 31.4566 mW for taper values of c_b = 0.1 and c_h = 0.1 shown in Figure 6.48 (a) and (b). However, with the same values of c_b and c_h the output power of axially FG Case (A) and Case (B) for mechanical loading and thermo-mechanical loading are 20.5476 mW, 23.6932 mW and 24.9095 mW, 28.5457 mW respectively. When, c_h increases to 0.3 the output power of axially FG Case (C) increases to 124.2968 mW and 138.496 mW under thermo-mechanical loading with temperature independent and dependent material properties respectively. Similarly, the output power of axially FG Case (A) and (B) varies as 28.6321 mW, 32.6653 mW and, 51.8313 mW, 58.0401 mW under thermo-mechanical loading with temperature independent and dependent material

properties, respectively. This indicates axially FG beams under thermo-mechanical loading with temperature dependent material properties generate more power than temperature independent material properties for a given values of cb and ch. Further, with an increase in ch, the output power of axially FG Case (C) increases 15% more whereas in Case (A) and Case (B), the output power increases 14% and 11% more, respectively. Figure 6.48 (c) represents the variation of power when c_b changes to 0.3. From Figure 6.48 (c) the output power of axially FG Case (C) changes to 51.5955 mW and 58.6314 mW while the output power of axially FG Case (A) and (B) increases to 23.3387 mW, 26.8728 mW and 33.3304 mW, 38.0714 mW under thermo-mechanical loading, respectively. In Figure 6.48 (d), when c_h increases to 0.3, the output power of axially FG Case (C) changes to 264.6845 mW and 294.7352 mW while the output power of axially FG Case (A) and (B) changes to 33.3757 mW, 38.0174 mW and 78.0562 mW, 87.273 mW under thermo-mechanical loading respectively. From the analysis, it is observed that in axially FG beam under thermo-mechanical loading, with increase in c_h, more power can be obtained compared to increase in c_b. It is also observed that simultaneous increase in c_b and c_h more output power can be scavenged in axially FG beams under thermo-mechanical loading with temperature dependent than temperature independent material properties. Also, axially FG Case (C) under thermo-mechanical loading generates 20% more power than case (A) and Case (B), respectively.

6.7.3   Time domain analysis

In time domain analysis, the tip displacement, output voltage and output power of the axially FG nonprismatic (Case (A), Case (B) and Case (C)) piezolaminated beam under thermo-mechanical loading with temperature independent and dependent material properties with pyroelectric effect have been compared and presented. For the analysis, the values for c_b, c_h, θ_t and θ_b are considered as 0.3, 0.3, 100^0C and 0^0C respectively. The average temperature has been taken as 50^0C.

6.7.3.1 Tip displacement response

-------- Impulse loading (Temp.independent material properties)

———————— Impulse loading (Temp. dependent material properties)

-·—·—·—·- Thermal loading (Temp.independent material properties)

———————— Thermal loading (Temp. dependent material properties)

-------- Combined impulse and thermal loading (Temp.independent material properties)

———————— Combined impulse and thermal loading (Temp. dependent material properties)

Figure 6.49 Tip displacement responses of axially FG piezolaminated beams with temperature independent and dependent material properties considering pyroelectric effect for c_b=0.3, c_h=0.3 of (a) Case (A) (b) Case (B) and (c) Case (C).

The tip displacement responses of axially FG beams (Case (A), Case (B) and Case (C)) with temperature independent and dependent material properties with pyroelectric effect in time domain for c_b= 0.3 and c_h= 0.3 are shown in Figure 6.49 (a-c). The tip displacements have been simulated for a time period of 5 sec as before. From Figure 6.49 (a), the peak amplitude of Case (A) under thermo mechanical loading with temperature independent material properties is 5.3e-3 mm and for temperature dependent material properties is 5.4e-3 mm. Similarly, for Case (B) and (C) the peak amplitude with temperature independent material properties are 10.3e-3 mm and 19.5e-3 mm, whereas with temperature dependent material properties are 10.4e-3 mm and 19.6e-3 mm as shown in Figure 6.49 (b) and (c) respectively. In view of the above results it is ascertain that the peak value of tip displacement under thermo mechanical loading with temperature dependent material properties is more compared to temperature

independent material properties for all cases of proposed beams. This is due to fact that as the young's modulus decreases with increase in temperature, the beam loses its stiffness than the original beam towards the free end. Therefore it is concluded that the deflection is more in temperature dependent material properties than temperature independent material properties. It is also observed that the time period of Case (C) under thermo mechanical loading is more compared to Case (A) and (B) beams for a given tapers.

6.7.3.2 Output voltage response

Figure 6.50 Output voltage responses of axially FG piezolaminated beams with temperature independent and dependent material properties considering pyroelectric effect for c_b=0.3, c_h=0.3 of (a) Case (A) (b) Case (B) and (c) Case (C).

The numerical analysis for output voltage responses of axially FG beams (Case (A), Case (B) and Case (C)) with temperature independent and dependent material properties with pyroelectric effect in time domain for c_b= 0.3 and c_h=0.3 are highlighted in Figure 6.50 (a-c). The output voltages have been simulated for a time period of 5 sec. From

Figure 6.50 (a), the peak output voltage of Case (A) under combined thermo mechanical loading with temperature independent material properties is 0.2667 V/mm whereas for temperature dependent material properties it is 0.2966 V/mm. Further, Case (B) and (C) beams have peak displacement values 0.3687 V/mm and 0.4737 V/mm with temperature independent material properties. However, for temperature dependent material properties these values are 0.4122 V/mm and 0.5332 V/mm as shown in Figure 6.50 (b) and (c) respectively. The output voltage, under thermo-mechanical loading with temperature dependent material properties is considerably more than temperature independent material properties for all cases of beams. This is due to the fact that an additional deflection of the beam is resulted due to thermal loading in the beam. Further, as the material property (Young's modulus) decreases with increase in temperature and the beam is axially FG, stiffness reduces towards the free end. Hence, more strain can be generated in the piezoelectric patch thereby increasing the output voltage.

6.7.3.3 Output Power responses
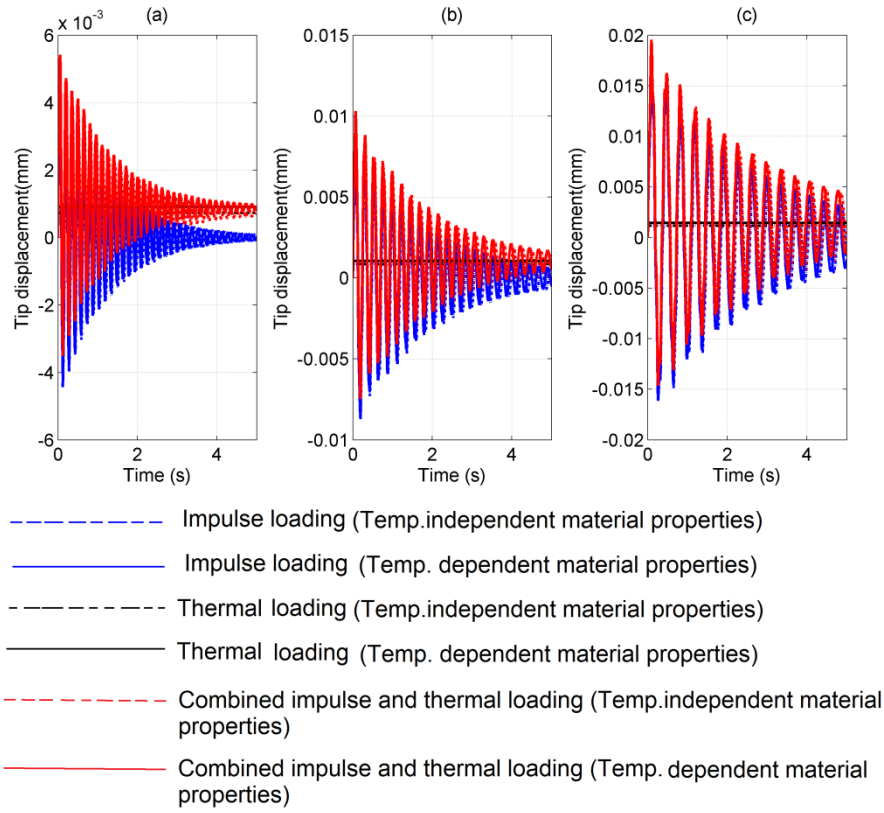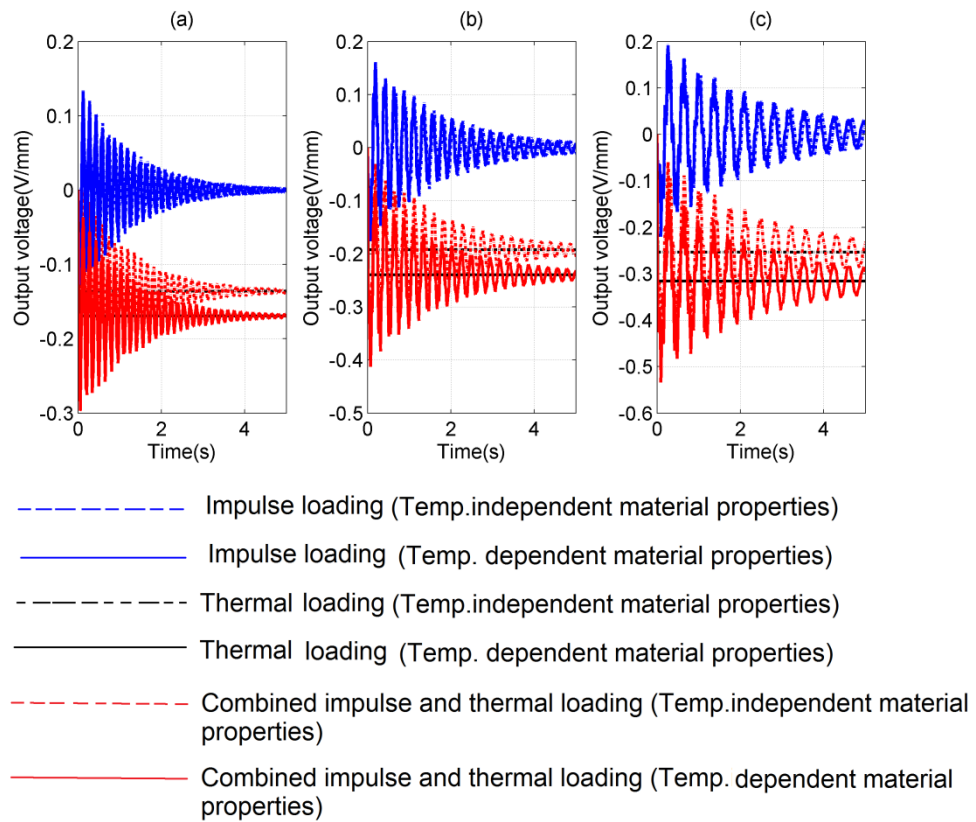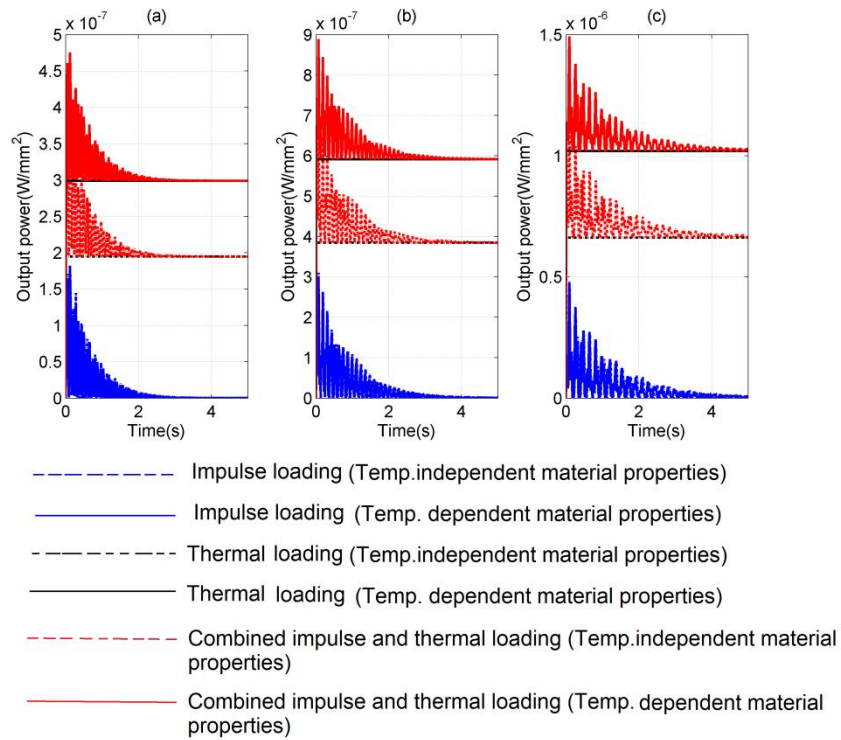

Figure 6.51 Output power responses of axially FG piezolaminated beams with temperature independent and dependent material properties considering pyroelectric effect for c_b=0.3, c_h=0.3 of (a) Case (A) (b) Case (B) and (c) Case (C).

The time histories of output power of axially FG beams (Case (A), Case (B) and Case (C)) with temperature independent and dependent material properties with pyroelectric effect for c_b= 0.3 and c_h= 0.3 are shown in Figure 6.51 (a-c). The simulation has been carried out for 5 sec as before. There are significant changes in output power for both temperature independent and dependent material properties as shown in Figure 6.51 (a-c).From Figure 6.51 (a), the peak output power of Case (A) under combined thermo mechanical loading with temperature independent material properties is 37.7e-8 W/mm2 and for temperature dependent material properties it is 47.6e-8 W/mm^2. For Case (B) and (C) the values are 69.4e-8 W/mm^2 and 114.5e-8 W/mm^2 for temperature independent material properties and 88.9e-8 W/mm^2 and 149.2e-8 W/mm^2 for temperature dependent material properties which are shown in Figure 6.51 (b) and (c) respectively. The output power under thermo mechanical loading with temperature dependent material properties is 30% more which is a remarkable change than temperature independent material properties for all proposed beams.

6.8 Chapter summary

The computer codes starting from finite element analysis of energy harvesting from prismatic and non-prismatic piezolaminated beams, homogeneous and axially FG non-prismatic piezolaminated beams under thermo-electro-mechanical loading have been validated with existing results available in the literatures. The results obtained are in good agreement with the existing results. Three types of cross-section profiles such as linear, parabolic and cubic with simultaneous variation of width and height tapers have been analysed to study the piezo-thermo-mechanical responses of such structures under different bottom and top surface temperatures. It has been observed that the combined thermo-mechanical loading laid significant impact in all cases of proposed profile cross sections than only mechanical loading. From the analysis, it has been observed that, axially FG beams in all cases of cross section profiles generate more output voltage and power than homogeneous profiles for arbitrarily chosen tapers. Further, the proposed beams generate more output voltage and power under thermo-mechanical loading than mechanical loading only for the same variation of tapers. It has also been observed that an improved output voltage and power can be obtained for the proposed beams, when the material properties vary with the average temperature found from the mean of top and bottom surface temperatures, respectively. Moreover, the cubic cross section profile

beam generates more output voltage and power than the linear and parabolic cross section profile beams.

Chapter 7

Electro-Mechanical Responses of Nonlinear Non-prismatic Axially FG Beam Structures

This chapter presents the results of nonlinear non-prismatic axially FG beams for energy harvesting. Based on the methodology developed (as discussed in Chapter 4) various responses have been obtained considering the effect of geometric nonlinearity. Initially the validation of the developed computer code which is capable of finite element analysis of nonlinear non-prismatic axially FG beam subjected to electro-mechanical loading have been presented. After validation of the developed code various coupled electro-mechanical responses of the modelled structures have been analyzed under mechanical loading.

7.1 Validation of present formulation

Based on the finite element formulations discussed in Chapter 4, a finite element code has been developed for nonlinear electro-mechanical analysis of non-prismatic axially FG piezolaminated beam for three different profile cross-sections (linear, parabolic and cubic). Further, a code has been developed for optimal harvesting of power from the mathematical formulations described in Chapter 5 for the said profile cross-sections. These two codes integrated lead to design and analysis of nonlinear non-prismatic axially FG piezolaminated beam for optimal harvesting of power from axially FG beam structures.

7.1.1 Structural validation

In this section the large deformation effect in the cantilever beam due to transverse load at its tip is investigated. For this purpose, a bimorph cantilever beam has been

considered made up of two PVDF layers (as shown in Figure 6.3).
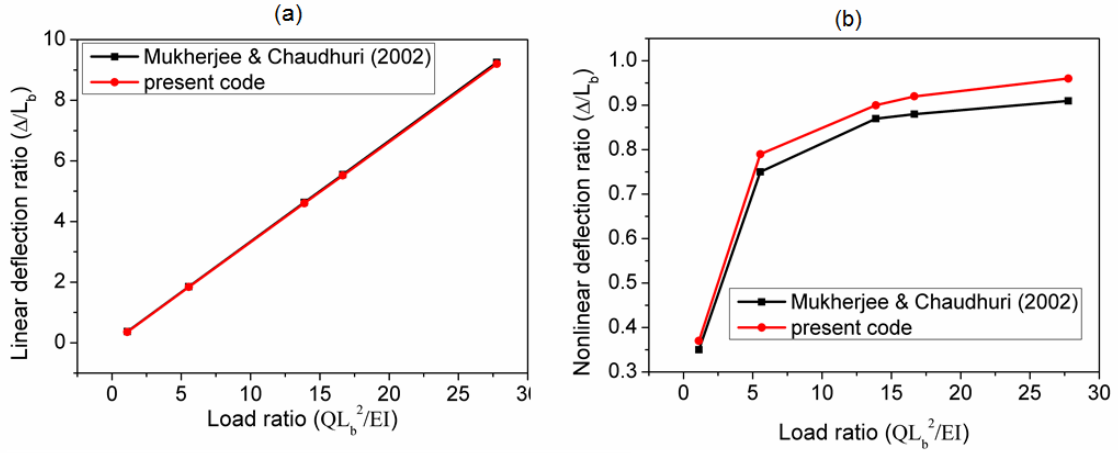
Figure 7.1 Comparison results of (a) linear (b) nonlinear deflection ratio responses for piezo bimorph cantilever beam.

The deflection ratios (Δ/L_b) for different values of load ratios (QL_b^2/EI) are shown in Figure 7.1 (a-b). The linear response result is compared with the existing result and is shown in Figure 7.1 (a) whereas, for nonlinear response the result is shown in Figure 7.1 (b). The results corroborate with the available existing results [108], and it is observed that the presently obtained results are comparable with the existing results.

7.2 Responses of axially functionally graded nonlinear non-prismatic beam

In this section, the static and dynamic responses (time domain responses) of proposed axially FG non-prismatic beams with geometric nonlinear effects are presented.

7.2.1 Static analysis

The tip displacements of the axially FG non-prismatic (Case (A),Case (B) and Case (C)) beams for both linear and nonlinear system with step load, have been discussed in this section. The displacement ratio (Δ/L_b; where Δ is the tip displacement) is the important criteria for distinction between linear and nonlinear systems. A comparative study is carried out for Cases (A), (B) and (C) with different values of c_b and c_h Figure 7.2 (a-d) show the variation of tip displacement of piezolaminated axially FG nonprismatic beam for above three cases with arbitrarily chosen taper values 0.1 and 0.3 in both width and height directions. To examine the large deformation effect, a varying transverse

impulse load up to 1 N is applied at the free end for all cases. It is observed from Figure 7.2 (a-d) that displacement ratio is less in the nonlinear system as compared to a linear one for all
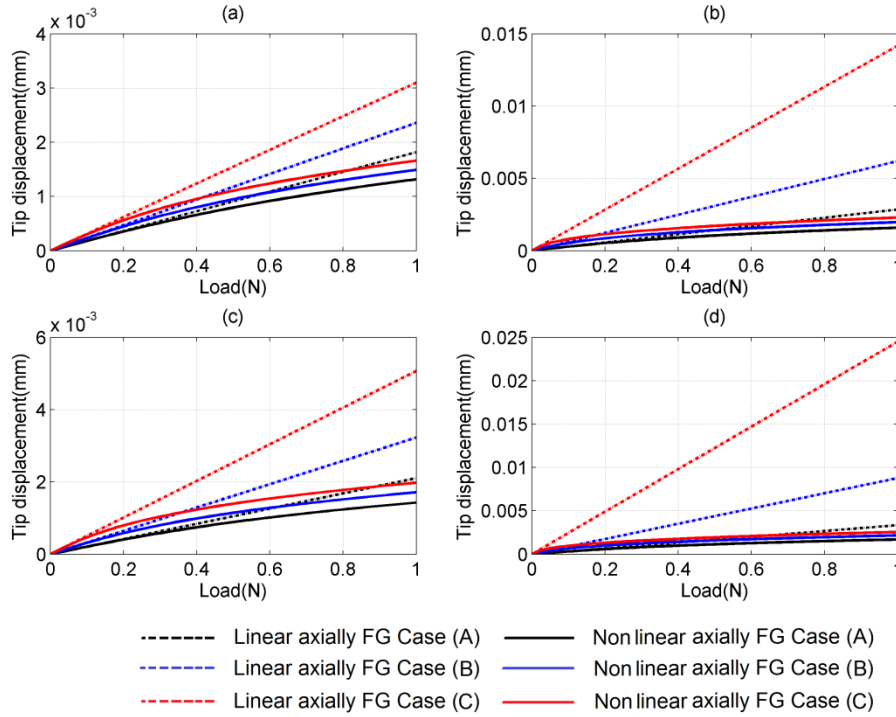
Figure 7.2 Variation of tip displacement with load of linear and nonlinear axially FG nonprismatic (Case (A),Case (B) and Case (C)) beams for (a) c_b=0.1, c_h=0.1 (b) c_b=0.1, c_h=0.3 (c) c_b=0.3, c_h=0.1 and (d) c_b=0.3, c_h=0.3

cases. It is due to the fact that for the nonlinear system, the vertical stiffness increases due to bending while preserving its overall length. On the contrary, the stiffness matrix in linear systems is independent of deflection. Due to the increased in stiffness value in the nonlinear system, the deflection is comparatively less than linear system. It is also observed that for a given width and height taper, the displacement ratio for Case (C) is more for both linear and nonlinear system as compared to other two cases. Further, if the taper value increases there is a significant change in displacement ratio for all cases.

7.2.2   Time domain analysis

In time domain analysis the tip displacement, output voltage and power of nonlinear axially FG non-prismatic (Case (A), Case (B) and Case (C)) piezolaminated beam subjected to mechanical loading for different taper values are presented.

7.2.2.1 Tip displacement response

Figure 7.3 Nonlinear transient tip displacement responses of axially FG nonprismatic (Case (A), Case (B) and Case (C)) beams for: for (a) c_b=0.1, c_h=0.1 (b) c_b=0.1, c_h=0.3 (c) c_b=0.3, c_h=0.1 and (d) c_b=0.3, c_h=0.3.

The tip responses of the piezo laminated cantilever beam for all cases (Cases (A), (B) and (C)) are also discussed in this section. The responses are shown in Figure 7.3 (a-d) for different taper values of c_b and c_h (such as 0.1, 0.3). The peak amplitude is obtained for all the cases considering geometric nonlinear effect of the beam. From Figure 7.3 (a-d), it is noticed that the period of vibration for Case (C) is more as compared to other cases for different taper values. The peak amplitude for the prismatic beam is 0.025e-4 mm. The peak amplitude for Case (C) is 0.043e-4 mm, whereas for Case (A) and Case (B), is the values are 0.03e-4 mm and 0.035e-4 mm for taper values of cb = 0.1 and ch = 0.1, respectively. When the height taper increased to 0.3, the peak amplitude for Case (C) is shifted to 0.0853e-3 mm, whereas for Case (A) and (B), the values are 0.04e-3 mm and 0.0607e-3 mm, respectively. Similarly, the peak amplitude for Case (C) is 0.0606e-4 mm, whereas for Case (A) and Case (B) are 0.0338e-3 mm and 0.0451e-3 mm for taper

values of $c_b = 0.1$ and $c_h = 0.3$, respectively. When the c_b increases to 0.3, the peak amplitude for Case (C) is shifted to 0.105e-3 mm, whereas for Case (A) and (B) the values are 0.0436e-3mm and 0.0728e-3 mm. From this analysis, it is evident that with an increase in c_h, peak amplitude is more for Case (C).

7.2.2.2 Output voltage response
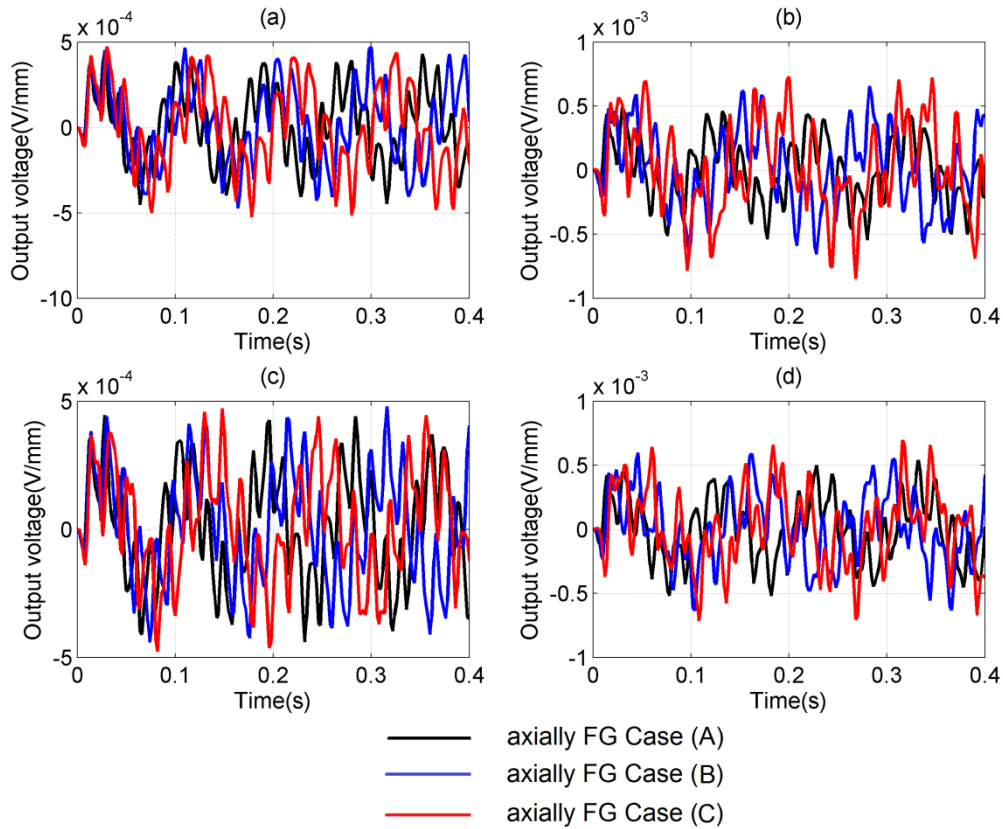
Figure 7.4. Nonlinear transient output voltage responses of axially FG nonprismatic (Case (A), Case (B) and Case (C)) beams for: for (a) c_b=0.1, c_h=0.1 (b) c_b=0.1, c_h=0.3 (c) c_b=0.3, c_h=0.1 and (d) c_b=0.3, c_h=0.3.

Voltage is produced in the piezoelectric patch when it is strained. The generated voltage is responsible for current flow through the electric circuit which is meant for power generation. Again, the amplitude of generated voltage depends on the cross section profile of the beam. This section provides a comparative study of voltage of piezo laminated beam by considering Cases (A), (B) and (C). The piezoelectric patch is attached near the clamped end of the beam where it experiences a maximum value of strain. As the beam vibrates, the charge gets accumulated over the surface of the piezoelectric patch from which the voltage can be calculated. By using equation (4.54),

the voltage generated in the piezoelectric patch is determined by the electro-mechanical coupling. Figure 7.4 (a-d) show the voltage responses in time domain for taper values of 0.1 and 0.3 respectively. From Figure 7.4 (a-d), it is observed that the peak voltage for Case (C) increases around 80% more with taper values cb = 0.3 and ch = 0.3, whereas for Case (A) and (B) the peak voltages are of 32% and 58% more respectively. From this analysis, it is concluded that the peak voltage for Case (C) is more as compared to Case (A) and Case (B).
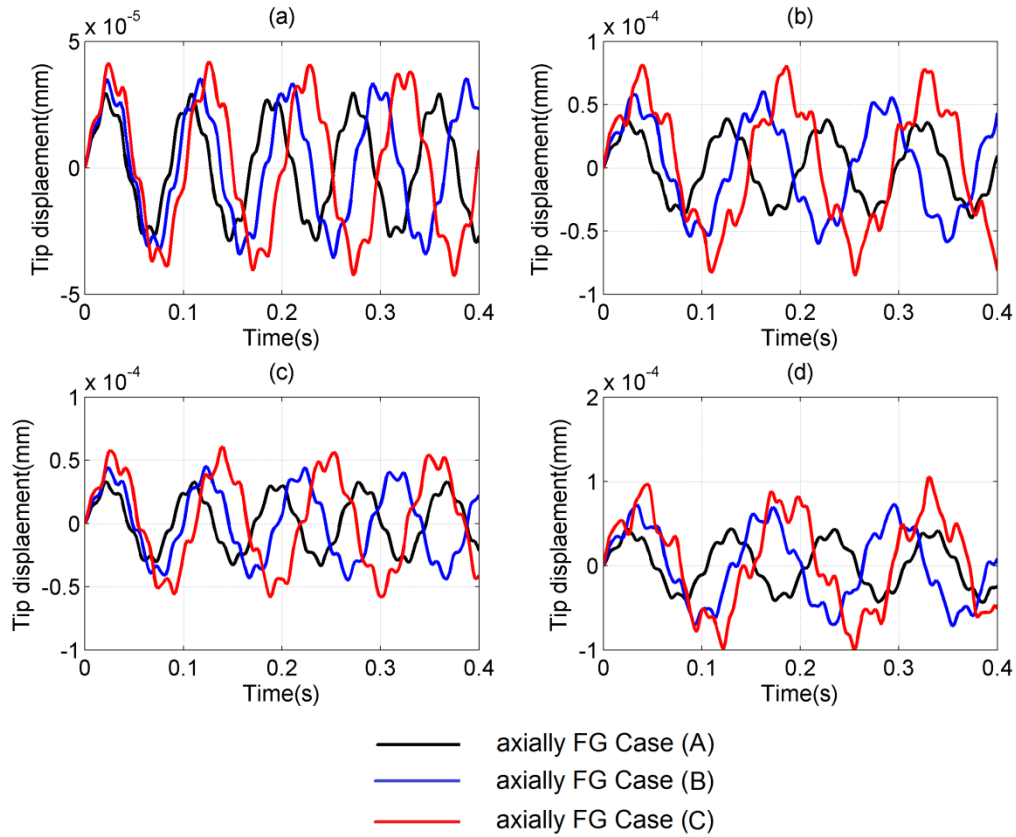
7.2.2.3 Output Power responses
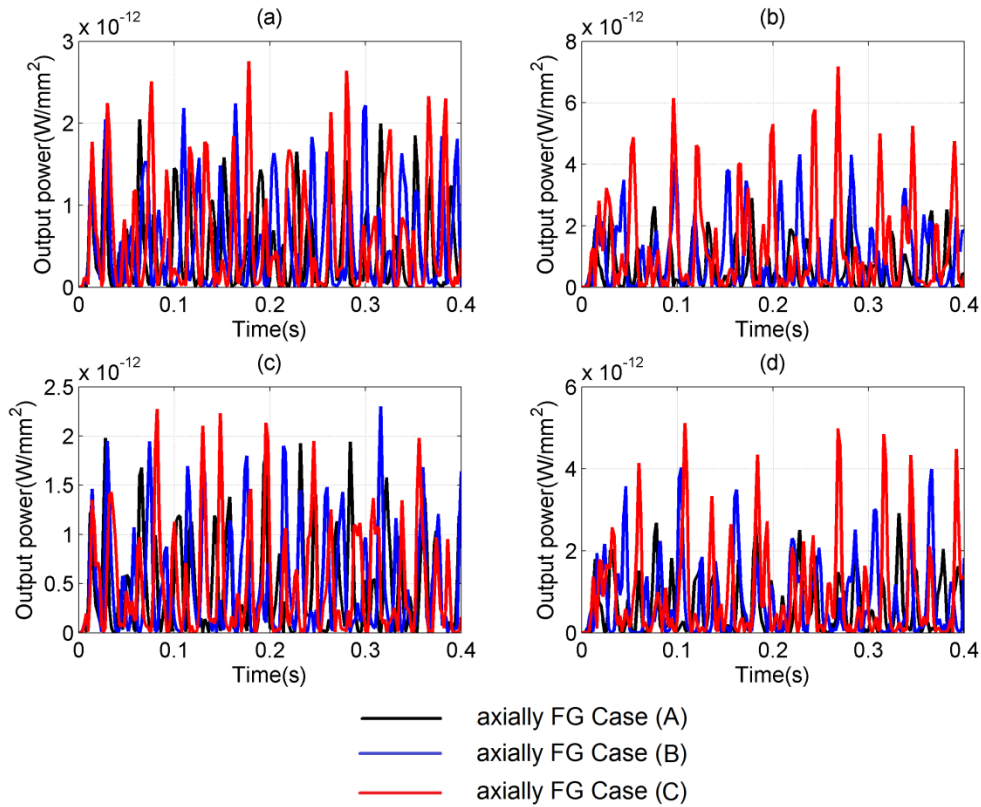
Figure 7.5 Nonlinear transient output power responses of axially FG nonprismatic (Case (A), Case (B) and Case (C)) beams for: for (a) c_b=0.1, c_h=0.1 (b) c_b=0.1, c_h=0.3 (c) c_b=0.3, c_h=0.1 and (d) c_b=0.3, c_h=0.3.

Figure 7.5 (a-d) depicts the output power responses of axially FG non-prismatic (Case (A), Case (B) and Case (C)) piezolaminated beams subjected to a transverse impulse load of 1 N with due consideration of geometric nonlinear effects. The response can be found by taking the constant external load resistance as 1 kΩ. From Figure 7.5 (a-d), it is

observed that the peak output power of Case (C) increases more than 50% with taper values c_b= 0.3 and c_h= 0.3, whereas for Case (A) and (B) the variations are of 25% and 38% more respectively. From this analysis, it is concluded that the peak output power of Case (C) is more compared to Case (A) and Case (B).

7.3 Chapter summary

This chapter depicts the energy harvesting from nonlinear finite element analysis of the proposed axially FG non-prismatic (linear, parabolic and cubic profile cross sections) beams. The computer code developed has been validated with the existing available literatures. The results obtained are in close agreement with the existing result. From the analysis it has been observed that geometric nonlinearity influences the output voltage and power for all cases of arbitrarily taken tapers. Moreover, the axially FG cubic profile beam generates more voltage and power compared to axially FG linear and parabolic profile beams.

Chapter 8

Optimal Output Power using Real Coded Genetic Algorithm

The present chapter depicts two sections illustrating the results of optimal power harvesting from proposed non-prismatic axially FG piezolaminated and nonlinear non-prismatic axially FG piezolaminated beams using real coded GA. Based on the methodology (as discussed in Chapter 5), the optimal output powers have been obtained from the proposed beams.

8.1 Optimal output power from axially FG nonprismatic beams

Based on the methodology discussed in Chapter 5, it has been observed that the output power from the proposed piezolaminated beam is influenced by several design variables such as c_b, c_h, R, tp, k and np. From the previous discussion in Chapter 6, it has been predicted that for every design variables, an optimum solution for output power can be obtained. However, it is difficult to predict the combination of best possible design variables for optimal output power. Therefore, a real coded GA based optimization technique has been proposed to obtain the best possible design variables for harvesting optimal output power. The mechanical, electrical and thermal properties used in this study have been presented in Table 6.7.

8.1.1 Optimal output power under impulse loading and combined impulse-thermal loading.

The present section includes the comparison of optimal output power from axially FG non-prismatic beams under impulse and combined impulse thermal loading. It should be noted that the parameter vector is restricted in a range of values based on the physical meaning. The ranges of c_b, c_h, R, t_p, np and k have been taken for the analysis

as $0 \leq c_b \leq 0.8$, $0 \leq c_h \leq 0.8$, $0 \leq R \leq 100000$, $0.0001 \leq t_p \leq 0.0004$, $1 \leq np \leq 10$ and $1 \leq k \leq 10$, respectively. The crossover and the mutation probability have been taken as 0.8 and 0.3 respectively. In the case of thermal loading, the bottom and top surface temperatures are taken such that $t_b = 0^0 C$ and $t_p = 100^0 C$. The allowable stresses of beam and PZT materials have been considered as 550 MPa and 14 MPa, respectively [137] .The allowable open circuit voltage of PZT material has taken as 500-1000 V per 1 mm piezo thickness [138].

Figure 8.1 Comparison of fitness values of axially FG nonprismatic (Case (A), (B) and (C)) beam under impulse and combined impulse-thermal loading.

In order to obtain the best set of design parameters and fitness value using real coded GA, a computer code has been developed. Figure 8.1 compares variation of fitness with number of generations for axially FG non-prismatic Case (A), (B) and (C) beams.

Table 8.1 Optimal parameters of axially FG non-prismatic (case (A),(B) and (C)) beam under impulse and combined impulse-thermal loading.

	c_b	c_h	$R(\Omega)$	$t_p(m)$	k	np	P_2 (W)
GA based optimized design variables for impulse loading							
Case (A)	0.641	0.00183	99993.8	0.0018	8.585	4.937	0.4163
Case (B)	0.364	0.00068	99670.1	0.0017	4.587	1.248	0.4271
Case (C)	0.289	3.99e-05	99612.7	0.0018	4.082	3.698	0.4441
GA based optimized design variables for combined impulse-thermal loading							
Case (A)	0.291	0.00109	99594	0.0026	1.0687	3.450	1.5398
Case (B)	0.1041	3.96e-04	99885	0.0025	1.255	4.8965	1.5422
Case (C)	0.150	9.59e-05	99945	0.0025	1.2459	4.992	1.5555

The best fitnesses for above three cases have been obtained by taking one hundred populations with five runs. From Figure 8.1, it has been observed that the fitness shows a steady value after 250 generations. The obtained optimal parameters along with the fitness values are presented in Table 8.1. It is observed that beams under combined impulse-thermal loading generate more output power using the design variables obtained from the developed real coded GA method than impulse loading. Moreover, the axially FG Case (C) beam generates more power than Case (A) and Case (B) beams. The optimal output responses (such as voltage, current and power) of axially FG non-prismatic Case (C) under combined impulse-thermal loading in time domain are shown in Figure 8.2-,Figure 8.4.

Figure 8.2 Optimised output voltage response of axially FG (Case (C)) beam under combined impulse-thermal loading.

Figure 8.3 Optimised output current response of axially FG (Case (C)) beam under combined impulse-thermal loading.

Figure 8.4 Optimised output power response of axially FG (Case (C)) beam under combined impulse-thermal loading.

8.1.2   Optimal output power under combined impulse-thermal loading with temperature independent and dependent material properties

The present section describes the optimal output power from axially FG non-prismatic beams under combined impulse-thermal loading with temperature independent and dependent material properties. The average temperature has been taken as 50^0C. The

ranges of c_b, c_h, R, t_p, np and k have been taken for the analysis as $0 \le c_b \le 0.8$, $0 \le c_h \le 0.8$, $0 \le R \le 100000$, $0.0001 \le t_p \le 0.0004$, $1 \le np \le 10$ and $1 \le k \le 10$, respectively as described in section 8.1.1.
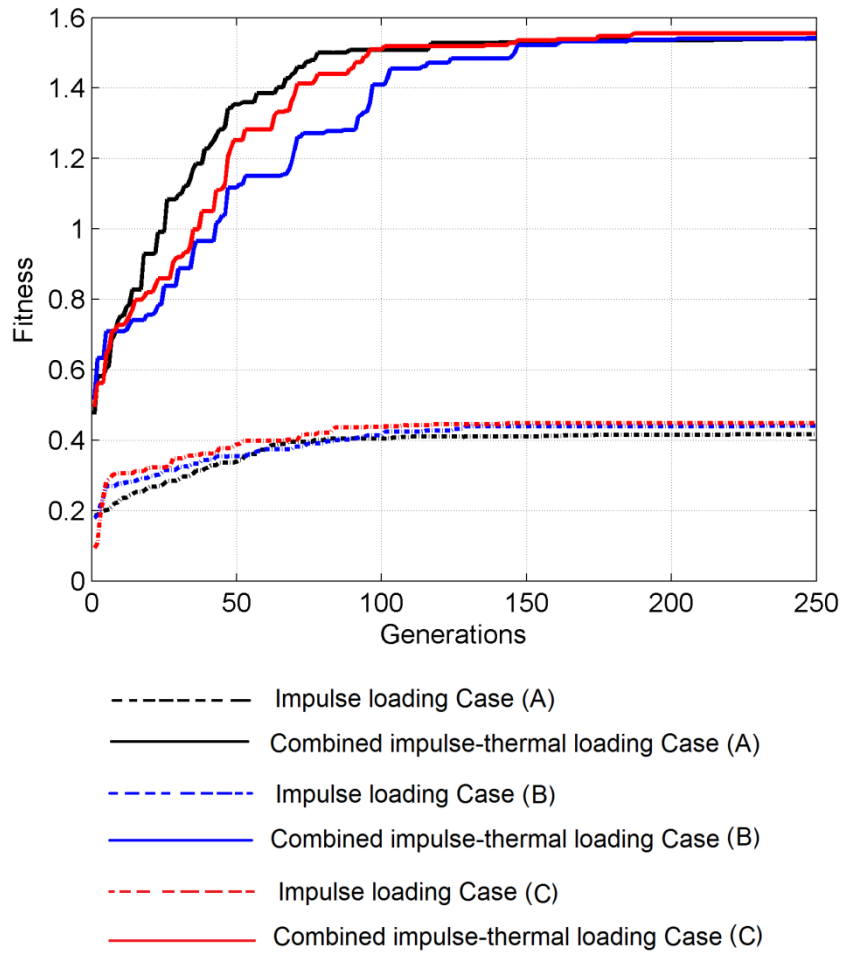

Figure 8.5 Comparison of fitness values of axially FG nonprismatic (Case (A), (B) and (C)) beam under combined impulse and thermal loading.

To obtain the best set of design parameters and fitness value using real coded GA, a computer code has been developed. Figure 8.5 compares fitness values with generation variation of axially FG non-prismatic Case (A), (B) and (C) beams under combined impulse-thermal loading with temperature independent and dependent material properties. The best fitnesses for above three cases have been obtained by taking 100 populations with five runs. From the Figure 8.5, it has been observed that the fitness

shows a steady value after 250 generations. The obtained optimal parameters along with the fitness values are presented in Table 8.2. Further, a comparison of output powers has been made between the proposed beams under combined impulse-thermal loading with temperature independent and dependent material properties using the developed real coded GA method. The obtained results have been listed in Table 8.2. Table 8.2, shows that more output power can be obtained from the beams under combined impulse-thermal loading with temperature dependent material properties.

Table 8.2 Optimal parameters of axially FG non-prismatic (case (A),(B) and (C)) beam under combined impulse-thermal loading with temperature independent and dependent material properties.

GA based optimized design variables for combined impulse-thermal loading with temperature independent material properties							
	c_b	c_h	$R(\Omega)$	$t_p(m)$	k	np	P_2 (W)
Case (A)	0.291	0.00109	99594	0.0026	1.0687	3.450	1.5398
Case (B)	0.1041	3.96e-4	99885	0.0025	1.255	4.8965	1.5422
Case (C)	0.150	9.59e-5	99945	0.0025	1.2459	4.992	1.5555
GA based optimized design variables for combined impulse-thermal loading with temperature dependent material properties							
Case (A)	0.201	0.004737	99551.6	0.00199	1.4058	7.55269	2.3489
Case (B)	0.101	1.17e-03	99302.2	0.00197	1.0235	2.37031	2.3720
Case (C)	0.141	1.22e-04	99785.5	0.00196	2.1646	7.08133	2.3794

Moreover, the axially FG Case (C) beam with temperature dependent material properties generate 50% more power compared to beam with temperature independent material properties under combined impulse-thermal loading. The optimal output responses (such as voltage, current and power) of axially FG nonprismatic Case (C) have been shown in Figure 8.6- Figure 8.8.
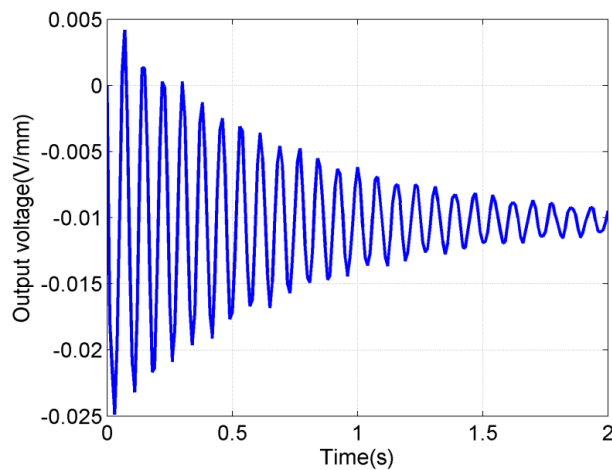
Figure 8.6 Optimised output voltage response of axially FG Case (C)) beam under combined impulse and thermal loading.
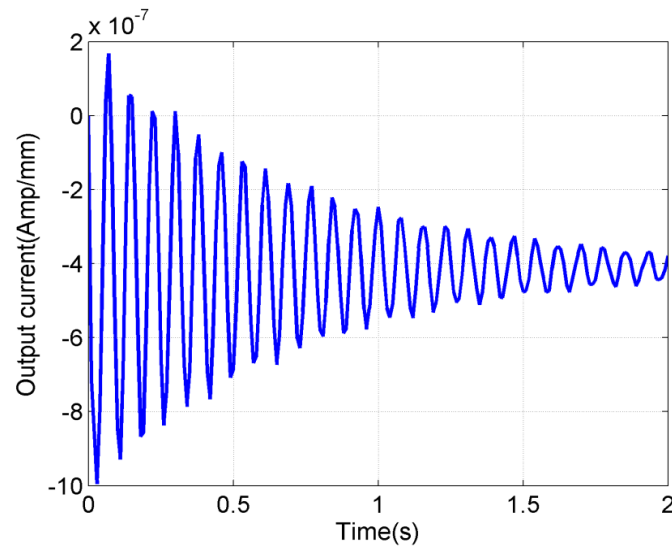

Figure 8.7 Optimised output current response of axially FG Case (C)) beam under combined impulse and thermal loading.
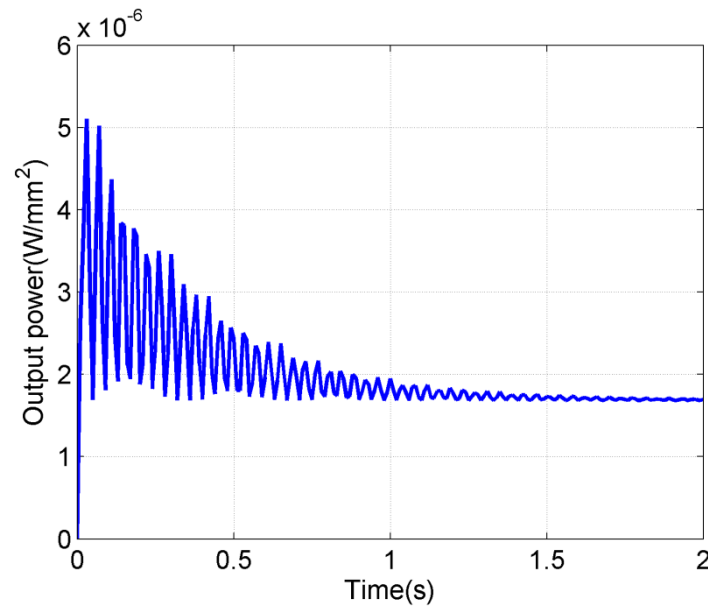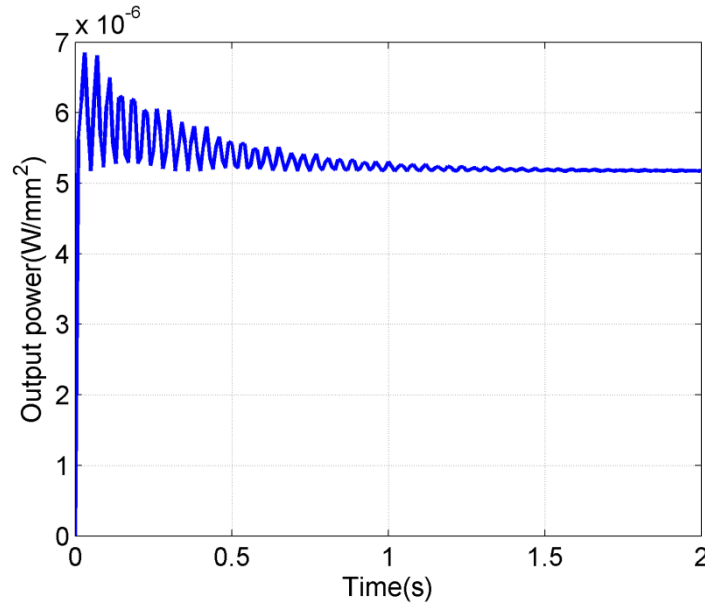
Figure 8.8 Optimised output power response of axially FG Case (C)) beam under combined impulse and thermal loading.

8.2 Optimal output power from axially FG nonprismatic beams with geometric nonlinearity.

Based on the methodology discussed in Chapter 5, it has been observed that the output power from the proposed piezolaminated beam is influenced by several design variables such as c_b, c_h, R, tp, k and np. From the previous discussions in Chapter 7, it has been predicted that for every design variables, an optimum solution for output power can be obtained. However, it is difficult to predict the combination of best possible design variables for optimal output power. Therefore, a real coded GA based optimization technique has been proposed to obtain the best possible design variables for harvesting optimal output power. This section describes the optimal output power from nonlinear axially FG non-prismatic beams under impulse loading. It should be noted that the design variable vectors are restricted in a range of values based on the physical meaning.
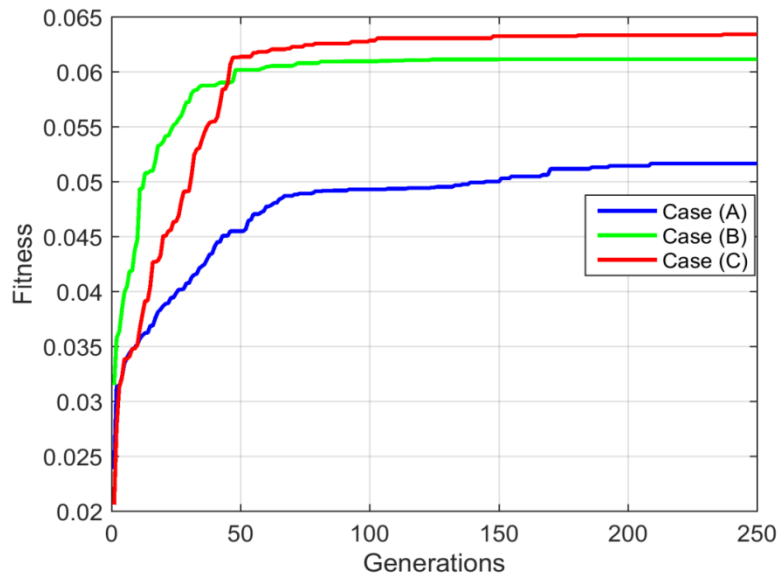
Figure 8.9 Comparison of fitness values of nonlinear axially FG nonprismatic (Case (A), (B) and (C)) beam under impulse loading.

The ranges of c_b, c_h, R, t_p, np and k are taken for the analysis such that $0 \leq c_b \leq 0.8$, $0 \leq c_h \leq 0.8$, $0 \leq R \leq 100000$, $0.0001 \leq t_p \leq 0.0004$, $1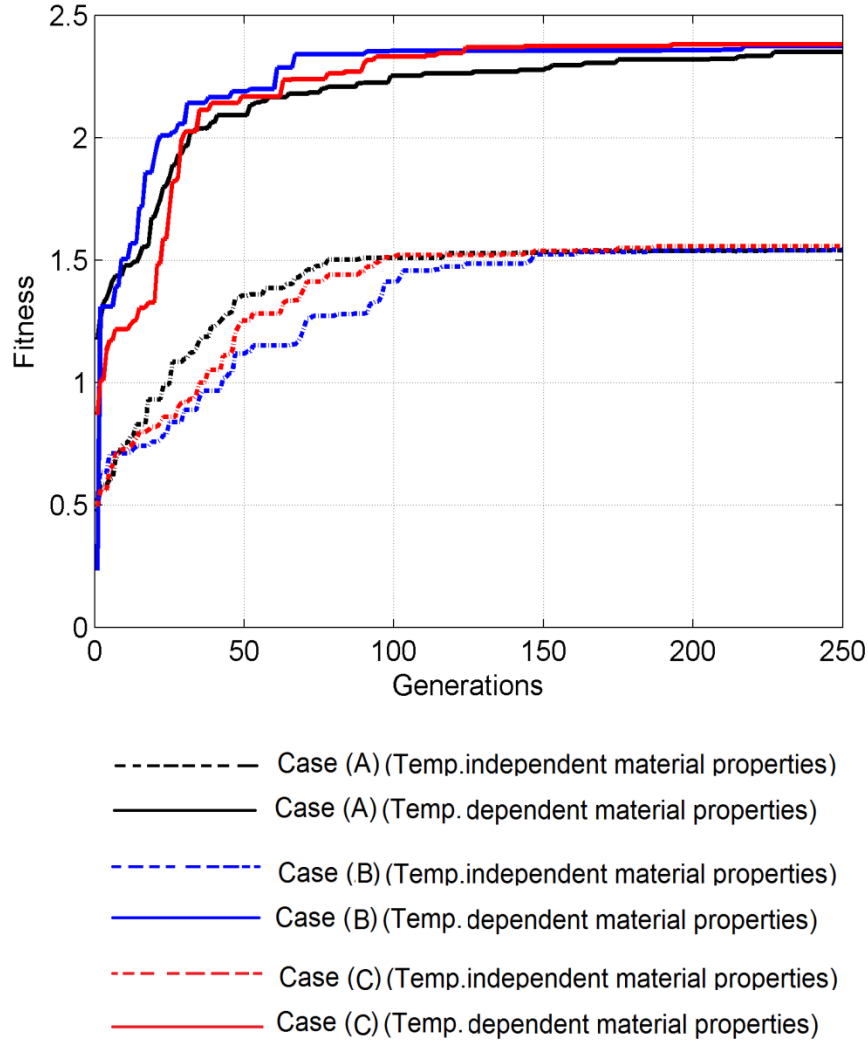 \leq np \leq 10$ and $1 \leq k \leq 10$, respectively. In order to get the best set of design parameters and fitness value using real coded GA, a computer code has been developed. Figure 8.9 compares fitness values with generation variation of nonlinear axially FG non-prismatic Case (A), (B) and (C) beams. The best fitnesses for above three cases have been obtained by taking 100 populations with 5 runs. Figure 8.9 shows that the fitness has a steady value after 250 generations.

Table 8.3 Optimal parameters of nonlinear axially FG non-prismatic (case (A),(B) and (C)) beam.

	c_b	c_h	$R(\Omega)$	$t_p(m)$	k	np	P_2 (W)
Any arbitrary values of design variables (Trial and Error Method)							
Case (A)	0.0753	0.0692	90245.9	0.0016	1.27	0.422	0.0153
Case (B)	0.0753	0.0692	90245.9	0.0016	1.27	0.422	0.0168
Case (C)	0.0753	0.0692	90245.9	0.0016	1.27	0.422	0.0184
GA based optimised design variables							
Case (A)	0.7998	0.0013	99992.4	0.0016	4.08	9.983	0.051
Case (B)	0.0753	6.70e-05	99989.8	0.0027	8.57	7.845	0.061
Case (C)	0.0753	1.00e-04	99986.2	0.0022	5.98	5.989	0.063

The obtained optimal parameters along with the fitness values are presented in Table 8.3. A comparison of output powers has also been made between the trial and error and the developed real coded GA method, which is also listed in the same table. We find that more power can be obtained using the developed real coded GA than trial and error method of the proposed beam. Moreover, the nonlinear axially FG Case (C) beam generates approximately 20% more power compared to Case (A) and Case (B) beams. Further the optimal output responses (such as voltage, current and power) of nonlinear axially FG nonprismatic Case (C) have been demonstrated in Figure 8.10- Figure 8.12.
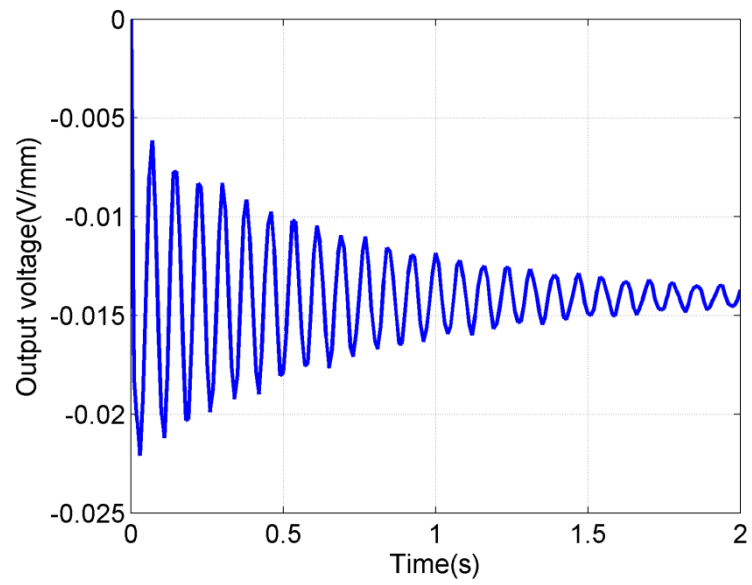

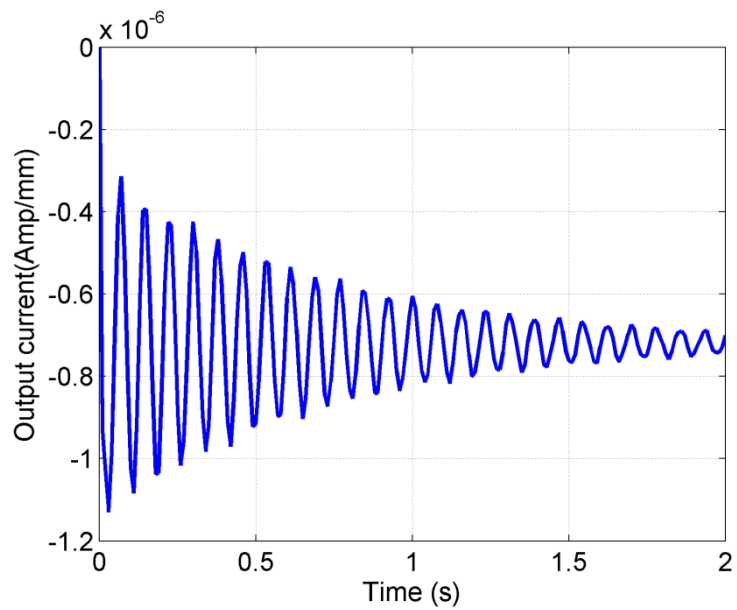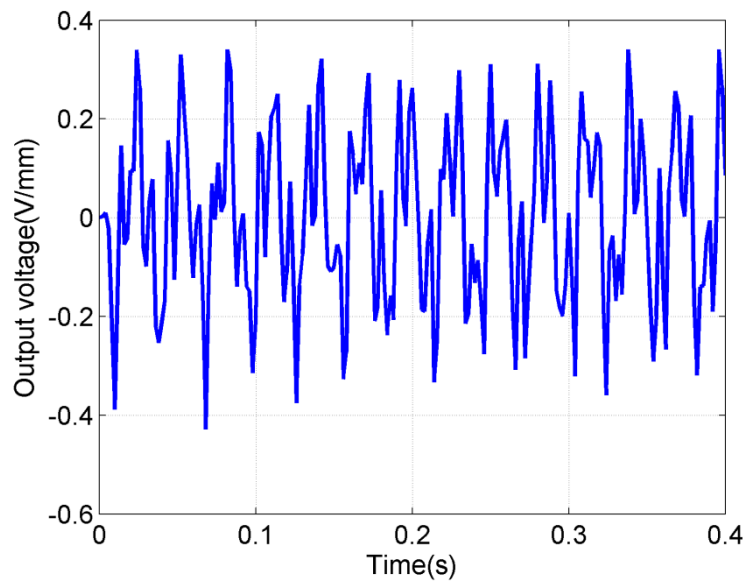Figure 8.10 Optimised output voltage response of nonlinear axially FG Case (C)) beam under impulse loading.
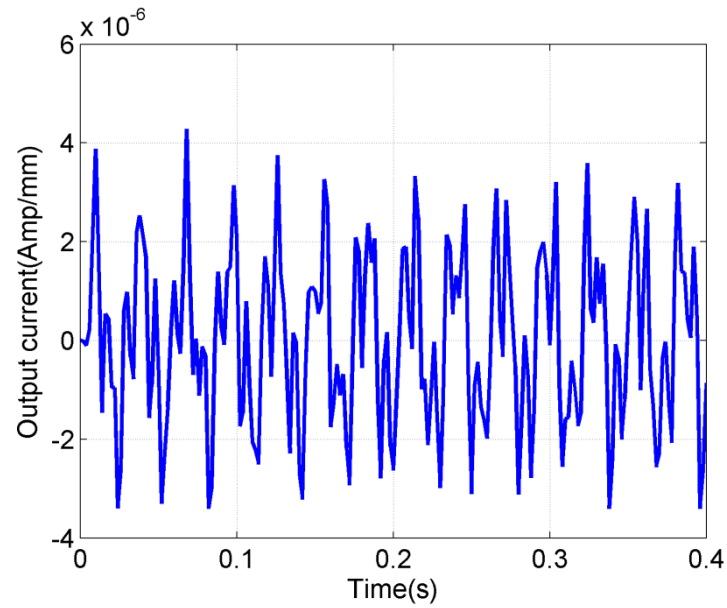
Figure 8.11 Optimised output current response of nonlinear axially FG Case (C)) beam under impulse loading.
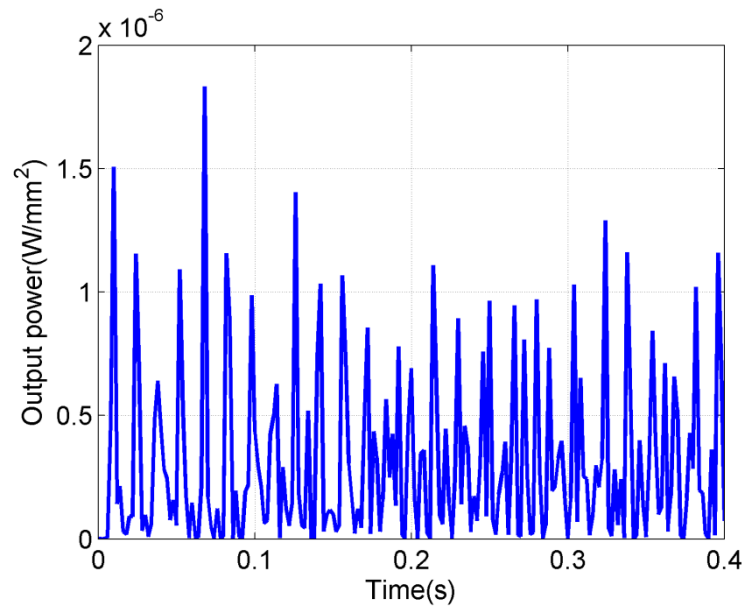
Figure 8.12 Optimised output power response of nonlinear axially FG Case (C)) beam under impulse loading.

8.3 Chapter summary

This chapter highlights the optimal energy harvesting using real coded GA based constrained optimization technique from the proposed axially FG nonprismatic, i.e., Case

(A), (B) and (C) profile beams. A detailed comparison has been made between beams under impulse and combined impulse-thermal loading to get the optimised parameters for maximising the output power. Furthermore, the analysis has been carried out for the comparison between beams under combined impulse-thermal loading with temperature independent and dependent material properties. From the numerical analysis, it has been seen that more output power can be obtained using the proposed methodology compared to the conventional trial and error method. Moreover, axially FG Case (C) profile beam under combined impulse- thermal loading generates an improved power compared to other cases of beams. The influence of geometric nonlinearity on output power has been discussed as well. It has been noticed that, with consideration of geometric nonlinearity, the GA based constrained optimization technique generates more power than the conventional trial and error method. Furthermore, the axially FG cubic profile beam generates more output power than the other two cases of beams.

Chapter 9

Conclusion and Scope for Further Work

This chapter presents the important conclusions based on the finite element analysis and optimal vibration energy harvesting for different cross section profiles using the methodologies developed in the present work. The scope of future work in this direction has also been presented in the subsequent sections.

9.1 Conclusion

The two noded FE based axially FG (based on proposed power law) non-prismatic (such as linear, parabolic and cubic) piezolaminated cantilever beam has been analysed for output power under thermo-mechanical loading using Hamilton's principle. Further, the nonlinear finite element based analysis of axially FG non-prismatic piezolaminated beam has been performed using classical beam theory with Von-Karman's nonlinear strain-displacement relationships for output power. A real coded GA based constrained optimization scheme with simulated binary crossover and parameter based mutation has been developed for optimal design variables in order to maximize the output power. A complete computer code starting from FE based axially FG non-prismatic piezolaminated beams under thermo-mechanical loading for output power, nonlinear FE based axially FG nonprismatic piezolaminated beams under mechanical loading and optimal output power from the axially FG non-prismatic piezolaminated beams has been developed. The developed code has been validated before using it for analysis and design of proposed axially FG beams for output power. After validation of the developed code the detailed analysis has been carried out for all proposed cross section profiles. From the theoretical and computational simulation analysis some important conclusions are drawn as follows.

- Combined variations of tapers have significant effect on the frequency and deflection of the piezolaminated beam.

- The fundamental frequency of Case (C) profile beam is less compared to the Case (A) and (B).

- The tip deflection of piezolaminated proposed profile cantilever beams is more than the prismatic beam for a given applied load condition.

- For a given load condition, the strain developed in the piezolaminated patch is more in Case (C) profile beam than other two proposed beams.

- The voltage developed in the piezoelectric patch is more in Case (C) profile beams.

- The output power generated in Case (C) profile piezolaminated beam has got more value than other two profile beams for a given external load resistance.

- The external load resistance has a significant effect on output power. There is an optimum resistance for which the output power is maximum.

- The optimum output power obtained is inversely proportional to the external load resistance.

Based on the variation of material properties in axial direction using the proposed power law based formula for all cases of profile beams, some important observations are laid down as follows.

- The power gradient index and the integer parameter have significant effect on the material properties of the axially FG nonprismatic beam.

- For a given integer parameter with increase in power gradient index, the material properties decreases towards the free end of the beam.

- The natural frequencies of axially FG nonprismatic proposed beams are less than the nonprismatic homogeneous beams.

- For a given load condition the axially FG nonprismatic proposed beams have more static deflection than the nonprismatic homogeneous beams. The voltage generated from the axially FG nonprismatic proposed beams are more compared to the nonprismatic homogeneous beams for a given load condition.

- The output power generated from the axially FG nonprismatic proposed beams are more compared to the nonprismatic homogeneous beams for a given external load resistance as well.

Further, some important observations are made for the proposed axially FG beams under impulse-thermal loading condition for energy harvesting.

- The static deflection of the axially FG beam under impulse-thermal loading is significantly more than impulse loading.

- The output voltage generated for Case (C) axially FG profile beam under impulse-thermal loading is also more than other axially FG profile beams.

- For Case (C) axially FG profile beam under impulse-thermal loading generates more power than other proposed axially FG profile beams.

The effect of temperature on material properties plays a predominant role when it is exposed to extreme hot or cold conditions for energy harvesting. Based on above some of the important observations are presented as follows.

- With increase in temperature the Young's modulus of the beam decreases. There is an increasing tendency of Poisson's ratio and coefficient of thermal expansion with increase in temperature.

- The static deflection of axially FG beams under combined impulse-thermal loading with temperature dependent material properties are more than temperature independent material properties.

- More output voltage and power can be obtained from the axially FG Case (C) profile beam under impulse-thermal loading with temperature dependent material properties.

Based on the effect of geometric nonlinearity on the proposed cross section profile piezolaminated axially FG beams some of the important observations are summarized as follows.

- Due to presence of nonlinearity, the static tip deflection of the beam reduces with increase in load.

- The geometric nonlinearity has a pronounced effect on output voltage and power for all tapers of axially FG nonprismatic beams.

- There is decreasing trend in output voltage and power for all cases of axially FG nonprismatic beams due to geometric nonlinearity.

Based on the concept of real coded GA based constrained optimization scheme for maximising the output power, some of the important observations are summarized as follows.

- The optimised output powers of axially FG nonprismatic beam are more compared to homogeneous beams.

- The optimised output powers of axially FG nonprismatic beam under combined impulse-thermal loading are more compared to impulse loading.

- The optimised output powers of axially FG nonprismatic beam under combined impulse-thermal loading with temperature dependent material properties are significantly high compared temperature independent material properties.

- For all cases, the optimised output power of Case (C) profile beam is more compared than Case (A) and (B).

- The axially FG Case (C) profile beam considering geometric nonlinearity generates considerably more power than axially FG Case (A) and (B) profile beams.

Finally, it can be concluded that more output power can be scavenged from axially FG nonprismatic profile piezolaminated beams under combined impulse-thermal loading with temperature dependent material properties. Furthermore, from the comparative study it is observed that Case (C) profile beam generates more output power than other profile piezolaminated beams.

9.2 Scope of further work

- In continuation to the present model, power generation for any arbitrary forcing function can be established (such as base excitation, wind pressure and transient thermal loading.)

- An accurate method for estimating damping ratio of the models with nonlinear effect needs further investigation. Damping ratio for a structure needs to be well estimated before using the model for predicting power generation.

- In the field of power generation, nano-tube reinforced piezoelectric energy harvester is a promising one since nanotubes can generate higher strain than PZT transducers due to their notable mechanical properties.

- More application for the use of the generated power need to be determined. Though the generated power is less it can be used intermittently if stored for a longer time.

- Modelling of vibration energy harvesting in the presence of nonlinear storage circuit need to be examined.

- Nonlinear vibration energy harvesting under thermal loading need to be examined.

References

[1]   S. Roundy, P. K. Wright, and J. Rabaey, "A study of low level vibrations as a power source for wireless sensor nodes," *Computer communications,* vol. 26, pp. 1131-1144, 2003.

[2]   H. A. Sodano, D. J. Inman, and G. Park, "A review of power harvesting from vibration using piezoelectric materials," *Shock and Vibration Digest,* vol. 36, pp. 197-206, 2004.

[3]   I. Chopra, "Review of state of art of smart structures and integrated systems," *AIAA journal,* vol. 40, pp. 2145-2187, 2002.

[4]   S. R. Anton and H. A. Sodano, "A review of power harvesting using piezoelectric materials (2003–2006)," *Smart materials and Structures,* vol. 16, p. R1, 2007.

[5]   S. Priya, "Advances in energy harvesting using low profile piezoelectric transducers," *Journal of electroceramics,* vol. 19, pp. 167-184, 2007.

[6]   N. S. Shenck and J. A. Paradiso, "Energy scavenging with shoe-mounted piezoelectrics," *IEEE micro,* pp. 30-42, 2001.

[7]   J. Kymissis, C. Kendall, J. Paradiso, and N. Gershenfeld, "Parasitic power harvesting in shoes," in *Wearable Computers, 1998. Digest of Papers. Second International Symposium on*, 1998, pp. 132-139.

[8]   A. Erturk, O. Bilgen, and D. Inman, "Power generation and shunt damping performance of a single crystal lead magnesium niobate-lead zirconate titanate unimorph: Analysis and experiment," *Applied Physics Letters,* vol. 93, p. 224102, 2008.

[9]   P. Rakbamrung, M. Lallart, D. Guyomar, N. Muensit, C. Thanachayanont, C. Lucat*, et al.*, "Performance comparison of PZT and PMN–PT piezoceramics for vibration energy harvesting using standard or nonlinear approach," *Sensors and Actuators A: Physical,* vol. 163, pp. 493-500, 2010.

[10]   M. A. Karami, O. Bilgen, D. J. Inman, and M. I. Friswell, "Experimental and analytical parametric study of single-crystal unimorph beams for vibration energy harvesting," *Ultrasonics, Ferroelectrics, and Frequency Control, IEEE Transactions on,* vol. 58, pp. 1508-1520, 2011.

[11]   S. E. Moon, S. Q. Lee, S.-k. Lee, Y.-G. Lee, Y. S. Yang, K.-H. Park*, et al.*, "Sustainable vibration energy harvesting based on Zr-doped PMN-PT piezoelectric single crystal cantilevers," *ETRI journal,* vol. 31, pp. 688-694, 2009.

[12]   B. Ren, Y. Zhang, Q. Zhang, X. Li, W. Di, X. Zhao*, et al.*, "Energy harvesting using multilayer structure based on 0.71 Pb (Mg1/3Nb2/3) O3– 0.29 PbTiO3 single crystal," *Applied Physics A,* vol. 100, pp. 125-128, 2010.

[13]   S.-J. Jeong, D.-S. Lee, M.-S. Kim, D.-H. Im, I.-S. Kim, and K.-H. Cho, "Properties of piezoelectric ceramic with textured structure for energy harvesting," *Ceramics International,* vol. 38, pp. S369-S372, 2012.

[14]   H.-B. Fang, J.-Q. Liu, Z.-Y. Xu, L. Dong, L. Wang, D. Chen*, et al.*, "Fabrication and performance of MEMS-based piezoelectric power

generator for vibration energy harvesting," *Microelectronics Journal,* vol. 37, pp. 1280-1284, 2006.

[15] C. M. T. Tien and N. S. Goo, "Use of a piezocomposite generating element in energy harvesting," *Journal of Intelligent Material Systems and Structures,* p. 1045389X10381658, 2010.

[16] R. Elfrink, T. Kamel, M. Goedbloed, S. Matova, D. Hohlfeld, Y. Van Andel*, et al.*, "Vibration energy harvesting with aluminum nitride-based piezoelectric devices," *Journal of Micromechanics and Microengineering,* vol. 19, p. 094005, 2009.

[17] D. Isarakorn, D. Briand, P. Janphuang, A. Sambri, S. Gariglio, J. Triscone*, et al.*, "The realization and performance of vibration energy harvesting MEMS devices based on an epitaxial piezoelectric thin film," *Smart Materials and Structures,* vol. 20, p. 025015, 2011.

[18] J. Twiefel, B. Richter, T. Sattel, and J. Wallaschek, "Power output estimation and experimental validation for piezoelectric energy harvesting systems," *Journal of Electroceramics,* vol. 20, pp. 203-208, 2008.

[19] M. Lumentut and I. Howard, "Analytical and experimental comparisons of electromechanical vibration response of a piezoelectric bimorph beam for power harvesting," *Mechanical Systems and Signal Processing,* vol. 36, pp. 66-86, 2013.

[20] L. Mateu and F. Moll, "Optimum piezoelectric bending beam structures for energy harvesting using shoe inserts," *Journal of Intelligent Material Systems and Structures,* vol. 16, pp. 835-845, 2005.

[21] L. Mateu and F. Moll, "Appropriate charge control of the storage capacitor in a piezoelectric energy harvesting device for discontinuous load operation," *Sensors and Actuators A: Physical,* vol. 132, pp. 302-310, 2006.

[22] J. Granstrom, J. Feenstra, H. A. Sodano, and K. Farinholt, "Energy harvesting from a backpack instrumented with piezoelectric shoulder straps," *Smart Materials and Structures,* vol. 16, p. 1810, 2007.

[23] K. M. Farinholt, N. A. Pedrazas, D. M. Schluneker, D. W. Burt, and C. R. Farrar, "An energy harvesting comparison of piezoelectric and ionically conductive polymers," *Journal of Intelligent Material Systems and Structures,* vol. 20, pp. 633-642, 2009.

[24] T. Eggborn, "Analytical models to predict power harvesting with piezoelectric materials," 2003.

[25] J. Ajitsaria, S.-Y. Choe, D. Shen, and D. Kim, "Modeling and analysis of a bimorph piezoelectric cantilever beam for voltage generation," *Smart Materials and Structures,* vol. 16, p. 447, 2007.

[26] M. Lumentut and I. Howard, "Electromechanical finite element modelling for dynamic analysis of a cantilevered piezoelectric energy harvester with tip mass offset under base excitations," *Smart Materials and Structures,* vol. 23, p. 095037, 2014.

[27] S. Korla, R. Leon, I. N. Tansel, A. Yenilmez, A. Yapici, and M. Demetgul, "Design and testing of an efficient and compact piezoelectric energy harvester," *Microelectronics Journal,* vol. 42, pp. 265-270, 2011.

[28]   N. G. Elvin, A. A. Elvin, and M. Spector, "A self-powered mechanical strain energy sensor," *Smart Materials and structures,* vol. 10, p. 293, 2001.

[29]   M. Umeda, K. Nakamura, and S. Ueha, "Analysis of the transformation of mechanical impact energy to electric energy using piezoelectric vibrator," *Japanese Journal of Applied Physics,* vol. 35, p. 3267, 1996.

[30]   N. Elvin, A. Elvin, and D. Choi, "A self-powered damage detection sensor," *The Journal of Strain Analysis for Engineering Design,* vol. 38, pp. 115-124, 2003.

[31]   T. Ng and W. Liao, "Sensitivity analysis and energy harvesting for a self-powered piezoelectric sensor," *Journal of Intelligent Material Systems and Structures,* vol. 16, pp. 785-797, 2005.

[32]   D. Shen, J.-H. Park, J. H. Noh, S.-Y. Choe, S.-H. Kim, H. C. Wikle*, et al.*, "Micromachined PZT cantilever based on SOI structure for low frequency vibration energy harvesting," *Sensors and actuators A: physical,* vol. 154, pp. 103-108, 2009.

[33]   J.-Q. Liu, H.-B. Fang, Z.-Y. Xu, X.-H. Mao, X.-C. Shen, D. Chen*, et al.*, "A MEMS-based piezoelectric power generator array for vibration energy harvesting," *Microelectronics Journal,* vol. 39, pp. 802-806, 2008.

[34]   A. Erturk and D. J. Inman, "Issues in mathematical modeling of piezoelectric energy harvesters," *Smart Materials and Structures,* vol. 17, p. 065016, 2008.

[35]   A. Erturk and D. J. Inman, "On mechanical modeling of cantilevered piezoelectric vibration energy harvesters," *Journal of Intelligent Material Systems and Structures,* 2008.

[36]   A. Erturk and D. J. Inman, "An experimentally validated bimorph cantilever model for piezoelectric energy harvesting from base excitations," *Smart Materials and Structures,* vol. 18, p. 025009, 2009.

[37]   J. M. Renno, M. F. Daqaq, and D. J. Inman, "On the optimal energy harvesting from a vibration source," *Journal of sound and vibration,* vol. 320, pp. 386-405, 2009.

[38]   G. Poulin, E. Sarraute, and F. Costa, "Generation of electrical energy for portable devices: Comparative study of an electromagnetic and a piezoelectric system," *Sensors and Actuators A: physical,* vol. 116, pp. 461-471, 2004.

[39]   C. D. M. Junior, A. Erturk, and D. J. Inman, "An electromechanical finite element model for piezoelectric energy harvester plates," *Journal of Sound and Vibration,* vol. 327, pp. 9-25, 2009.

[40]   Y. Shu and I. Lien, "Efficiency of energy conversion for a piezoelectric power harvesting system," *Journal of micromechanics and microengineering,* vol. 16, p. 2429, 2006.

[41]   Y. Hu, T. Hu, and Q. Jiang, "Coupled analysis for the harvesting structure and the modulating circuit in a piezoelectric bimorph energy harvester," *Acta Mechanica Solida Sinica,* vol. 20, pp. 296-308, 2007.

[42]   J. Dietl, A. Wickenheiser, and E. Garcia, "A Timoshenko beam model for cantilevered piezoelectric energy harvesters," *Smart Materials and Structures,* vol. 19, p. 055018, 2010.

[43]   J. M. Dietl and E. Garcia, "Beam shape optimization for power harvesting," *Journal of Intelligent Material Systems and Structures,* 2010.

[44]   M. Marzencki, M. Defosseux, and S. Basrour, "MEMS vibration energy harvesting devices with passive resonance frequency adaptation capability," *Microelectromechanical Systems, Journal of,* vol. 18, pp. 1444-1453, 2009.

[45]   X. Gao, W.-H. Shih, and W. Y. Shih, "Vibration energy harvesting using piezoelectric unimorph cantilevers with unequal piezoelectric and nonpiezoelectric lengths," *Applied physics letters,* vol. 97, p. 233503, 2010.

[46]   L. Gammaitoni, I. Neri, and H. Vocca, "The benefits of noise and nonlinearity: Extracting energy from random vibrations," *Chemical Physics,* vol. 375, pp. 435-438, 2010.

[47]   R. R. Knight, C. Mo, and W. W. Clark, "MEMS interdigitated electrode pattern optimization for a unimorph piezoelectric beam," *Journal of electroceramics,* vol. 26, pp. 14-22, 2011.

[48]   R. Ly, M. Rguiti, S. D'Astorg, A. Hajjaji, C. Courtois, and A. Leriche, "Modeling and characterization of piezoelectric cantilever bending sensor for energy harvesting," *Sensors and Actuators A: Physical,* vol. 168, pp. 95-100, 2011.

[49]   C. D. Richards, M. J. Anderson, D. F. Bahr, and R. F. Richards, "Efficiency of energy conversion for devices containing a piezoelectric component," *Journal of Micromechanics and Microengineering,* vol. 14, p. 717, 2004.

[50]   R. Masana and M. F. Daqaq, "Electromechanical modeling and nonlinear analysis of axially loaded energy harvesters," *Journal of Vibration and Acoustics,* vol. 133, p. 011007, 2011.

[51]   A. Abdelkefi, F. Najar, A. Nayfeh, and S. B. Ayed, "An energy harvester using piezoelectric cantilever beams undergoing coupled bending–torsion vibrations," *Smart Materials and Structures,* vol. 20, p. 115007, 2011.

[52]   A. Abdelkefi, M. Hajj, and A. Nayfeh, "Piezoelectric energy harvesting from transverse galloping of bluff bodies," *Smart Materials and Structures,* vol. 22, p. 015014, 2013.

[53]   A. Abdelkefi, A. Nayfeh, and M. Hajj, "Effects of nonlinear piezoelectric coupling on energy harvesters under direct excitation," *Nonlinear Dynamics,* vol. 67, pp. 1221-1232, 2012.

[54]   A. Syta, C. Bowen, H. Kim, A. Rysak, and G. Litak, "Experimental analysis of the dynamical response of energy harvesting devices based on bistable laminated plates," *Meccanica,* vol. 50, pp. 1961-1970, 2015.

[55]   A. Bibo and M. F. Daqaq, "Energy harvesting under combined aerodynamic and base excitations," *Journal of Sound and Vibration,* vol. 332, pp. 5086-5102, 2013.

[56]   A. Bibo, A. Abdelkefi, and M. F. Daqaq, "Modeling and characterization of a piezoelectric energy harvester under Combined Aerodynamic and Base Excitations," *Journal of Vibration and Acoustics,* vol. 137, p. 031017, 2015.

[57]   H. Dai, A. Abdelkefi, and L. Wang, "Piezoelectric energy harvesting from concurrent vortex-induced vibrations and base excitations," *Nonlinear Dynamics,* vol. 77, pp. 967-981, 2014.

[58]   G. Litak, M. I. Friswell, and S. Adhikari, "Regular and chaotic vibration in a piezoelectric energy harvester," *Meccanica,* pp. 1-9, 2015.

[59]   S. Jiang, X. Li, S. Guo, Y. Hu, J. Yang, and Q. Jiang, "Performance of a piezoelectric bimorph for scavenging vibration energy," *Smart Materials and Structures,* vol. 14, p. 769, 2005.

[60]   S. Roundy, E. S. Leland, J. Baker, E. Carleton, E. Reilly, E. Lai*, et al.*, "Improving power output for vibration-based energy scavengers," *Pervasive Computing, IEEE,* vol. 4, pp. 28-36, 2005.

[61]   S. B. Ayed, A. Abdelkefi, F. Najar, and M. R. Hajj, "Design and performance of variable-shaped piezoelectric energy harvesters," *Journal of Intelligent Material Systems and Structures,* p. 1045389X13489365, 2013.

[62]   M. Rosa and C. De Marqui Junior, "Modeling and analysis of a piezoelectric energy harvester with varying cross-sectional area," *Shock and Vibration,* vol. 2014, 2014.

[63]   M. Brojan, T. Videnic, and F. Kosel, "Large deflections of nonlinearly elastic non-prismatic cantilever beams made from materials obeying the generalized Ludwick constitutive law," *Meccanica,* vol. 44, pp. 733-739, 2009.

[64]   S. Matova, M. Renaud, M. Jambunathan, M. Goedbloed, and R. Van Schaijk, "Effect of length/width ratio of tapered beams on the performance of piezoelectric energy harvesters," *Smart Materials and Structures,* vol. 22, p. 075015, 2013.

[65]   F. Goldschmidtboeing and P. Woias, "Characterization of different beam shapes for piezoelectric energy harvesting," *Journal of micromechanics and microengineering,* vol. 18, p. 104013, 2008.

[66]   D. Benasciutti, L. Moro, S. Zelenika, and E. Brusa, "Vibration energy scavenging via piezoelectric bimorphs of optimized shapes," *Microsystem Technologies,* vol. 16, pp. 657-668, 2010.

[67]   M. Karami Khorramabadi, "Free vibration of functionally graded beams with piezoelectric layers subjected to axial load," *Journal of Solid Mechanics,* vol. 1, pp. 22-28, 2009.

[68]   N. Wattanasakulpong and V. Ungbhakorn, "Free vibration analysis of functionally graded beams with general elastically end constraints by DTM," *World Journal of Mechanics,* vol. 2, p. 297, 2012.

[69]   S. Mohanty, "Free vibration analysis of a pretwisted functionally graded material cantilever Timoshenko beam," 2012.

[70]   H. Yaghoobi and A. Fereidoon, "Influence of neutral surface position on deflection of functionally graded beam under uniformly distributed load," *World Applied Sciences Journal,* vol. 10, pp. 337-341, 2010.

[71]   G. R. Koochaki, "Free Vibration Analysis of Functionally Graded Beams," *World Academy of Science, Engineering and Technology, International Journal of Mechanical, Aerospace, Industrial, Mechatronic and Manufacturing Engineering,* vol. 5, pp. 514-517, 2011.

[72]   M. Rafiee, H. Kalhori, and S. Mareishi, "Nonlinear resonance analysis of clamped functionally graded beams," in *16th International Conference on Composite Structures*, 2011.

[73]   M. Şimşek, "Static analysis of a functionally graded beam under a uniformly distributed load by Ritz method," *Int J Eng Appl Sci,* vol. 1, pp. 1-11, 2009.

[74]   S. Sina, H. Navazi, and H. Haddadpour, "An analytical method for free vibration analysis of functionally graded beams," *Materials & Design,* vol. 30, pp. 741-747, 2009.

[75]   C. A. Almeida, J. C. Albino, I. F. Menezes, and G. H. Paulino, "Geometric nonlinear analyses of functionally graded beams using a tailored Lagrangian formulation," *Mechanics Research Communications,* vol. 38, pp. 553-559, 2011.

[76]   S. Li, J. Hu, C. Zhai, and L. Xie, "Static, Vibration, and Transient Dynamic Analyses by Beam Element with Adaptive Displacement Interpolation Functions," *Mathematical Problems in Engineering,* vol. 2012, 2012.

[77]   S. Mohanty, R. Dash, and T. Rout, "Static and dynamic analysis of a functionally graded Timoshenko beam on Winkler's elastic foundation," *Journal of Engineering Research and Studies,* vol. 1, pp. 149-165, 2010.

[78]   T. H. Daouadji, A. Tounsi, L. Hadji, A. H. Henni, and A. B. El Abbes, "A theoretical analysis for static and dynamic behavior of functionally graded plates," *Materials Physics and Mechanics,* vol. 14, pp. 110-128, 2012.

[79]   A. Nikkhoo and M. Amankhani, "Dynamic behavior of functionally graded beams traversed by a moving random load," *Indian Journal of Science and Technology,* vol. 5, pp. 3727-3731, 2012.

[80]   C. A. D. Fraga Filho, F. C. M. Menandro, R. H. P. de Romero, and J. S. R. Saenz, "Dynamic Analysis with Stress Recovery for Functionally Graded Materials: Numerical Simulation and Experimental Benchmarking," *International Journal on Advanced Materials and Technologies (IREAMT),* vol. 2, pp. 21-31, 2014.

[81]   A. E. Alshorbagy, M. Eltaher, and F. Mahmoud, "Free vibration characteristics of a functionally graded beam by finite element method," *Applied Mathematical Modelling,* vol. 35, pp. 412-425, 2011.

[82]   L.-L. Ke and Y.-S. Wang, "Size effect on dynamic stability of functionally graded microbeams based on a modified couple stress theory," *Composite Structures,* vol. 93, pp. 342-350, 2011.

[83]   S.-R. Li and R. C. Batra, "Relations between buckling loads of functionally graded Timoshenko and homogeneous Euler–Bernoulli beams," *Composite Structures,* vol. 95, pp. 5-9, 2013.

[84]   K. S. Anandrao, R. Gupta, P. Ramachandran, and G. V. Rao, "Free vibration analysis of functionally graded beams," *Defence Science Journal,* vol. 62, pp. 139-146, 2012.

[85]   N. Omidi, M. Karami Khorramabadi, and A. Niknejad, "Dynamic stability of functionally graded beams with piezoelectric layers located on a continuous elastic foundation," *Journal of Solid Mechanics,* vol. 1, pp. 130-136, 2009.

[86]   M. Şimşek, T. Kocatürk, and Ş. D. Akbaş, "Dynamics of an axially functionally graded beam carrying a moving harmonic load," in *16th International conference on composite structures*, 2011.

[87]   I. Elishakoff and S. Candan, "Apparently first closed-form solution for vibrating: inhomogeneous beams," *International Journal of Solids and Structures,* vol. 38, pp. 3411-3441, 2001.

[88] I. Elishakoff and Z. Guede, "Analytical polynomial solutions for vibrating axially graded beams," *Mechanics of Advanced Materials and Structures,* vol. 11, pp. 517-533, 2004.

[89] L. Wu, Q.-s. Wang, and I. Elishakoff, "Semi-inverse method for axially functionally graded beams with an anti-symmetric vibration mode," *Journal of sound and vibration,* vol. 284, pp. 1190-1202, 2005.

[90] B. Sankar, "An elasticity solution for functionally graded beams," *Composites Science and Technology,* vol. 61, pp. 689-696, 2001.

[91] Y. Huang and X.-F. Li, "A new approach for free vibration of axially functionally graded beams with non-uniform cross-section," *Journal of Sound and Vibration,* vol. 329, pp. 2291-2303, 2010.

[92] A. Shahba, R. Attarnejad, and S. Hajilar, "Free vibration and stability of axially functionally graded tapered Euler-Bernoulli beams," *Shock and Vibration,* vol. 18, pp. 683-696, 2011.

[93] A. Shahba, R. Attarnejad, M. T. Marvi, and S. Hajilar, "Free vibration and stability analysis of axially functionally graded tapered Timoshenko beams with classical and non-classical boundary conditions," *Composites Part B: Engineering,* vol. 42, pp. 801-808, 2011.

[94] A. Shahba and S. Rajasekaran, "Free vibration and stability of tapered Euler–Bernoulli beams made of axially functionally graded materials," *Applied Mathematical Modelling,* vol. 36, pp. 3094-3111, 2012.

[95] M. Aydogdu, "Semi-inverse method for vibration and buckling of axially functionally graded beams," *Journal of Reinforced Plastics and Composites,* 2008.

[96] J. Murin, M. Aminbaghai, and V. Kutiš, "Exact solution of the bending vibration problem of FGM beams with variation of material properties," *Engineering structures,* vol. 32, pp. 1631-1640, 2010.

[97] A. Görnandt and U. Gabbert, "Finite element analysis of thermopiezoelectric smart structures," *Acta Mechanica,* vol. 154, pp. 129-140, 2002.

[98] S. S. Vel and R. Batra, "Generalized plane strain thermopiezoelectric analysis of multilayered plates," *Journal of Thermal Stresses,* vol. 26, pp. 353-377, 2003.

[99] M. Sanbi, R. Saadani, K. Sbai, and M. Rahmoune, "Thermoelastic and pyroelectric couplings effects on dynamics and active control of smart piezolaminated beam modeled by finite element method," *Smart Materials Research,* vol. 2014, 2014.

[100] H.-J. Ding, F.-L. Guo, and P.-F. Hou, "A general solution for piezothermoelasticity of transversely isotropic piezoelectric materials and its applications," *International journal of engineering science,* vol. 38, pp. 1415-1440, 2000.

[101] F. Heidary and M. R. Eslami, "Piezo-control of forced vibrations of a thermoelastic composite plate," *Composite structures,* vol. 74, pp. 99-105, 2006.

[102] S. N. Ahmad, C. Upadhyay, and C. Venkatesan, "Electro-thermo-elastic formulation for the analysis of smart structures," *Smart Materials and Structures,* vol. 15, p. 401, 2006.

[103] R. Kumar, B. Mishra, and S. Jain, "Thermally induced vibration control of cylindrical shell using piezoelectric sensor and actuator," *The International Journal of Advanced Manufacturing Technology,* vol. 38, pp. 551-562, 2008.

[104] J. Oh, M. Cho, and J.-S. Kim, "Enhanced lower-order shear deformation theory for fully coupled electro-thermo-mechanical smart laminated plates," *Smart Materials and Structures,* vol. 16, p. 2229, 2007.

[105] T. Roy, P. Manikandan, and D. Chakraborty, "Improved shell finite element for piezothermoelastic analysis of smart fiber reinforced composite structures," *Finite Elements in Analysis and Design,* vol. 46, pp. 710-720, 2010.

[106] J. P. Jiang and D. X. Li, "A new finite element model for piezothermoelastic composite beam," *Journal of Sound and Vibration,* vol. 306, pp. 849-864, 2007.

[107] U. Icardi and M. Di Sciuva, "Large-deflection and stress analysis of multilayered plates with induced-strain actuators," *Smart Materials and Structures,* vol. 5, p. 140, 1996.

[108] A. Mukherjee and A. S. Chaudhuri, "Piezolaminated beams with large deformations," *International Journal of Solids and Structures,* vol. 39, pp. 4567-4582, 2002.

[109] S. Yi, S. F. Ling, and M. Ying, "Large deformation finite element analyses of composite structures integrated with piezoelectric sensors and actuators," *Finite elements in analysis and design,* vol. 35, pp. 1-15, 2000.

[110] S. Lentzen and R. Schmidt, "Nonlinear finite element modeling of vibration control of composite piezolaminated composite plates and shells," in *Smart Structures and Materials*, 2005, pp. 130-141.

[111] G. Shi and S. Atluri, "Active control of nonlinear dynamic response of space-frames using piezo-electric actuators," *Computers & structures,* vol. 34, pp. 549-564, 1990.

[112] Y.-H. Zhou and J. Wang, "Vibration control of piezoelectric beam-type plates with geometrically nonlinear deformation," *International Journal of Non-Linear Mechanics,* vol. 39, pp. 909-920, 2004.

[113] W. Wang, J. Cao, C. R. Bowen, S. Zhou, and J. Lin, "Optimum resistance analysis and experimental verification of nonlinear piezoelectric energy harvesting from human motions," *Energy,* vol. 118, pp. 221-230, 2017.

[114] H. Tzou and Y. Zhou, "Dynamics and control of piezoelectric circular plates with geometrical nonlinearity," *J. Sound Vib,* vol. 188, pp. 189-207, 1995.

[115] H. Tzou and Y. Zhou, "Nonlinear piezothermoelasticity and multi-field actuations, Part 2: Control of nonlinear deflection, buckling and dynamics," *Journal of Vibration and Acoustics,* vol. 119, pp. 382-389, 1997.

[116] Y.-H. Zhou and H. Tzou, "Active control of nonlinear piezoelectric circular shallow spherical shells," *International Journal of Solids and Structures,* vol. 37, pp. 1663-1677, 2000.

[117] A. Mukherjee and A. S. Chaudhuri, "Nonlinear dynamic response of piezolaminated smart beams," *Computers & structures,* vol. 83, pp. 1298-1304, 2005.

[118] A. Lazarus, O. Thomas, and J.-F. Deü, "Finite element reduced order models for nonlinear vibrations of piezoelectric layered beams with applications to NEMS," *Finite Elements in Analysis and Design,* vol. 49, pp. 35-51, 2012.

[119] S. Stoykov, C. Hofreither, and S. Margenov, "Isogeometric analysis for nonlinear dynamics of Timoshenko beams," in *Numerical Methods and Applications*, ed: Springer, 2014, pp. 138-146.

[120] A. Mitra, P. Sahoo, and K. Saha, "Large amplitude forced vibration analysis of cross-beam system through energy method," *International journal of engineering, science and technology,* vol. 2, pp. 113-133, 2010.

[121] K. Deb, *Multi-objective optimization using evolutionary algorithms* vol. 16: John Wiley & Sons, 2001.

[122] F. Herrera, M. Lozano, and J. L. Verdegay, "Tackling real-coded genetic algorithms: Operators and tools for behavioural analysis," *Artificial intelligence review,* vol. 12, pp. 265-319, 1998.

[123] T. Roy and D. Chakraborty, "Optimal vibration control of smart fiber reinforced composite shell structures using improved genetic algorithm," *Journal of Sound and Vibration,* vol. 319, pp. 15-40, 2009.

[124] A. R. Biswal, T. Roy, and R. K. Behera, "Genetic algorithm-and finite element-based design and analysis of nonprismatic piezolaminated beam for optimal vibration energy harvesting," *Proceedings of the Institution of Mechanical Engineers, Part C: Journal of Mechanical Engineering Science,* p. 0954406215595253, 2015.

[125] Y.-C. Chuang, C.-T. Chen, and C. Hwang, "A real-coded genetic algorithm with a direction-based crossover operator," *Information Sciences,* vol. 305, pp. 320-348, 2015.

[126] Y.-C. Chuang, C.-T. Chen, and C. Hwang, "A simple and efficient real-coded genetic algorithm for constrained optimization," *Applied Soft Computing,* vol. 38, pp. 87-105, 2016.

[127] G. Singh, N. Gupta, and M. Khosravy, "New crossover operators for real coded genetic algorithm (RCGA)," in *2015 International Conference on Intelligent Informatics and Biomedical Sciences (ICIIBMS)*, 2015, pp. 135-140.

[128] Q. Pan, X. He, Y.-z. Cai, Z.-h. Wang, and F. Su, "Improved real-coded genetic algorithm solution for unit commitment problem considering energy saving and emission reduction demands," *Journal of Shanghai Jiaotong University (Science),* vol. 20, pp. 218-223, 2015.

[129] N. S. Kwak and J. Lee, "An enhancement of selection and crossover operations in real-coded genetic algorithm for large-dimensionality optimization," *Journal of Mechanical Science and Technology,* vol. 30, pp. 237-247, 2016.

[130] K. Deep, "A Novel Crossover Operator Designed to Exploit Synergies of Two Crossover Operators for Real-Coded Genetic Algorithms," in *Proceedings of Fifth International Conference on Soft Computing for Problem Solving*, 2016, pp. 343-350.

[131] J. Reddy and C. Chin, "Thermomechanical analysis of functionally graded cylinders and plates," *Journal of Thermal Stresses,* vol. 21, pp. 593-626, 1998.

[132] J. M. Gere and S. Timoshenko, "Mechanics of materials Brooks," *Cole, Pacific Grove, CA,* pp. 815-39, 2001.

[133] S. Khot and N. P. Yelve, "Modeling and response analysis of dynamic systems by using ANSYS© and MATLAB©," *Journal of Vibration and Control,* p. 1077546310377913, 2010.

[134] J. N. Reddy, *An Introduction to Nonlinear Finite Element Analysis: with applications to heat transfer, fluid mechanics, and solid mechanics*: OUP Oxford, 2014.

[135] K.-J. Bathe, *Finite Element Procedures*: Klaus-Jurgen Bathe, 2006.

[136] K. Deb and S. Gulati, "Design of truss-structures for minimum weight using genetic algorithms," *Finite elements in analysis and design,* vol. 37, pp. 447-465, 2001.

[137] A. M. Flynn and S. R. Sanders, "Fundamental limits on energy transfer and circuit considerations for piezoelectric transformers," *Power Electronics, IEEE Transactions on,* vol. 17, pp. 8-14, 2002.

[138] J. Bruch Jr, J. Sloss, S. Adali, and I. Sadek, "Optimal piezo-actuator locations/lengths and applied voltage for shape control of beams," *Smart Materials and Structures,* vol. 9, p. 205, 2000.

[139] K. Deb, K. Sindhya, and T. Okabe, "Self-adaptive simulated binary crossover for real-parameter optimization," in *Proceedings of the 9th annual conference on Genetic and evolutionary computation*, 2007, pp. 1187-1194.

[140] S. S. Rao and F. F. Yap, *Mechanical vibrations* vol. 4: Addison-Wesley Reading, 1995.

[141] W.-S. Hwang and H. C. Park, "Finite element modeling of piezoelectric sensors and actuators," *AIAA journal,* vol. 31, pp. 930-937, 1993.

Dissemination

A. International journals

- AR Biswal, T Roy and RK Behera, Optimal vibration energy harvesting from nonprismatic piezolaminated beam. **Smart structures and systems** 2017, Vol. 19 (4) 403-413.

- AR Biswal, T Roy and RK Behera, Optimal Vibration Energy Harvesting from Nonprismatic Axially Functionally Graded Piezolaminated cantilever Beam using Genetic Algorithm. **Journal of Intelligent material system and structures.** 2017: 1045389X16682842.

- Alok Ranjan Biswal, Tarapada Roy, and Rabindra Kumar Behera, Geometric nonlinear finite element and genetic algorithm based optimal vibration energy harvesting from nonprismatic axially functionally graded piezolaminated beam. **Journal of Vibration and Control,** 2016, DOI: 1077546316671482.

- A.R.Biswal, T.Roy, R.K.Behera, P.K.Parida and S.K.Pradhan, Finite element based modelling of a piezolaminated tapered beam for voltage generation. **Proceedia Engineering**, 144 (2016) 613 – 620.

- AR Biswal, T Roy and RK Behera, Genetic algorithm-and finite element-based design and analysis of nonprismatic piezolaminated beam for optimal vibration energy harvesting. Proc. IMechE Part C: **J Mechanical Engineering Science** 2016, Vol. 230(14) 2532–2548.

B. International conferences

- A.R.Biswal, R.K.Behera and T.Roy, Finite element based modelling of a piezolaminated tapered beam for voltage generation. International Conference on Vibration problem (ICOVP-2015), IIT, Guwahati, Assam, 14-17th December, 2015.

- R.K.Behera, A.R.Biswal and T.Roy, Finite element based vibration analysis of a nonprismatic Timoshenko beam with transverse open crack. International Conference on Vibration problem (ICOVP-2015), IIT, Guwahati, Assam, 14-17th December, 2015.

- A.R.Biswal, T.Roy and R.K.Behera, Finite element modelling of a beam coupled with piezoelectric patch for voltage generation. Sixth International Conference on Theoretical, Applied, Computational and Experimental Mechanices (ICTACEM-2014), IIT Kharagpur, West Bengal, 29-31st December, 2014.

- A.R.Biswal, R.K.Behera and T.Roy, Vibration analysis of a Timoshenko beam with transverse open crack by Finite Element Method. International Mechanical Engineering Congress (IMEC, 2014), NIT, Tiruchirappalli, Tamil Nadu, 13-15th june2014.

- A.R.Biswal, R.K.Behera and T.Roy, Vibration Analysis of a Cracked Timoshenko Beam. International conference on Industrial Engineering Science and Applications (IESA, 2014), NIT, Durgapur, West Bengal, 2-4th April, 2014.

- A.R.Biswal, T.Roy and R.K.Behera, Free Vibration Analysis of a Cracked Beam. In: Proceedings of All India seminar on Recent Advances in mechanical Engineering, Bhubaneswar, Odisha, 16-17th march 2013.